Design of a modular one Newton hydrogen peroxide monopropellant thruster, including feed system and test setup

T. Franken

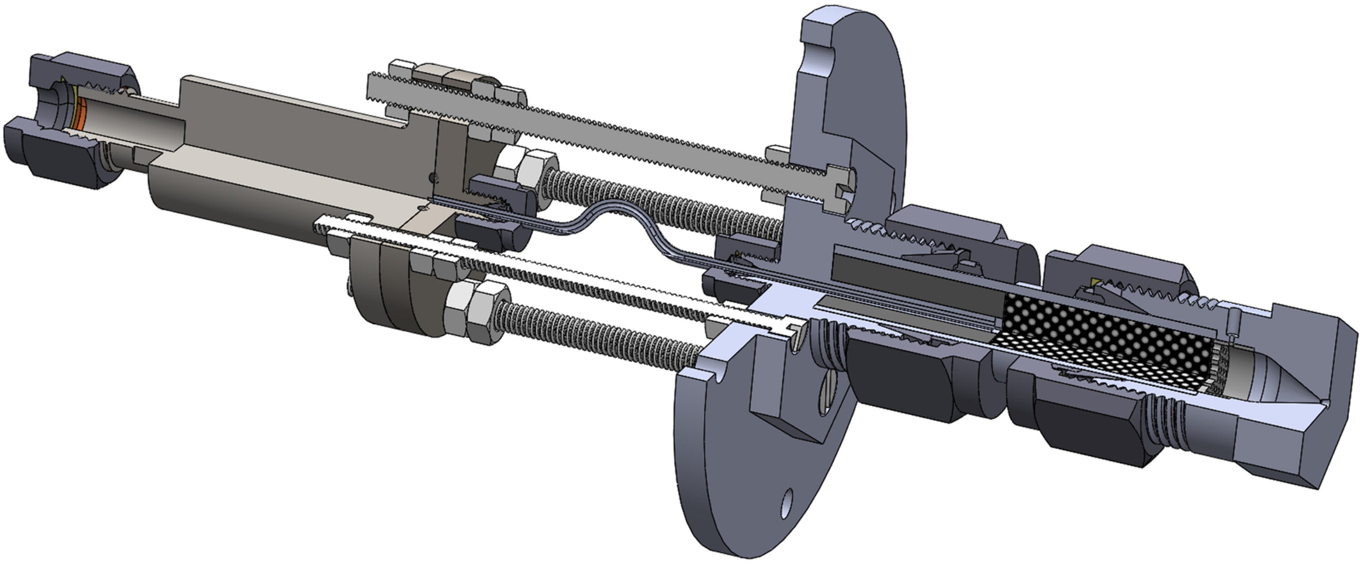

Design of a modular one Newton hydrogen peroxide monopropellant thruster, including feed system and test setup

by

T. Franken

to obtain the degree of Master of Science
at the Delft University of Technology,
to be defended publicly on Thursday 10 September, 2020 at 10:00 am.

Student number:	4617282		
Project duration:	15 July, 2019 – 10 September, 2020		
Thesis committee:	Dr. J. Guo,	Delft University of Technology	*Chairman*
	Dr. B.V.S. Jyoti,	Delft University of Technology	*Supervisor*
	Ir. F. Valencia Bel,	European Space Agency	*Supervisor*
	Ir. R. Noomen,	Delft University of Technology	

TU Delft

Preface

This document is the product of a year's work on the design of a monopropellant thruster, in collaboration with the Chemical Propulsion department in the European Space Agency (ESA). I would like to thank my supervisor, Mr. Valencia Bel, for his extensive support throughout the entire project. Additionally, I would like to thank the academic supervisor, Dr. Jyoti, for her guidance during the thesis, as well as the preceding literature review. Finally, I would like to express my gratitude to my family, for supporting my academic career, as well as my girlfriend, for her support and for making our home a pleasant working environment during the coronavirus pandemic.

T. Franken
Delft, August 2020

Contents

List of Figures

List of Tables

List of Acronyms

CNC	Computer Numerical Control
DLR	Deutsches Zentrum für Luft- und Raumfahrt
EPDM	Ethylene Propylene Diene Monomer Rubber
ESA	European Space Agency
ESTEC	European Space Research and Technology Centre
EU	European Union
FFKM	Perfluoroelastomers
FKM	Fluoroelastomers
HTP	High Test Peroxide
MEOP	Maximum Expected Operating Pressure
MGT	Modular Green Thruster (requirement indicator)
NBR	Nitrile Butadiene Rubber
NPT	National Pipe Thread
PCTFE	Poly Chloro Tri Fluoro Ethylene
PEEK	Polyether Ether Ketone
PTFE	Poly Tetra Fluoro Ethylene
REACH	Registration of Evaluation Authorisation and Restriction of Chemicals
SS	Stainless Steel

Executive Summary

In the latest years, there has been a significant interest in the use of green propellants in the space industry. One of these propellants is hydrogen peroxide and, even though it has been around as a propellant for a while, there is an interest in finding new ways to maximize its performance, either by the use of catalyst beds, or new technological solutions. The goal of this design a platform that provides the capability of testing and comparing the performance of these solutions. This was done by designing a modular one Newton hydrogen peroxide monopropellant thruster, including feed system and test setup. To better understand the decomposition of hydrogen peroxide and predict the performance of catalyst beds, a simplified mathematical model was created of the decomposition process. Though calibration with test data is required for reliable results, results similar to other available model were found by varying some of the reaction parameters and the model was able to show the effect of the feed pressure and mass flow rate on the required catalyst bed length as well as the associated pressure drop. The actual design process was started by listing the design requirements and creating a design concept. A solution for the modular concept was found in combining commercially available tube fittings with custom fitting bodies on the thruster components. A thermal assessment was used to confirm the suitability of these components for use in the thruster. A baseline thruster design was created for use with catalyst beds. This includes the detailed design of all thruster subcomponents, a pressure drop assessment and a thermal model in EcosimPro. Additionally, a concept plan was described for the testing of several alternative decomposition concepts. These concepts are the initiation of decomposition by heating the propellant, creating a spark and using a laser to create a plasma arc. For each of these technologies, a concept level design was created for the potential integration onto the thruster decomposition chamber. The propellant is provided to the thruster through the means of a propellant feed system. This system is designed to be a single assembly within a frame of aluminium extrusions, making the system very portable. A mass flow sensor capable of measuring the mass flow rate in pulsed mode operation was not found. Therefore, this system contains two propellant tanks. One of the propellant tanks is small and mounted on an accurate scale and connected to the rest of the feed system using flexible tubes. The propellant used is measured by weighing the propellant tank before and after the completion of a pulse train. A test setup was designed in which the thruster is mounted in a down-firing orientation. As was the case for the propellant feed system, the test setup is created using aluminium extrusions to make the frame. This makes the test setup highly portable as well. A plan was created for the thruster test campaign, for verification of the thruster performance requirements. Finally, a guide was created for the manufacturing of the custom components in the thruster design using traditional methods. However, since the scale of the thruster is small and some components are complex, computer-controlled machines or even additive manufacturing methods are advised. Overall, this report describes the entire design phase, including the required assessments, for the design of the complete system, which includes the modular thruster, propellant feed system, test setup and a plan for the test campaign.

1

Introduction

High concentration Hydrogen Peroxide, also known as High Test Peroxide (HTP), has been around as rocket propellant for several decades. It was popular as a monopropellant in reaction control thrusters until the discovery and technical viability of Hydrazine [109], which has an improved performance over Hydrogen Peroxide. However, in 2011 the European Commission has added Hydrazine to its candidate list of ”substances of very high concern” in its Registration of Evaluation Authorisation and Restriction of Chemicals (REACH) framework [1], as Hydrazine is very toxic. This means that there is a risk that the use of Hydrazine will be prohibited in the near future. As this causes an interest in low-toxicity ”green” alternatives, Hydrogen Peroxide is considered again [2], though it struggles with a bad image based on anecdotal collections of accidents as well as the way it was treated in textbooks, emphasizing the disadvantages such as its stability [110]. Using a green propellant reduces risk to personnel handling the propellant, simplifies and reduces the duration of overall system operations, and reduces recurring costs associated with the system and handling of the propellant [8]. Additionally, other advantages are recognized such as its high density. Though a vast amount of research already exists on the topic the European Space Agency (ESA) and staff from the Space Systems Engineering department at the Delft University of Technology have expressed an interest in the development of new, more efficient technologies to improve the efficiency and performance of Hydrogen Peroxide based systems to compete with existing Hydrazine thrusters [2]. This includes research into increasing the propellant concentration for a higher density and specific impulse, performance effects due to stability and storability issues of Hydrogen Peroxide and the possibility of decomposition without the use of a catalytic bed, possibly allowing for the simplification of this type of thrusters. To support this goal, this thesis will describe the design of a 1 N class propulsion system capable of using 87.5% and 98% concentrated Hydrogen Peroxide as its propellant, in which parts can be exchanged to test different technologies and compare the performance when using different concentrations of propellant. This approach will also help to develop and demonstrate a re-usable system for different propulsion applications. The thesis includes the design of a thruster, test setup including feed system and a test plan.

1.1. Motivation

Within the Space Systems Engineering section at TU Delft there is a general interest in the physics of thermal rocket propulsion and green propellants. Some staff members within the section are giving full attention to hydrogen peroxide propulsion specifically. They aim to find new approaches, other than using traditional catalyst beds, to make such propulsion systems more feasible in terms of economy, safety, reliability, simplicity as well as improving long term storability of hydrogen peroxide. This is in line with the interest in the use of green propellants at the European Space Agency, who was planning the design, build and test of a very flexible fully modular 1 N class monopropellant thruster operated with hydrogen peroxide at high concentration (87.5% and 98%). Flexible, in this case, indicating the capability to test different technologies by changing the configuration of the thruster. This is the thruster described in this work. The arguments for a thrust level of 1 N have been identified by the thesis supervisor in ESA/ESTEC as the following:

- The thrust level is limited by the capability of the vacuum testing facilities at ESA/ESTEC. Though the design described in this thesis will be used for testing in atmospheric conditions, ESA/ESTEC has expressed interest in future vacuum tests to test how this affects the ignition of the propellant as well as transient behavior. The thruster that will be tested in the vacuum facilities will be an iteration on the one described in this thesis, rather than a new design;
- It is expected that this level of thrust is the main need within the European Union (EU). This has been determined by the supervisor from ESA/ESTEC in an internal statistical analysis regarding the number of purchases of thrusters of different thrust levels within the EU. This is supported by [60], which states that 1 N thrusters have the highest market volume. A similar analysis has been done for the market in the United States of America up to and including 2011, where both 1 N class and 22 N class thrusters were identified as the main market [81];
- Minimizing associated costs are the final consideration. Developing high thrust engines is generally expensive and requires elaborate and expensive test facilities, whereas miniaturizing for lower thrust levels may also bring extra costs. Nevertheless, the market that is aimed at is that of thrust levels of 1 N.

Other than testing of different technologies, some results that are relevant for ESA/ESTEC are the differences between the usage of 87.5% and 98% concentrated hydrogen peroxide. Especially any differences in the transient phases are of interest as this would affect the achievable minimum impulse bit. Minimizing the minimum impulse bit on thrusters in pulsed mode increases the accuracy with which the required impulse is achieved, which can be crucial in attitude control systems.

1.2. Thesis goals and outline

To define the scope of the thesis a clear research objective was created. The main objective of this thesis is:

To provide the capability of testing catalyst beds and alternative technologies, using a wide range of initial conditions as well as different decomposition technologies, by designing a fully modular 1-N class monopropellant thruster operated with hydrogen peroxide at high concentration, the associated test setup and a test plan.

As stated in the objective, the thruster can be used to perform tests with varying initial conditions. Examples of these initial conditions are the concentration of hydrogen peroxide, temperature and pressure. The thruster is designed in a modular way, such that parts can be exchanged and several thruster configurations can be achieved. This allows for the easy exchange of catalyst beds as well as other decomposition technologies. A list of goals for the work is generated below, to guide the work towards the complete design of a thruster, feed system and test setup:

1. Create a mathematical model of the decomposition of hydrogen peroxide;
2. List thruster requirements and generate a concept for the thruster;
3. Create the baseline design for use with catalyst beds, including thermal and structural analysis;
4. Generate a concept for the testing and integration of alternatives to catalyst beds;
5. Create the design of a propellant feed system;
6. Create the design of a test setup and test plan;
7. Generate manufacturing guidelines.

The structure of the report follows the logic of the goals described above. Each point is addressed by a single chapter. The results have been discussed in a concluding chapter (9).

2

Decomposition model

As preparation for the design of the monopropellant thruster, a mathematical model is created of the hydrogen peroxide decomposition process and the interaction of the flow with the catalyst bed. There are two main reasons for creating this model. Firstly, it is used to create an estimate of the pressure drop that is expected over the catalyst bed. Secondly, the required catalyst bed length can be determined using the simulations performed with this model. Initially, an attempt was made to use existing models. However, after this proved unsuccessful, a simplified model was created (2.1). Some special considerations were required as the decomposition of hydrogen peroxide occurs in the form of a multiphase reaction (2.2). Though proper verification of the model should be performed using the results from tests with the designed thruster in the future, some comparisons were made with another model as part of this thesis (2.3). This chapter is ended with a concluding section that summarizes the main findings (2.4).

2.1. Simplified model

Prior to attempting the modelling of hydrogen peroxide decomposition, some effort was made into researching already existing models. One of the models found was the one described in [41]. The main calculation of this model is done using three differential equations, which are used to determine the flow velocity, enthalpy and composition. Each of the differential equations uses a number of source terms to calculate the effects of decomposition, evaporation, pressure losses and others. Since clear descriptions of the source terms were available and the author was willing to provide support, an attempt was to create a similar model. However, after a number of attempts, employing such a model proved too significant an effort for the time frame of this work. Though unfortunately significant time was already lost in the attempt to create such model, some lessons were learned and several subcomponents of the model were used to create a simpler model using a different method. The simplified model was created using the tubular (plug flow) reactor design process described in [25]. It starts with the definition of the mole balances (2.1.1) within the reactor. Decomposition of hydrogen peroxide is then described using a conversion factor (2.1.2). The concentrations and flow rates of all species are calculated using basic stoichiometry (2.1.3). The decomposition reaction of hydrogen peroxide is defined and a reaction rate model was selected (2.1.4). The decomposition temperature is calculated using the enthalpies and specific heats of each of the present species (2.1.5). Finally a model was used to simulate the pressure drop over the catalyst bed (2.1.6). A large number fluid property calculations are included in the model. An overview of the fluid properties is provided in Annex B.

2.1.1. Mole balances

In [25] it is stated that the general mole balance in a plug-flow tubular reactor is described by the following equation:

$$F_{j0} - F_j + \int^{V} r_j \, dV = \frac{dN_j}{dt} \tag{2.1}$$

In which F_{j0} describes the flow of a certain species into the reactor volume, F_j describes the flow out of the volume and the integral describes the new generation of this species. The reaction rate is indicated by r_j. The term dN_j/dt describes the accumulation rate of a species within the volume. All are given in $mol\,s^{-1}$, except for the reaction rate, which is given in $mol\,m^{-3}\,s^{-1}$. Finally, the volume V is given in m^3. By writing a generation term for a differential section of the tubular reactor the author defines the following equation:

$$\Delta G_j = \int^{\Delta V} r_j\, dV = r_j\, \Delta V \tag{2.2}$$

In a continuous flow system, there is no accumulation within the control volume. Therefore the term dN_j/dt equals zero. Substitution of Equation 2.2 into Equation 2.1 and rearranging leads to the following equation:

$$\frac{F_j|_{V+\Delta V} - F_j|_V}{\Delta V} = r_j \tag{2.3}$$

Finally the author takes the limit as ΔV approaches zero, which leads to the differential form of the mole balance equation for a steady-state plug flow reactor:

$$\frac{dF_j}{dV} = r_j \tag{2.4}$$

This equation describes the change in flow rate dF of a certain species j over the control volume dV as a function of the reaction rate.

2.1.2. Conversion

The progression of a reaction in a tubular reactor is described in [25] using a conversion factor. In order to do so, the reaction equation is written in the following form:

$$A + \frac{b}{a}B \rightarrow \frac{c}{a}C + \frac{d}{a}D \tag{2.5}$$

Now, the conversion factor is defined with respect to species "A". In the case of this work, species A is Hydrogen Peroxide. The conversion factor is written as the following:

$$X_A = \frac{\text{Moles of A reacted}}{\text{Moles of A fed}} \tag{2.6}$$

The conversion factor is dimensionless. Using the definition of this conversion factor [25] now rewrites Equation 2.4 as the following:

$$F_{A0}\frac{dX}{dV} = -r_A \tag{2.7}$$

In which F_{A0} is the initial flow rate of species A in $mol\,s^{-1}$, dX/dV is the change in the conversion factor over the reactor volume in m^{-3} and r_A is the reaction rate of species A in $mol\,m^{-3}\,s^{-1}$.

2.1.3. Stoichiometry

The flow rates and concentrations of each different species in the reactor are monitored by relating the initial flow rate of the reacting species A and the conversion factor. Firstly, the flow rate of the reacting species A is defined in [25] as:

$$F_A = F_{A0}(1 - X) \tag{2.8}$$

The flow quantities of the other species are calculated using the stoichiometric relations defined in Equation 2.5. In this equation, species B is a reacting species and its flow rate is calculated by [25] as:

$$F_B = F_{A0}\left(\Theta_B - \frac{b}{a}X\right) \tag{2.9}$$

The other species in the reaction are reaction products and therefore, the minus sign is replaced by a plus sign:

$$F_C = F_{A0}\left(\Theta_C + \frac{c}{a}X\right) \tag{2.10}$$

$$F_D = F_{A0}\left(\Theta_D + \frac{d}{a}X\right) \tag{2.11}$$

In these equations the flow rates are indicated by F_j in $mol\,s^{-1}$, in which j is replaced by the indicator of the species of interest. The fractions multiplied with the conversion factor X are the stoichiometric relations from Equation 2.5, which are dimensionless. The symbol Θ_j indicates the initial presence of a certain species in the reaction and is defined as the dimensionless ratio of the initial flow rate of a species and the initial flow rate of species A:

$$\Theta_j = \frac{F_{j0}}{F_{A0}} \tag{2.12}$$

Finally the concentration of a species in the reactor is calculated by the author using the following equation:

$$C_j = \frac{F_j}{v} \tag{2.13}$$

In which C_j is the concentration in $mol\,m^{-3}$ and v is the volumetric flow rate in $m^3\,s^{-1}$.

2.1.4. Decomposition reaction

The decomposition of hydrogen peroxide is defined by the following reaction equation in [20]:

$$H_2O_{2(aq)} \rightarrow H_2O_{(l)} + \frac{1}{2}O_{2(g)} + \Delta H \tag{2.14}$$

The reaction equation shows an aqueous solution of hydrogen peroxide on the left, while water and oxygen make up the reaction products on the right. Additionally, ΔH indicates the change in enthalpy as the reaction is exothermic. The rate at which this reaction occurs is given by the following first order equation [41]:

$$\frac{d[H_2O_2]}{dt} = k_1[H_2O_2] \tag{2.15}$$

In which $[H_2O_2]$ is the concentration of hydrogen peroxide in $mol\,m^{-3}$. The factor k is a reaction rate constant, which is temperature dependent. An expression for this parameter is given by the means of the Arrhenius equation [25, 41]:

$$k_1(T) = A_0 e^{-E_A/R_cT} \tag{2.16}$$

In this equation A_0 is named the pre-exponential factor, E_A is the activation energy in $J\,mol^{-1}$, R_c is the universal gas constant in $J\,mol^{-1}\,K^{-1}$ and T the temperature in K. Using the Arrhenius equation, a reaction rate model was created in [41] that defines the catalytic reaction rate using:

$$\dot{r}_{H_2O_2} = -A_0 e^{\frac{-E_A}{R_cT}}[H_2O_2]a_{sp}M_{H_2O_2} \tag{2.17}$$

And the thermal decomposition reaction rate by the means of the following equation:

$$\dot{r}_{H_2O_2} = -A_0 e^{\frac{-E_A}{R_cT}}[H_2O_2]M_{H_2O_2} \tag{2.18}$$

Both lead to a reaction rate in $kg\,m^{-3}\,s^{-1}$. The difference between both equations lies in the factor a_{sp}, which is the catalyst surface interface area, which is given as the interface area (m^2) per unit volume (m^{-3}), which results in m^{-1}. Due to the introduction of this parameter, the pre-exponential factor A_0 for the catalytic reaction is given in $m\,s^{-1}$, whereas the one for thermal decomposition is given in s^{-1}. Though the pre-exponential factor in itself is also temperature dependent, it was found in [41] that most research did not take this into account, due to the added complexity of the problem. Therefore, the author did not include it in their reaction rate model and it will also not be included into the model in this work. The determination of the actual values of the parameters used in the reaction model was done in [41] by the means of a literature review. The author mentions the dependency on catalyst material for some of the values, as well as a range of different values for each of the other parameters. The values used in this work will be the same as the final values used in [41], which are given in Table 2.1.

Table 2.1: Overview of used Arrhenius equation parameters [41]

Parameter	Value	Unit
$A_0(l)\ Catalytic$	2.6×10^4	$m\ s^{-1}$
$A_0(l)\ Thermal$	6.3×10^5	s^{-1}
$A_0(g)\ Catalytic$	1×10^1	$m\ s^{-1}$
$A_0(g)\ Thermal$	1×10^{15}	s^{-1}
$E_A(l)\ Catalytic$	52.5×10^3	$J\ mol^{-1}$
$E_A(l)\ Thermal$	71×10^3	$J\ mol^{-1}$
$E_A(g)\ Catalytic$	41.8×10^3	$J\ mol^{-1}$
$E_A(g)\ Thermal$	200×10^3	$J\ mol^{-1}$

For the catalyst bed interface area a model was created in [41], by modeling the catalyst material as a rod. The diameter of the rod is equal to the diameter of the pellets, d_p. The length of this rod is calculated by:

$$L_{rod} = \frac{\epsilon_s V_{bed}}{\pi(0.5 d_p)^2} \tag{2.19}$$

In which L_{rod} is given in m, ϵ_s is the catalyst bed void fraction and V_bed is the total catalyst bed volume in m^3. The length of the wet part of the rod is calculated by multiplying this equation with the liquid volume fraction, ϵ_l. The catalyst interface area is now calculated as the surface of a rod with diameter d_p and the wet rod length. This leads to the following equation for the liquid phase catalyst interface area:

$$A_{sl} = 4\epsilon_l \frac{\epsilon_s V_{bed}}{d_p} \tag{2.20}$$

and subsequently for the gas phase:

$$A_{sg} = 4\epsilon_g \frac{\epsilon_s V_{bed}}{d_p} \tag{2.21}$$

2.1.5. Temperature

The calculation of the temperature in the thruster follows the method explained in [25] and is based on the first law of thermodynamics applied to a closed system:

$$\delta\hat{E} = \delta Q - \delta W \tag{2.22}$$

This describes that the change in total energy in the system is equal to the amount of heat flow to the system (δQ) minus the work done by the system on the environment (δW). This is adapted to an open system in [25] by adding the rate of energy entering the system and subtracting the rate of energy leaving the system:

$$\frac{d\hat{E}_{sys}}{dt} = \dot{Q} - \dot{W} + F_{in}E_{in} - F_{out}E_{out} \tag{2.23}$$

All components of the equation that are added or subtracted are given in $J\ s^{-1}$. F represents the flow in $mol\ s^{-1}$ and E represents the energy in $J\ mol^{-1}$. The energies in this equation are an addition of the internal energy (enthalpy), kinetic energy, potential energy and others, however it is assumed by the author that in the case of a chemical reactor, all energy terms other than the internal energy are negligible compared to the other terms in the equation. With the assumption that the flow is well mixed the following equation is derived:

$$\frac{d\hat{E}_{sys}}{dt} = \dot{Q} - \dot{W} + \sum F_i H_i|_{in} - \sum F_i H_i|_{out} \tag{2.24}$$

In which H_i is the enthalpy of species i in $J\ mol^{-1}$. For the purpose of the model developed in this thesis, adiabatic operation is assumed, which means there is no heat flow into the volume and no work is done on the environment. This means that both terms $\dot{Q}$ and $\dot{W}$ are equal to zero. The model is created for the steady-state operation of the thruster, which means the total energy in the system remains constant over time and the term $d\hat{E}_{sys}/dt$ equals zero as well. When considering a small volume within the reactor this leads to:

$$\sum F_i H_i|_V - \sum F_i H_i|_{V+\Delta V} = 0 \tag{2.25}$$

By taking the limit as ΔV approaches zero this can be written as:

$$-\frac{d\sum(F_i H_i)}{dV} = 0 \tag{2.26}$$

This is expanded in [25] to:

$$-\frac{dF_i}{dV}H_i - \sum F_i \frac{dH_i}{dV} = 0 \tag{2.27}$$

Now Equation 2.4 is adapted by the author to the following:

$$\frac{dF_i}{dV} = r_i = v_i(-r_A) \tag{2.28}$$

In which v_i is the stoichiometric ratio for the species i and r_A is the reaction rate of species A. Additionaly it is stated in [25] that the enthalpy of a species at a certain temperature is related to the enthalpy of formation at a reference temperature T_R by means of the following equation.

$$H_i(T) = H_i^\circ(T_R) + \int_{T_R}^{T} C_{P_i}\, dT \tag{2.29}$$

In which C_P is the specific heat capacity in $J\ kg^{-1}\ K^{-1}$. This equation is differentiated with respect to the volume V, which leads to:

$$\frac{dH_i}{dV} = C_{P_i}\frac{dT}{dV} \tag{2.30}$$

Equations 2.28 and 2.30 are substituted into 2.27 to create:

$$-\sum v_i H_i(-r_A) - \sum F_i C_P \frac{dT}{dV} = 0 \tag{2.31}$$

The term $v_i H_i$ is equal to the heat of reaction ΔH_{Rx} [25]. Substitution and rearranging leads to the final equation used to calculate the temperature in the decomposition chamber:

$$\frac{dT}{dV} = \frac{(r_A)[\Delta H_{Rx}(T)]}{\sum F_i C_{P_i}} \tag{2.32}$$

The heat of reaction is given by [25] as:

$$\Delta H_{Rx}(T) = \frac{d}{a}H_D(T) + \frac{c}{a}H_C(T) - \frac{b}{a}H_B(T) - H_A(T) \tag{2.33}$$

2.1.6. Pressure drop

According to [25], the most common method to calculate the pressure drop through a porous catalyst bed is by means of the Ergun equation, which is given by:

$$\frac{dP}{dz} = -\frac{G}{\rho D_p}\left(\frac{1-\phi}{\phi^3}\right)\left[\frac{150(1-\phi)\mu}{D_p} + 1.75G\right] \tag{2.34}$$

In which the following parameters are identified:

P	Pressure in kPa
z	Length of the catalyst bed in m
G	Superficial mass velocity in $kg\ m^{-2}\ s^{-1}$
ρ	Fluid density in $kg\ m^{-3}$
D_P	Diameter of catalyst bed pellets in m
Φ	Porosity or Void fraction
μ	Dynamic viscosity of fluid passing through the bed in $Pa\ s$

The superficial mass velocity in this equation is calculated using the following equation:

$$G = \rho \cdot u \tag{2.35}$$

In which u is the superficial velocity in m/s, given by:

$$u = \frac{v}{A} \tag{2.36}$$

In which v is the volumetric flow rate in $m^3\ s^{-1}$ and A is the frontal surface of the tubular reactor. Finally, the void fraction is given by:

$$\phi = \frac{\text{Volume of void}}{\text{Bed volume}} \tag{2.37}$$

In [41] a comparison is made between the results of the Ergun equation and adaptations made by Macdonald [52] and Tallmadge [96]. It was found that the Ergun equation as well as the Macdonald adaptation significantly overestimate the pressure losses at higher Reynolds numbers. Therefore, the final model used in [41] was the Tallmadge equation, which is given by the following equation:

$$\frac{\Delta P}{L} = K\mu u + \eta \rho^{5/6} u^{11/6} \mu^{1/6} \tag{2.38}$$

Where:

$$K = \frac{150}{D_p^2} \frac{\epsilon_s^2}{(1-\epsilon_s)^3} \tag{2.39}$$

$$\eta = \frac{4.2}{D_p^{7/6}} \frac{\epsilon_s^{7/6}}{(1-\epsilon_s)^3} \tag{2.40}$$

In which ϵ_s is the void fraction (ϕ in the Ergun equation). The Tallmadge equation was finally used for the decomposition model in this work.

2.2. Multi-phase considerations

As was seen in Equation 2.14, the decomposition of hydrogen peroxide is a multi-phase problem. Initially, the hydrogen peroxide will be a liquid aqueous solution. As the decomposition reactions progresses, liquid water as well as gaseous oxygen is produced. Additionally, low pressure vapors are present from the liquid mixture. The heat released from the reaction will increase the temperature of the mixture until all components have been evaporated into the gas phase. However, since hydrogen peroxide and water have different boiling points, the phases between these two may also differ. Such a multi-phase flow causes some difficulties in the modeling process. First of all, the conversion rate used in [25] needs to be adapted to allow for simultaneous decomposition of both liquid hydrogen peroxide and the gaseous vapours (2.2.1). Secondly, the rate of evaporation of the liquid needs to be determined (2.2.2). Finally, some considerations are made regarding the pressure losses due to interaction with the catalyst bed (2.2.3).

2.2.1. Conversion

The method by [25] in principle is only written for a single phase reaction, either liquid or gaseous. In order to deal with multi-phase problem some adjustments have been made. In the model created for this thesis the flow rates of each of the components are calculated for all phases. This means that there is a flow rate for liquid and gaseous hydrogen peroxide and water as well as gaseous oxygen.

The reaction is simulated for each phase individually. Unfortunately, using Equation 2.7 to calculate a conversion factor for each phase individually introduces an error, as the conversion factor is determined relative to the initial flow rate of hydrogen peroxide in each phase and does not take into account the constant evaporation of hydrogen peroxide. Rather, the rates of change are used to calculate the rate of change of the total hydrogen peroxide flow:

$$\frac{dF_{H_2O_2}}{dL} = \frac{dX_l}{dL} F_{H2O2_{(l)}} + \frac{dX_g}{dL} F_{H2O2_{(g)}} \tag{2.41}$$

This is then used to calculated the overall conversion factor with respect to the total initial flow rate of hydrogen peroxide (both phases combined).

$$\frac{dX}{dL} = \frac{dF_{H_2O_2}}{dL} \cdot \frac{1}{F_{0,H2O2}} \tag{2.42}$$

Using this conversion factor the new total flow rates are calculated using the equations from Section 2.1.3. To determine the final flow rates for both phases, the liquid/gas fractions are calculated using the method described in Section 2.2.2.

2.2.2. Evaporation

In [41] an evaporation model is created, in which the mass flow rate from the liquid phase to the gas phase is calculated. This mass flow rate is calculated according to an equation from [9]:

$$\dot{m}_{evap} = -2\pi \sum_{\alpha} r_{V,\alpha} \rho_g D_{\alpha,g} Sh_{\alpha}^{*} \ln(1 + B_{M,\alpha}) \tag{2.43}$$

In which $\dot{m}_{evap}$ is the evaporation mass flow rate in $kg\, s^{-1}$. $r_{V,\alpha}$ is named the volume equivalent radius and is a factor that is introduced to take into account the presence of other components at the droplet surface. The value of this parameter is determined experimentally. ρ_g is the density of the gas phase in $kg\,m^{-3}$, $D_{\alpha,g}$ is the binary diffusion coefficient, which was assumed by [41] equal to that of water vapour in air. The modified Sherwood number Sh_{α}^{*} is used and finally, the Spalding Mass Transfer number is identified as the main driver of the evaporation. It is given by the following equation:

$$B_{M,\alpha} = \frac{Y_{\alpha,s} - Y_{\alpha,\infty}}{1 - Y_{\alpha,s}} \tag{2.44}$$

In this equation, $Y_{\alpha,s}$ is the gas mass fraction of a component at the droplet surface, determined by the vapour pressure. $Y_{\alpha,\infty}$ is the gas mass fraction of the component in the main flow. The evaporation is driven by the difference between the two. Due to the way the complete decomposition model was created, the integration of this model proved significantly complicated. Additionally, the calculation described above requires the experimental determination of the volume equivalent radius. Taking these factors, as well as time limitations into account, the choice was made to use a significantly simplified model instead that was initially used on a temporary basis. The mole fractions in a gas mixture are calculated using [82]:

$$x_i = \frac{P_i}{P_{tot}} \tag{2.45}$$

In which x_i is the mole fraction of component i in the vapor composition, P_i is the partial pressure of the component and P_{tot} is the total pressure. Though the assumption is not physical, this mole fraction was used as the mole fraction of a component in the gas phase relative to the total quantity of the component in all phases. In the end, with tuning of the decomposition model parameters, satisfactory results were found and therefore the decision was made to keep this assumption in place.

2.2.3. Pressure drop

The pressure drop is calculated using the Tallmadge equation for each phase separately. A model was developed in [79] to combine these for a multi phase model. This is also the method that was used in [41]. It works by first calculating the pressure drop over each phase individually, and then calculating a factor that is used to combine these values. Though this pressure drop model was first considered, initially a simple addition of both the pressure drop of the liquid phase and that of the gas phase was performed. As will be discussed in Section 2.3, the estimated effect of this error is not significant for the purpose of this model. Therefore, no more effort was put into implementing the multi-phase model by [79].

2.3. Results and discussion

During the development of the model it became clear that the exact outcome is significantly dependent on a wide selection of parameters. This ranges from the thruster geometry to catalyst bed specifications, including the values of the Arrhenius parameters used, but also factors such as the starting temperature, mass flow rate and feed pressure. Additionally, several parameters rely on calibration using thruster test data, including parameters in the reaction rate equations. Calibration of these parameters was done in [41], though the values found by the author are specific to that model. Due to the fact that the current model operates very differently than the reference, the values of these parameters lead to significantly different results. However, by varying several parameters it was possible to find results (Figure 2.1) for the decomposition of 87.5% hydrogen peroxide, similar to the results found in [41].

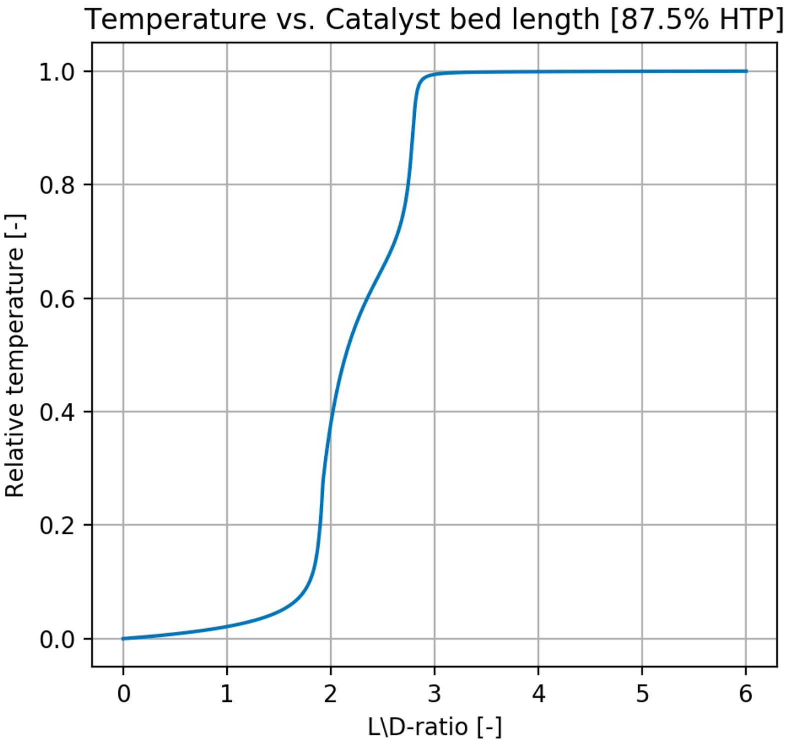

Figure 2.1: Results from the decomposition model, tuned to provide similar results as were found in [41]

Figure 2.1 shows the ratio of the length of the catalyst bed relative to its diameter on the horizontal axis. The vertical axis shows the relative temperature, which ranges from zero (temperature at time zero) to one, which is the full adiabatic decomposition temperature. The results from [41] are seen in Figure 2.2. The curve shows that initially, when the propellant temperature is still low, the decomposition process is slow. The reaction rate initially increases slowly, after which rapid decomposition starts, until the adiabatic decomposition temperature is reached. According to [41], initially the catalytic decomposition rate is dominant, but when the temperature increases, this is surpassed by the thermal decomposition rate.

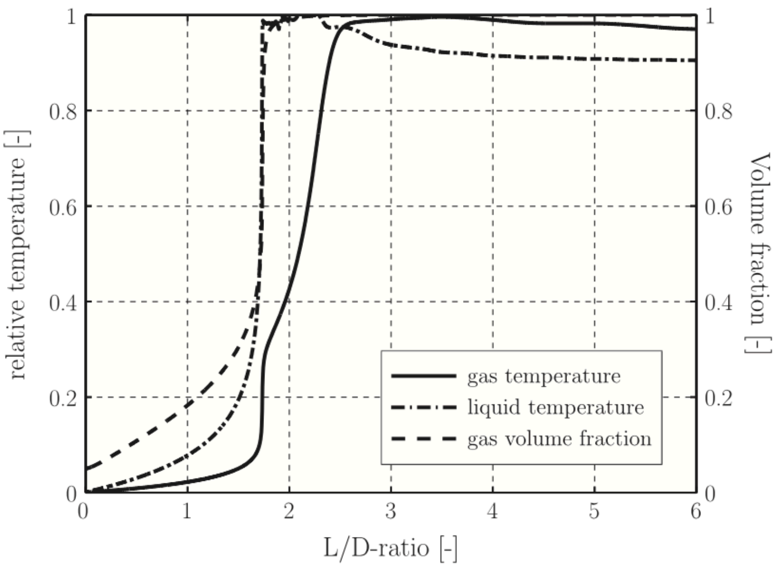

Figure 2.2: Relative decomposition temperature results from [41]

Since the model is currently not calibrated to any test data, the absolute results are not considered relevant at this stage. However, some interesting information is still gained from the results of the model. In Figure 2.3 an overview is seen of the decomposition temperature over the catalyst bed length for a certain set of guessed parameters (as no calibration data was available). The simulation was performed four times with the same parameters, while varying the feed pressure and mass flow rate accordingly. The input for the upstream pressure of the catalyst bed was taken as determined in Section 4.5.4, while the mass flow rates were used as determined in Section 3.1.3.

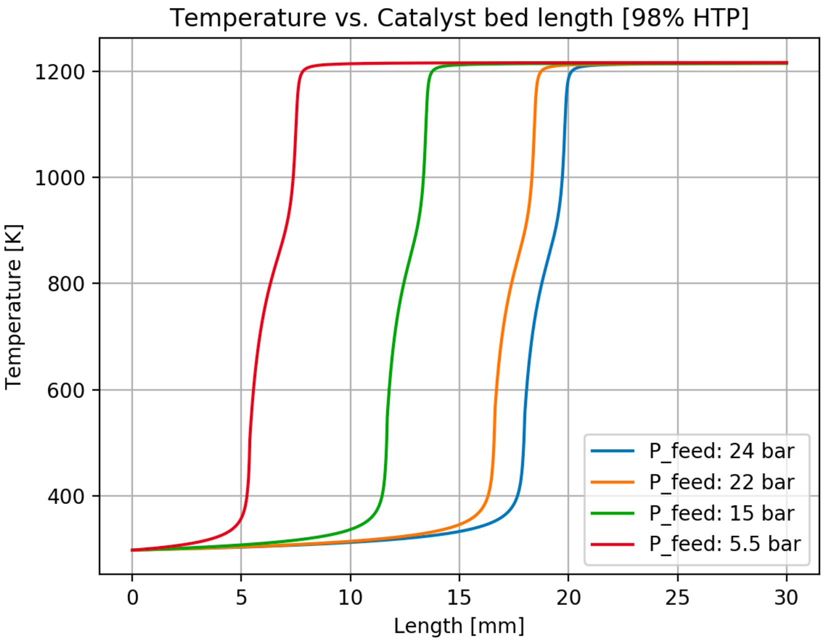

Figure 2.3: Comparison of decomposition temperature profiles for 98% hydrogen peroxide, at different feed pressures

If the mass flow rate was kept equal, a reduction in feed pressure would lead to an increase in the required catalyst bed length for complete decomposition. However, since a reduction in feed pressure also leads to a reduction in mass flow rate, the catalyst bed length required to complete decomposition (and thus achieve the adiabatic decomposition temperature) is actually lower. Unfortunately, it was found that when the propellant feed temperature is varied, the temperature model occasionally produces errors. Therefore, it is recommended extra effort should be put into improving the temperature model. In Figure 2.4 an overview of the results for the pressure drop is seen, for the same set of simulations.

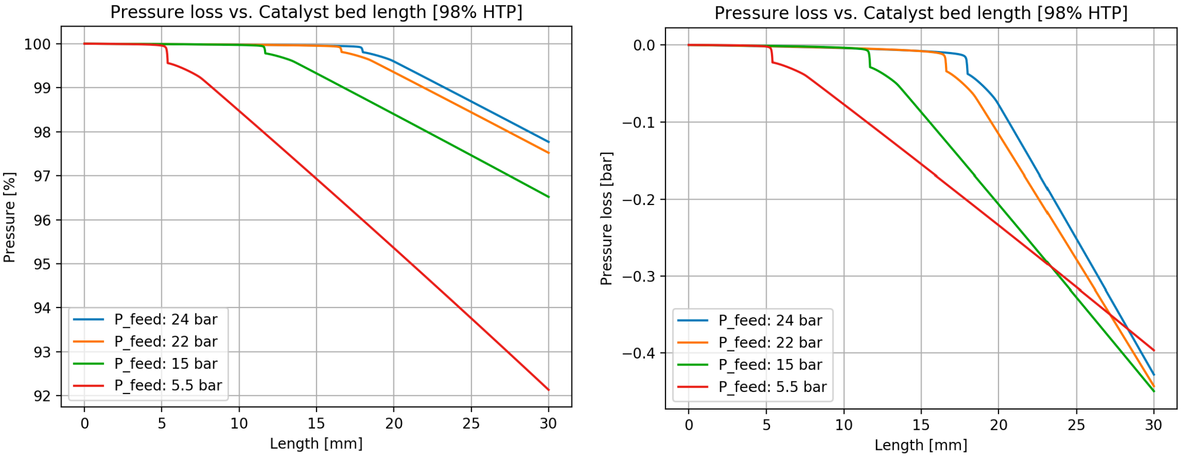

Figure 2.4: Modeled catalyst bed pressure losses for multiple feed pressures

In the left part of the figure, the pressure throughout the catalyst bed is seen relative to the upstream pressure, starting at 100% and reducing while moving downstream. The figure shows that initially the pressure losses are very small. This is followed by a short rapid loss in pressure and finally a gradual change in pressure. The short region of rapid pressure loss occurs due to the fact that the velocity of the liquid and gas phase is assumed equal. As the amount of gas in the system increases, the average density of the flow decreases and the velocity of the flow increases, causing the rise in pressure losses. The viscosity of the liquid phase is much higher than that of the gas phase and therefore, once the last liquid has evaporated, only the gas is present and therefore the pressure loss gradient stabilizes. A better estimation of the pressure losses at this point in the catalyst bed may be achieved by decoupling the liquid and gas flow velocity as well as implementing a multi-phase pressure drop model, such as the one from [79]. However, the effect on the final result was considered minimal and therefore, this was neglected. The relative pressure drop (left graph) is highest in the low feed pressure case. When looking at the absolute pressure drop (right graph), it is seen that with a higher feed pressure case, the pressure losses downstream of the point of full decomposition are larger. It is concluded that the pressure drop over the catalyst bed increases rapidly when the catalyst bed is longer than the length required for complete decomposition.

2.4. Conclusion

An attempt was made to create a mathematical model of the decomposition of hydrogen peroxide in a thruster using a catalyst bed. After some attempts to create a model based on the model described in [41], this proved too significant an effort for this work and therefore, a simplified model was created using the methods described in [25]. To create this simplified model, some non-physical assumptions were made in the evaporation model. It was found that the absolute results from the model are heavily dependent on selected catalyst bed parameters, as well as tuning of several parameters in the reaction rate model. Therefore, the absolute results of the decomposition model are not relevant at this stage of the work. Prior to employing this model to determine catalyst bed lengths and estimate pressure drops it should be calibrated using test data. Some effort could be put into improving the evaporation model, though it is considered that with proper calibration the current model is satisfactory. It is recommended that some effort is put into improving the temperature model, as currently it may produce errors in certain scenarios. The current pressure drop model ignores multi-phase effects, though it is considered that the influence on the results is small, as the region in which the flow consists of multiple phases is small. From the results of the model it is concluded that the cases with higher feed pressures require a longer catalyst bed. A large portion of the pressure losses occur when the catalyst bed is longer than required.

3

Design preparation

The design process was started by generating a requirement specification (3.1). This was followed by the creation of a design concept. The main design ideology is to take a modular approach. By dividing the thruster components into easily exchanged separate modules, maximum flexibility in use of the thruster is achieved. This way an alternative decomposition chamber can be designed for decomposition technologies other than catalyst beds, but also other components such as injectors and nozzles can be exchanged. An overview was created of the components of the thruster and the interfaces required between these components (3.2). Initially the plan was to create a custom design for the interfaces between components, however a commercially available solution was found and assessed (3.3). Finally an overview of commercially available valves was created, from which a suitable inlet valve was selected (3.4). This chapter serves as a thorough preparation of the design process, the results of which are summarized in a concluding section (3.5).

3.1. Requirement specification

The requirements have been collected into a requirement specification document, which is found in Annex C. It contains several requirements regarding the performance of the thruster. The key requirements were identified and an overview of these requirements was created (3.1.1). The most important inputs for the design phase are the requirements regarding the thrust and specific impulse of the thruster (3.1.2), as these affect the sizing of the thruster to a large extent. Using these requirements, the expected mass flow in the thruster can be calculated (3.1.3), which is a parameter that serves as input for several analyses that are part of the design phase. The requirements only mention the values of these parameters at certain feed pressure levels and therefore some interpolation is required to have the information available for all feed pressures.

3.1.1. Key requirements

The requirements specification document contains a wide range of requirements, varying from performance requirements to material requirements. Though the full specification is found in Annex C, a number of requirements that are considered driving for the design are highlighted. The full operating range of the thruster is described using requirements *MGT-002*, *MGT-004*, *MGT-056* and *MGT-062*. This operating range is summarized by the data displayed in Table 3.1. The second set of requirements that is considered driving for the thruster design is the set of specific impulse and thruster requirements. These requirements have been analyzed in more detail in Section 3.1.2.

Table 3.1: Thruster operating range summary from requirements

Parameter	Value	Unit
Reference supply pressure	22	bar
Reference mean vacuum thrust	1	N
Supply pressure window	5.5 - 24	bar
Propellant inlet temperature	7 - 60	C
Nominal ambient pressure	1013	mbar
Nominal ambient temperature	20	C

The thruster will be used not only in steady-state operation, but also in pulsed operation, which is the way it would function in a reaction control system. For the pulsed mode performance, a number of extra requirements are highlighted. Some of the key requirements on this topic are found in *MGT-088*, *MGT-092*, *MGT-096*, *MGT-110 MGT-170* and *MGT-172*. These are summarized in Table 3.2.

Table 3.2: Key requirements related to pulsed mode operation

Parameter	Value	Unit
Minimum impulse bit (P_{feed} = 5.5 bar)	< 0.023	Ns
Minimum impulse bit (P_{feed} = 22 bar)	< 0.07	Ns
Centroid delay time	< 150	ms
Number of pulses	> 8000	-
Cold start cycles	≥ 30	-
Valve opening response time	< 15	ms
Valve closing response time	< 10	ms

The impulse bit is a measure of the total impulse produced per pulse. A lower value means more accurate impulse control is possible. The centroid delay time is the time that passes between the centroid of the electrical “on” signal and the centroid of the thrust curve that is achieved [78]. The total number of pulses mentioned is the amount of pulses required for the full test campaign of a single catalyst bed or decomposition technology. The thruster components themselves should be inspected after each full test campaign and replaced if required. The valve opening and closing response times were mentioned in Table 3.2, as they impact the overall response time of the thruster, which is an important parameter for attitude control systems. Additionally, the required duty cycles for testing were mentioned in *MGT-098*. These are summarized in Figure 3.1. Though the values mentioned in this section describe the

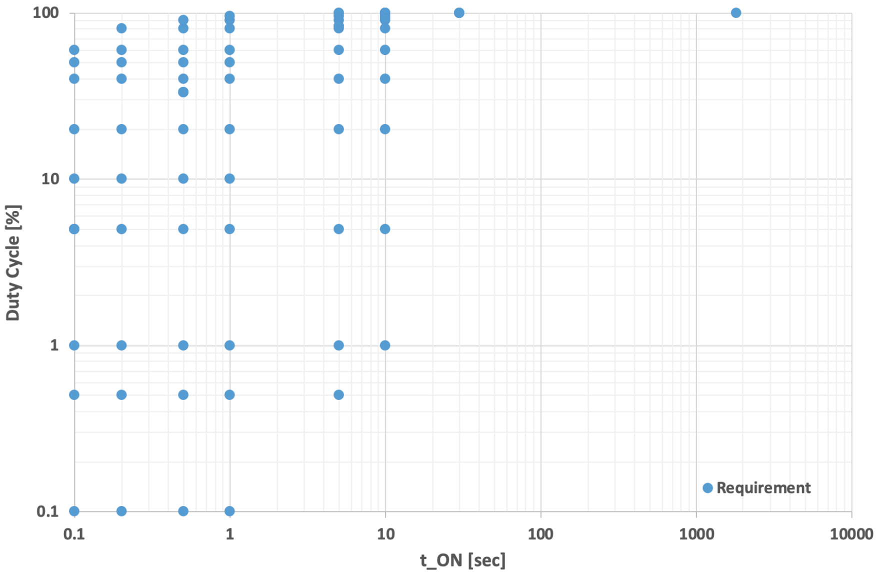

Figure 3.1: Duty cycle requirement from *MGT-098*

requirements, the specification document in some cases mentions a second, higher value, as a goal. It is considered that the requirements mentioned in the current, as well as the two following sections, together give a decent description of the expectations from the thruster and test campaign. Naturally, requirements not listed as a key requirement in this section will be referenced throughout the design phase as well.

3.1.2. Thrust and Specific impulse requirement interpretation

The thrust level requirements are defined in *MGT-062*, whereas the specific impulse requirements are defined in *MGT-074*. In these requirements thrust and specific impulse values are found for three different feed pressure levels; 24, 15 and 5.5 bar. An overview of the requirements is found in Table 3.3.

Table 3.3: Thrust and Specific Impulse requirements from *MGT-062* and *MGT-074*

Feed pressure [bar]	Min. thrust [N]	Max. thrust [N]	Min. Specific Impulse [s]
24	0.99	1.2	173
15	0.65	0.72	169
5.5	0.26	0.32	160

Furthermore, requirements *MGT-002* and *MGT-062* state that the reference thrust at a feed pressure of 22 bar is 1.0 N. A brief analysis of these requirements is performed to create a performance overview for all thrust levels. This is done by the means of interpolation. The interpreted thrust requirements are found in Figure 3.2.

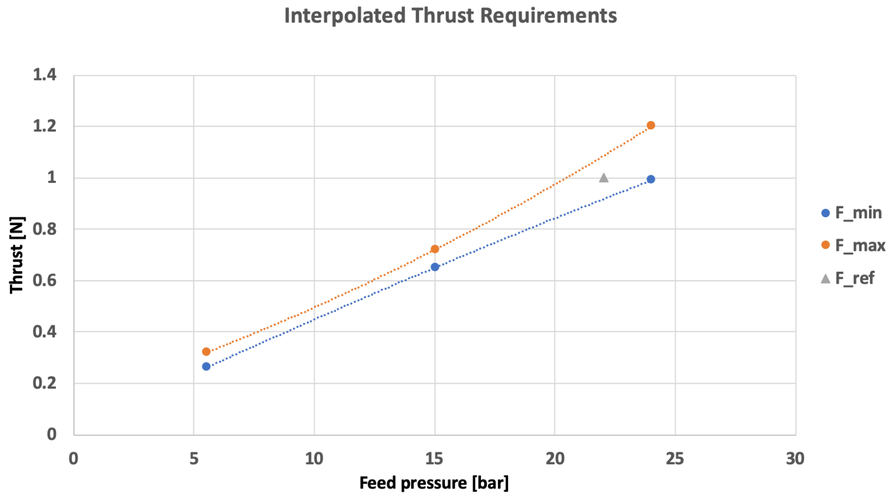

Figure 3.2: Interpolated thrust requirements

In this figure, a second-order polynomial trend line is used to interpolate the minimum and maximum thrust values for all feed pressures. The figure shows that the specified reference thrust falls in the center of the thrust range. For the specific impulse a similar graph is created and is found in Figure 3.3. Note that these requirements are valid for vacuum operation and therefore, they need to be adjusted when operation in other conditions is considered.

3.1.3. Calculated mass flows

An important parameter for the design process is the expected mass flow, which serves as an input for sizing of the thruster and is used in, amongst others, the decomposition model and thermal analysis. There are no specific mass flow requirements mentioned in the requirement specification, however the values can be calculated from the requirements mentioned in the previous sections. The mass flow is calculated using the following equation according to [113]:

$$\dot{m} = \frac{F}{g \cdot I_{sp}} \tag{3.1}$$

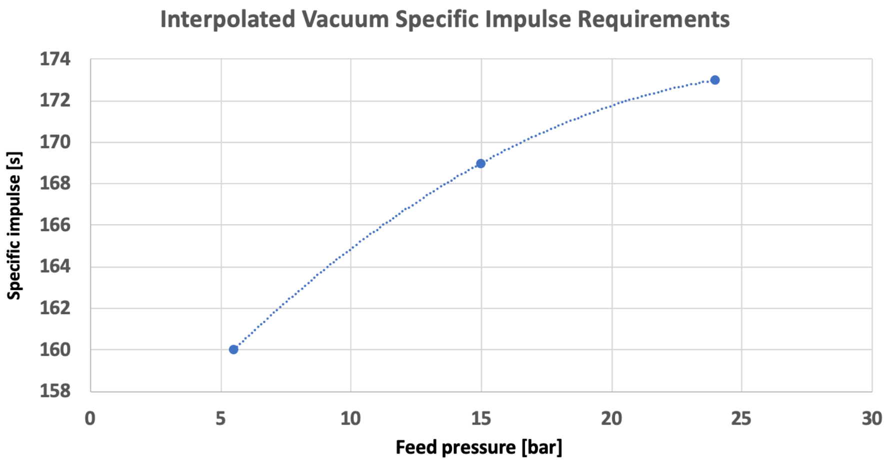

Figure 3.3: Interpolated specific impulse requirements

In which $\dot{m}$ is the mass flow in $kg\ s^{-1}$, F is the thrust level in N, g is the gravitational acceleration in $m\ s^{-2}$ and I_{sp} is the specific impulse in s. The thrust and specific impulse requirements concern the final measured results and therefore, already take into account the several thruster efficiencies. However, since a simple conical nozzle will be used for the design, there is a loss in thrust in the axial direction due to the divergence of the exhaust causing a radial thrust component. This divergence loss is calculated in [113] by means of:

$$\epsilon_{div} = 0.5 \cdot (1 - \cos\alpha) \tag{3.2}$$

In which ϵ_{div} is the percentage thrust loss due to divergence and α is the divergence half angle in rad. The corrected required thrust level is calculated by the following relation in the case of optimum expansion:

$$F_{cor} = \frac{F_{req}}{1 - \epsilon_{div}} \tag{3.3}$$

In which F_{cor} is the equivalent thrust requirement to achieve the level of F_{req} in the axial direction. Using a conical nozzle with a divergence half angle of 15 degrees leads to a divergence loss of 1.7%. It is important to note that the divergence loss does not apply to the pressure thrust component and therefore the above relation is only valid in the case of optimum expansion. Assuming optimum expansion and applying the correction leads to the mass flows as displayed in Figure 3.4. The figure shows that at the reference conditions (22 bar feed pressure) the expected mass flow is approximately 0.6 $g\,s^{-1}$.

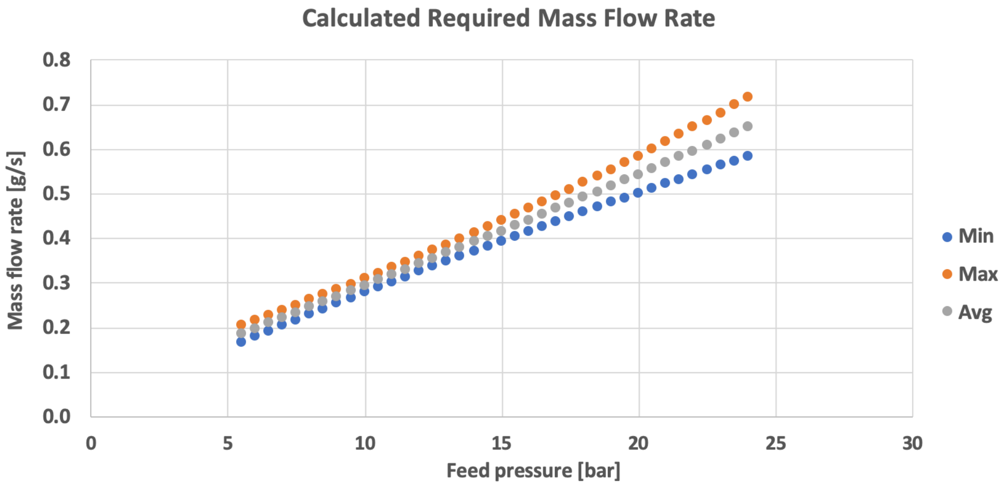

Figure 3.4: Calculated mass flow requirements

3.2. Thruster components and interface specification

In preparation of the design phase an overview is made of the envisioned thruster, which is found in Figure 3.5. The components can be clearly identified as the following (from left to right):

1. Inlet valve
2. Thermal standoff and capillary tube
3. Injector module
4. Decomposition chamber and catalyst bed (including retainers)
5. Nozzle module including pressure/temperature tap

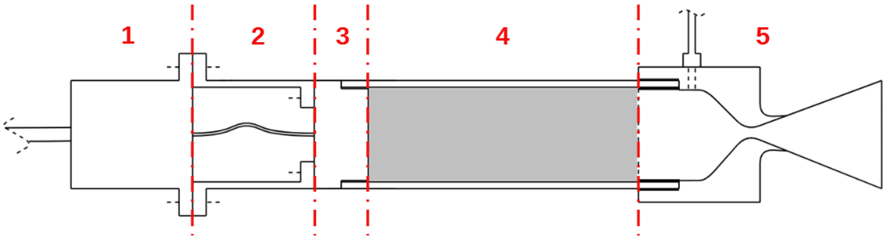

Figure 3.5: Conceptual overview of thruster

The inlet valve serves the purpose of starting and stopping the flow of propellant. It has been chosen from a selection of commercially available valves, by the means of an elimination process, which is performed in Section 3.4. A thermal stand-off is put in place between the inlet valve and the thruster body, to reduce the amount of heat soak back into the valve. This will prevent undesired decomposition effects in the valve and feed system. In this section of the thruster, the propellant flows through a capillary tube with a small diameter to make the propellant travel the thermal stand-off distance at a high velocity. This minimizes the impact on the response time of the thruster and prevents thermal decomposition effects from occurring before the propellant arrives in the decomposition chamber. Downstream of the thermal standoff, the injector module is located. The goal of the injector is to break up the propellant flow into small droplets and spray them into the decomposition chamber. The injector is designed with a pressure drop, so that the pressure effects in the decomposition chamber are decoupled from the upstream section of the thruster and the propellant feed system. The decomposition chamber in the baseline design is filled with a catalyst bed. The catalyst bed is assumed to be made out of ceramic pellets, onto which an active catalytic material is deposited. The catalyst bed is held in place by the means of two retainers, one on each side of the catalyst bed. Downstream of the catalyst bed, the decomposition chamber is connected to the nozzle module. This module will consist of a simple conical converging-diverging nozzle with a hot gas tap upstream of the convergent section, for the measurement of pressure and/or temperature in the chamber. As was mentioned before, the thruster design is completely modular. Therefore, several interfaces in the thruster are identified:

1. Inlet valve - Thermal Standoff;
2. Inlet valve - Capillary tube;
3. Thermal standoff - Injector;
4. Capillary tube - Injector;
5. Injector - Decomposition chamber;
6. Decomposition chamber - Nozzle assembly.

Some of these interfaces do not experience large forces or pressure loads and are not in contact with the propellant or hot gas. For these interfaces simple designs can be created without in-depth analysis. An example of this are the connections of the thermal standoff, on both sides. The interfaces with the capillary tube are in touch with the liquid propellant, but not with hot gas. The decomposition chamber interfaces, both on the injector side and on the nozzle side, are considered the most critical. These interfaces have to seal the hot gas in the decomposition chamber and will endure significant thermal loads, especially on the nozzle side. Additionally, as the catalyst bed and decomposition chamber are expected to be exchanged most often, these interfaces should be simple to assemble and disassemble.

3.3. Swagelok concept

Though initially a plan was made to make a custom design for each interface, a potentially suitable off the shelf solution was found by using tubes and tube fittings produced by Swagelok (3.3.1). In order to assess the suitability of this solution, a simple thermal network model was created to determine the expected wall temperatures in the decomposition chamber (3.3.2). The several modes of heat transfer are represented in the thermal network by the use of resistors (3.3.3). The results were calculated using a worst-case scenario (3.3.4), after which they have been compared to the capabilities of the Swagelok components (3.3.5).

3.3.1. Interfaces

Swagelok is a producer of components for gas and fluid systems with a large presence in the space industry. One of the components they produce is a line of tube fittings [90]. These tube fittings are easily installed and are capable of sustaining significant pressures. For this reason, it was assessed whether they are suitable to serve as the interfaces of the decomposition chamber on both the upstream and downstream sides. The Swagelok tube interface (Figure 3.6) consists of a number of components.

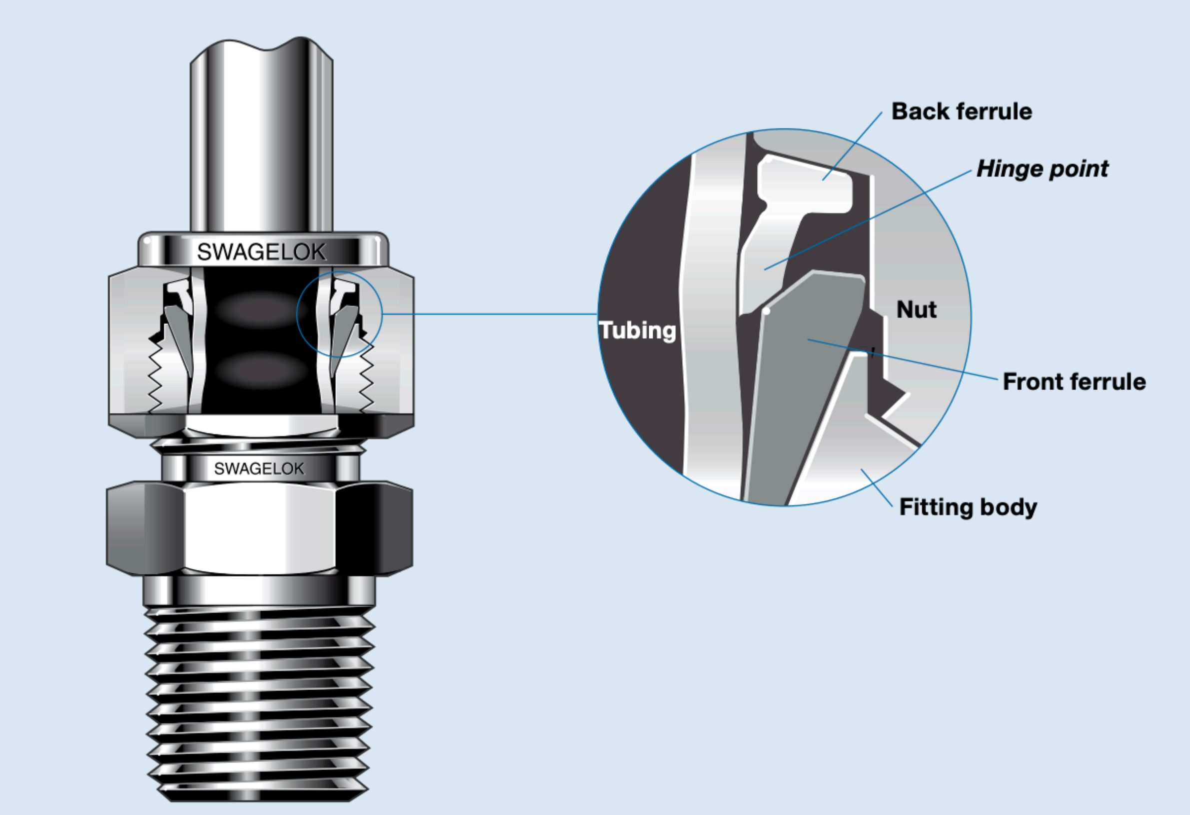

Figure 3.6: Swagelok tube fitting [90]

The design includes a nut and two ferrules that are slid over the tube. The tube is then inserted into a fitting body, which has a thread running over the outside. The nut is slid over the ferrules and then screwed onto the fitting body. By tightening the nut, the front ferrule is pushed forward by the back ferrule and slides against the slanted edge of the fitting body. This slanted edge causes the front ferrule to be firmly pressed against the tube, creating a seal. While pushing forward the front ferrule, the back ferrule is also pushed into the tube, creating a small indentation in the tube wall, which results in a very firm grip on the tube. After the first tightening, the connection can be unscrewed and re-tightened, though the ferrules remain attached to the tube. Swagelok advertises that the design of their back ferrule achieves excellent gas-tight sealing and grip on the tube, easy installating, consistent remakes and excellent resistance against fatigue. All parts of the Swagelok design are available in Stainless Steel 316, which has good compatibility properties for use with Hydrogen Peroxide [20, 80].

Using the Swagelok concept for the interfaces of the decomposition chamber of a hydrogen peroxide monopropellant thruster requires some creativity. The envisioned use requires the design of a nozzle and injector module that are capable of functioning as a custom fitting body. The tube, nuts and ferrules are then used as commercially available from Swagelok. In this way, the decomposition chamber design is reduced to a simple tube of an arbitrary length. This means exchanging catalyst beds and decomposition chambers is turned into a simple process, even if a different length is required. All that is required, is simply cutting off a new section of tube with the desired length. Since the interface would be used on both sides of the tube, it is not possible to remove the nuts off the tube after the components are integrated for first use, as they are held in place by the ferrules on either end of the tube. To change decomposition chambers, either a new set of nuts is required, or the old section of tube is sacrificed. New ferrules are required for every decomposition chamber.

3.3.2. Thermal modeling

In the catalogs available on the website of Swagelok [83], an overview of the performance capabilities is provided at different temperatures. To assess the feasibility of this concept, the capabilities of the Swagelok fittings are compared to the requirements of the design. A thermal model has been created, to estimate the expected temperatures in the decomposition chamber wall, as input for this assessment. The thermal model was made using the logic displayed in Figure 3.7. The assessment is performed at the hottest point in the decomposition chamber, at the adiabatic decomposition temperature. For simplicity, the conservative assumption has been made that there is no heat transfer in the wall along the length of the decomposition chamber. Rather than a calculation at a single point, the assessment was performed on a cylinder of unit length, with a uniform temperature distribution.

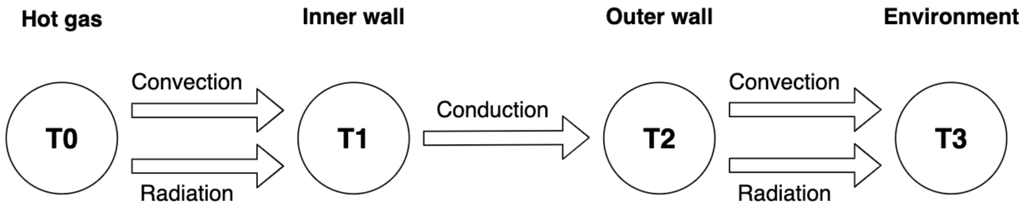

Figure 3.7: Conceptual overview of the chamber wall thermal model

The conceptual thermal model as seen in the figure above can be translated into an equivalent electrical network (Figure 3.8), for simple thermal analysis of steady-state situations [51]. In this model, the heat transfer coefficients are converted into resistances. The temperature of a node is equal to the measured voltage between the node and the ground. The temperature boundary conditions are set using a voltage source.

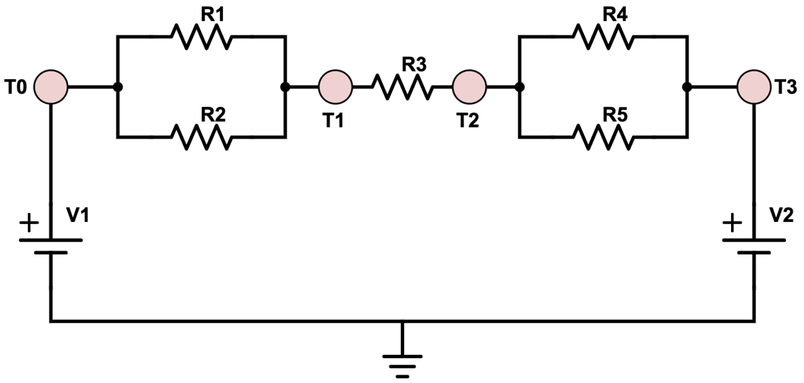

Figure 3.8: Schematic overview of the electric network representation of the thermal model

Each of the resistors in the electrical network represents a form of heat transfer. The heat flow is determined by calculating the current through the resistor, which is done using Ohm's law [51]:

$$U = I \cdot R \tag{3.4}$$

The parameters in this equation are the following:

Table 3.4: Electrical parameters and their thermal equivalent [51]

Parameter	Electrical	Thermal equivalent
U	$Potential\ [V]$	$Temperature\ [K]$
I	$Current\ [I]$	$Heat\,flow\ [W]$
R	$Resistance\ [\Omega]$	$Thermal\ coupling\ reciproke\ [K/W]$

The calculation of heat flows is based on Kirchoff's first law and is described in [51]. This law states that the current flowing into the node is equal to the current flowing out of the node. This means the node is not a sink or source of current, or heat in the thermal case.

$$\sum_{k=0}^{n} I_k = 0 \tag{3.5}$$

Combinations of resistances within an electrical or thermal network can be exchanged by a replacement resistance. In the case of two parallel resistances, this can be done using the following relation:

$$\frac{1}{R_{r,ij}} = \frac{1}{R_i} + \frac{1}{R_j} \tag{3.6}$$

When resistances are put in series, the values can simply be added together.

$$R_{r,ij} = R_i + R_j \tag{3.7}$$

These rules can be applied to the schematic in Figure 3.8 to calculate the total heat flow from the beginning until the end of the model. This results in the following relation:

$$R_{TOT} = \frac{1}{\frac{1}{R_1} + \frac{1}{R_2}} + R_3 + \frac{1}{\frac{1}{R_4} + \frac{1}{R_5}} \tag{3.8}$$

To solve any model, some boundary conditions need to be set. In this case, three boundary conditions have been specified. The first is the hot gas temperature T_0, which is set at the adiabatic temperature. Secondly, a boundary is set for the ambient temperature T_3. The third boundary condition is given by Kirchoff's first law and is defined as the following:

$$Q_{TOT} = Q_{01} = Q_{12} = Q_{23} \tag{3.9}$$

Which translates to:

$$\frac{T_0 - T_3}{R_{TOT}} = \frac{T_0 - T_1}{R_{01}} = \frac{T_1 - T_2}{R_{12}} = \frac{T_2 - T_3}{R_{23}} \tag{3.10}$$

As seen in the equation above, the total heat flow from node zero to node three is calculated using the total resistance calculated in Equation 3.8. As was mentioned before, T_0 and T_3 are set as boundary conditions. The results of interest are the inner wall temperature T_1 and the outer wall temperature T_2. The solutions are found using a solver in Microsoft Excel that varies T_1 and T_2, until the boundary condition defined in Equation 3.9 is satisfied.

3.3.3. Thermal resistances

In the previous section, a description was given of the thermal model used to asses the suitability of Swagelok tube fittings as decomposition chamber interfaces. In this model five resistances are used that are still undefined. These resistances represent the five heat flow paths in the thermal model, which are the following:

- Convection from the hot gas to the chamber wall (R_1);
- Radiation from the hot gas to the chamber wall (R_2);
- Conduction from the inner chamber wall to the outer chamber wall (R_3);
- Convection from the outer chamber wall to ambient air (R_4);
- Radiation from the outer chamber wall to the environment (R_5).

The calculation of these resistances is discussed in this section.

$\mathbf{R_1}$ **- Hot gas convection** The main mode of heat transfer from the hot gas to the chamber wall is through convection. In case of convection, the following equation is used to calculate the heat flux. It is based on Newton's law of cooling [113]:

$$q_\alpha = h_\alpha \cdot (T_c - T_w) \tag{3.11}$$

In which q is the heat flux rate in $W\ m^{-2}$, h_α is the convective heat transfer coefficient in $W\ m^{-2}\ K^{-1}$, while T_c and T_w represent the chamber and wall temperatures respectively, in K. The resistance value of the resistor representing this mode of heat transfer in the thermal network described in the previous section is calculated using the following equation:

$$R = \frac{1}{h_\alpha A} \tag{3.12}$$

In which R is the resistance value in $K\ W^{-1}$ and A is the contact surface in m^2. Several models are available to calculate the convection from the hot gas in a rocket chamber to the wall. The following relation for the convective heat transfer coefficient in a thermal rocket chamber is referenced in [113] as taken from [17]:

$$h_\alpha = a \cdot \rho_c^{0.8} \cdot v_c^{0.8} \cdot (1/D_c)^{0.2} \cdot (k \cdot Pr^{0.33}/\mu^{0.8}) \tag{3.13}$$

In which:

a	0.023 in the combustion chamber, 0.025 - 0.028 in the nozzle throat $[-]$
ρ_c	Hot gas density $[kg/m^3]$
v_c	Hot gas velocity $[m/s]$
D_c	Diameter of the chamber $[m]$
k	Hot gas conductivity $[W/m/K]$
Pr	Prandtl number $[-]$
μ	Dynamic viscosity $[Pa\ s]$

Some additional examples that are mentioned in [113] are the Standard Bartz and a modified version of it. The latter is a slightly simpler equation and is defined as:

$$h_\alpha = 0.026 \cdot (G^{0.8}/D^{0.2}) \cdot (\mu^{0.2} \cdot c_{p,g}/Pr^{0.6}) \cdot (T_0/T_f)^{0.68} \tag{3.14}$$

Here, the mass flux G is used in $kg\ m^{-2}\ s^{-1}$ and $c_{p,g}$ is the specific heat at constant pressure in $J/kg/K$. T_0 represents the total (stagnation) temperature and T_f the film temperature, both in K. In this assessment, both coefficients have been calculated and the highest value is used to create the most conservative assessment. The film temperature is calculated according to [114] as:

$$T_f = 0.5T_w + 0.28T + 0.22T_r \tag{3.15}$$

In which T is the hot gas temperature and T_r is the adiabatic wall temperature, all in K. The latter is calculated by [113] as:

$$T_r = T_0 \cdot \left(1 + r \cdot \frac{\gamma - 1}{2} \cdot M_0^2\right) \tag{3.16}$$

In which T_0 is the static temperature in K and γ is the specific heat ratio. r is a recovery factor calculated by $r = Pr^{1/2}$ for laminar boundary layers, and $r = Pr^{1/3}$ for turbulent boundary layers. M_0 is the Mach number. In the decomposition chamber, the Mach number is very low (order of 10^{-2}), the recovery factor is smaller than one and the specific heat ratio is approximately 1.25. This results in the difference of the adiabatic wall temperature from the hot gas temperature being a percentage in the order of 10^{-4} %. Therefore in the decomposition chamber the following relation is simply used:

$$T_f = \frac{T_w + T_c}{2} \tag{3.17}$$

The Prandtl number is a dimensionless number that represents the ratio between thermal- and momentum diffusivity. It is calculated using the following relation [113]:

$$Pr = \frac{\mu \cdot c_p}{k} \tag{3.18}$$

Though it is stated that for gases a simplified approximation can be used:

$$Pr \approx \frac{4\gamma}{9\gamma - 5} \tag{3.19}$$

R_2 - Hot gas radiation It is mentioned in [113] (as referenced from [82]) that, in combustion chambers with temperatures lower than 800 K, the heat transfer due to hot gas radiation is negligible. According to NASA's CEA the adiabatic decomposition temperature of 98% hydrogen peroxide is at 1218 K and therefore, it is assumed that this portion of the heat transfer is non-negligible. In [113], it is also mentioned that at temperatures between 1900 and 3900 $°K$ the heat transfer due to radiation is between 5 and 35% of the total heat transfer to the walls and, that the presence of, among others, water vapor makes a significant contribution. Since the expected hot gas temperature for a thruster that works with 98% hydrogen peroxide is between the given ranges and the products contain water vapor, an attempt was made to determine the emissivity of the hot gas. The calculation of radiative heat flux is described in [113]. Several options are described using black body and grey body radiation. For the decomposition chamber, the concept of a grey medium surrounded by a grey body can be used. It is assumed that, for both the gas and the chamber wall, the absorptivity is equal to the emissivity. In this case the total heat flux can be calculated using:

$$q = \frac{\sigma(T_1^4 - T_2^4)}{\frac{1}{\epsilon_1} + \frac{1}{\epsilon_2} - 1} \tag{3.20}$$

In which ϵ_1 is the emissivity of the hot gas, ϵ_2 is the emissivity of the chamber wall, σ is the Stefan-Boltzmann constant and T_1 and T_2 are the temperatures in the gas and wall respectively, both given in K. Since nodes of the thermal model are defined in T and not in T^4, some conversion is required to calculate the resistance value. Mathematically it can be said that:

$$T_1^4 - T_2^4 = (T_1^2 - T_2^2)(T_1^2 + T_2^2) = (T_1 - T_2)(T_1 + T_2)(T_1^2 + T_2^2) \tag{3.21}$$

Now defining an arbitrary parameter B as:

$$B = (T_1 + T_2)(T_1^2 + T_2^2) \tag{3.22}$$

The heat flux equation can be calculated as the following:

$$q = \frac{\sigma B(T_1 - T_2)}{\frac{1}{\epsilon_1} + \frac{1}{\epsilon_2} - 1} \tag{3.23}$$

This means that the resistance value for the thermal network becomes temperature dependent and can be calculated using:

$$R(T) = \frac{\frac{1}{\epsilon_1} + \frac{1}{\epsilon_2} - 1}{\sigma A B} \tag{3.24}$$

In which A is the wall contact surface in m^2. The emissivity of water vapor is determined using the method described in [59]. As oxygen molecules are symmetrical, there is no strong infrared absorption due to dipole transitions [33]. Therefore radiation from oxygen is not considered in this model. At reference conditions, the emissivity of water vapor can be read from Figure 3.9, which shows the relation between the emissivity, pressure path length and temperature. The pressure path length is calculated through multiplication of the partial pressure p_a of water vapor and the path length L in cm. In case of the decomposition chamber, this path length is equal to the inner radius of the tube.

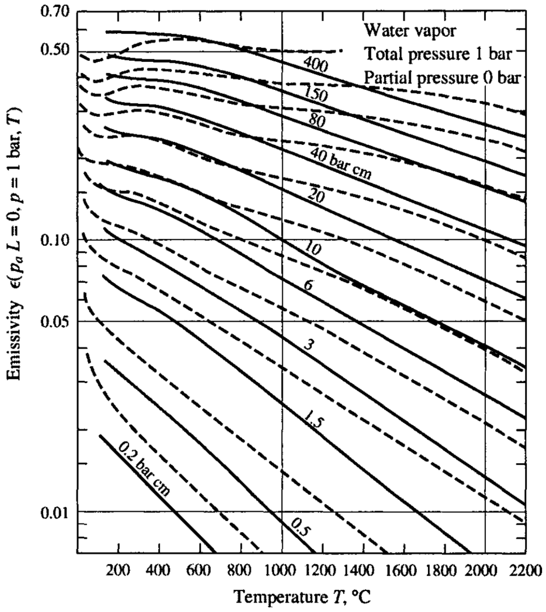

Figure 3.9: Emissivity of water vapors as a function of temperature and pressure path length [59],[45]

The solid lines are results from [31], while the dashed lines are from [45]. According to [59], the results of the latter are improved for more extreme conditions. Therefore, these values will be used. The equation represented by the dashed lines is the following:

$$\epsilon_0(p_a L, p = 1\, bar, T_g) = exp\left[\sum_{i=0}^{M}\sum_{j=0}^{N} c_{ji}\left(\frac{T_g}{T_0}\right)^j \left(\log_{10}\frac{p_a L}{(p_a L)_0}\right)^i\right], \qquad T_0 = 1000\,K,\ (p_a L)_0 = 1\, bar\, cm \tag{3.25}$$

In which:

$$\begin{bmatrix} c_{00} & \cdots & c_{N0} \\ \vdots & \ddots & \vdots \\ c_{0M} & \cdots & c_{NM} \end{bmatrix} = \begin{bmatrix} -2.2118 & -1.1987 & 0.035596 \\ 0.85667 & 0.93048 & -0.14391 \\ -0.10838 & -0.17156 & 0.045915 \end{bmatrix} \tag{3.26}$$

However, the results shows the emissivity values for a reference case with a total pressure of 1 bar and a partial pressure of 0 bar. A conversion factor is calculated in [59] using the following equation from [45]:

$$\left(\frac{\epsilon}{\epsilon_0}\right)_{H_2O} = \frac{(1-a)(1-P_e)}{(a+b-1+P_e)} exp\left(-c\left[\log_{10}\frac{(p_aL)_m}{p_aL}\right]^2\right) \tag{3.27}$$

For which the following parameters are used (Table 3.5):

Table 3.5: Variables as referenced in [59] from [45]

P_E	$(p + 2.56p_a/\sqrt{t})/p_0$
$(p_aL)_m/(p_aL)_0$	$13.2t^2$
a	$1.888 - 2.053\log_{10} t$
b	$1.10/t^{1.4}$
c	0.5
t	T/T_0
T_0	$1000\,°K$
p_0	$1\,bar$
$(p_aL)_0$	$1\,bar\,cm$

For a chamber pressure of 18 bar, a temperature of 1218 $°K$ (944.85 $°C$), inner tube diameter of 0.010922 m and H_2O_2 mole fraction of 0.675, this leads to a partial pressure of 12.2 bar and a pressure path length of 6.64 bar cm. The emissivity is then 0.156 (in the graph a value of 0.098 is found, before the correction is applied). In [113], an emissivity between 0.1 and 0.2 is mentioned for hydrogen and oxygen combustion products as is estimated in [114]. Therefore, this value is considered realistic. Some alternatives to Equation 3.20 were mentioned in [113], however these were not as easily converted into a thermal resistance. The results were compared to those of the method described above. In all cases the heat flux from the alternatives was slightly lower. The effect of this was checked by manually adjusting the thermal resistance until the same heat flux was achieved. The temperature deviation was always less than 5 $°K$. Therefore, it was considered not of major impact on the model. For this reason, the more conservative and more convenient equation 3.20 was used.

R_3 - Wall conduction In steady-state conditions, the conductive heat transfer rate through a bar can be calculated with the following expression [113]:

$$Q_x = \frac{kA}{L}\cdot\Delta T \tag{3.28}$$

In which Q_x is the heat flow rate in W, k is the conductivity coefficient in $W\,m^{-1}\,K^{-1}$ and L is the length of the bar in m. In the case of this model however, the heat flow is not calculated along the chamber, but from the inner wall to the outer wall of the chamber. For a cylindrical shell the relation above is adapted to the following:

$$Q_r = \frac{2\pi\cdot k\cdot L}{\ln\left(\frac{r_o}{r_i}\right)}\cdot(T_i - T_o) \tag{3.29}$$

With r_o representing the outer diameter of the shell and r_i representing the inner diameter. T_i and T_o respectively represent the temperature at the inner and outer walls in $°K$. The resistance value for use in the thermal model is calculated using the following relation:

$$R_T = \frac{\ln\left(\frac{r_0}{r_i}\right)}{2\pi\cdot k\cdot L} \tag{3.30}$$

R_4 - Free convection at the outer wall Convective heat transfer from the outer chamber wall to the ambient air happens through the means of free convection. The concept of free convection is explained in [35]. This form of convection occurs when the velocity of the surrounding fluid (in this case air) is not forced, but a natural current exists. This current occurs due to buoyancy forces in the fluid, often caused by a temperature gradient in the fluid. The calculation in this thermal model is done according to the example calculation for a long horizontal cylinder in [35], which starts with the following expression:

$$h_\alpha = \frac{Nu_D\cdot k}{D} \tag{3.31}$$

In which h_α is the heat transfer coefficient in $Wm^{-2}K^{-1}$, Nu_D is the Nusselt number, k is the conductivity of air in $Wm^{-1}K^{-1}$ and D is the outer diameter of the cylinder in m. From this equation, it becomes clear that the Nusselt number is a dimensionless number that represents the ratio of heat transfer through convection and heat transfer through conduction. For a cylinder, it is calculated using the following equation [35]:

$$\overline{Nu_D} = \left\{0.60 + \frac{0.387 Ra_D^{1/6}}{[1 + (0.559/Pr)^{9/16}]^{8/27}}\right\}^2 \tag{3.32}$$

The equation above shows the relation between the Rayleigh number and the Prandtl number. The calculation of the Prandtl number was already shown in Equation 3.18. The Rayleigh number is calculated by using the following equation [35]:

$$Ra_D = \frac{g\beta\rho^2 C_p (T_s - T_\infty) D^3}{k\mu} \tag{3.33}$$

In which:

g	Gravitational acceleration (9.81) $[m/s]$
β	Thermal expansion coefficient $[1/K]$
ρ	Density $[kg/m^3]$
C_p	Specific heat at constant pressure $[J/kg/K]$
k	Conductivity coefficient $[W/m/K]$
μ	Dynamic viscosity $[Pa\ s]$
T_s	Temperature at the cylinder surface $[K]$
T_∞	Ambient temperature $[K]$

All properties of air are determined at the film temperature. An overview of these properties is found in Annex B. The film temperature is determined by the means of Equation 3.17. The heat flux is calculated by plugging Equation 3.31 into Equation 3.11. This means the thermal resistance can be calculated using 3.12.

$\mathbf{R_5}$ - Radiation at the outer wall Radiation from the outer wall to the environment has been modeled by the means of black body radiation. The equation for the heat flux is given in [113] as:

$$q = \epsilon\sigma(T_1^4 - T_2^4) \tag{3.34}$$

In which q is the heat flux in $W\ m^{-2}\ K^{-1}$, ϵ is the emissivity, σ is the Stefan-Boltzmann constant and T_1 and T_2 are the outer wall and the air temperature respectively, given in K. As the thermal network model is given in terms of T and not T^4, the equation needs to be adapted as was done for the hot gas radiation, by introducing an arbitrary parameter B, as was done in Equation 3.22:

$$q = \sigma\epsilon B(T_1 - T_2) \tag{3.35}$$

The thermal resistance has now become dependent of the temperatures and is calculated using the following equation:

$$R(T) = \frac{1}{\sigma\epsilon AB} \tag{3.36}$$

In which A is the contact surface in m^2.

3.3.4. Results from the thermal model

To assess the maximum temperatures in the wall a worst-case approach is taken. It is assumed that no catalyst bed is present, which would be representative of the case that an alternative decomposition technology is used. The feed pressure is taken as the maximum feed pressure of 24 bar. An injector pressure drop of 20% of the chamber pressure is assumed, which is mentioned as a typical pressure drop in [82]. To create a worst-case scenario case, it is assumed that the pressure drop of anything upstream of the injector is zero. Additionally, it is assumed that an alternative decomposition method is used and therefore no pressure drop is present over the catalyst bed. Using the value for the injector pressure drop as mentioned before and the maximum feed pressure of 24 bar, this leads to a chamber pressure of 20 bar. The decomposition temperature and gas composition are determined using NASA's CEA. An ambient temperature of 25 C or 298.15 K is assumed. Higher mass flows lead to higher wall temperatures and therefore the maximum mass flow of 0.72 g/s was used as is determined in Section 3.4. A catalyst bed void fraction of 0.4215 was used, which is called a representative value in [41]. The void fraction is a parameter that indicates the ratio of the void space and catalyst material in the pipe area. This means that the effective pipe area used for calculation of the flow velocity is equal to the product of the void fraction and the total pipe area. The Swagelok tube that was used has an outer diameter of 0.5 $inch$ and a thickness of 0.049 $inch$. The selection of the tube diameter is discussed further in Section 4.1. An overview of the inputs is provided in Table 3.6.

Table 3.6: Overview of inputs for the thermal model for Swagelok suitability assessment

Parameter	Value	Unit
T_c	1218	K
T_a	298.15	K
P_c	20	bar
x_{H_2O}	0.675	$-$
x_{O_2}	0.325	$-$
$\dot{m}$	0.72	g/s
D_o	0.5	$inch$
t	0.049	$inch$
$void\,fraction$	0.4215	$-$

The calculation is performed solely for the area in the chamber with the highest gas temperature. Furthermore, no heat transfer within the wall in the axial direction is assumed. This means that the results from this assessment will indicate higher temperatures than should be expected and thus represent a conservative assessment. The results of the assessment using the input values above are given in Table 3.7.

Table 3.7: Wall temperature results from the Swagelok thermal assessment

	$\mathbf{T_0}$	$\mathbf{T_1}$	$\mathbf{T_2}$	$\mathbf{T_3}$
Kelvin	1218	1010.3	1009.1	298.15
Celsius	944.85	737.1	736.0	25

In which T_0 is the hot gas decomposition temperature, T_1 is the temperature of the inner wall, T_2 is the temperature of the outer wall and T_3 is the ambient temperature. These temperatures occur in the decomposition chamber, before the nozzle. The wall temperature in the nozzle throat will be higher due to the increased convective heat transfer rate from the hot gas to the wall. However, the wall thickness in the nozzle throat is much higher and therefore, it is able to sustain higher pressures. For this reason, this is not considered relevant for the suitability assessment of the Swagelok tubes and fittings. The parameters used and calculated during the assessment of the heat transfer from the hot gas to the inner wall are presented in Table 3.8.

Table 3.8: Overview of parameters for convective and radiation heat transfer from the hot gas to the inner wall

Convection				**Radiation**		
Par.	**Value**	**Unit**		**Par.**	**Value**	**Unit**
γ	1.2516	-		σ	$5.67 \cdot 10^{-8}$	$W/m^2/K^4$
Pr	0.799	-		ϵ_1	0.149	-
μ	$4.53 \cdot 10^{-5}$	$Pa\ s$		ϵ_2	0.633	-
c_p	1851.6	$J/kg/K$		A	0.0342	m^2
k	0.10	$W/m/K$				
T_f	1114.1	K				
h_a	232.21	$W/m^2/K$				
L	1	m				
D_c	0.01021	m				
A	0.0321	m^2				
$\mathbf{R_1}$	**0.1343**	$\mathbf{K/W}$		$\mathbf{R_2}$	**0.716**	$\mathbf{K/W}$

Similarly, the parameters used in the calculation of conductive heat transfer within the wall are shown in Table 3.9.

Table 3.9: Parameters for the calculation of conductive heat transfer within the chamber wall

Conduction		
Par.	**Value**	**Unit**
k	24.40	$W/m/K$
r_1	0.00511	m
r_2	0.00635	m
$\mathbf{R_3}$	**0.00618**	$\mathbf{K/W}$

Finally, the same has been done for the calculation of the convective and radiative heat transfer from the outer chamber wall to the environment. These parameters are presented in Table 3.10.

Table 3.10: Overview of parameters for convective and radiation heat transfer from the outer wall to the environment

Convection				**Radiation**		
Par.	**Value**	**Unit**		**Par.**	**Value**	**Unit**
Ra	2914.87	-		σ	$5.67 \cdot 10^{-8}$	$W/m^2/K^4$
Nu	3.290	-		ϵ	0.633	-
h_a	12.79	$W/m^2/K$		A	0.399	m^2
A	0.0399	m^2				
$\mathbf{R_4}$	**1.96**	$\mathbf{K/W}$		$\mathbf{R_5}$	**0.482**	$\mathbf{K/W}$

The meaning of each symbol is defined in the section describing the calculation of each heat transfer mode. Using the values from the tables above, the final replacement resistances are calculated. An overview of the resistances used in the final calculation is given in Table 3.11.

Table 3.11: Overview of thermal resistances

Resistor	**Value**	**Unit**
$R_{1,2}$	0.113	K/W
R_3	$6.17 \cdot 10^{-4}$	K/W
$R_{4,5}$	0.387	K/W
R_{TOT}	0.501	K/W

3.3.5. Swagelok capability and suitability

The working pressure capabilities of the Swagelok tube fittings have been published in the catalog [90] at a reference temperature. To assess these capabilities at higher temperatures, Swagelok have provided safety factors for a range of temperatures that can be multiplied with the published maximum pressure at reference temperature. The following factors have been supplied:

Table 3.12: Safety factors published in the Swagelok tube fitting catalog [90]

T [°C]	Safety factor
93	1.00
204	0.96
315	0.85
426	0.79
537	0.76

As is seen from Table 3.12, these safety factors have been provided until a temperature of 537 $°C$. However, the expected temperature in the chamber walls, and thus the fittings, is around 740 $°C$. To assess the suitability of the Swagelok fittings, an extension of the safety factors is created. The swagelok seamless tubing catalog [91] mentions that the published operating pressured are calculated using the method described in ASME B31.3 [4]. The pressure calculations are based on ASTM A269 piping with an S-value of 20 ksi in the temperature range of -28 to 37 $°C$. In ASME B31.3 the design equation for pressure piping is mentioned as the following:

$$t = \frac{PD}{2(SEW + PY)} \tag{3.37}$$

In which:

t	Pipe thickness [inch]
P	Internal gauge pressure [PSI]
D	Outside diameter [inch]
S	Maximum stress value [PSI]
E	Quality factor [-]
W	Weld joint strength reduction factor [-]
Y	Temperature dependent coefficient [-]

In the case of seamless tubing, no weld joint is present, meaning the parameter W is equal to 1. The coefficient Y is temperature dependent and is determined from a table in the document, which gives the following values for austenitic steels:

Table 3.13: Y coefficient from ASME B31.3 [4]

Temperature [°C]	<482	510	538	566	593	621	649	>677
Y	0.4	0.4	0.4	0.4	0.5	0.7	0.7	0.7

For seamless ASTM A269 tubing, the quality factor E should be equal to 1. However, in the case of this calculation, the value has been tuned down to a value of 0.87 to get an agreement with the results from the Swagelok manual. This quality factor may be affected by the tolerances used by Swagelok. The maximum allowable stress values are taken from the tables in ASME B31.3 for ASTM A269 Stainless Steel 316 piping and are depicted in Figure 3.10.

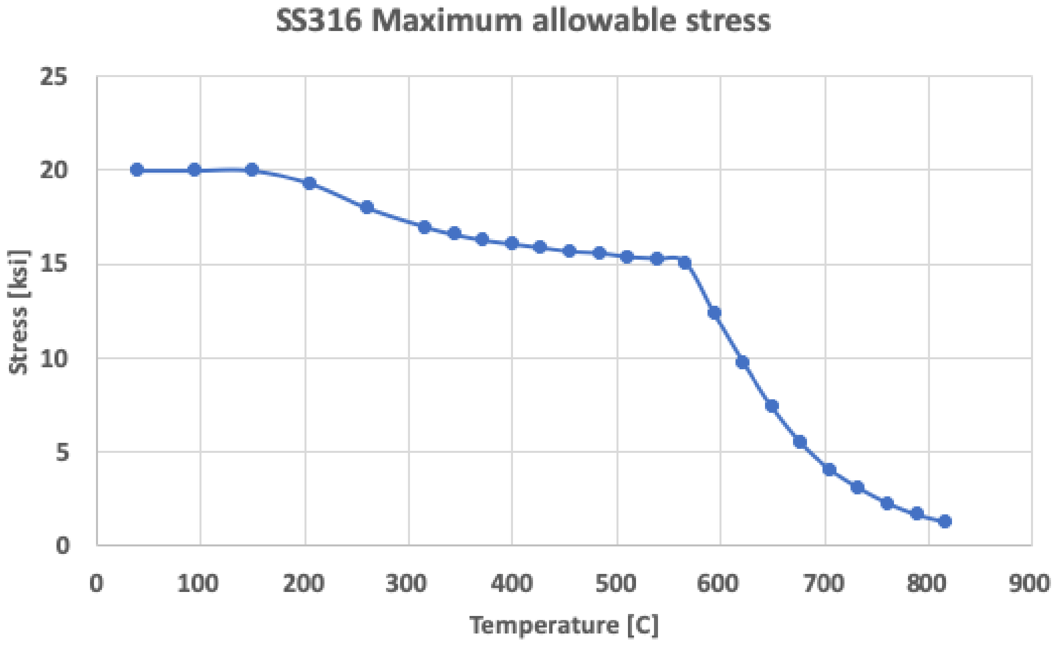

Figure 3.10: Maximum allowable stress for ASTM A269 Stainless Steel 316 piping from ASME B31.3 [4]

To calculate the allowable working pressure, Equation 3.37 is rewritten in the following form:

$$P = \frac{2tSE}{D - 2tY} \tag{3.38}$$

The results for a stainless steel 316 tube, with an outer diameter of 0.5 inch and a wall thickness of 0.049 inch, are displayed in Figure 3.11, which also shows the allowable working pressures calculated using the pressures and safety factors published by Swagelok in [90].

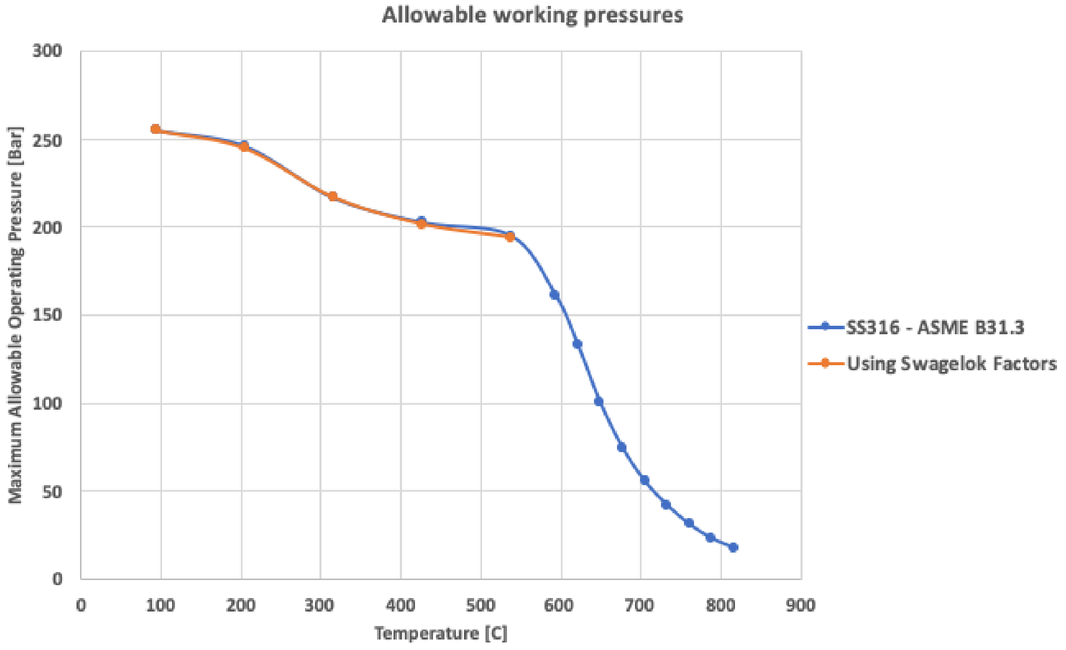

Figure 3.11: Comparison between Swagelok published working pressures and the ones calculated using ASME B31.3 [4]

The figure clearly shows that the calculation provides the exact results described by Swagelok. The standard tube fittings from Swagelok have been rated for the same working pressures as the seamless tubing. Therefore, they do not require separate analysis. For a wall temperature of 740 $^{\circ}C$, as was calculated in the thermal model before, a maximum allowable gauge working pressure of 39.2 bar was calculated. In atmospheric conditions this translates to a maximum chamber pressure of 40.2 bar, which is well over MEOP (with a factor of approximately 1.7), defined at 24 bar. A maximum allowable chamber pressure of 24 bar is found at a wall temperature of approximately 788 $^{\circ}C$.

Other than working pressures, the requirements documentation also specifies values for the proof and burst pressure. *MGT-010* mentions a required minimum proof pressure of 1.5 times MEOP and *MGT-016* mentions a required minimum burst pressure of four times MEOP. The expected proof pressure is calculated using the 0.2% Yield Strength of stainless steel 316 as a maximum stress value, whereas the burst pressure is estimated using the Ultimate Tensile Strength (Annex B). Using the calculations above, the proof pressure of the tube at the expected temperature of 740 C is about 240 bar, whereas the burst pressure is around 443 bar. These values are significantly higher than the requirements of 36 and 96 bar respectively. In fact, a safety factor of over four can be applied while still fulfilling the requirement. Additionally stainless steel 316L has successfully been used in a 5N thruster using 98% hydrogen peroxide in [66]. Therefore, it is expected that the Swagelok tube fittings are suitable for the intended use in the design. Should the interfaces unexpectedly proof unsuitable during testing, this would most likely occur during steady-state testing, as the thruster is not likely to reach its maximum temperature during pulsed mode operation. A recovery action is identified, by creating an extra decomposition chamber with an integrated nozzle, eliminating the downstream Swagelok interface. This decomposition chamber can then be used for steady-state tests, if required.

3.4. Inlet valve selection

The last step taken, before the detailed design process was started, is the selection of the inlet valve. An overview of several valves has been created to provide input for a technology trade-off. A list of key parameters has been generated to serve as criteria for the trade-off (3.4.1). Some of the considered valve options are described in detail with respect to the trade-off criteria (3.4.2). Though initially a trade-off was envisioned, the valve was eventually selected in an elimination process (3.4.3). Finally, a calculation of the expected pressure drop during operation is made (3.4.4).

3.4.1. Relevant trade-off parameters

In order to successfully execute the inlet valve selection process, a set of criteria was generated with ESA. The parameters that were deemed most important for the selection process are the following:

- Chemical compatibility
- Valve response time
- Dribble volume
- Cycle life

Chemical compatibility The first, and most important, parameter used in the valve selection process concerns the chemical compatibility of the propellant and the materials used in the construction of the inlet valve. This is in compliance with requirements *MGT-250* and *MGT-412*. Using compatible materials is vital for safe and continued operation of the the thruster and test equipment. As the material compatibility is a hard requirement, not satisfying it will result in the automatic elimination of the candidate valve from the selection process.

Valve response time The valve response times have been included in the requirements specification document. The valve opening response time shall be less than 15 ms as per *MGT-170*. The valve closing time shall be less than 10 ms as per *MGT-172*. Any valves unable to follow these specifications are eliminated from the candidate list. For all valves that fulfill these requirements, a general rule can be followed for both response times: lower (faster) is better.

Dribble volume The dribble volume associated with the valve shall be minimized as per requirement *MGT-312*. This is the volume within the valve body, downstream of the closing orifice. When opening the valve, this volume is filled before the propellant can continue to towards the injector and decomposition chamber. Additionally, when the valve is closed, the propellant that is still present in this volume will continue to flow through the thruster. Therefore, the dribble volume affects the response times of the thruster during operation. For this parameter the following rule is applied: lower is better.

Cycle life The amount of pulses required from the thruster has been described in requirement *MGT-110*. As a minimum requirement of 8,000 pulses exists. Inlet valves incapable of fulfilling this number of cycles are eliminated from the candidate list. In the requirement, a goal of more than 13,000 pulses is stated. Therefore, the following rule applies to the inlet valve selection: A higher cycle life is better.

3.4.2. Valve options

To provide input for the inlet valve trade-off, a list containing a collection of potential valves was generated. A range of manufacturers, that ESA is already familiar with, was included. For each of the considered valves, a description is included in this section. The list of valves included in the selection process is as follows:

1. GSR Ventil Technik: Rapid Reaction Valve 95
2. Parker: Fast Switching Valve
3. Parker: Pulse Valve
4. Danfoss: Type EV210B
5. ERA-SIB: Types WH and WPH
6. ERA-SIB: EN52050 and 51
7. RSG Regel- und Steuergeräte: Type 267
8. CS Fluid Power Co Ltd: ADS Series 8000

GSR Rapid Reaction Valve 95 The RRV 95 is a normally closed solenoid ball valve developed by the DLR and licensed by GSR Ventil Technik. It is designed for very fast response times and high control frequencies in a pressure range of 20 - 200 bar [40], though a range of 0.5 - 200 bar has also been advertised [39]. In the standard version of this valve, the metal internals are constructed using 420C Stainless Steel and the housing is made of 430F Stainless Steel [40], both of which should be avoided according to [20]. It is mentioned in [39] that the valve can be tailored for specific applications and some special materials may be used upon request, including other steels. Seals are created using either NBR, FKM, EPDM or PEEK [40], of which FKM [38] and PEEK [69, 72] are compatible options. The response time is claimed to be less than 10 ms according to [40], which fulfills requirements *MGT-170* and *MGT-172*. No information on the dribble volume was provided, though it is considered relatively large (compared to for example a flange connection), due to the 1/8 inch tube fitting connection. With respect to the life cycle, a claim was made that the system has a life cycle 100 times higher than other standard valves.

Figure 3.12: GSR RRV 95 [40]

Figure 3.13: Parker FSV [63]

Parker Fast Switching Valve The Parker Fast Switching Valve [63] is a normally closed pilot operated poppet valve with magnalift. It is designed for a maximum allowable pressure differential of 7 bar. The reference claims an ”extremely short” response time (electric response 9.5 - 12 ms for opening and 4 - 8 ms for closing), which fulfills requirements *MGT-170* and *MGT-172*. The internals are made using stainless steel, though the case material is brass, which is not compatible with hydrogen peroxide [80]. The seals are made using polyurethane, which is also not compatible [20]. No information is provided on the dribble volume, though from the technical drawings it appears relatively large, compared to for example a direct flange connection. The specification boasts a life of more than 500 million cycles, though the response time starts increasing after 300 million cycles.

Parker Pulse Valve The Parker Pulse Valve [64] is a normally closed solenoid valve that is aimed at high speed response. It operates up to a pressure of 86.2 bar. The body of the valve is made using non-corroding passivated stainless steel and the wetted parts are made using Vespel or PTFE, combined with FFKM. Both PTFE [23] and FFKM (Perfluorelastomer) [22] are compatible with hydrogen peroxide. The response time is stated as less than 2 ms, and could be reduced until 160 μs in combination with the Parker IOTA ONE Valve Driver. Both advertised response times fulfill requirements *MGT-170* and *MGT-172*. No information is available regarding the dribble volume, though from the technical drawings the dribble volume is seen to be small. No life cycle information is available.

Figure 3.14: Parker Pulse Valve [64]

Figure 3.15: Danfoss EV210B [19]

Danfoss Type EV210B and BW The Danfoss Type EV210B and EV210BW [19] describes a wide range of solenoid valves, suitable for many different working conditions. It is suitable for a differential pressure from 0 to 30 bar. Different versions are available in both brass and stainless steel. The stainless steel versions are made using a combination of alloys 301, 304, 316 and 430, of which alloy 430 should be avoided according to [20]. Seals are available in both FKM and EPDM. Though FKM is compatible with hydrogen peroxide [80], it can only be selected when brass is chosen for the valve material. For the stainless steel version only EPDM seals are available, which are not compatible with high concentration hydrogen peroxide [38, 80]. Opening response times are mentioned in [19] between 10-20 ms, depending on the chosen model. The closing response time is listed as 20 ms, which exceeds the maximum value stated in *MGT-172*. Though no dribble volume is listed, it is considered relatively large (compared to for example a flange connection), due to the tube fitting connection (smallest diameter is 1/8 inch). No life cycle information is available.

Figure 3.16: ERA-SIB WH [47]

ERA-SIB WH and WPH The Type WH and Type WPH valves [47, 48] are normally closed valves produced by ERA-SIB, designed for a pressure between 0 and 200 bar. The valves are made using stainless steel for both the body and internals, though a more exact description of the used alloys was not found. The seals used in the valves can be made of either NBR, FKM, PTFE or EPDM, of which FKM [38, 80] and PTFE [23] are compatible with high concentration hydrogen peroxide. The maximum response time is mentioned to be lower than 20 ms, which is too high according to *MGT-170* and *MGT-172*. No information is provided regarding the dribble volume, though it is considered relatively large (compared to for example a flange connection), due to the tube fitting connections. No life cycle information is provided.

Figure 3.17: ERA-SIB EN52050-51 [49]

ERA-SIB EN52050-51 The ERA-SIB EN52050-51 is a normally closed valve produced by ERA-SIB, designed for a pressure between 0 and 300 bar. The valve is made using stainless steel for both the body and internals however, as was the case for the ERA-SIB type WH and WPH valves. No information was found on the actual alloys used for construction. The seals used in the valve are made using PTFE and FKM, which are both compatible for use with high concentration hydrogen peroxide [23, 38, 80]. The maximum response time is mentioned to be lower than 20 ms, which is too high according to *MGT-170* and *MGT-172*. No information is provided regarding the dribble volume, though it is considered relatively large (compared to for example a flange connection), due to the tube fitting connections. No life cycle information is provided.

Figure 3.18: RSG Type 267 [107]

RSG Regel- und Steuergeräte Type 267 The type 267 [107] is a normally closed coaxial valve produced by RSG Regell- und Steuergeräte. It has been designed for a pressure range of 0 to 300 bar. The standard version of this valve is made using galvanized or nickel-plated steel. The website does state that any components coming into contact with the working media can be produced in V2A (AISI 304, 304L) or V4A (AISI 316L) quality stainless steel, which are suitable for use with hydrogen peroxide [20]. The seals are made of FKM and PTFE, both compatible materials with high concentration hydrogen peroxide [23, 38, 80]. An opening response time of 29 ms is mentioned, which is not sufficient when comparing it to requirement *MGT-170*. The closing response time is stated as 200ms, which is significantly worse than the required value from *MGT-172*. No information is provided regarding the dribble volume, though it is considered relatively large (compared to for example a flange connection), due to the tube fitting connections. No life cycle information is provided.

Figure 3.19: CS Fluid Power ADS8000 series [50]

CS Fluid Power Co Ltd Series 8000 The CS Fluid Power Co Ltd 8000 series [50] is a solenoid valve for high pressure application. It was designed for a differential pressure of 0 to 150 bar (depending slightly on working media). Its components can be produced in 316 Stainless Steel (body) and 304 stainless steel (tube), which are suitable for use with high concentration hydrogen peroxide [20]. Seals are available in NBR, Silicone, EPDM, Viton and PTFE. Viton A [20, 80] as well as PTFE [23] are hydrogen peroxide compatible materials. The response time is mentioned to be less than 20 ms, which is not sufficient to fulfil requirements *MGT-170* and *MGT-172*. No information is provided on the dribble volume, though it is considered relatively large (compared to for example a flange connection), due to the tube fitting connections. No life cycle information is provided.

3.4.3. Selected valve

The valve selection was initially envisioned to be a trade-off process. After review of the valves described in the previous section however, it turned out that for most options some characteristic is present that makes it unsuitable. Therefore the selection was done through the means of an elimination, rather than a trade-off. In all cases, the eliminating characteristic is related to either the response time or the materials of construction. The requirements regarding the response times are defined as lower than 15 ms for opening and lower than 10 ms for closing, in *MGT-170* and *MGT-172* respectively. Additionally, *MGT-250* and *MGT-412* state that the equipment shall be designed to operate with the working media (hydrogen peroxide). This is done by choosing compatible materials. The response times and materials of construction were described for each valve in Section 3.4.2. By comparing the data to the requirements, the elimination was performed, for which an overview is created in Table 3.14.

Table 3.14: Overview of inlet valve eliminating properties

Valve	**Reason for elimination**
GSR RRV 95	Material incompatibility (without special ordering)
Parker FSV	Material incompatibility
Parker Pulse Valve	-
Danfoss Type EV210B	Material incompatibility Response time too high
ERA-SIB WH and WPH	Unknown stainless steel alloy Response time too high
ERA-SIB EN52050-51	Unknown stainless steel alloy Response time too high
RSG Type 267	Response time too high
CS Fluid Power ADS-8000 series	Response time too high

From the table, it is concluded that the only valve from the collection that is suitable off the shelf, is the Parker Pulse Valve. A number of different versions of this valve are available [64]. The determination of the correct model was done in several steps. First of all, the orifice diameter was chosen from four available options (0.10, 0.51, 0.79 and 0.99 mm). The maximum allowable working pressure of the three smallest options is 86.2 bar, whereas the largest orifice has a maximum allowable working pressure of 51.7 bar. The proof pressure is defined by Parker at 1.5 times the maximum allowable working pressure. Taking into account the pressure requirements in *MGT-004* and *MGT-010*, all options were considered suitable for the defined pressure environment. To minimize the pressure drop over the valve, a larger orifice was considered favorable. Test data is available in ESA for the valve with the second largest orifice (0.79 mm) [108], therefore this diameter was selected. The seal material was chosen as PTFE, due to its compatibility with concentrated hydrogen peroxide [20]. Finally, the outlet porting was chosen as a flange with a straight orifice (no exit cone), to minimize the dribble volume. An overview of the chosen valve model characteristics is seen in Table (3.15):

Table 3.15: Selected valve characteristics and ordering information [64]

Parameter	**Value**
Manufacturer	Parker
Series	Pulse Valves
Model number	009-0381-900
Orifice Size	0.031” (.79 mm)
Operating pressure	Vac - 1250 PSI (86.2 bar)
Seal Material	PTFE/FFKM
Voltage	28 V
Outlet port	Flange, no cone

3.4.4. Pressure drop

The expected pressure drop for the Parker Pulse Valve using hydrogen peroxide is calculated using a method that is used by the thesis supervisor in ESA. Testing data of the valve pressure drop related to the mass flow is available within ESA [108]. To convert this data to a pressure drop using hydrogen peroxide initially the assumption is made that the Reynolds number remains equal:

$$Re_{H_2O_2} = Re_{H_2O} \tag{3.39}$$

For pipe flow, the Reynolds number is calculated using [113]:

$$Re = \frac{\rho v D}{\mu} \tag{3.40}$$

Here ρ represents the density of the fluid in kgm^{-3}, v is the flow velocity in ms^{-1}, D is the tube diameter in m and μ is the dynamic viscosity in $Pa\ s$. Substitution into Equation 3.39 leads to:

$$\frac{\rho_{H_2O_2} v_{H_2O_2} D}{\mu_{H_2O_2}} = \frac{\rho_{H_2O} v_{H_2O} D}{\mu_{H_2O}} \tag{3.41}$$

The continuity equation dictates [113]:

$$v = \frac{\dot{m}}{\rho A} \tag{3.42}$$

In which $\dot{m}$ is the mass flow in $kg\ s^{-1}$ and A is the pipe area in m^2. Substitution of this equation into Equation 3.41 then leads to the following relation for the equivalent mass flows, which should be used for the calculation of the pressure drop:

$$\frac{\dot{m}_{H_2O_2}}{\mu_{H_2O_2}} = \frac{\dot{m}_{H_2O}}{\mu_{H_2O}} \tag{3.43}$$

Typically, the pressure drop of a valve is calculated using the following equation [34]:

$$\Delta P = K \cdot \frac{\rho v^b}{2} \tag{3.44}$$

In which ΔP is the pressure drop in Pa, K is an experimentally determined pressure drop coefficient and b is expected by theory to be equal to 2. However, using ESA's method, b is adjusted to fit results from experiments. Writing this equation for both hydrogen peroxide and water and then dividing to calculate the ratio leads to:

$$\frac{\Delta P_{H_2O_2}}{\Delta P_{H_2O}} = \frac{\rho_{H_2O_2} v_{H_2O_2}^b}{\rho_{H_2O} v_{H_2O}^b} = \frac{\rho_{H_2O_2}}{\rho_{H_2O}} \cdot \left(\frac{v_{H_2O_2}}{v_{H_2O}}\right)^b \tag{3.45}$$

Substitution of the continuity equation into the above equation then gives:

$$\frac{\Delta P_{H_2O_2}}{\Delta P_{H_2O}} = \frac{\rho_{H_2O_2}}{\rho_{H_2O}} \cdot \left(\frac{\dot{m}_{H_2O_2}}{\dot{m}_{H_2O}} \cdot \frac{\rho_{H_2O}}{\rho_{H_2O_2}}\right)^b = \left(\frac{\dot{m}_{H_2O_2}}{\dot{m}_{H_2O}}\right)^b \cdot \left(\frac{\rho_{H_2O}}{\rho_{H_2O_2}}\right)^{b-1} \tag{3.46}$$

Using the mass flow relation from Equation 3.43 gives the final equation to calculate the hydrogen peroxide pressure drop:

$$\Delta P_{H_2O_2} = \Delta P_{H_2O} \cdot \left(\frac{\mu_{H_2O_2}}{\mu_{H_2O}}\right)^b \cdot \left(\frac{\rho_{H_2O}}{\rho_{H_2O_2}}\right)^{b-1} \tag{3.47}$$

As mentioned before, the value of b was calculated from test data using the Parker Pulse Valve. For this calculation, b is equal to 1.5815 [108]. From the same test data, the pressure drop using water was determined and was used in the calculation above. The complete calculation was done for a reference scenario (described in Section 3.1.3). In Table 3.16 an overview of used parameters is used. The method to determine b is described in Section 4.4.3, where this method was used to determine the pressure drop over the catalyst bed retainers.

Table 3.16: Valve pressure drop inputs

Parameter	Value	Unit
T	20	C
ρ_{H_2O}	999.4	kg/m^3
$\rho_{H_2O_2}$ (98%)	1441.7	kg/m^3
μ_{H_2O}	0.00102	$Pa\,s$
$\mu_{H_2O_2}$ (98%)	0.00127	$Pa\,s$
$\dot{m}_{H_2O_2}$	0.6	g/s

The resulting expected pressure drop in the reference scenario is equal to 0.065 bar. For more information on the determination of the fluid properties, the reader is referred to Annex B.

3.5. Conclusion

To prepare for the design of a one newton hydrogen peroxide monopropellant thruster, an overview was made of the key requirements. The thruster will operate in a feed pressure window of 5.5 to 24 bar and will be placed in atmospheric conditions. The requirements specification lists an overview of duty cycles to be performed during testing. For the full test campaign for a single catalyst bed or decomposition technology a requirement is set of at least 8000 pulses. The performance requirements describe the thrust and specific impulse ranges at 24, 15 and 5.5 bar feed pressure. An interpolation was performed to generate a complete overview of the thrust and specific impulse requirements, over the entire operating range. From these requirements, the expected mass flow rates were calculated, ranging from 0.16 g/s at the low end of the operating range to 0.72 g/s at the high end. At the reference point, which is at a feed pressure of 22 bar and with a thrust of 1 N, the mass flow rate is expected to be approximately 0.6 g/s.

For the thruster design, a modular concept was generated consisting of five modules: the inlet valve, thermal standoff and capillary tube, injector, decomposition chamber and the nozzle. All required interfaces were listed. It was concluded that the most critical interfaces are the upstream and downstream interfaces of the decomposition chamber, as they come in contact with the decomposing hydrogen peroxide and high temperature reaction products. A commercially available solution for these interfaces was found in using tube fittings from the manufacturer Swagelok. These tube fittings consist of a fitting body, a nut and two ferrules. The interface works by compressing the ferrules into a tube, which creates a grip and seal.

To assess the suitability of this concept, a thermal model was created for the chamber wall. The thermal model considers radiation and convection from the hot gas to the wall, conduction through the wall and finally, radiation from the wall to the environment as well as free convection from the outer wall to the surrounding air. Several conservative choices were made in this model, which led to a maximum expected wall temperature of 740 $°C$. Since the published Swagelok pressure capabilities are only listed until 537 $°C$, calculations were performed to extend this data. It was determined that the tube fittings are able to withstand the pressure environment at the expected temperatures and, with the wall thickness chosen as described in Chapter 4, at MEOP the wall temperature is allowed to increase to 788 $°C$.

With the interface concept known, the final step taken in preparation to the design phase was the selection of an inlet valve. A list of potential valves was generated for a trade-off, though this finally resulted in an elimination process, as most valves could not fulfill either the material requirements, or the response time requirements specified in the requirements specification document. As a result of this assessment, the Parker Pulse Valve was selected. This valve has a response time below 2 ms, is constructed using hydrogen peroxide compatible materials and has a very small dribble volume. A pressure drop assessment was performed, based on available water flow test data. It was determined that the Parker Pulse Valve has a theoretical pressure drop of 0.065 using 98% hydrogen peroxide at the performance reference point specified in the requirements.

4

Baseline design

The conceptual design of the thruster has been completed in the previous chapter. This is followed by the design of the thruster subcomponents in detail. To get an idea of the detailed thruster design for reference, an image of the assembled model is seen in Figure 4.1. The first step in the detailed design process was the determination of the chamber geometry (4.1), in particular the selection of the diameter. After this, the components upstream of the injector were designed as the design of the downstream components is dependent on the pressure losses of the upstream components. The inlet valve was already selected during the design preparation. Therefore, the design of the thermal standoff and capillary tube is next (4.2). With the pressure drop upstream of the injector known, the chamber pressure is determined and the injector is designed (4.3). This is followed by the design of the catalyst bed retainers (4.4). All components relevant to the pressure drop of the thruster are now completed. Therefore, this is followed by a complete assessment of the pressure drops in the thruster in the full operating range (4.5). The final component designed is the nozzle module (4.6). Lastly, a fluid and thermal model was created using EcosimPro, to assess the thermal performance and response times of the system (4.7). The chapter is ended with a summarizing conclusion (4.8).

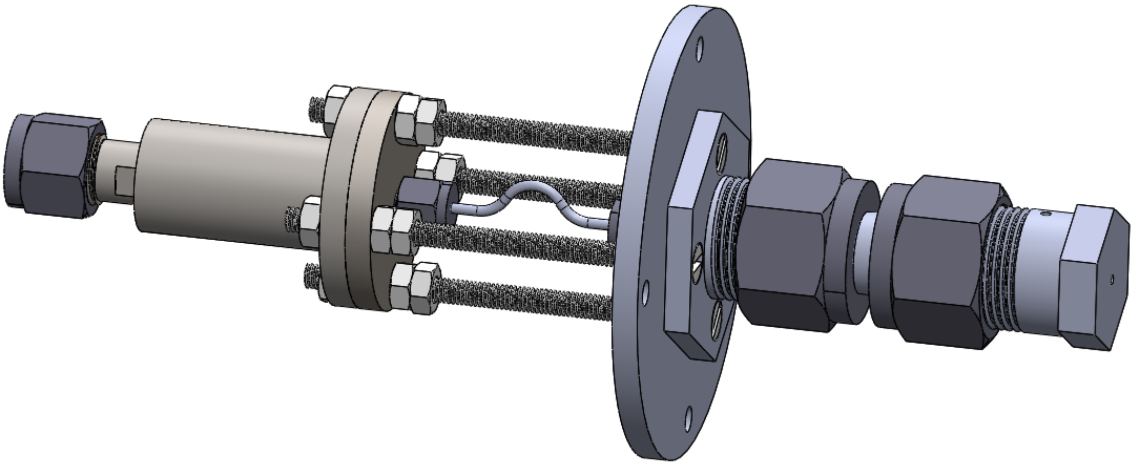

Figure 4.1: Overview of the completed thruster design

4.1. Decomposition chamber

As the thruster will be used for testing of different catalyst beds as well as alternative technologies, the approach taken for the design is to maximize the simplicity of the decomposition chamber. Additionally, the exchange of different decomposition chambers should be made as easy as possible. This is what inspired the use of Swagelok tube fittings, which make it possible for the decomposition chamber to consist of a simple tube. For sizing of the decomposition chamber, the main parameter that should be considered is its diameter. Since the baseline design of the thruster will employ a catalyst bed, the internal diameter of the decomposition chamber determines the catalyst bed loading. The catalyst bed loading is a measure for the catalyst bed frontal surface area with respect to the propellant mass flow and is given in $kg\, m^{-2}\, s^{-1}$. To determine a good value of catalyst bed loading, a review was made of values for the catalyst bed loading, at the nominal point, in existing thrusters. The collection of data is shown in Figure 4.2.

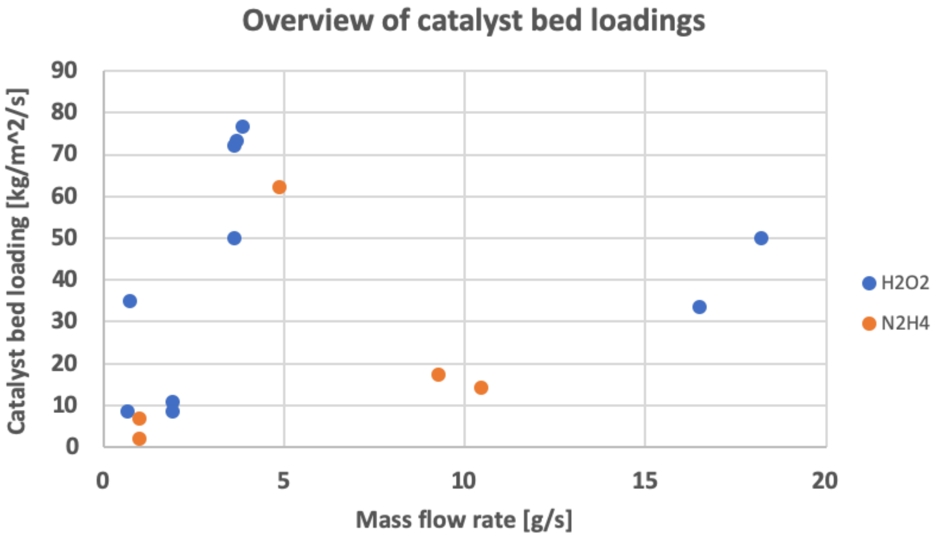

Figure 4.2: Catalyst bed loading at nominal point found in other thrusters with respect to mass flow rate (data from [3, 14, 18, 21, 53, 65, 76, 106]

The overview shows a spread of data points for both hydrazine thrusters and hydrogen peroxide thrusters. Though the values vary, a general trend that is spotted is that the catalyst bed loading reduces with reducing mass flow rate. In the region below 2 $g\, s^{-1}$ most data points show a catalyst bed loading around or below 10 $kg\, m^{-2}\, s^{-1}$. As was seen in Section 3.1.3, the average mass flow rate for the reference scenario is determined at approximately 0.6 $g\, s^{-1}$. The internal chamber diameter flow area is now calculated using:

$$A = \frac{\dot{m}}{G} \tag{4.1}$$

In which A is the flow area in m^2 and $\dot{m}$ is the mass flow rate in $kg\, s^{-1}$. The catalyst bed loading is indicated by G in $kg\, m^{-2}\, s^{-1}$. The internal diameter of the decomposition chamber can now simply be calculated using:

$$D_c = \sqrt{\frac{A \cdot 4}{\pi}} \tag{4.2}$$

Using the values described in the section above this results in a decomposition chamber diameter of approximately 9 mm. This value was compared to the internal diameters available in Swagelok tubing [91]. The tube diameters available are in sizes defined as fractions of inches, though metric options are available as well. The two options differ slightly from each other. As ESA has worked with Swagelok components before, some parts are still available within ESTEC. Most of these components are in the fractional sizes. As this offers the possibility to measure certain parameters if required, it was chosen to design the thruster using fractional Swagelok components. The tube diameter closest to the chamber diameter calculated above is the one for a Swagelok tube with a 1/2 inch diameter. Three options for the wall thickness were available: 0.035 inch, 0.049 inch and 0.065 inch. The Swagelok catalog mentions the 0.035 inch tube is not recommended for use with gases. After the results from the Swagelok capability assessment in Section 3.3.2 the final choice was made for the 0.049 inch wall thickness. Though this results in a lower wall strength and a lower catalyst bed loading (approximately 7.3 $kg\ m^{-2}\ s^{-1}$) than the thickest tube, the slightly increased diameter leaves some extra space in the decomposition chamber, making it slightly easier to manufacture and handle small components, such as the catalyst bed retainers. Additionally, it is possible to test slightly higher pellet diameters without creating a large void fraction. Furthermore, in Section 3.3.4 it has been shown that the 0.049 inch thick tube is sufficiently capable of sustaining the expected loads.

The length of the decomposition chamber is variable, meaning a piece of tubing can be cut to the specifications of the to be tested catalyst bed or in case of another technology. This also means that the pressure drop of the decomposition chamber as well as the response time are completely dependent on this choice.

4.2. Thermal standoff and capillary tube

During operation, the main body of the thruster, consisting of the injector, decomposition chamber and nozzle, will increase in temperature significantly. This heat will flow towards the inlet valve, especially in the moments after firing, when the propellant is no longer flowing and therefore does not provide any cooling effects. A maximum safe temperature is determined in the inlet valve (4.2.1) to prevent any thermal decomposition effects from happening in the valve and propellant feed system. A thermal standoff is created between the inlet valve and injector assembly to reduce the amount of heat transfer to the inlet valve (4.2.2). To bridge the gap between the valve and injector, a capillary tube is used (4.2.3). The diameter of this tube is selected based on the combination of a pressure drop analysis and an assessment of the tube diameters available (4.2.4). Due to the thermal cycles, the tube will undergo thermal expansion. To deal with the stresses in the tube caused by this, some bending in the tube is required to form an expansion loop (4.2.5). The bending must be performed in such a way, that the tube is not flattened, which would limit the flow of propellant (4.2.6). Using this information, the pressure drop of the capillary tube is calculated (4.2.7). This is followed by the design selection and an overview of the final thermal standoff and capillary tube design (4.2.8).

4.2.1. Inlet valve maximum temperature

The maximum allowable temperature of the inlet valve has been assessed by ESA and is given in the form of a requirement in *MGT-278*. Though no further calculations are required in this thesis as the maximum temperature is fully defined, this section provides a brief background to the origin of this requirement. Two main considerations are involved in this assessment. From research starting in 1951 it was found that vapors can ignited once a certain concentration of hydrogen peroxide in the vapor is reached [73]. This concentration is called the ignition limit in [20]. The relation between the concentration and temperature of a hydrogen peroxide solution and its ignition limit at atmospheric pressure is shown in Figure 4.3. An extension of this figure for multiple pressure levels is found in [15]. With increasing pressure, the temperatures required to obtain these vapor concentrations increase.
At all times, the temperature in the valve should be below the lowest temperature of the hazardous region, after a safety factor is applied. Since the propellant feed system can be depressurized directly after a firing, this assessment should be performed for atmospheric pressure. Additionally, ESA has performed an assessment of the decomposition rate of hydrogen peroxide at increasing temperatures. Using information from both assessments and comparing the results to existing requirements for other projects, they have defined requirement *MGT-278* to determine the maximum allowable inlet valve temperature at 50 degrees Celsius.

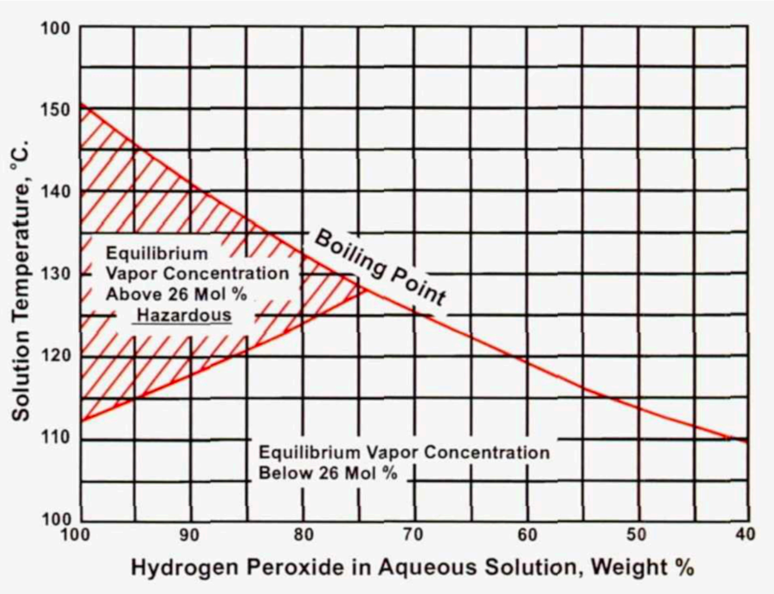

Figure 4.3: Hazardous hydrogen peroxide vapor concentrations [20]

4.2.2. Thermal standoff concept

As was mentioned before, a thermal standoff is put in place to minimize the heat transfer from the hot section of the thruster to the inlet valve. This is done by letting the propellant flow through a capillary tube, towards the injector, while minimizing the contact surface of the structural part of the standoff. This way, heat transfer is minimized, as it mainly occurs in the form of conduction, which is largely dependent on this contact surface, as was seen in Eq. 3.28. In case of this work, a design based on threaded rods or screws was chosen, to support the modular and flexible design of the thruster. An overview of this design is found in Figure 4.4.

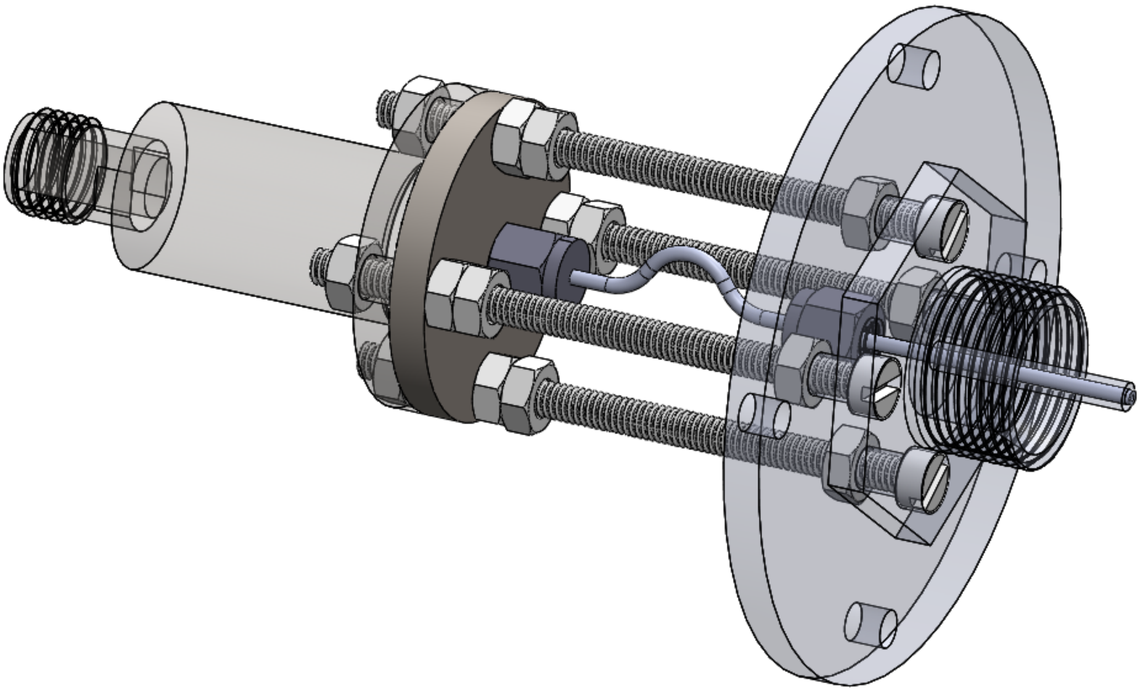

Figure 4.4: Thermal standoff design overview

The figure shows the assembly of the inlet valve, thermal standoff and injector module. Both the inlet valve and injector module are made transparent in the figure to highlight the components of the thermal standoff. The design utilizes the existing mounting holes in the inlet valve to create the structural geometry. On the left, a custom flange is seen that interfaces with the inlet valve. This flange is flat on the valve side and has a hole in its center, large enough to fit the capillary tube. The seal is made by the O-ring that fits in the O-ring groove of the valve. On the standoff side, the flange consists of a Swagelok compatible tube fitting body. The capillary tube is placed in the fitting body and goes through the flange, until it touches the valve face. Using a Swagelok COTS nut, as well as ferrules, the tube is fixed in place and a seal is made. Four bolts are used to connect the injector module to the valve. The holes in the valve, flange and injector module are not threaded. Instead, on each of the rods four nuts are used. Each nut has a specific purpose:

1. The first nut locks the bolt to the injector module;
2. The second nut clamps the valve and flange together on the valve side;
3. The third nut clamps the valve and flange together on the flange side;
4. The last nut locks the flange side clamping nut in place at the correct standoff distance.

The connection of the capillary tube with the injector module is, again, made using a Swagelok connection and a custom fitting body.

4.2.3. Capillary tube geometry

During thruster operation, the capillary tube will undergo many temperature changes. At the starting point, all components of the thruster will be at room temperature. Once the thruster starts firing, heat from the decomposition chamber will flow to the thermal standoff and capillary tube. During a firing, cold propellant will cool the capillary tube. The highest capillary tube temperature is expected after a firing, when heat from the decomposition chamber still flows into the capillary tube, but there is no more cooling from the propellant flow. Because of these thermal cycles, the capillary tube will undergo thermal expansion. This will create stress, due to the fact that it is constrained on both ends. A resolution for this problem is the use of a thermal expansion loop. The design chosen for the capillary tube has to be able to fit in the space available within the thermal standoff. Therefore, some calculations for the geometry of the capillary tube have been made. The basic geometry of the bend is shown in Figure 4.5.

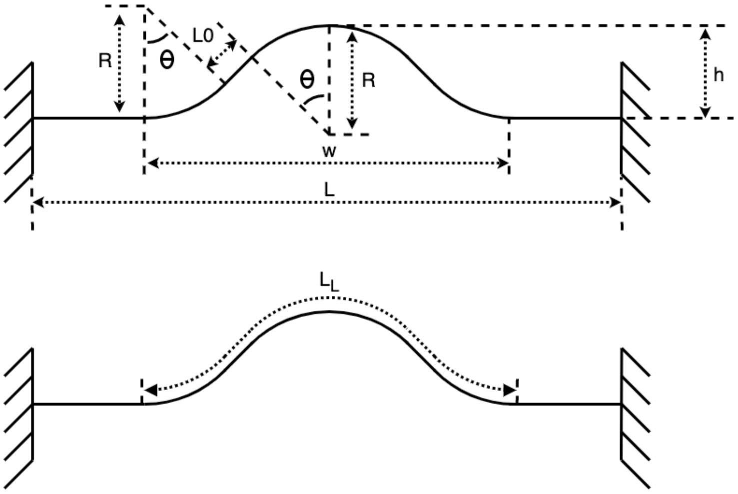

Figure 4.5: Capillary tube geometrical parameters

The effects of the bend on the width and height are calculated using the cartesian representation of a circle, which is seen in Figure 4.6.

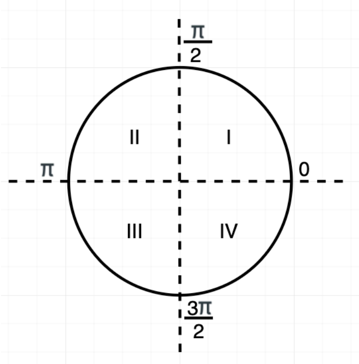

Figure 4.6: Unit circle

The equations for the x and y-coordinates of a circle are the following:

$$x = R\cos\theta \tag{4.3}$$

$$y = R\sin\theta \tag{4.4}$$

In which R is the radius of the circle in m and θ is the angle in rad. In Figure 4.6 the circle is divided in four regions (I, II, III and IV) each region covering an angle of $\pi/2\ rad$. When looking at the path of the capillary tube from left to right, the first bend (from horizontal to an angle up) is best estimated by the circle arc of region IV. This means that the horizontal distance covered can be calculated using:

$$\Delta x_{bend} = R\cos(\theta - \pi/2) = R\sin(\theta) \tag{4.5}$$

There are a total of four of these bends in the capillary tube. Additionally, there are two straight sections (L_0) between the bends. Therefore the total horizontal distance covered by the expansion loop is calculated using:

$$w = 4 \cdot R\sin\theta + 2 \cdot L_0\cos\theta \tag{4.6}$$

Similarly an equation is created for the height of the expansion loop. First the height distance covered by a single bend is calculated. Again section IV of the circle in 4.6 is used, however as the y-coordinate of this section is equal to $-R$ at the starting point, this needs to be compensated:

$$\Delta y_{bend} = R + R\sin(\theta - \pi/2) \tag{4.7}$$

There are two bends and one straight section with length L_0 that contribute to the height of the expansion loop. Additionally, since this calculation is performed for the neutral axis of the tube, the contribution of the outer diameter needs to be taken into account. Since the height is only relevant from the axis of symmetry of the thermal stand-off, this is only necessary for the top of the bend. Therefore, the height equation is the following:

$$H = 2(R + R\sin(\theta - \pi/2)) + L_0\sin\theta + \frac{D_o}{2} \tag{4.8}$$

4.2.4. Tube diameter

The selection of the diameter for the capillary tube depends on a few factors. It is key to minimize the capillary tube volume, to reduce the response time of the thruster as much as possible. By decreasing the tube diameter, the velocity of the propellant in the capillary tube will increase, thus reducing the response time. However, once a transitional or turbulent flow regime is reached, the pressure drop over the capillary tube increases significantly. To analyse the type of flow regime, the Reynolds number is used, which is calculated for pipe flow using the following equation[113]:

$$Re = \frac{\rho v D}{\mu} \tag{4.9}$$

In which Re is the non-dimensional Reynolds number, ρ is the fluid density in $kg\ m^{-3}$, v is the flow velocity in $m\ s^{-1}$ and D is the inner diameter of the tube in m. The flow regime is considered laminar when the Reynolds number is below 2320 according to [113]. It is considered in transition for Reynolds numbers between 2320 and 10000. A pressure drop occurs in the tube due to friction with the tube wall. This pressure drop is calculated with the following equation [113]:

$$\Delta P = f\left(\frac{L}{D}\right)\left(\frac{\rho v^2}{2}\right) \tag{4.10}$$

For laminar flow, the Poisseuille relation is mentioned for the friction factor in smooth pipes:

$$f = \frac{64}{Re}, \qquad Re < 2320 \tag{4.11}$$

For higher Reynolds numbers the Blasius equation is used:

$$f = 0.316\left(\frac{1}{Re}\right)^{0.25}, \qquad 2320 < Re < 2 \cdot 10^4 \tag{4.12}$$

A short analysis was performed of the influence of the tube diameter on the pressure drop. The input parameters seen in Table 4.1. The length was based on a first, rough estimate of the required standoff distance.

Table 4.1: Input parameters for the pressure drop assessment in a straight, smooth-walled tube

Parameter	Value	Unit
ρ	1.441	kg/m^3
μ	0.00127	$Pa\ s$
$\dot{m}$	0.6	g/s
L	40	mm

The pressure drop was calculated for a range of tube diameters. A graphic representation is given in Figure 4.7.

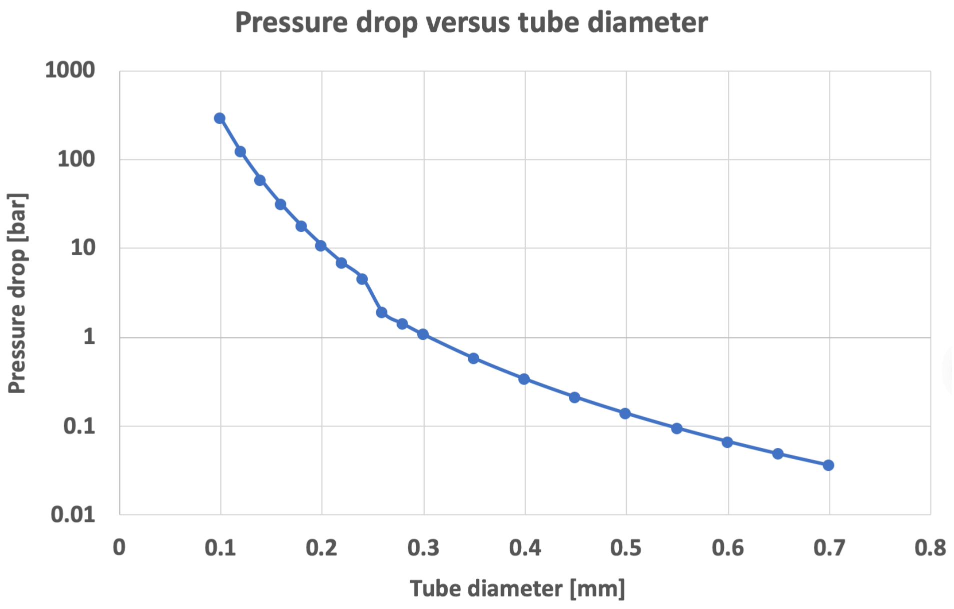

Figure 4.7: Calculated pressure drop of a straight capillary tube as function of tube diameter

From the figure, it becomes clear that the pressure drop will rise exponentially with decreasing tube diameter (the figure uses a logarithmic scale for the pressure drop). At tube diameters higher than 0.4 mm, the pressure reduction with increasing diameter is small. Therefore, this was chosen as the lower limit for the capillary tube diameter. To minimize the response time, the lowest diameter for stainless steel 316 tubing available at Swagelok was chosen [91]. It has an outer diameter of 1/16 Inch (1.5875 mm) and, with the thickest tube wall, an inner diameter of 0.5715 mm, which is significantly larger than the minimum diameter set earlier.

4.2.5. Thermal stresses in the capillary tube

In piping systems, thermal expansion is often dealt with using an expansion loop, which means a straight section is replaced by a U-shaped bend. The calculation of stresses in such loops is performed in [16] by means of the guided cantilever method. It is assumed that the pipe is constrained on one end, while displacement is allowed on the other end, though rotation is not allowed. This situation is described in Figure 4.8 for an example case of a 90 degree pipe bend.

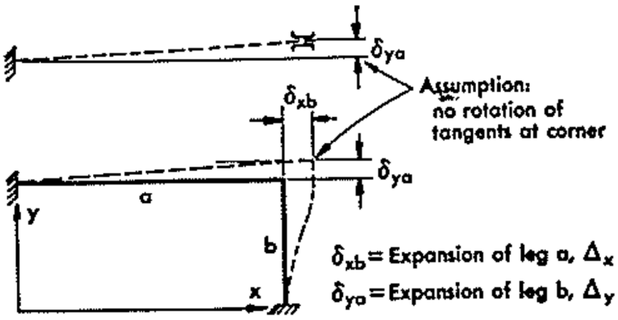

Figure 4.8: Guided cantilever beam (top) and 90 degree pipe bend (bottom) from [16]

A more clear picture of the guided cantilever beam problem is provided in Figure 4.9. It is clear that the bending moment is divided over both end points of the beam, as the rotation is constrained. Therefore the bending moment is calculated using the following equation [44]:

$$M = \frac{FL}{2} \tag{4.13}$$

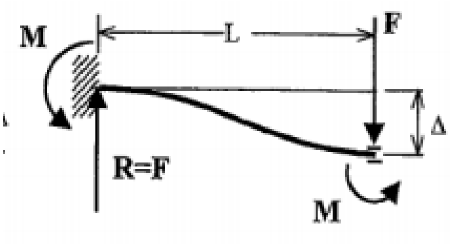

Figure 4.9: Guided cantilever beam from [7]

In which M is the bending moment in Nm, F is a force in N and L is the length of the pipe section in m. The deflection of the beam is calculated by [7] using:

$$\Delta = \frac{FL^3}{12EI} \tag{4.14}$$

In which Δ is the expansion in m, E is the Young's Modulus of the beam material in Pa and I is the second moment of inertia of the beam in m^4. Substitution of Eq. 4.14 into Eq. 4.13 gives the following equation for the bending moment:

$$M = \frac{6EI}{L^2}\Delta \tag{4.15}$$

The second moment of inertia is calculated for thick-walled pipes by means of the second moment of inertia for a hollow circular section. The calculation of which is done in [28] using the following equation:

$$I = \frac{\pi}{4}(r_o^4 - r_i^4) \tag{4.16}$$

In which r_o is the radius of the outer wall and r_i is the radius of the inner wall, both in m. With the bending moment known the stress in the pipe is calculated using [7]:

$$\sigma = \frac{M}{S} \tag{4.17}$$

In which S is the section modulus in m^3. The section modulus for a hollow circular section according to [28] is calculated using:

$$S = \frac{\pi(r_o^4 - r_i^4)}{4r_o} \tag{4.18}$$

The final stress equation is found by first substituting Eq. 4.16 into Eq. 4.15. After substitution of Eq. 4.15 and Eq. 4.18 into Eq. 4.17 the following relation is found:

$$\sigma = \frac{6Er_o}{L^2}\Delta = \frac{3ED_o}{L^2}\Delta \tag{4.19}$$

In which σ is the stress in Pa. This equation has been rewritten to calculate the required loop length for the maximum acceptable thermal stress. This method leads to the following equation:

$$L_L = \sqrt{\frac{3ED_o\Delta}{\sigma_{max}}} \tag{4.20}$$

This equation was also used in [112], with a unit conversion. Finally, the thermal expansion is calculated using the coefficient of thermal expansion of the material, the horizontal distance between the fixed points on either side of the thermal standoff and the temperature difference that will be experienced.

$$\Delta = \alpha \cdot L \cdot \Delta T \tag{4.21}$$

With α as the thermal expansion coefficient in K^{-1}, L the horizontal distance between the fixed points in m as described in Figure 4.5 and ΔT the temperature increase or decrease in K. This method was initially used to calculate the stresses in the capillary tube, however it was developed for expansion loops with 90 degree bends. Though some capillary tube design options do employ such bend angles, a far more likely option would be a capillary tube with smooth bends of lower angles. Therefore, an alternative method was found. The ASME code for pressure piping contains a section about the flexibility of piping systems. It mentions that:

”No formal analysis of adequate flexibility is required for a piping system that is of uniform size, has no more than two points of fixation, no intermediate restraints and falls within the limitations of empirical” Eq. 4.22[4].

$$\frac{Dy}{(L-U)^2} \leq K_1 \tag{4.22}$$

In this equation, D is the outside diameter of the pipe in mm and y is the displacement strain in mm, as was calculated in Eq. 4.21. L is the total length of piping between the anchors in m and U the horizontal distance between these anchors in m. The value of K_1 is calculated using the following relation:

$$K_1 = 208\,000\frac{S_A}{E_a} \tag{4.23}$$

In which S_A is the maximum allowable displacement stress and E_A is the Young’s Modulus, both in MPa. K_1 is given in mm^2/m^2. The maximum allowable displacement stress was calculated both for the expansion loop method, as well as the ASME piping flexibility method, using the following relation from [4]:

$$S_A = f(1.25S_c + 0.25S_h) \tag{4.24}$$

In which S_c is the basic allowable stress at the minimum metal temperature, and S_h is the basic allowable stress at the maximum metal temperature, both given in MPa. The parameter f is called the Stress Range Factor and is a function of the number of expected thermal cycles. The number of cycles is determined in *MGT-110* at 8 000 and a goal is set for 13 000 cycles. Therefore, a calculation was made using the goal number of cycles and a safety factor of four. This means that the analysis is performed for 52 000 thermal cycles. The value of the safety factor was determined by the thesis supervisor from ESA. A value for the stress range factor of 0.65 was found in [4]. The allowable stresses were those of seamless ASTM A269 tubing, from the same document.

The method described in [4] always held more conservative results than the expansion loop method and was therefore used to calculate the final results. The expansion loop method was used as a secondary check for the results.

4.2.6. Tube deformation due to bending

In [97], a stress analysis has been performed that describes the deformation effects caused by bending of tubes, which is the source for this entire section. The author considers longitudinal stress as well as circumferential stresses in the tube. The stress analysis is performed on the basis of a 180 degree bend.

Feed preparation length The longitudinal stresses in the outer semi-circle of the bend are tensile, whereas the longitudinal stress in the inner semi-circle is compressive. This causes the wall on the outside of the bend to become thinner, whereas the wall on the inside becomes thicker. The author states that, due to this effect, the neutral axis of the tube moves towards the inside of the bend. This has an effect on the feed preparation length, which is the actual flow path length. This is displayed in Figure 4.10.

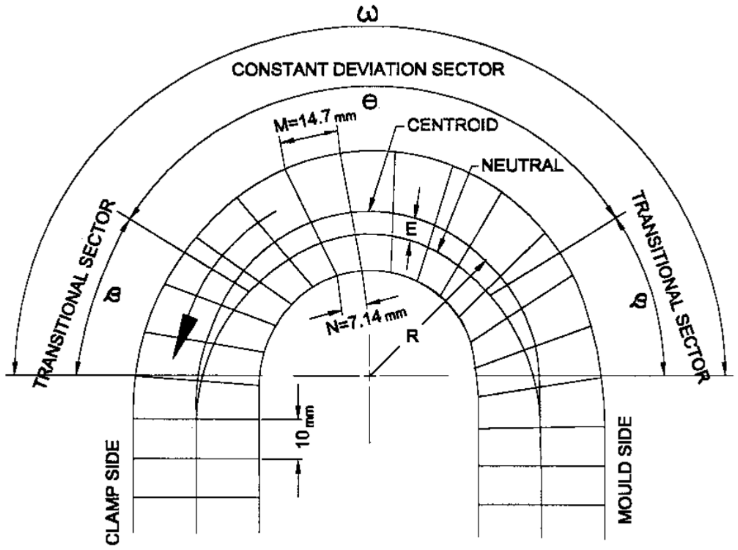

Figure 4.10: Tube deformation in a 180 degree bend [97]

As is seen in the figure, the bend is divided into a section with a constant neutral axis deviation and two transitional sectors. The author calculates the feed preparation length by determining the arc length of the ideal curve and then subtracting the arc length reduction caused by the neutral axis deviation. The effect of the transitional section is taken into account by dividing the feed preparation length compensation of this section by two. Since there are two transitional sections this leads to the following equation:

$$L = R\omega - E(\omega + \beta) \tag{4.25}$$

In which L is the total feed preparation length, R is the curve radius and E is the neutral axis deviation, all in m. The total arc angle ω and the arc angle of the transitional section β are given in rad. The author has determined through experiments that the arc angle of the transitional sector is between 30 and 35 degrees. However, no relation is given for tube bends with smaller angles. For the purpose of this work, the assumption is made that the angle of the transitional section is directly proportional to the total curve angle and is calculated as follows:

$$\beta = \omega \cdot \frac{\beta_0}{180°} \tag{4.26}$$

The author of [97] has determined a simple calculation for the neutral axis deviation by means of the following relation:

$$E = \frac{0.42}{k} r \tag{4.27}$$

In which E is the neutral axis deviation and r is the average of the inner and outer radius of the tube, both in m. The variable k is calculated using:

$$k = \frac{R}{2r} \tag{4.28}$$

Tube flattening Another effect caused by the difference in stresses in the tube wall is flattening of the tube. This analysis is performed in [97] as well and starts by defining the bending moment for a thin ring cross-section, which they have stated as the following:

$$M_F = S\sigma_s \frac{3.43r^2}{Rt} \tag{4.29}$$

In which M_F is the bending moment in Nm, S is the section modulus m^3, σ_s is the stress in Pa and t is the wall thickness in m. It is stated that the point where the tube begins to flatten is when the elastic limit is reached, which is defined by Equation 4.17. Substitution of this equation into Equation 4.29 leads to the fraction becoming equal to one and therefore the following requirement can be deduced to prevent flattening from occurring:

$$\frac{3.43r^2}{t} < R \tag{4.30}$$

4.2.7. Pressure drop

Though in Section 4.2.4 some mention has already been made of the pressure drop due to friction in tubes, this assessment was performed for straight tubes and served for the sole purpose of showing the influence of tube diameter on the pressure drop. For the actual pressure drop calculation, the bends in the tube have to be taken into account. To calculate this pressure drop, equations are used for a by-pass bend (Figure 4.11) in smooth pipes as characterized in [34].

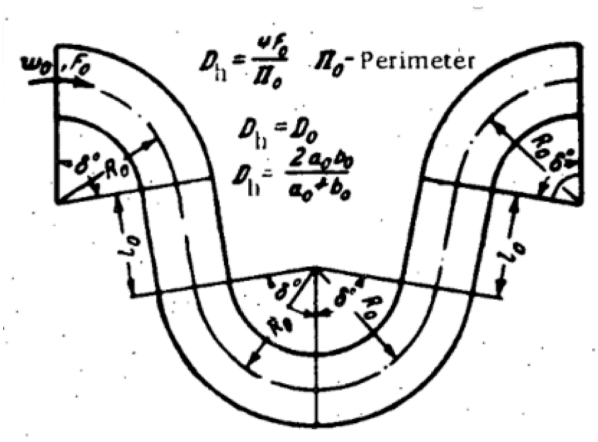

Figure 4.11: By-pass bend from [34]

The calculation of pressure losses in pipe bends is done by the author using the following equation:

$$\Delta H = \zeta\left(\frac{\rho v^2}{2}\right) \tag{4.31}$$

In which ΔH is the pressure loss in $kg\, m^{-2}$, ρ is the density of the fluid in $kg\, m^{-3}$, w is the flow velocity in $m\, s^{-1}$ and g is the gravitational acceleration in $m\, s^{-2}$. ζ is the fluid resistance coefficient, which is calculated as follows:

$$\zeta = A\zeta' \tag{4.32}$$

In which ζ' is the fluid resistance coefficient for a single bend. The value of A depends on the ratio of the length of the straight sections in the bypass (l_0) and the hydraulic diameter (D_h). It is determined from Table 4.2.

Table 4.2: Values of A for calculation of the by-pass pressure loss in [34]

$\mathbf{l_0/D_h}$	**0**	**≥1.0**
A	6.0	4.0

This shows that a significant reduction in pressure drop (factor of 2/3) can be attained, by simply creating a straight section with a length larger than the hydraulic diameter of the tube, which is small. The fluid resistance coefficient that is used in Equation 4.32 is calculated using:

$$\zeta_{fr} = 2\left(\frac{l_0}{D_h} + 0.035\frac{R_0}{D_h}\delta^0\right)\lambda \tag{4.33}$$

In which R_0 is the radius of the bend, δ^0 is the curve angle in deg. The author determines the value of λ from the curves defined by the equations in Table 4.3:

Table 4.3: Determination of λ for the calculation of the fluid resistance coefficient using Equation 4.33 [34]

$$\begin{array}{ll}
50 < Re\sqrt{\frac{D_h}{2R_0}} < 600 & \lambda = \frac{20}{Re^{0.65}}\left(\frac{D_h}{2R_0}\right)^{0.175} \\
600 < Re\sqrt{\frac{D_h}{2R_0}} < 1400 & \lambda = \frac{10.4}{Re^{0.55}}\left(\frac{D_h}{2R_0}\right)^{0.225} \\
1400 < Re\sqrt{\frac{D_h}{2R_0}} < 5000 & \lambda = \frac{5}{Re^{0.45}}\left(\frac{D_h}{2R_0}\right)^{0.275}
\end{array}$$

For the straight sections on the left and right of the bypass, the equations for straight smooth pipes have been used. The pressure losses of these sections are described by Equation 4.10, using Equation 4.11 for the friction factor in laminar flow and 4.12 for transition flow.

4.2.8. Final design

The solution finding process, as described in the previous section, was performed for a curve radius range from 2 to 6 mm, with a 0.5 mm spacing. This led to the following design options for the thermal stand-off and capillary tube:

Table 4.4: Generated capillary tube bend design options

Radius [mm]	Standoff length [mm]	Angle [deg]	$\mathbf{L_0}$ [mm]	ΔP [bar]	Height [mm]
2	33.4	90	2.9	0.56	7.7
2.5	35.4	90	1.6	0.54	7.4
3	37.4	90	0.4	0.75	7.2
3.5	39.5	90	1.2	0.51	6.9
4	41	64.1	1.4	0.50	6.5
4.5	42	61.7	0.8	0.49	6.2
5	43	53.8	1.2	0.48	5.9
5.5	44	44.3	2.3	0.48	5.5
6	44.2	51.6	0	0.66	5.3

A few factors were taken into account while choosing the most suitable option. First of all, though the minimum curve radius calculated at 1.98 mm using the flattening condition as described in Section 4.29 was met in all design options, it was considered that the bends in the capillary tube with the smallest curve radii would be hard to manufacture. Additionally, a lower pressure drop was considered beneficial. The response time of the entire capillary tube, including the section that continues into the injector (as is shown in Section 4.3), was calculated at the reference conditions from the requirement specification (*MGT-062*) for each option. This was done using a linear equation that was calibrated using the EcosimPro model described in Section 4.7. The results varied from 9.1 ms for the option with the smallest curve radius, to 9.7 ms for the option with the largest curve radius. Finally, the entire capillary tube bend was required to fit within the radius of the thermal stand-off, which was the case for all options. The option that was selected is the one in Table 4.4 with a curve radius of 5 mm. However, other suitable options exist as well. The final design of the thermal stand-off, as is explained further in this section, allows for easy adaptation of the bend in the future. The expected response time at reference conditions for the chosen option is 9.61 ms.

Using the chosen geometry, new simulations were performed using EcosimPro. Using stainless steel screws for the thermal standoff resulted in high temperatures in the inlet valve. Therefore, an alternative solution is required. To overcome this issue, the material was replaced by MACOR (Annex B), which has a low conductivity, good strength properties and is machinable. For the design of the Swagelok interfaces reference is made to Section 8.1.

4.3. Injector

To distribute the propellant to the decomposition chamber, an injector module is created (4.3.1). Some design challenges occurred related to the propellant temperature within the injector module as a result the Swagelok interface (4.3.2). A pressure drop over the injector is required for stability and serves as an input for the final injector geometry (4.3.3).

4.3.1. Injector concept

As the design logic that was used was to simplify the decomposition chamber as much as possible, the injector module is required to function as the fitting body for a Swagelok interface on the upstream side of the decomposition chamber. Additionally, the injector module was chosen as the interface to the test setup. An overview of the injector module is seen in Figure 4.12.

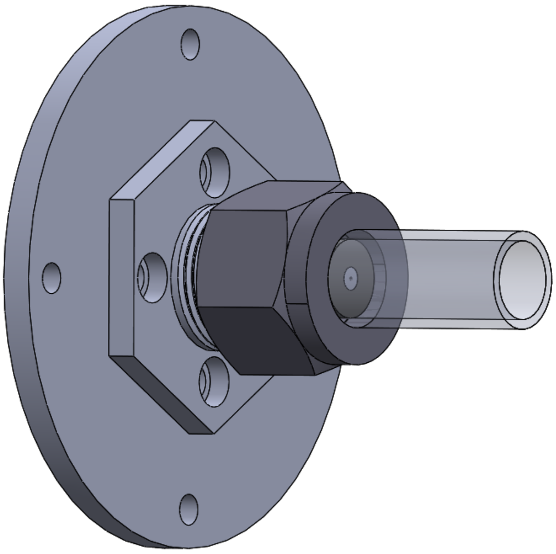

Figure 4.12: Overview of the injector module design

In this image, the decomposition chamber tube is present, though transparent. The main injector module body is a large flange with four mounting holes, which are used to mount the thruster to the test setup. Additionally, on top of the circular flange, a hexagon shape is seen. This shape is present to provide grip for a tool when tightening the Swagelok nut. Within this hexagon shape, an additional four holes are seen, which are used for the screws of the thermal standoff, as was seen in Figure 4.4. As the thruster is designed not only for use with catalyst beds, but also as a testing platform for alternative technologies (described in Chapter 5), it was considered there should be a possibility to access the area directly downstream of the injector plate. This allows for the placement of an alternative technology, such as a heater wire or laser unit. Since on the outside of this interface a large nut is in place, which can be removed and re-tightened, this is a challenge. Therefore, the choice was made to let the injector protrude into the chamber and have the injector plate flush with the expected end surface of the Swagelok nut. This is seen in Figure 4.13, which contains a drawing of an early stage concept of the injector module. Using this logic, the area directly downstream of the injector can be accessed simply

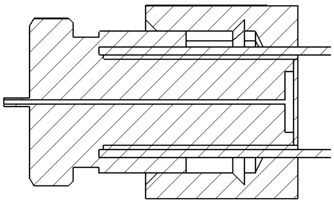

Figure 4.13: Early concept of injector module including chamber interface

through the chamber wall. A layer of PTFE is used to provide thermal insulation from the chamber wall to the inside of the injector module. This is discussed in more detail in the next section. In Figure 4.14

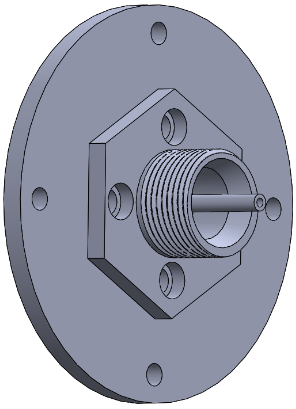

Figure 4.14: Body of the injector module (capillary tube and injector plate not present)

some features are clearly visible. There is a Swagelok compatible thread on the outer cylinder of the Swagelok interface. The chamber is inserted into this cylinder until it touches the rear wall within the cylinder. The injector plate is welded onto the smaller cylinder that holds the capillary tube. A PTFE insert is fitted over this cylinder, within the chamber. The end of the inner wall of the Swagelok interface is slanted to fit the sealing ferrules. The latter is described in more detail in Section 8.1. For the interface on the thermal standoff side, reference is made to Figure 4.15. It shows a Swagelok interface that seals the capillary tube and keeps it in place. The thermal standoff bolts are kept in place by a nut on the standoff side and the bolt head on the decomposition chamber side.

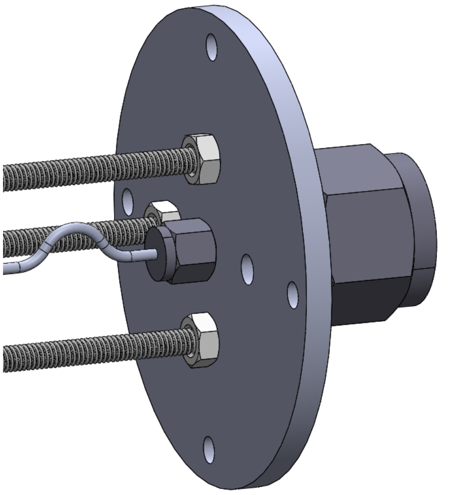

Figure 4.15: Injector - thermal standoff interface (one standoff bolt left out for a better overview)

4.3.2. Thermal aspects

By letting the injector protrude into the chamber, the interface area between the hot chamber wall and the injector body is increased, which creates a high heat transfer rate to the propellant tube within the injector. High temperatures, combined with low pressures in the propellant tube after a firing, can cause leftover propellant to vaporize within the propellant tube, causing bubbles. The bubbles can block the flow path for new incoming propellant, which is called vapor lock. Though this state is temporary as new propellant will cool down the propellant tube, it can cause a short period of unpredictable behaviour at the start of a firing [104]. To deal with this issue, a new design approach was taken, in which the capillary tube from the thermal standoff enters the injector module, until it touches the injector plate. The thickness of the walls around the capillary tube, as well as the thickness of the PTFE insulation layer around this wall, are determined using the EcosimPro model. Due to the complexity of the model, it was chosen to determine the thickness in a trial-and-error manner until an acceptable option was found, rather than attempting to calculate an optimal solution. The resulting thickness of the PTFE insulation layer was higher than initially expected, but an acceptable value was found. To determine the maximum allowable temperature in the capillary tube, the vapour concentrations were calculated at a pressure of 4 bar, assuming the 5.5 bar feed pressure case and the instantaneous pressure drop over the capillary, which was determined using EcosimPro. The maximum concentration shall remain below the ignition limits found in [75]. The vapour concentration was calculated using [41]:

$$x_i = \frac{p_{i,vap}}{p} \tag{4.34}$$

In which p is the total pressure in Pa and $p_{i,vap}$ is the vapor pressure of the component, calculated as [41]:

$$p_{\alpha,vap} = \gamma_\alpha x_\alpha p_\alpha^\circ \tag{4.35}$$

In which x_α is the molar fraction of a component in the liquid phase, γ_α is the activity coefficient as calculated using the method in [41] and p_α° is the vapor pressure of the pure component. Using this calculation, a maximum allowable temperature of approximately 115 ° was determined. The modelling of the injector in EcosimPro is explained in Section 4.7.2.

4.3.3. Pressure drop

The injector pressure drop is defined at 20% of the total chamber pressure based on representative values given in [82]. This pressure drop is required to decouple the pressure effects downstream of the injector from the pressure in the propellant feed system. This pressure drop is calculated for the highest expected chamber pressure at the reference conditions. This means the feed pressure is equal to 22 bar and no catalyst bed or retainer pressure drop is present (alternative technology scenario). The expected pressure drop of the inlet valve and capillary tube upstream of the injector need to be taken into account. An overview of the values used for the calculation is seen in Table 4.5 Taking this data into account, the pressure upstream of the injector is approximately equal to 21.45 bar. Since the injector pressure drop was calculated at 20% of the chamber pressure, the latter is calculated by dividing the upstream pressure by 1.2. This leads to an expected chamber pressure of 17.87 bar, which means the injector pressure drop at reference conditions is calculated at 3.57 bar. The injector assembly is covered with a face plate (Figure 4.16), which was decided to have a single orifice as opposed to multiple, due to the small scale of the plate and orifices. For an orifice the following equation is used to calculate the mass flow [82].

Table 4.5: Input values for the calculation of the injector pressure drop

Parameter	Value	Unit
P_{feed}	22	bar
ΔP_{Valve}	0.073	bar
$\Delta P_{Capillary}$	0.48	bar

$$\dot{m} = C_d A \sqrt{2\rho \Delta P} \tag{4.36}$$

In which $\dot{m}$ is the mass flow rate in $kg\ s^{-1}$, C_d is the discharge coefficient of the orifice, ρ is the fluid density in $kg\ m^{-3}$ and ΔP is the orifice pressure drop in Pa. This equation is used to calculate the orifice radius. The discharge coefficient that is used is 0.7, which is a common value taken from [82]. An overview of the inputs and results is seen in Table 4.6. Using the calculated orifice diameter, determined mass flow rates and Equation 4.36, the expected pressure drops at other feed pressures can be calculated. An overview of these values is found in Section 4.5.3.

Table 4.6: Inputs and results for the injector orifice diameter calculation

Parameter	Value	Unit
$\Delta P_{injector}$	3.57	bar
$\dot{m}$	0.6	g/s
ρ	1441	kg/m^3
A	$2.67 \cdot 10^{-8}$	m^2
$D_{orifice}$	0.18	mm

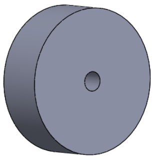

Figure 4.16: Injector face plate with a single orifice

4.4. Catalyst bed retainers

The catalyst bed in the baseline design consists of structural pellets with a deposited active material. To function within the thruster, the catalyst needs to be kept in position, which is done using catalyst bed retainers (4.4.1). As a pressure drop over the catalyst bed will be present, this pushes on the downstream retainer. A structural analysis was performed to ensure the retainer is capable of carrying this load (4.4.2). The presence of a retainer disrupts the flow in the decomposition chamber and therefore causes pressure losses. The retainer design ends with the calculation of these pressure losses (4.4.3).

4.4.1. Conceptual design

To stop catalyst material from being lost through the nozzle, the retainers need to be able to stop all particles over a certain size. As an absolute minimum, particles larger than the nozzle throat need to be stopped, as these could otherwise clog the nozzle. Additionally, requirements regarding the catalyst material have been set in *MGT-408*. To be able to retain these small particles a wire mesh will be used. This wire mesh however does not have the structural strength to keep the catalyst bed in place. Therefore the downstream retainer was designed to consists of two parts; a structural part and a fine mesh on top. The structural part consists of a cylinder that fits within the decomposition chamber and rests on the nozzle module to be kept in place. The top of the cylinder is closed, but perforated with holes of one mm. On the bottom of the cylinder small tabs are created that interface with the nozzle module to prevent the retainer from rotating, which is further explained in Section 4.25. Two holes are drilled in the sides of the retainer cylinder, to accommodate a pressure and temperature tap. The wire mesh is simply put on top of the structural component to stop the finer particles from being lost.

4.4.2. Structural analysis of the downstream retainer

As the downstream retainer is carrying the load caused by the pressure drop of the catalyst bed and resides in the hottest part of the decomposition chamber, a structural analysis is required. Initially, to determine the minimum thickness of the retainer cylinder, a simple stress calculation was performed. The stress is calculated using:

$$\sigma = \frac{F}{A_1} \tag{4.37}$$

In which σ is the stress in Pa, F is the force pushing down on the cylinder in N and A_1 is the frontal surface area of the cylinder. To calculate the force, a maximum allowable catalyst bed pressure drop was determined at 5 bar. The force is now calculated using:

$$F = P \cdot A_2 \tag{4.38}$$

With F in N, P in Pa ($N\ m^{-2}$) and A_2 the catalyst bed frontal area in m^2. The adiabatic decomposition temperature of 98% hydrogen peroxide is determined at 1218 $^{\circ}K$ (approximately 945 $^{\circ}C$) using NASA's CEA. The actual decomposition temperature will be lower due to thermal losses and the retainer plate itself will not quite reach that temperature as it transfers heat to the chamber walls. Nevertheless, since the highest temperature for which properties of stainless steel 316 was found is 816 $^{\circ}C$, extra precaution was taken by implementing a safety factor of at least four. The input parameters used in the analysis are displayed in Table 4.7. The minimum required cylinder surface area was calculated using Equation 4.37. A very low minimum wall thickness of 0.1 mm was determined. Therefore, the strength of the cylinder is not considered of significant concern. However, from the point of view of manufacturing, as well as maintaining the fit within the nozzle module, it was chosen to not reduce the thickness below 0.5 mm at this stage of the design. The thickness could be further reduced if it proves feasible during manufacturing, to minimize the chamber diameter reduction. The structural integrity of the perforated disk on top of the cylinder is of greater concern. To make an assessment of this and the entire retainer structure, a simple simulation was performed using Solidworks. A force of 41 N was calculated using the pressure drop and chamber flow area and distributed over the retainer plate. The following information was used as input (stainless steel 316 properties taken from Annex B (Poisson ratio from [6]):

Table 4.7: Input parameters for the retainer cylinder stress calculation

Parameter	Value	Unit
Pressure drop	5	bar
Catalyst diameter	10.21	mm
Max yield stress	110	MPa

Table 4.8: Overview of input for the structural assessment of the downstream retainer using Solidworks

Parameter	Value	Unit
Cylinder thickness	0.5	mm
Perforated plate thickness	1	mm
Hole diameter	1	mm
Perforation pitch	1.4	mm
Catalyst bed pressure drop	5	bar
Pressure load	41	N
Temperature	816	C
Ultimate tensile strength	186	MPa
Max yield stress	110	MPa
Elastic modulus	132	MPa
Shear modulus	52	MPa
Poisson's ratio	0.24	-

A graphical representation of the von Mises stresses and (exaggerated) displacement in the retainer is seen in Figure 4.17. The bottom of the retainer was fixed, with the exception of the tabs, which are assumed to be slightly shorter than the recess in the nozzle module. Therefore, they do not carry any load. In the legend of the figure, it is visible that the complete scale is below the yield strength. However, for the purpose of comparing the stresses to the yield stress, a different representation is more useful. In Figure 4.18, a representation is made of the achieved safety factor within the retainer. The lowest achieved safety factor according to Solidworks was 5.4. On the left, the areas shown in red have a safety factor lower than 7 and, on the right, the areas are shown with a safety factor lower than 8.5.

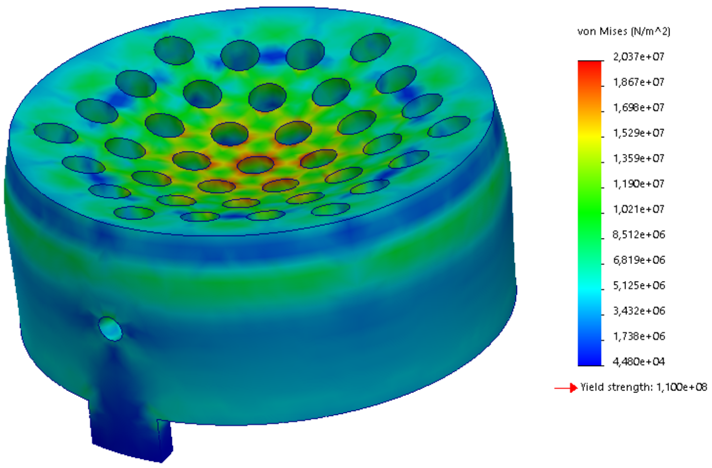

Figure 4.17: Downstream retainer stress analysis using Solidworks

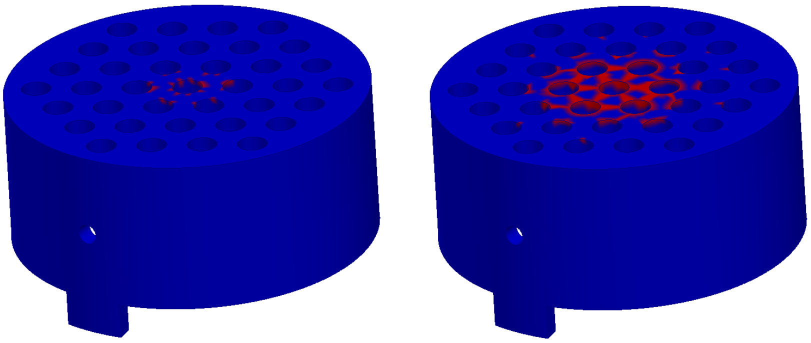

Figure 4.18: Retainer Safety Factor (SF) analysis. Red areas: Left SF < 7, right SF < 8.5

Further optimization of the perforated plate thickness was not done, as it is expected that other performance parameters are not significantly affected.

4.4.3. Pressure drop calculation

The calculation of the pressure drop for the downstream retainer is divided into two parts. First, the pressure drop is calculated for the fine mesh on top of the retainer. Secondly, the pressure drop due to the structural component of the retainer is calculated. As the upstream retainer doesn't have the same support structure, the pressure drop is only calculated for the fine mesh.

Fine mesh The pressure drop of the fine mesh is calculated using the same method as was used for the pressure drop over the inlet valve (described in Section 3.4.4), by means of a Reynolds number analogy. As a minimum, the mesh should stop particles large enough to plug the nozzle throat (720 μm), with an applied safety factor. A size commonly used is an 80x80 mesh, which has a pore size of 178 μm [108]. As a reference, pressure drop data from mesh filters created by Swagelok is used [87]. Though the available filters are much finer than the requirement, the 15 μm pore size sintered element was used for the assessment. This makes the pressure drop assessment conservative. As was mentioned for the valve, the factor b is determined from experimental data. The following equation is written to calculate the pressure drop (see Section 3.4.4):

$$\Delta P = K_1 \cdot \frac{\rho v^b}{2} \tag{4.39}$$

In which ΔP is the pressure drop in Pa, K_1 is a constant, ρ is the fluid density in $kg\ m^{-3}$ and v is the flow velocity in $m\ s^{-1}$. Using the continuity equation [113], the flow velocity is written as:

$$v = \frac{\dot{m}}{\rho A} \tag{4.40}$$

Substitution of this equation into Equation 4.39 leads to:

$$\Delta P = \frac{K_1}{2\rho^b A^b}\dot{m}^b \tag{4.41}$$

The experimental data given for the pressure drop over the filters from Swagelok are done with either water or air, at 20 degrees Celsius. For this assessment, both are considered incompressible, which means that the fluid density remains constant. Additionally, the flow area is equal for all tests. Therefore the surface A is also considered constant. A new constant K_2 is introduced which leads to the following equation:

$$\Delta P = K_2 \cdot \dot{m}^b \tag{4.42}$$

By taking the natural logarithm of the equation, it can be witten in the following form:

$$\ln \Delta P = \ln K_2 + b \ln \dot{m} \tag{4.43}$$

The test data given are values of the pressure drop and volumetric flow rate, which can be converted to the mass flow rate using the density. By plotting the natural logarithm of the test data ($\ln \Delta P$ versus $\ln \dot{m}$), a linear trend line can be calculated, represented by the following equation:

$$y = a + bx \tag{4.44}$$

The values of a and b can be determined from this trendline. This means that finally the pressure drop for the test fluid at any mass flow is calculated using:

$$\ln \Delta P = e^a + \dot{m}^b \tag{4.45}$$

As the hydrogen peroxide at the upstream retainer has not yet reached the catalyst bed, it is liquid. Therefore, the pressure drop is determined using the Swagelok water test data. As the downstream retainer sees only gaseous flow, the air test data is used. Both data sets are taken from [87]. The final pressure drop is calculated using:

$$\Delta P_{H_2O_2} = \Delta P_{test} \cdot \left(\frac{\mu_{H_2O_2}}{\mu_{test}}\right)^b \cdot \left(\frac{\rho_{test}}{\rho_{H_2O_2}}\right)^{b-1} \tag{4.46}$$

Which was derived in Section 3.4.4. The swagelok filter surface area is listed as 283 mm^2, whereas the thruster retainer area is calculated at 78.5 mm^2. Therefore the expected pressure drop is determined by multiplication with the factor 283/78.5. An example calculation as done at the reference conditions. The parameters used as input for the analysis are shown in Table 4.9. A complete overview of the pressure drop analysis results is given in Section 4.5.5.

Table 4.9: Input parameters for the catalyst bed retainer pressure drop assessment at reference conditions (fine mesh)

Parameter	**Value**	**Unit**
$\rho_{H_2O}(20°C)$	999.4	kg/m^3
$\rho_{H_2O_2(98\%)}(20°C)$	1441.7	kg/m^3
$\rho_{products(98\%)}(1218°K)$	3.99	kg/m^3
$\mu_{H_2O}(20°C)$	$1.01991 \cdot 10^{-3}$	$Pa\ s$
$\mu_{H_2O_2(98\%)}(20°C)$	$1.27117 \cdot 10^{-3}$	$Pa\ s$
$\mu_{products(98\%)}(1218°K, 17.87bar)$	$4.527 \cdot 10^{-5}$	$Pa\ s$
$\dot{m}_{H_2O_2}$	0.6	g/s

A complete overview of the properties of water and hydrogen peroxide is found in Annex B. The results of the assessment using the input parameters seen above are displayed in Table 4.10.

Table 4.10: Results for the catalyst bed retainer pressure drop assessment at reference conditions (fine mesh)

Parameter	Value	Unit
$\dot{m}_{air(eq)}$	0.24	g/s
$\dot{m}_{H_2O(eq)}$	0.48	g/s
$\Delta P_{air(eq)}$	0.020	bar
$\Delta P_{H_2O(eq)}$	0.0019	bar
$\Delta P_{Downstream}$	0.17	bar
$\Delta P_{Upstream}$	0.0082	bar

As is seen in the table, the assessment resulted in a pressure drop over the mesh of the downstream retainer of 0.17 bar and a pressure drop over the mesh of the upstream retainer 0.0082 bar. The total pressure drop budget, not including the retainers and catalyst bed is close to 4 bar (Section 4.5.4). This means that the upstream retainer mesh makes up only approximately 0.2% of the total pressure drop budget. Therefore, it is neglected from this point forward and only the downstream retainer pressure drop is considered.

Structural component The pressure drop over the structural component of the downstream retainer consists of two parts. Firstly, there is the pressure drop due to the flow passing through a perforated plate. Secondly, it is assumed that the pressure drop over the catalyst bed is defined such, that the flow has already expanded to the full chamber flow area. Therefore, a retainer pressure drop is present due to a contraction in the flow area (due to the thickness of the retainer cylinder). To calculate the pressure drop of the perforated plate, the following relation was found in [34].

$$\Delta P = k\left(\frac{\rho v^2}{2}\right) \tag{4.47}$$

In which ΔP is the pressure drop in Pa, ρ is the fluid density in $kg\,m^{-3}$ and v is the flow velocity in $m\,s^{-1}$. The factor k is fully dependent on the open area ratio of the perforated plate and is calculated using:

$$k = (1.707 - f)^2 \frac{1}{f^2} \tag{4.48}$$

The value of the density of the decomposition products was determined using NASA's CEA. The flow velocity was then calculated using the reference mass flow of 0.6 $g\,s^{-1}$, Equation 3.42 and an assumed catalyst bed void fraction of 0.4. The latter is similar to a representative value given in [41]. The calculation was performed using the following reference values:

Table 4.11: Input parameters for the retainer structure pressure drop calculation

Parameter	Value	Unit
Open area ratio	0.46	-
Fluid density	4.0	kg/m^3
Flow velocity	4.6	m/s

Using this input, the expected pressure drop over the perforated plate at the reference point is calculated at approximately 0.0003 bar, which is several orders of magnitude below the expected pressure drop from the fine mesh. Therefore, this pressure drop is neglected. In [34] the pressure drop over a sudden contraction is calculated again using Equation 4.47. In this case k is calculated using:

$$k = 0.5\left(1 - \frac{A_1}{A_0}\right) \tag{4.49}$$

In which A_0 is the flow area before the contraction and A_1 is the area after the contraction. In the case of the retainer, the ratio A_1/A_0 is approximately 0.98. This results in a k-value of 0.0092 and thus a negligible pressure drop. Though this last calculation is meant for Reynolds numbers above 10^4, for these small contraction ratios no information was available for Reynolds numbers under 10^4 in [34]. The expected Reynolds number is approximately 10^3. For this Reynolds number a k-value of 0.24 is given for a contraction ratio of 0.6, which would still result in a negligible pressure drop.

4.5. Pressure drop overview

An overview of the entire pressure drop budget in the thruster was created using the calculations found earlier in this chapter. To determine the chamber pressure at all feed pressures, the pressure losses have been assessed in components upstream of the decomposition chamber, namely the inlet valve (4.5.1), the capillary tube (4.5.2) and the injector (4.5.3). The pressure drop over the catalyst bed itself is variable, depending on the catalyst used. Therefore, the pressure drop calculations assume no pressure drop over the catalyst bed, as is the case when an alternative technology as described in Chapter 5 is used. For an estimate of the catalyst bed pressure drop, the model described in Chapter 2 can be used, after it has been calibrated with test data. An overview of the expected chamber pressures is described (4.5.4). Finally, a calculation of the expected pressure losses over the retainers is made for completeness (4.5.5).

4.5.1. Inlet Valve

The pressure drop over the inlet valve has been calculated using the mass flow rates as calculated in Section 3.1.3 and the method explained in Section 3.4.4. An overview of the expected pressure drops is seen in Figure 4.19. A minimum, maximum and average line is displayed. The lines represent the pressure drop with the expected minimum, maximum and average mass flow as calculated from the requirements in Section 3.1.3.

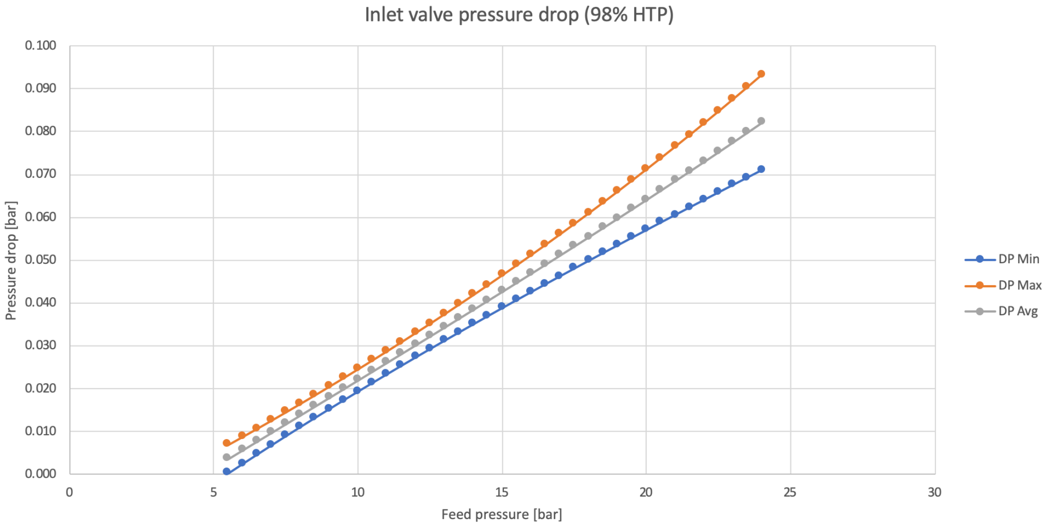

Figure 4.19: Expected inlet valve pressure drops for the full feed pressure range

The pressure drop over the inlet valve is rather small due to the low mass flow rate of the thruster. It varies between almost 0 to close to 0.1 bar over the full feed pressure range.

4.5.2. Capillary tube

The calculation of the capillary tube pressure drop is described in Section 4.2.7 and is largely dependent on the amount of bending in the tube. The pressure drop at the reference conditions was already calculated in Section 4.2.8. However, the relation between the expected pressure drop and all feed pressures is shown in Figure 4.20. The figure contains a number of sudden jumps in the pressure drop. This is caused by the way the equations in [34] are set up. In Table 4.3 it is seen how the equations suddenly change once a certain Reynolds number is reached. The impact of this shortcoming was considered not significant and therefore no attempt is made to research a potential improvement of this calculation.

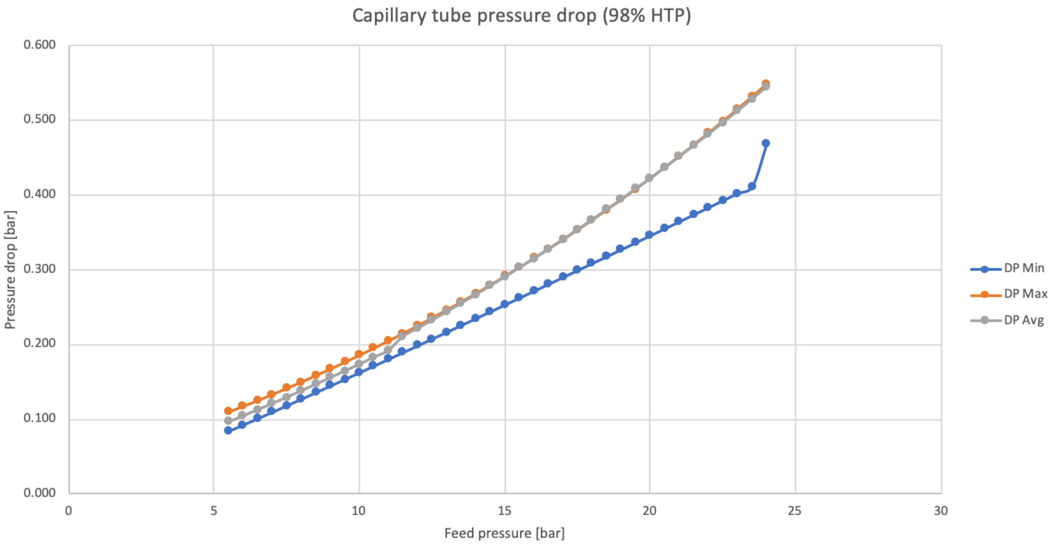

Figure 4.20: Expected capillary tube pressure drops for the full feed pressure range

4.5.3. Injector

As was explained in Section 4.3.3, the injector geometry is actually dependent on the desired pressure drop rather than the pressure drop being a product of the geometry. The injector was designed such, that the required pressure drop is created at the reference conditions. However, using the now known size of the orifice, Equation 4.36 and the mass flow rates calculated in Section 3.1.3, the pressure drop over the injector can be calculated for all other feed pressures. The results of this calculation are displayed in Figure 4.21.

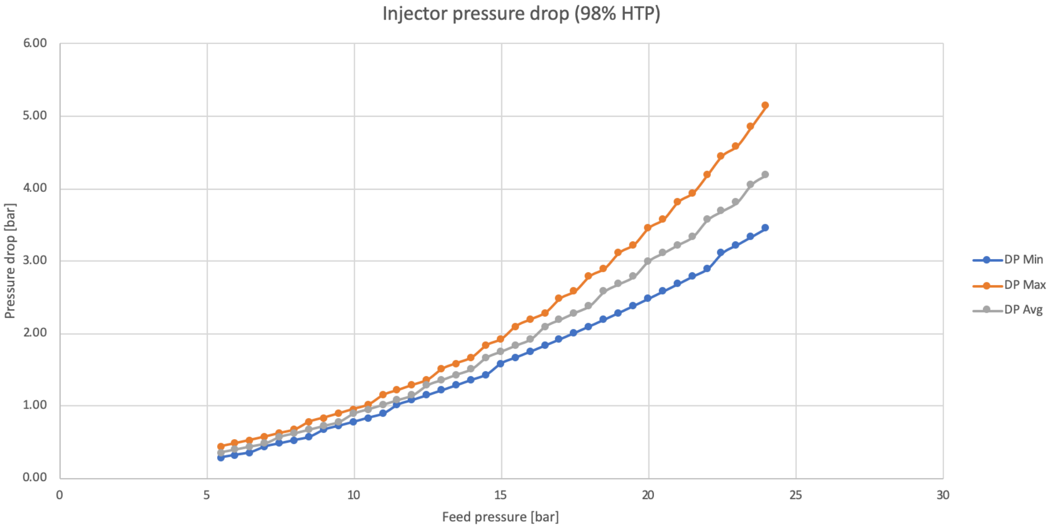

Figure 4.21: Expected injector pressure drops for the full feed pressure range

4.5.4. Chamber pressure

With the information calculated in the previous sections, all pressure drops upstream of the decomposition chamber are known. To determine the expected chamber pressures for all feed pressures, the information has been combined to calculate the pressure at each section upstream of the decomposition chamber. This is shown in Figure 4.22. In this figure, it is clearly visible that by far the largest contribution to the pressure drop comes from the injector. The average chamber pressure at reference

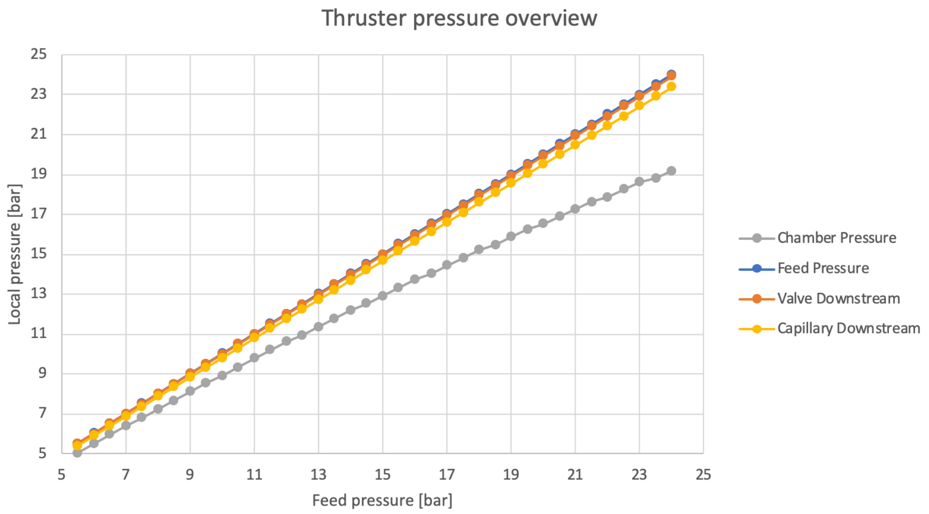

Figure 4.22: Expected pressures throughout the thruster as function of feed pressure (averages)

conditions is calculated at approximately 17.8 bar, but it ranges from 5.0 to 19.2 bar. The maximum expected chamber pressure is calculated by subtracting the lowest pressure drops of each component from the feed pressure. For a feed pressure of 24 bar, the chamber pressure is then calculated at 20.0 bar. This is also the value used for the chamber pressure in the thermal assessment in Section 3.3.2.

4.5.5. Retainers

Using the calculations explained in Section 4.4.3, an overview was made of the pressure losses caused by the downstream retainer for the complete feed pressure range. For this analysis, the gas density was determined for each chamber pressure using results from NASA's CEA. The chamber pressure is assumed as was calculated in Section 4.5.4, meaning a catalyst pressure drop is assumed not present. An overview of the results is given in Figure 4.23. With a reduction in chamber pressure, the pressure drop over the retainer reduces as well. This means that the current assessment is conservative, as the presence of a catalyst bed will reduce the pressure further, before the flow reaches the retainer.

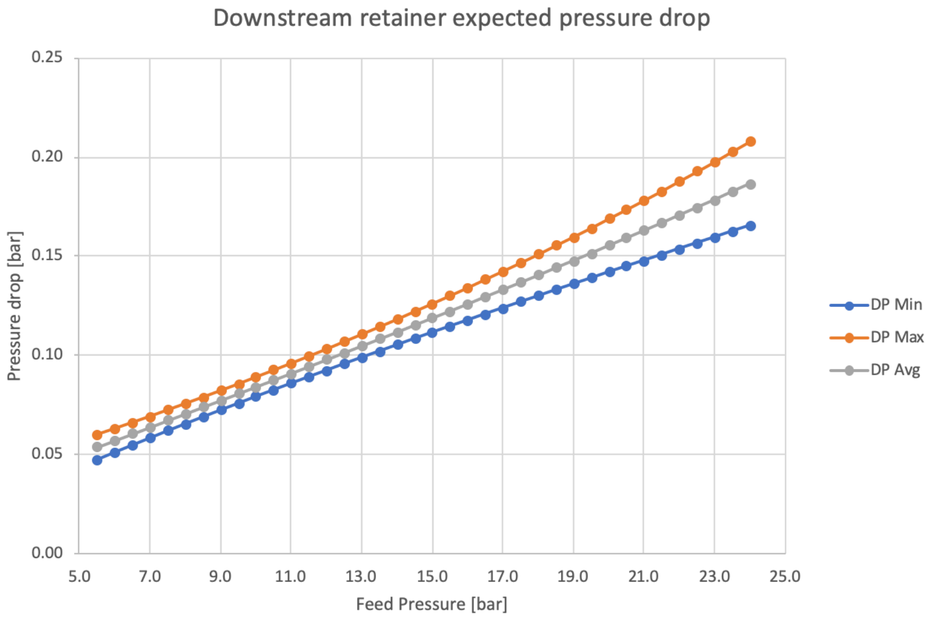

Figure 4.23: Expected pressure drop over the downstream retainer (assuming no catalyst bed pressure drop)

4.6. Nozzle module

The final thruster component to be described is the nozzle. A nozzle module was created that serves as the fitting body for the Swagelok interface (4.6.1). Within this module, an extra interface was created to support the catalyst bed retainers (4.6.2). The throat diameter was calculated for optimal performance at the reference conditions (4.6.3). Finally, the geometry of the complete nozzle profile is defined (4.6.4).

4.6.1. Design concept

Similar to the design of the injector, the logic used to design the nozzle module was to maximize simplification of the decomposition chamber. For this purpose the entire nozzle module functions as the fitting body for the Swagelok connection. An overview of the design is seen in Figure 4.24. Two radial holes are drilled into the nozzle module on opposite sides. These holes fit a 1/16 inch seamless tube, which is then welded in place. One of the tubes will be connected with a pressure transducer, while the other serves as the access point for a thermocouple. This allows for measurement of both the chamber pressure and temperature. The downstream side of the module is made in the shape of a hexagonal nut, so tools can be used to create the required pretension in the Swagelok interface. A converging-diverging conical nozzle is manufactured within the fitting body. The end of the main body is flush with the nozzle exit, meaning no thin-walled nozzle cone is used, as this would be more difficult to manufacture and no significant benefits would be achieved.

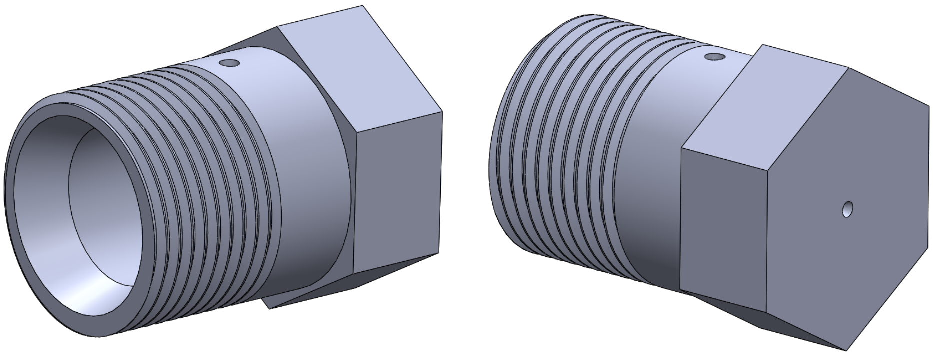

Figure 4.24: Overview of the nozzle module design

4.6.2. Retainer interface

As was described in Section 4.4, retainers are used to keep the catalyst bed in place. Since the decision was made to use retainers as a removable insert, some kind of interface is required within the nozzle module, for the downstream (load bearing) retainer to rest on. This has been done by reducing the inner radius of the last straight section of the nozzle module to the inner radius of the retainer cylinder. This is seen in a section cut drawing as displayed in Figure 4.25.

Additionally, since two orifices were created in the nozzle module to allow for the addition of a decomposition chamber pressure tap and thermocouple, the retainer includes two orifices with a diameter equal to the inner tube diameter of the tap. For this tap to function, the two orifices need to line up perfectly and no rotation of the retainer cylinder is allowed. To achieve this, two cuts have been made in the supporting ledge of the nozzle module, as was seen in Figure 4.25. The tabs on the retainer cylinder slide into these recesses. This prevents rotation and ensures the alignment of the orifices.

4.6.3. Throat diameter and expansion ratio

In ideal rocket theory, the throat diameter can be calculated by rearranging the following equation [113]:

$$m = \frac{\Gamma \cdot p_c \cdot A_t}{\sqrt{R \cdot T_c}} \tag{4.50}$$

In which m is the mass flow rate in $kg\ s^{-1}$, p_c is the chamber pressure in Pa, A_t is the throat area in m^2, R is the specific gas constant in $J\ kg^{-1}\ K^{-1}$ and T_c is the chamber temperature in K. Γ is called the

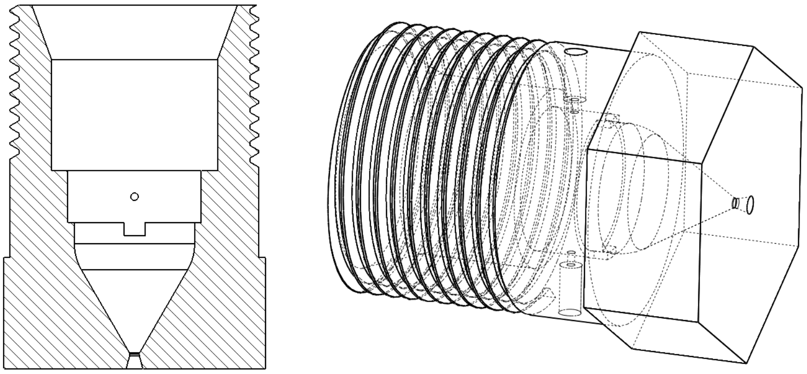

Figure 4.25: Section cut and perspective view of the nozzle module with visible retainer interface

Vandenkerckhove constant and is calculated by the following equation:

$$\Gamma = \sqrt{\gamma} \cdot \left(\frac{2}{\gamma+1}\right)^{\left(\frac{\gamma+1}{2(\gamma-1)}\right)} \tag{4.51}$$

In which γ is the specific heat ratio of the gas. Figure 4.26 shows the calculated ideal throat diameters. This calculation was performed using the performance parameters determined in Section 3.1 and the chamber pressures from Section 4.5.

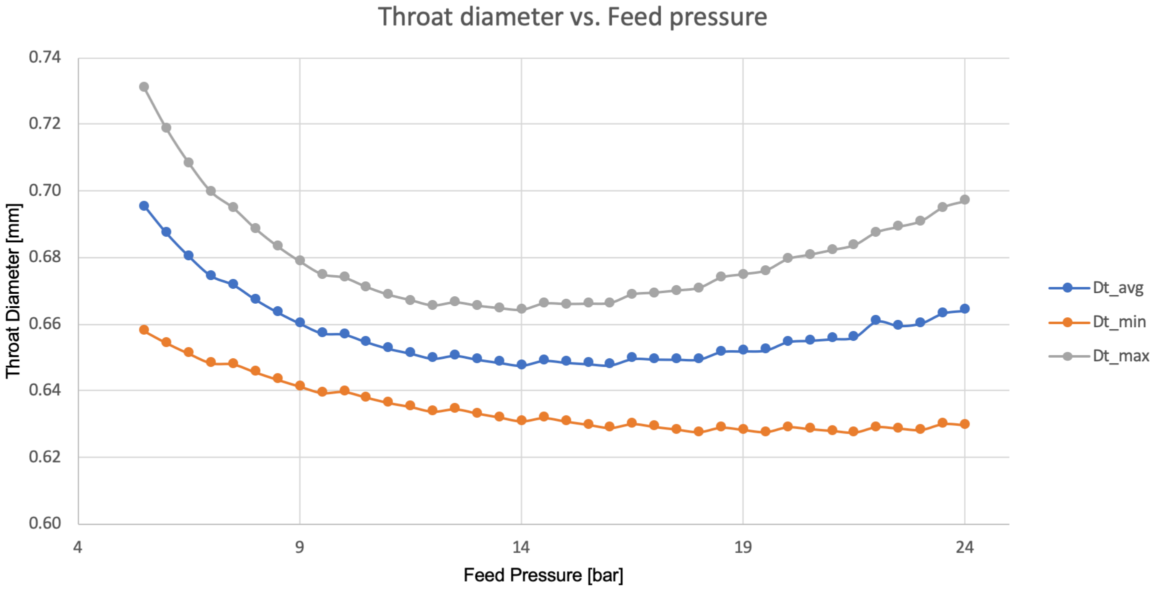

Figure 4.26: Calculated optimum throat diameters using ideal rocket theory

The mass flow used in this calculation already has most thruster performance losses included, as the value of the mass flow rate is determined from the requirements, which are a design input. However, to calculate the correct throat diameter, some effects need to be taken into account. It is stated in [113] that the throat area available for the gases to pass through is reduced due to the boundary layer and radial pressure of the flow. The actual mass flow rate is calculated using a discharge coefficient (C_d):

$$m_{real} = C_d \cdot m_{ideal} \tag{4.52}$$

According to [113], several attempts have been made to relate the discharge coefficient to the Reynolds number in the throat. The Reynolds number in the nozzle throat according to i be calculated using:

$$Re_t = \frac{4m}{\pi d_t \mu_t} \tag{4.53}$$

In which d_t is the throat diameter in m and μ_t the dynamic viscosity of the hot gas. The value of the dynamic viscosity was determined for the gas mixture in the nozzle throat using data in Annex B. Using the throat diameter estimates from Figure 4.26, the expected Reynolds number is approximately 26,000 for the reference scenario and goes down to approximately 7,500 for the 5.5 bar feed pressure scenario.

In [62] a nozzle discharge coefficient of 0.9 was estimated for a 20N hydrogen peroxide monopropellant thruster. After testing however, they mentioned that the nozzle discharge coefficient for their thruster should have been much closer to 1, if used at all. Calculating the Reynolds number for a thruster using 17.5 $g\ s^{-1}$ of hydrogen peroxide, with a concentration of 87.5%, and a nozzle throat diameter of 4.3 mm, leads to Reynolds numbers in the order of 10^5. This is an order of magnitude larger than the expected Reynolds number in the nozzle of a 1 N thruster, therefore a different method is required to determine the discharge coefficient.

In [14], the throat diameter is calculated using the frozen-flow approximation. In this case the throat area is calculated using:

$$A_t = \frac{F}{C_F p_c} \tag{4.54}$$

In which F is the thrust in N and C_F is the thrust coefficient. The latter can be calculated using:

$$C_F = \gamma \sqrt{\left(\frac{2}{\gamma+1}\right)^{\left(\frac{\gamma+1}{\gamma-1}\right)} \frac{2}{\gamma-1}\left[1-\left(\frac{p_e}{p_c}\right)^{\frac{\gamma-1}{\gamma}}\right]} + \left(\frac{P_e - P_a}{P_c}\right)\frac{A_e}{A_t} \tag{4.55}$$

In which p_e and p_a are the nozzle exit pressure and ambient pressure respectively, in Pa. A_e/A_t is the ratio between the nozzle exit area and throat area, which is calculated using:

$$\frac{A_e}{A_t} = \frac{1}{M_e}\left[\frac{2}{\gamma+1}\left(1+\frac{\gamma-1}{2}M_e^2\right)\right] \tag{4.56}$$

In this equation, M_e is the nozzle exit Mach number, which is calculated using:

$$M_e = \sqrt{\frac{2}{\gamma-1}\left[\left(\frac{p_c}{p_e}\right)^{(\gamma-1)/\gamma} - 1\right]} \tag{4.57}$$

This method was applied to the reference conditions, where the chamber pressure is 17.87 bar, assuming adiabatic decomposition (chamber temperature 1218 $°K$ and γ 1.2516 from NASA's CEA). The nozzle is assumed to be designed for optimum expansion at sea level (1.01325 bar). This leads to the following results:

Table 4.12: Nozzle throat diameter results using the frozen flow method from [14]

Variable	Value	Unit
M_e	2.491	-
A_e/A_t	3.122	-
C_F	1.375	-
D_t	0.720	mm

The equivalent discharge coefficient is determined by adjusting the mass flow rate in the ideal rocket theory calculation (Equation 4.50), until the same throat diameter is obtained. This resulted in an equivalent nozzle discharge coefficient of approximately 0.85 at the adiabatic decomposition temperature and the average expected mass flow rate for the reference conditions. When applying the frozen flow method to the thruster parameters from [62] and comparing that to the results from the ideal method, a discharge coefficient of approximately 1.0 is found, which supports the findings from the author. Therefore, it was chosen to determine the throat diameter using the method from [14] for the reference case, at 0.72 mm.

4.6.4. Nozzle profile

The final step of the nozzle design is the full definition of the the converging-diverging nozzle geometry. As was described earlier in this chapter, a conical nozzle design was chosen. In [113] an overview was made of parameters relevant to the geometry definition, collected from literature. An overview of these parameters is given in the form of a graphic illustration in Figure 4.27.

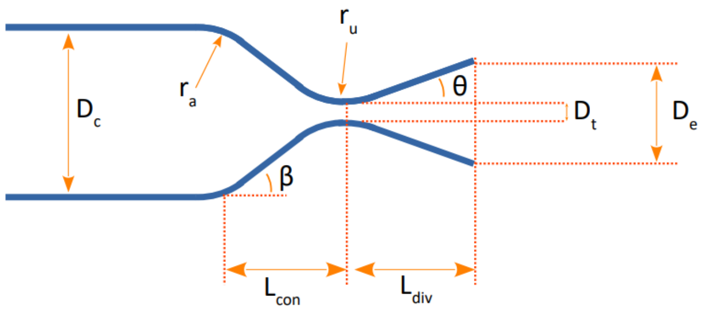

Symbol	Definition
D_c	Chamber diameter
D_t	Throat diameter
D_e	Nozzle exit diameter
r_a	Contraction radius
r_u	Throat longitudinal radius
L_{con}	Converging length
L_{div}	Diverging length
β	Contraction half angle
θ	Divergence half angle

Figure 4.27: Nozzle geometry schematic

The values of the different radii, as well as the contraction half angle, are determined using typical values found in literature. Some typical values mentioned in [113] and [32] are shown in Table 4.13.

Table 4.13: Typical values for the nozzle geometry

Parameter	Value
r_a/D_c	< 0.5
r_u/D_t	$0.5 - 1.0$
β	$20 - 45°$
θ	$12 - 18°$

For the actual design, the value of r_u was chosen at 0.5 mm, which is approximately 0.7 times the throat diameter of 0.72mm. For r_a, a value was chosen of 4mm, which is approximately 0.4 times the chamber diameter of 10.2 mm, or 0.43 times the chamber diameter when taking into account the diameter reduction due to the placement of the retainer. For the contraction half angle B, a value of $30°$ was chosen, as [113] mentions this as a good typical value. Finally the divergence half angle was set at $15°$, which according to [32] has almost become the standard as it is a good compromise between weight, length and performance. A section view of the final profile is seen in Figure 4.28.

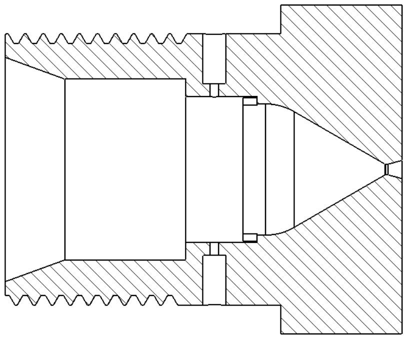

Figure 4.28: Final nozzle geometry (section view)

4.7. Thermal modeling

A brief, first order assessment of the Swagelok thermal capabilities was already performed in Section 3.3.2. However, a more elaborate model was needed for the design of the thermal standoff and the injector module. Therefore, a model was created using EcosimPro. The model was divided into two separate sections. The first sections is the fluidic section (4.7.1), which describes the propellant flow through the thruster. The second is the thermal model (4.7.2), which describes the heat flow through the thruster components. The two sections have an interface, which describes the heat flow from the thruster body to the propellant (4.7.3). The description of the model is followed by an overview of the results (4.7.5).

4.7.1. Fluidic part of the EcosimPro model

The fluidic part of the model describes the propellant flow upstream of the injector plate, as this is the region of interest. A technical drawing of this section of the thruster is displayed in Figure 4.29. From left to right this section consists of the inlet valve, thermal standoff with capillary tube and the injector module.

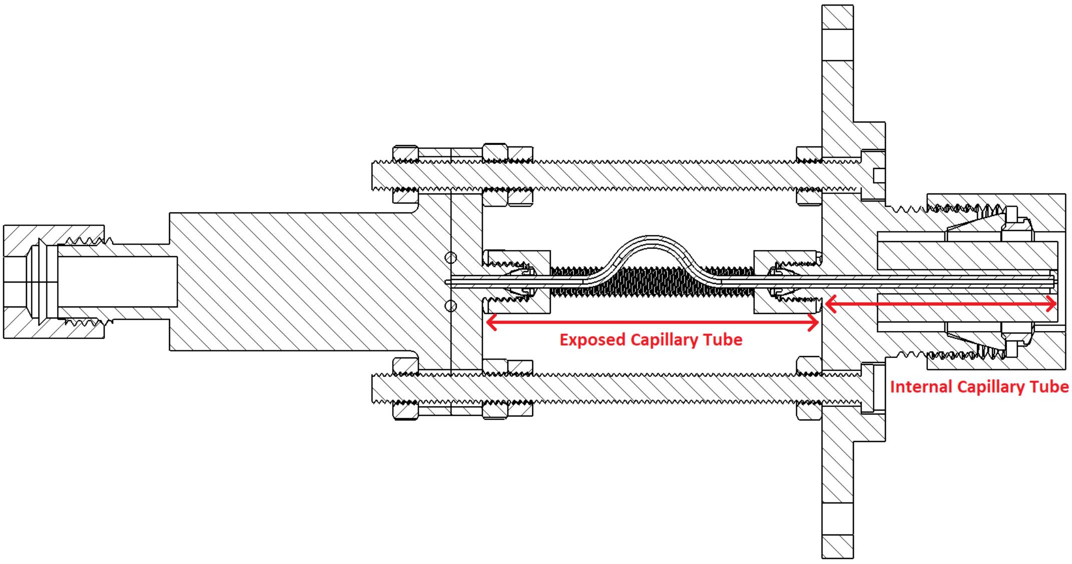

Figure 4.29: Technical drawing of the thruster section upstream of the injector plate

As is seen in the drawing, the capillary tube is exposed in the thermal stand-off, but continues within the injector module, up to the injector plate. The fluid dynamics library used in EcosimPro contains two types of components, namely volumetric and pressure components. A volumetric component should interface with a pressure component and cannot interface with another volumetric component. Some components exist that are both volumetric and pressure components, and the type can be chosen on each side of the component. An overview of the fluidic section of the model is seen in Figure 4.30.

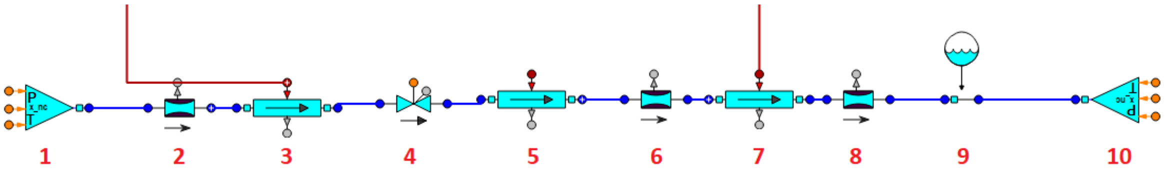

Figure 4.30: Overview of the fluidic model in EcosimPro

A list of components according to the numbers displayed in the figure is found in Table 4.14.

Table 4.14: Component list of the fluidic model in EcosimPro

Number	Component
1	Inlet boundary condition
2	Flow trimming orifice
3	Inlet valve (Volumetric part)
4	Inlet valve (Pressure part)
5	Capillary tube (Exposed part)
6	Connecting junction
7	Capillary tube (Internal part)
8	Injector pressure drop
9	Working fluid definition
10	Downstream boundary condition

The description of the components will follow using the number indicators as seen in the Figure 4.30 and Table 4.14. Boundary conditions have been put in place on both ends of the fluid model. The first boundary condition (1) sets the propellant feed pressure and temperature, before the inlet valve. The boundary condition at the downstream side of the model (10) sets the pressure downstream of the injector. The working fluid is defined in EcosimPro by placing a working fluid component (9) in the model, which in the case of this model is 98% Hydrogen Peroxide, as this is the highest concentration that will be used, which brings the highest decomposition temperature. An orifice is included in the model (2) to calibrate the model for a correct propellant mass flow rate. This is followed by the volumetric component of the inlet valve (3), which is modeled as a tube. An EcosimPro valve component is used to simulate the valve functionality and valve orifice pressure drop (4). Opening and closing of the valve component can be scripted in EcosimPro to simulate thrust pulses. After the inlet valve, the propellant flows through the exposed section of the capillary tube (5), which leads to the internal section (7). Since both components are volumetric components, a dummy junction (pressure component) is placed in between, with a pressure drop equal to zero. This component is essentially another orifice, with a diameter equal to the regular tube diameter. The injector plate is modeled as another orifice with a pressure drop equal to 20% of the expected chamber pressure (8). The selection of this pressure drop was described in Section 4.3.

4.7.2. Thermal part of the EcosimPro model

In order to create a clear overview of the thermal part of the EcosimPro model, the thruster has been divided into three subsections, which will be discussed independently. These three subsections are the inlet valve & thermal standoff, the injector and the decomposition chamber & nozzle and are highlighted in Figure 4.31.

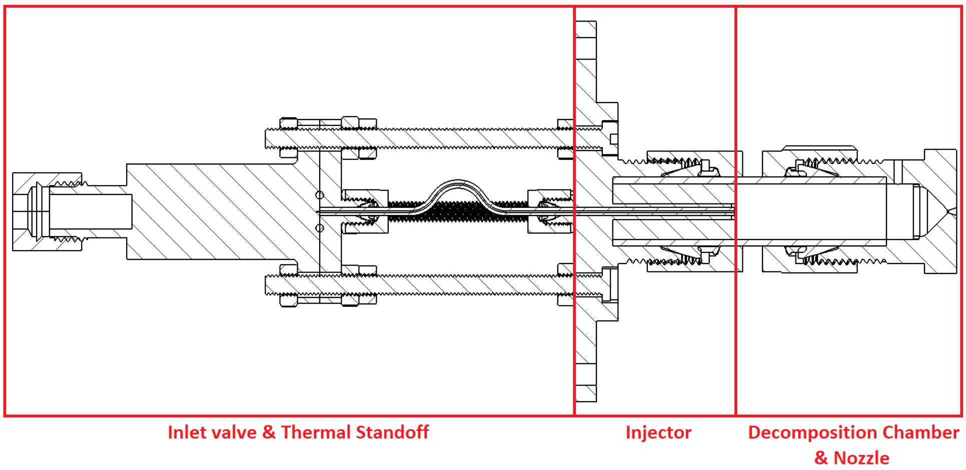

Figure 4.31: Division of thruster sections in the EcosimPro thermal model

Valve and Thermal Standoff As is seen in Figure 4.31, three main components need to be modeled in the first section. These components are the body of the inlet valve and connecting flange, the capillary tube and the four bolts that form the thermal standoff. Both the thermal standoff bolts and the capillary tube are thermally connected to the injector module. The model of this section in EcosimPro is displayed in Figure 4.32. The components in the model are numbered and named in the figure. The first component is the body of the inlet valve (1). This body is connected to the fluidic model (2), as there is heat exchange between the valve body and the propellant flowing through the valve. To reach the inlet valve, heat flows from the injector module (5) through the thermal standoff by means of conduction (3), which is modeled using a thermal resistance. Conduction through the capillary tube wall is modeled in the same way (4). No heat exchange to the environment is modeled, which is considered a worst case approach as the temperature in the thruster components will be higher than the ambient temperature. To achieve this, the last open connection on the valve body component in the model is connected to insulation (6). To split the heat flow from the injector module to the two parallel heat transfer modes, a ”demuxer” component (7) is used. The values of the resistances are calculated using the method for conduction as described in Section 3.3.3, using the MACOR properties for the thermal standoff bolts and stainless steel 316 properties for the capillary tube (found in Annex B).

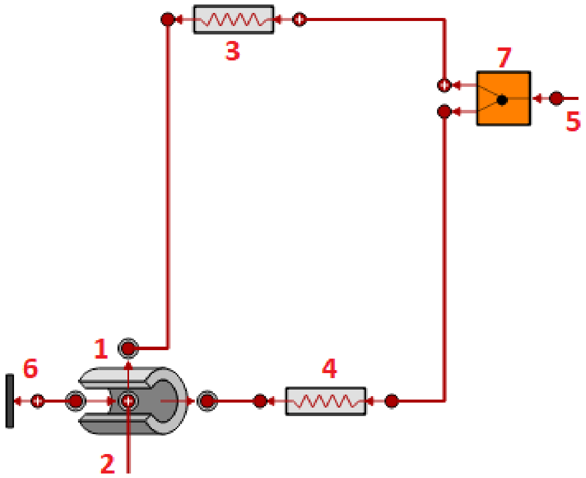

Nr.	Component
1	Valve body
2	Connection to fluid model
3	Thermal standoff resistance
4	Exposed capillary tube resistance
5	Connection to injector model
6	Insulation
7	Demuxer (signal splitter)

Figure 4.32: Model of the inlet valve and thermal standoff in EcosimPro

Injector The thermal model of the injector module is slightly more complicated. To assist in the explanation, an overview of the components in the injector module is provided in Figure 4.33. Each component is numbered, corresponding to the numbering and components names shown in Figure 4.34.

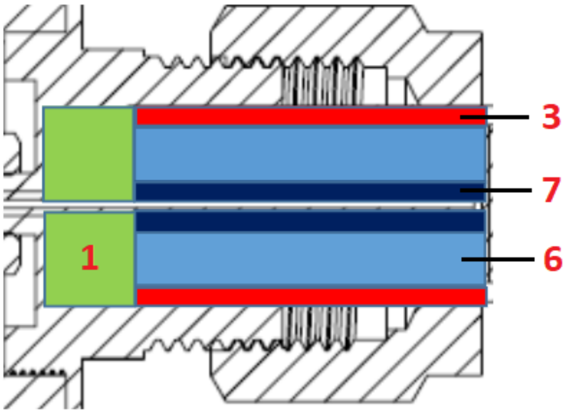

Figure 4.33: Thermal interfaces within the injector module for the EcosimPro thermal model

Figure 4.33 shows a section cut of the injector module. The capillary tube is shown, entering the module on the left, and continuing until the injector plate on the right. In the first part of the module, the capillary tube interfaces with the stainless steel of the injector body (1), which in turn has interfaces with the chamber wall (3), the wall around the capillary tube further downstream (7) and the PTFE insulation sleeve (6). The wall around the capillary tube further downstream forms a barrier between the capillary tube and the PTFE insulation. The PTFE insulation sleeve is meant to reduce the heat transfer from the hot chamber wall to the capillary tube. Taking these interfaces into account leads to the thermal model as displayed in Figure 4.34. Again, some muxing and demuxing components are used to split and combine signals. On the left, a connection to the thermal standoff is seen (2), whereas the connection with the rest of the chamber wall (5) is seen on the right. Additionally, a thermal connection is made between the injector plate and the contents of the decomposition chamber (10). The final thermal interface that is modeled is the one between the capillary tube wall within the injector module and the propellant flow in the fluidic model (12). Again, a worst case scenario is modeled, where no heat exchange takes place between the injector module and the ambient air.

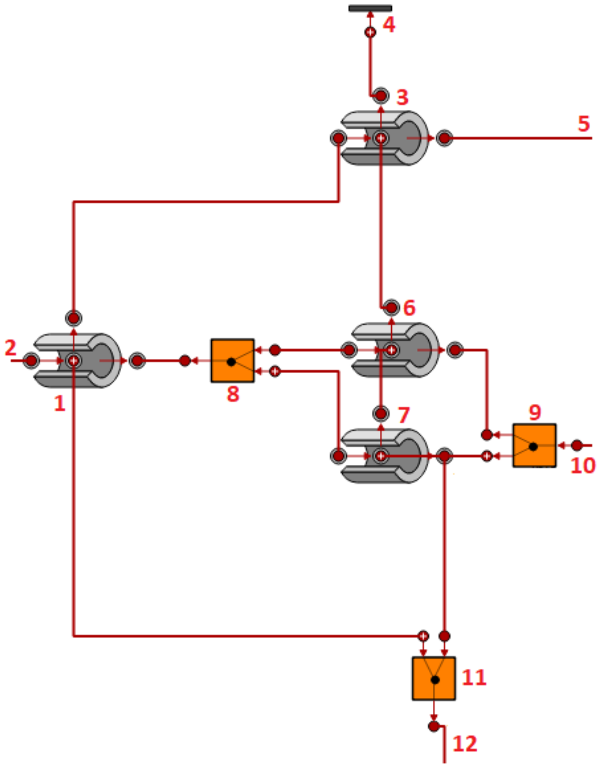

Nr.	Component
1	Internal capillary tube wall 1
2	Connection to the thermal stand-off
3	Chamber wall interface
4	Insulation
5	Connection to chamber wall
6	Teflon insulator
7	Internal capillary tube wall 2
8	Muxer (signal combiner)
9	Demuxer (signal splitter)
10	Connection to chamber model
11	Muxer (signal combiner)
12	Connection to fluid model

Figure 4.34: Thermal model of the Injector in EcosimPro

Decomposition chamber and Nozzle The decomposition chamber is modelled (Figure 4.35) by using a mass that represents the catalyst material (1). This mass is connected to heaters (2), which are calibrated such, that the temperatures and thermal inertia are representative of the real decomposition chamber. The decomposition chamber temperatures have been used from a temperature profile that was the result of a worst case scenario simulated using the decomposition model described in Chapter 2. The model is broken down in four parts. The first section represents the part of the decomposition chamber where the flow inside the catalyst is dominated by propellant vaporization, with maximum temperatures of approximately 525 to 550. The main propellant decomposition takes place in the second section, which terminates at the point where the adiabatic decomposition temperature is reached (approximately 1220 K). The third section contains the rest of the decomposition chamber, where the temperature is roughly stable at the adiabatic decomposition temperature. The final section represents the nozzle. Each of the four sections contains four nodes (sixteen in total). Heat transfer from the decomposition products to the chamber wall (4) is modeled using convective resistances (3). Heat

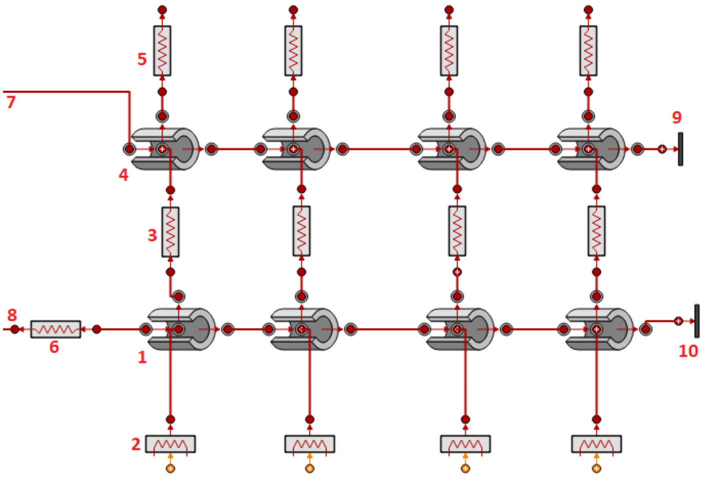

Nr.	Component
1	Catalyst mass
2	Heater
3	Convection to wall
4	Chamber wall
5	Radiation to environment
6	Convection to injector
7	Connection to injector
8	Connection to injector
9	Insulation
10	Insulation

Figure 4.35: Thermal model of the Injector in EcosimPro

transfer from the chamber wall to the environment has been modeled only through radiation (5), as significant calibration effort would be required to calculate the correct values of convective heat transfer. Due to the reduction in heat transfer to the environment, this model is considered conservative. The values of these thermal resistances follows the methods explained in Section 3.3.3. No extra heat transfer is considered at the nozzle exit. Therefore, these nodes are connected to insulation in the model (9, 10). The chamber wall is connected directly to the thermal model of the injector (7), whereas an extra convective resistance (6) is modeled for the heat transfer from the contents of the decomposition chamber to the injector plate (8). The value of this resistance is calculated as the convective heat transfer coefficient for combustion gases, as calculated in Section 3.3.3, at a chamber pressure of 1 bar, which is the case during the heat soak back after a firing.

4.7.3. EcosimPro model overview

The thermal models described above are connected into a single large thermal network. This thermal network is in turn connected to the fluidic model. An overview of the complete model is seen in Figure 4.36. This figure does not include the labels of all subcomponents, but does highlight the four mentioned parts of the completed model. For the definition of the subcomponents, the reader is referred back to the previous sections that describe the different parts of the EcosimPro model. A thermal connection is seen between the valve body and the volumetric valve component in the fluidic model. This is where heat transfers from the valve body to the propellant that resides within the inlet valve. Additionally, a thermal connection is shown between the injector module and the propellant in the capillary within the injector. This is the critical area in the case of the vapor lock problem.

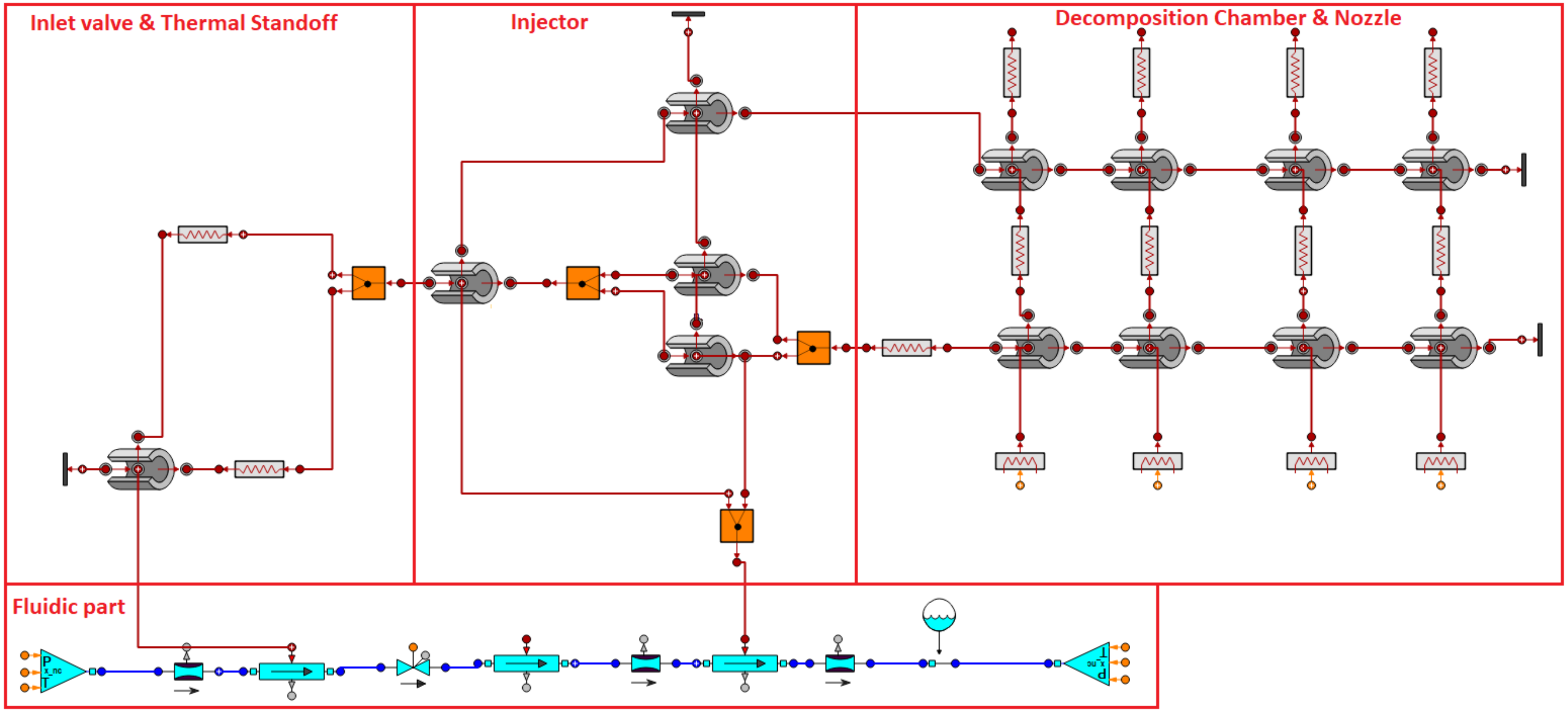

Figure 4.36: Complete schematic overview of the EcosimPro thermal model (for component labels, the reader is referred back to the model descriptions in the previous sections)

4.7.4. Calibration and simulation

Before correct simulation of the thermal model, some calibration steps were required. The first calibration was done in the fluidic model, to create the correct propellant mass flow. The orifice (component 2 in Figure 4.30) was determined such, that the pressure difference over the orifice creates a steady-state mass flow rate of approximately 0.6 g/s, at the reference conditions (feed pressure of 22 bar for 98% hydrogen peroxide). This mass flow rate was chosen according to the calculation of the average mass flow rate at reference conditions, as was performed in Section 3.1.3. To determine the pressure difference over the orifice, the pressure drop of the other components in the fluid model are calculated as was done in Section 4.5. After this calibration, the calculation of mass flow rates for different feed pressures is done automatically by EcosimPro. The simulations have been performed for a worst case scenario, in which the heaters and thermal resistances are calibrated for the high pressure case (24 bar feed pressure), as this results in the highest wall temperatures. The fluid model then assumes the low pressure case (5.5 bar feed pressure), as the lowest mass flow occurs at the lowest feed pressure. This scenario essentially simulates a low pressure firing immediately after the completion of a high pressure firing. In this situation, the local maximum temperature in the capillary tube is highest (when compared to other feed pressures). The mass flow rates, calculated by EcosimPro for the low pressure case, are seen in Figure 4.37.

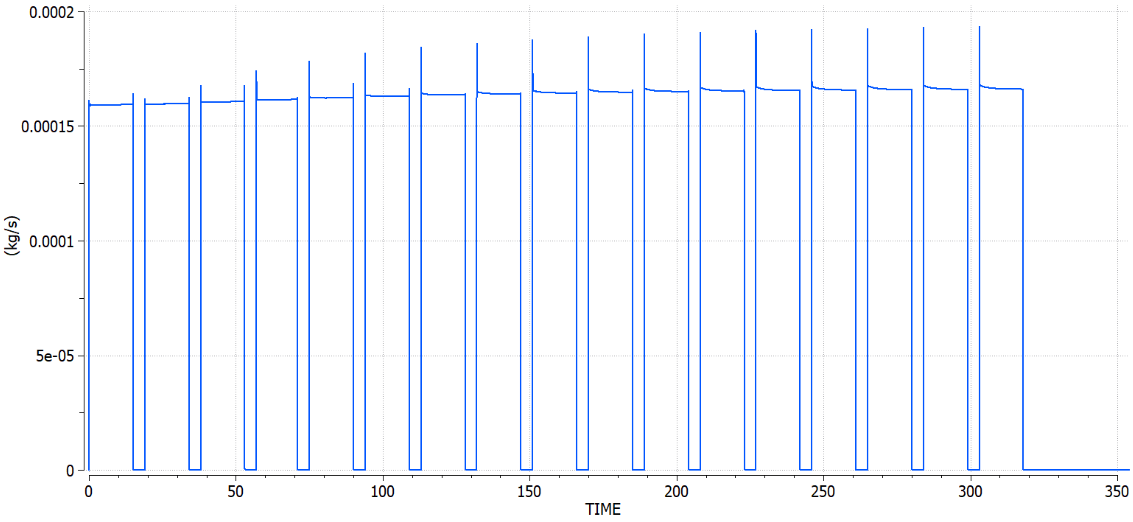

Figure 4.37: Calculated mass flow rates in EcosimPro at 5.5 bar feed pressure

The figure shows long pulses with small peaks due to transient (startup and shutdown) effects, with a mass flow rate of approximately 0.16 g/s when steady operation is reached. This mass flow rate is slightly lower than the minimum mass flow rate calculated from the performance requirements in Section 3.1.3, which is approximately 0.17 g/s. Therefore, this scenario is representative as a worst case for the entire range of operating conditions. Simulations are performed for two scenarios: a steady-state firing and a series of thruster pulses. The final results displayed in this chapter are from a simulation of an 800 second firing and a series of 15 second pulses with a 4 second interval.

4.7.5. Results

After the thermal model was used for several design iterations of the injector module and thermal standoff, a final simulation was performed using the parameters of the definitive design. The following results are considered of interest and described in this section:

- Temperature of the valve block and propellant in the valve;
- Propellant temperature in the capillary tube;
- Temperatures in the chamber wall.

Valve temperatures An overview of the temperatures in the inlet valve is provided in Figure 4.38. The figure shows the pulsating behaviour of the propellant temperature within the valve. The highest

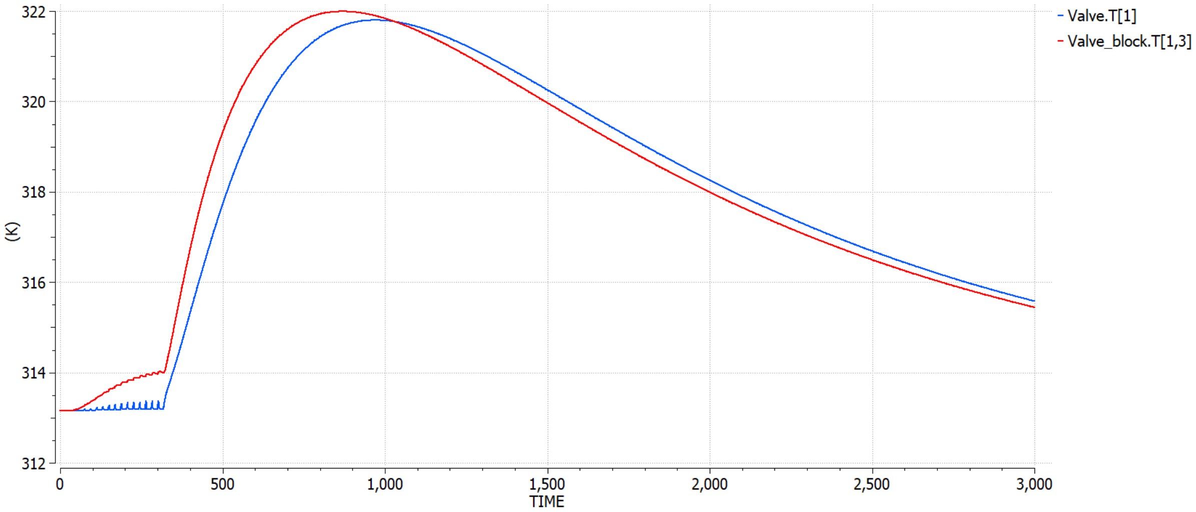

Figure 4.38: EcosimPro model results for the inlet valve temperatures

valve body temperature is represented in the figure by the line named ”Valve_Block.T[1,3]”, whereas the internal temperature is represented by the line named ”Valve.T[1]”. After every pulse, the propellant residing in the valve heats up due to the increased temperature of the valve body. With a new firing, new cold propellant flows from the feed system into the valve, which reduces the rate at which the valve temperature increases to the point that the valve body temperature reaches a plateau around 313.5 °K. Once the pulsing stops, the heat soak back from the warm thruster body still occurs, but there is no flow of cold propellant to cool down the valve. In the figure, it is shown that the valve body temperature rapidly increases until it reaches a peak at 322 °K (approximately 49 °C). This is below the 50 °C maximum that was imposed in *MGT-278*. The temperature rise and subsequent decline of the propellant still residing in the inlet valve is seen to lag behind slightly, as the heat transfer process takes time. The maximum temperature remains slightly lower as well. In a nominal situation this maximum temperature should not occur, as the thruster will be vented using Nitrogen gas after each pulse train.

Propellant temperatures One of the issues of concern, during the design of the injector, is the heat transfer from the chamber, through the injector, to the propellant in the capillary tube. As was explained in Section 4.3, a high temperature in the injector may cause a so-called vapor lock. Several design iterations were performed, in which the thickness of the PTFE insulation layer was adjusted. The final results for the capillary tube propellant temperatures are shown in Figure 4.41. The figure shows the

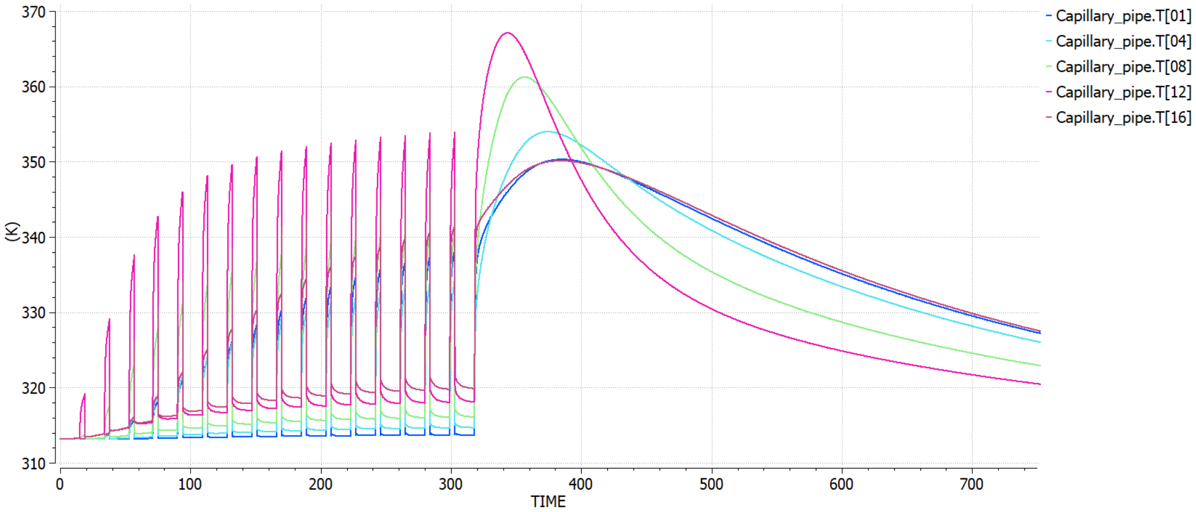

Figure 4.39: EcosimPro model results for the capillary tube propellant temperatures

propellant temperature at several locations in the capillary tube, up to the injector plate (location moves further downstream with increasing node number). It is seen that the peak temperatures increase as the propellant moves downstream, as expected. Again the pulsating behaviour of the temperatures is visible, as after every pulse new cold propellant is added into the capillary tube. As the thruster is cold at the beginning of the test, the maximum temperature increases until a peak is reached. Once the pulsing stops, the heat soak-back effect increases the small amount of remaining propellant to a maximum temperature of 367 °K (Approximately 94 °C), which is below the maximum temperature determined in Section 4.3. In case of the capillary tube, the heat soak back effect is more visible after a steady-state firing. The results of the steady-state simulation are shown in Figure 4.40. The maximum propellant temperature in the capillary tube stabilizes at approximately 322 $^{\circ}K$ (approximately 49 $^{\circ}C$) during operation. After termination, the heat soak back effect causes a temperature rise up to approximately 378 $^{\circ}K$ (approximately 105 $^{\circ}C$). Though more critical, the temperature still remains below the requirement set in 4.3. In a nominal situation this maximum temperature should not occur, as the thruster will be vented using Nitrogen gas after each steady-state firing.

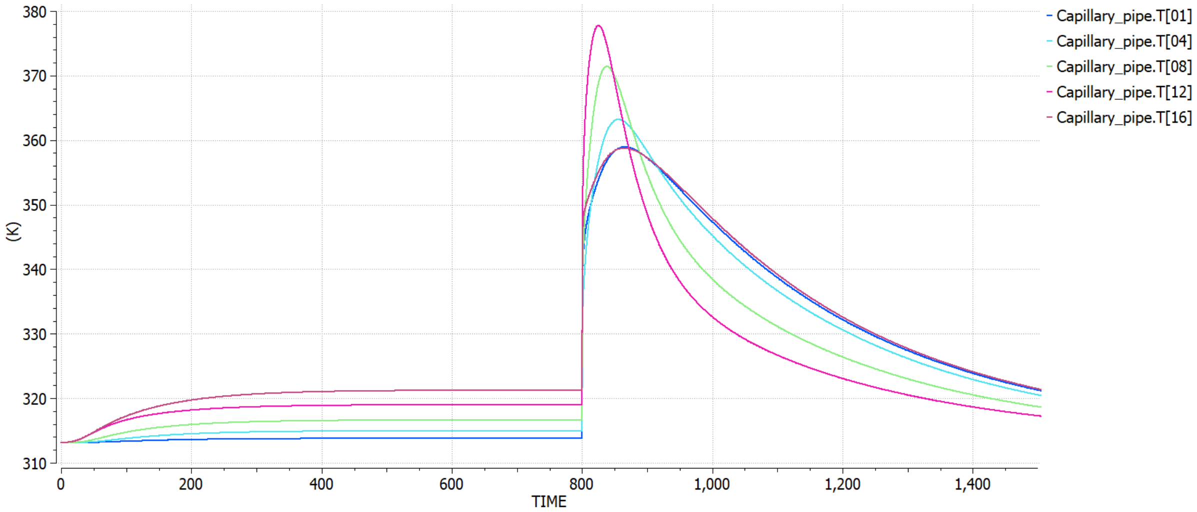

Figure 4.40: EcosimPro model steady-state results for the capillary tube propellant temperatures

Decomposition chamber temperatures As described earlier in this section, the decomposition chamber wall temperatures have been calculated using resistance values for convection and radiation as were calculated earlier in Section 3.3.3. An overview of the results is seen in Figure 4.41 for several points in the decomposition chamber and nozzle. The location of the measurement moves downstream with increasing node number, where the highest node number represents the highest wall temperature in the nozzle. Each of the four sections described in Section 4.7.2 is represented by a single line that shows the highest temperature in that section. The first (upstream) section is an exception, as it is represented by two lines, one showing the lowest wall temperature (first node) and one showing the highest wall temperature (node number four). Again, the pulsating behaviour is clearly seen in the figure, where the temperatures rise to a maximum with every pulse and reduce as soon as the pulse is over. A brief maximum temperature transient is seen at the beginning of operation as a result of the cold start. At the end of operation, the temperature follows the same temperature decline profile as after a pulse, which continues until a cool steady-state is achieved. As expected, the maximum temperatures further downstream of the injector are higher, as a larger portion of the hydrogen peroxide has decomposed and thus, the hot gas temperature is higher. As was mentioned before, the temperatures of the hot gas follow the temperature profile determined in the decomposition model from Chapter 2. The nodes in the first section of the decomposition chamber all remain cooler than 500 °K (approximately 226 °C), which is well under the maximum operating temperature of PTFE at 260 °C [23]. The highest wall temperatures are expected in the nozzle throat, where the model goes up to temperatures of 1090 °K (817 °K), which remains below the maximum intermittent operating temperature of stainless steel 316 (Annex B). As the nozzle module is made out of a solid piece of metal with thick walls, the Swagelok tubing capability calculation is not applicable to the nozzle and higher pressures are acceptable.

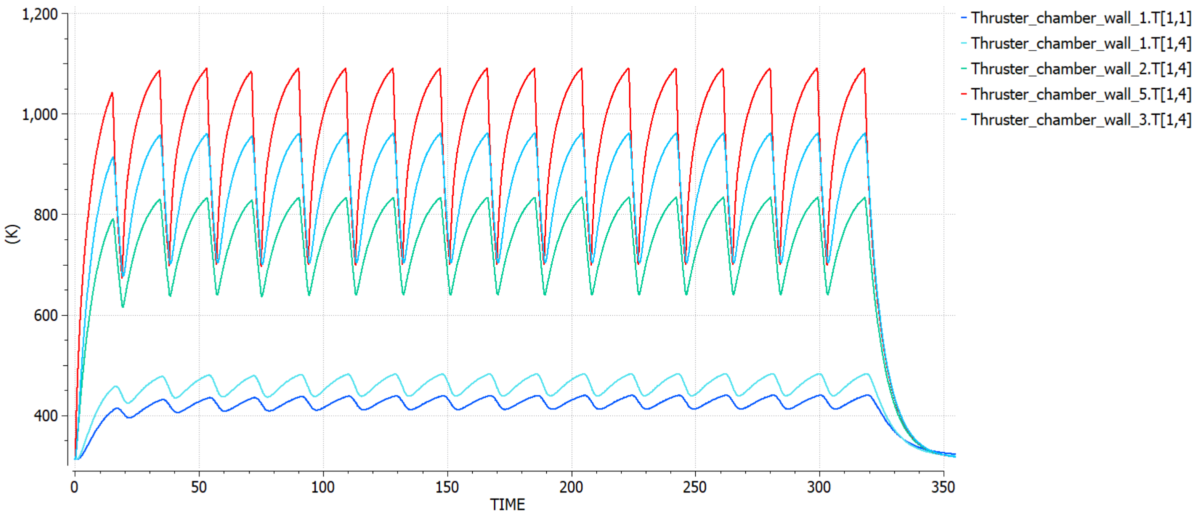

Figure 4.41: EcosimPro model results for the decomposition chamber and nozzle temperatures

4.8. Conclusion

The first step in the detailed design of the thruster was the determination of the decomposition chamber diameter. This has been done by first determining the catalyst bed loading at the reference point for a range of existing thrusters. This was compared to the available tube diameters at Swagelok. As result, a 1/2 inch tube diameter was chosen with a wall thickness of 0.049 inch. At the reference point of this thruster (22 bar feed pressure), the catalyst bed loading is approximately 7.3 $kg\ m^{-2}\ s^{-1}$. A specific catalyst bed has not been design in this work, as the thruster is capable of testing a range of different catalyst beds.

A thermal standoff was created to prevent the inlet valve from increasing past the maximum temperature of 50 $^{\circ}C$, which is determined in requirement *MGT-278*. The design features four threaded rods as the standoff structure. To reduce the required length, the rods are created using MACOR rather than stainless steel, which is a machinable ceramic material. In the thermal standoff, the propellant flows through a 1/16 inch capillary tube. As this tube is constrained on both sides of the thermal standoff using Swagelok compatible tube fittings, an expansion loop is required, to manage stress caused by thermal expansion. Deformation effects due to bending were assessed to include in the estimation of pressure drop in the capillary tube, as well as the response time . In the final design, the thermal standoff bridges a horizontal distances of 43 mm. A bypass bend is created in the capillary tube, with a curve radius of 5 mm and the arc angle is 53.8 degrees.

An injector module was designed, using one Swagelok compatible fitting to connect to the capillary tube and another to connect the decomposition chamber. A large flange on the injector module is used to connect the structure to the test setup as well as the thermal standoff threaded rods. The capillary tube enters into the injector, until it reaches the injector plate, which should be flush with the top Swagelok nut. This allows easy access for alternative technologies, directly through the decomposition chamber wall. The injector plate contains a single orifice with a diameter of 0.18 mm. Due to the large interface with the chamber wall, a layer of PTFE insulation is required between the capillary tube housing cylinder and the decomposition chamber wall. This prevents vapor lock in the capillary tube.

The catalyst bed is held in place using retainers. The upstream retainer is made using a simple mesh, but the downstream retainers requires a structural component onto which the mesh is placed. The mesh prevents small particles from the catalyst bed to be ejected out of the nozzle. The structural component keeps the catalyst bed pellets in place and consists of a perforated plate with 1 mm holes on top of a cylinder. A conservative assessment shows a pressure drop over the downstream retainer of 0.17 bar at the reference point. The pressure drop over the upstream retainer is considered negligible.

A complete overview of the expected pressure drops for the complete operating range was created for the valve, capillary tube, injector and retainers. Using this, an assessment of the expected chamber pressures (without catalyst bed pressure drop) was created. At the reference point, the expected chamber pressure without catalyst bed pressure drop is 17.87 bar. The main contributor to the total pressure drop is the injector, which has a design pressure drop of 20% of the chamber pressure at the reference conditions.

The final component of the thruster is the nozzle module. Similarly to the injector, the nozzle module is created as a fitting body for the Swagelok interface. It contains a pressure and temperature tap, as well as an interface for the downstream catalyst bed retainer. The throat diameter was calculated using the frozen flow method described in [14] and was determined at 0.72 mm. A conical nozzle design was chosen, with a 30 degree contraction angle and a 15 degree divergence half angle.

The complete design (Figure 4.42) was of an iterative nature and not performed exactly in the order of the topics discussed above. A thermal model was created in EcosimPro to support the design with several points. This was mainly relevant to determine the required thermal standoff length and the required thickness of the PTFE insulation in the injector. The EcosimPro model was divided into a fluidic and thermal part. A worst-case scenario was used for the assessment of the vapor lock problem in the capillary tube. It assumes a low pressure, low mass flow firing (minimum heat required to heat the propellant) directly after a high pressure, high mass flow firing (highest heat transfer rate in the capillary tube). The chamber temperatures were calibrated according to the temperature profile found in the decomposition model in Section 2. Both pulsed mode and steady-state simulations performed. In the final design, the maximum temperature in the valve remains slightly below the allowed 50 $^{\circ}C$. The maximum propellant temperature in the capillary tube during heat soak back is 105 $^{\circ}C$, which is below the determined maximum temperature.

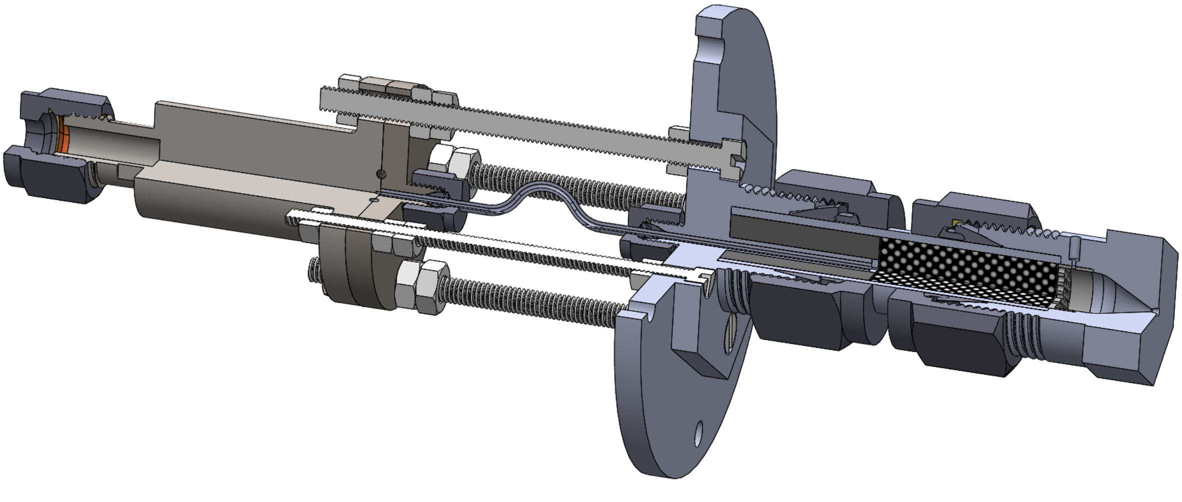

Figure 4.42: Final thruster design overview with section cut and catalyst bed impression

5

Alternative decomposition technologies

Prior to starting this work, a literature review was performed in which a number of concepts were explored to pose as an alternative for the decomposition of hydrogen peroxide using catalyst beds. A short first order assessment of the feasibility of these concepts was performed, based on findings in literature. After initiation of the decomposition process using one of these technologies, the reaction should be able to sustain itself due to thermal decomposition effects, if the propellant concentration is above 64% [43]. The concepts that were chosen as most likely to succeed were the use of a heater assembly to start thermal decomposition (5.1), using a spark gap to initiate the decomposition of hydrogen peroxide (5.2) and finally, the use of a laser ignition system to start decomposition (5.3). The thruster designed in this work could be used to test the usage of these concepts in a monopropellant thruster. Therefore, a first order assessment is performed of how these technologies could be applied. An overview of the main findings and recommendations is given in the conclusion of this section (5.4).

5.1. Thermal decomposition

One of the most likely to succeed alternatives to a catalyst bed, is the exploitation of thermal decomposition characteristics of hydrogen peroxide. Some research has already been performed on this topic. A functioning version of the concept was demonstrated in [58], though further research is required. The thruster designed in this work will provide a platform to test this technology further. Before applying the technology, an assessment should be made of the expected power requirements, for which a concept plan was generated (5.1.1). Additionally, a concept was generated for the integration of a thermal decomposition system into the modular thruster (5.1.2).

5.1.1. Testing the thermal decomposition concept

Before applying the thermal decomposition concept in a thruster, it would be interesting to know some more details about the temperature and power requirements for such a concept. To assess these requirements, an experiment could be performed by conducting a test using droplets of hydrogen peroxide and a hot plate. Such an experiment was also performed in [71], to assess temperature requirements for the thermal decomposition of hydrogen peroxide at different concentrations. They used a borosilicate vessel containing several thermocouples to measure the temperature at several positions. Successful decomposition was determined by the temperature profile development within the vessel. The vessel was positioned on top of a heating plate, so that the bottom serves as the thermal source for the propellant. A mechanism using syringe pumps was used to create an accurate droplet volume, which was dropped into the vessel from the top. The authors found that, for concentrations of 75% and lower, the water in the solution absorbs too much of the energy for thermal decomposition to start, even with a heating plate plate temperature of 270 $^{\circ}C$ at atmospheric pressure. The experiments were performed for several heating plate temperatures, an overview of the results found for the lowest required heating plate temperature are found in Table 5.1.

Table 5.1: Overview of minimum heating plate temperatures for thermal decomposition of hydrogen peroxide from [71]

HTP Concentration	80%	85%	90%	95%
Required heating plate temperature	250 $^\circ C$	200 $^\circ C$	200 $^\circ C$	200 $^\circ C$

Additionally, the author found that the decomposition delay time significantly reduces with increasing temperature of the heating plate. For more detailed results, a similar experiment could be performed for hydrogen peroxide at concentrations of 87.5% and 98%, with smaller steps between the heating plate temperatures. However, since the modular thruster will be built regardless, and the thermal decomposition of droplets will be different than that of a propellant flow, the question rises how relevant more detailed results are. Therefore, it is suggested to use data found in [71] as a rough first estimate for the power requirements and, tp simply apply the thermal decomposition concept to a 1/2 inch tube for integration with the thruster. Testing can be done by performing small firings at different pressure levels and heater power input levels, while monitoring whether decomposition takes place using visual observations, as well as thrust and chamber temperature measurements.

5.1.2. Integration of thermal decomposition in the thruster

A concept level design of a thermal decomposition system was developed and is shown in Figure 5.1. It shows a heater coil inserted in the flow path within the decomposition chamber. For access to the decomposition chamber, a hole is drilled in the side, downstream of the injector side Swagelok nut. Additionally, an interface structure can be welded in which the heater coil is mounted and sealing of the decomposition chamber is achieved. Though this concept uses a heater coil that accesses the tube from one side of the decomposition chamber, some alternatives are recognized. Heating of the propellant could be done using a heater wire or coil that enters the decomposition chamber on one side and leaves on the other, which creates symmetry in the flow path, but requires two interfaces. Another option would be the use of a heater plug, rather than a coil. Though this significantly reduces the contact area between the heater and the propellant flow, it may be more efficient at heating a local area of the flow. The decomposition of the flow in this section can heat the rest of the propellant to the point of rapid decomposition. This may have a positive effect on the heater power required. If heating of the entire flow turns out more effective, another alternative may be the creation of a heated metal mesh within the flow.

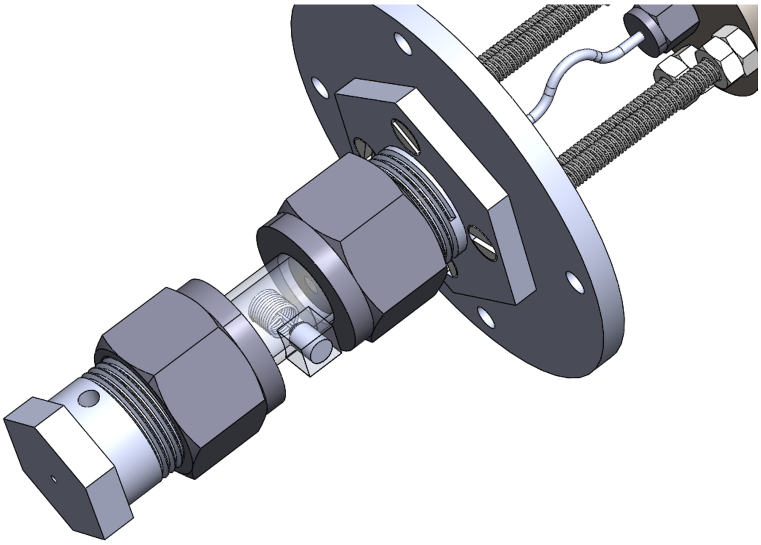

Figure 5.1: Potential integration of the thermal decomposition concept

The expected injection velocity of the propellant is calculated using [82]:

$$v = \frac{Q}{A} \tag{5.1}$$

In which v is the flow velocity in m/s, Q is the volumetric flow rate in m^3/s and A is the orifice area in m^2. For the injector described in Section 4.3 this would result in an injection velocity of approximately 15 m/s at the reference conditions. The initial velocity of the flow may make it difficult for a coil to heat the flow fast enough to initiate thermal decomposition. This could be overcome, by creating a mechanism that slows down part of the main flow and routing it past the heater. Alternatively, a longer heater path can be created, in the longitudinal direction of the decomposition chamber.

5.2. Spark decomposition

The second considered alternative to a catalyst bed for the decomposition of hydrogen peroxide, is the use of a spark. At this moment, no evidence was found in literature for the possibility of using the spark concept to initiate decomposition of hydrogen peroxide. Some information regarding the ignition of hydrogen peroxide vapors using a spark was found in [73–75], though it was assessed that the vapor concentrations required for this to work would not occur at the pressures expected in the thruster, without significant heating of the propellant. This assessment was done in the literature review preceding this work, by comparing the mole fractions of hydrogen peroxide in the vapor with the ignition limits mentioned in [73–75]. The determination of these fractions was done using the same method described in Section 4.3.2. The results that were found are seen in Figure 5.2.

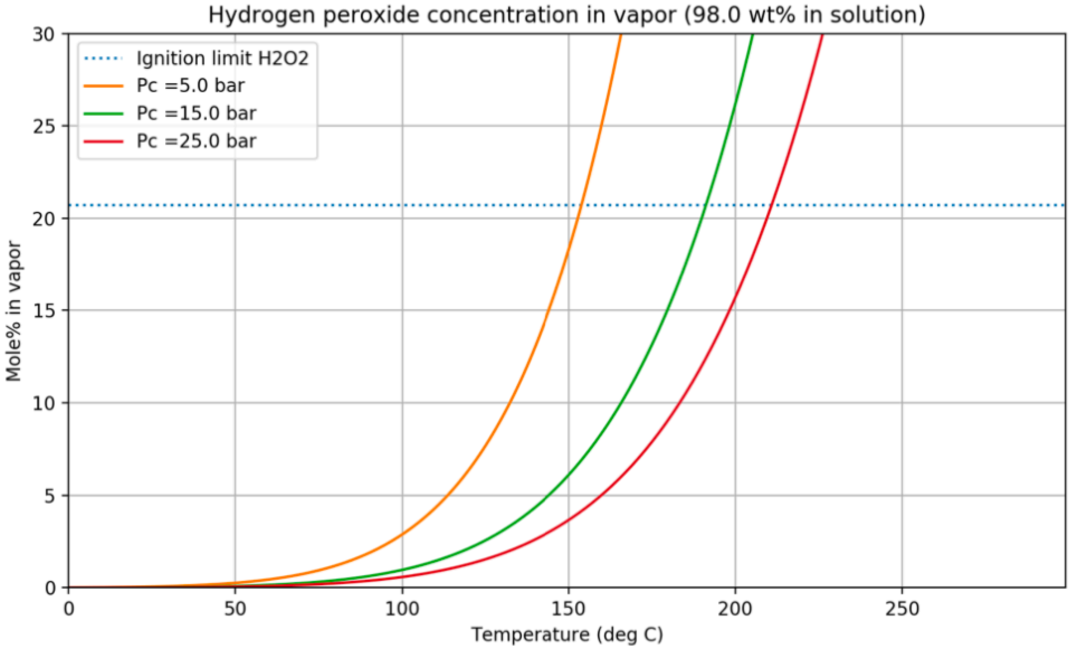

Figure 5.2: Results from the spark ignition limit assessment performed in the literature review

From this figure, it was concluded that using a spark to ignite hydrogen peroxide vapors in the thruster is not a feasible concept. However, it is expected that a spark could significantly heat a local area within the flow in a short time and cause a decomposition reaction. To assess the feasibility of using a spark for this purpose, a lab test should be performed (5.2.1). A concept level design was developed, for the integration of this technology with the thruster from this work (5.2.2).

5.2.1. Testing the spark decomposition concept

A spark is created by introducing a gap in a circuit and charging the circuit with a very high voltage. For air at atmospheric pressure a dielectric strength of 3 kV/mm was found [29], which means that for a spark to cross a 1 mm distance in air between two wires, the voltage differential across these wires should be at least 3 kV. It is expected that for hydrogen peroxide a significantly higher voltage is required. No explicit values were found, however, for comparison, (distilled) water has a dielectric strength of 65-70 kV [29]. For the assessment, an initial, simple test could be performed, by using a widely available plasma lighter. The expected output voltage of these lighters was found often around 10 kV. To step up the voltage a voltage multiplier could be used, though building one may be costly since the diodes and capacitors involved require high voltage ratings. Alternatively, some pre-manufactured step-up modules were found at a low price point, though since the reliability appeared questionable, it is advisable to purchase a number of backup units and several different types, should this road be taken. It was also found that, when the spark is unable to cross (for example if the distance is too high), the load on the unit may damage it. For the same reason, it is advised to use a battery pack as power source, rather than using an expensive power source, to prevent damaging of expensive equipment. For safety, relays connected to a separate circuit could be used, to keep the operator out of the high power loop. The easiest solution for conducting a laboratory test would be a high voltage power source that can generate the spark directly. It should then be capable of outputting between 50 and 100 kV.

Two testing concepts are recognized. In the first concept, an attempt is made to create a spark within a small volume of liquid hydrogen peroxide. This could be done by inserting the electrodes in a small borosilicate vessel (as was used in the testing described in Section 5.1.1) containing hydrogen peroxide. Since the spark would have to be generated within a purely liquid fluid, the required voltage will be high. Observation of decomposition can be performed visually. The second concept simulates the thruster environment a little more. A test could be performed by using an injection mechanism with a tiny nozzle to create a spray of tiny droplets of hydrogen peroxide. The spray is aimed at a continuous spark between two electrodes in air. Decomposition could potentially be observed visually, or by using temperature measurements downstream of the spark. The last concept may have some more strict requirements regarding safe distances than the first. Alternatively, the test could be performed by simply integrating the technology into the modular thruster and performing test firings.

5.2.2. Integration of a spark gap in the thruster

For the integration of a spark gap to start decomposition, two concepts have been developed. Both concepts are based on the placement of a spark gap directly downstream of the injector. The first concept describes the placement of two electrodes that enter the decomposition chamber at opposite sides. The gap between the electrodes is reduced to a predetermined distance and is centered in the decomposition chamber. To mount the electrodes, a structure can be welded on the outer wall of the decomposition chamber, as was done in the thermal decomposition concept. A hole should be drilled into the decomposition chamber through which the electrodes can enter and an interface should created to hold the electrodes in place and seal the decomposition chamber. Good electrical insulation between the electrode modules and the chamber walls is required to prevent current from flowing to other parts of the thruster. A concept level design is shown in Figure 5.3.

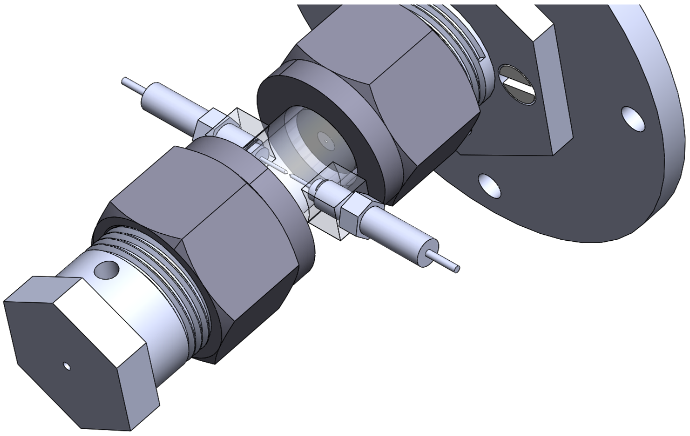

Figure 5.3: Spark initiated decomposition concept using two electrodes

The second concept is more similar to the use of a spark plug in a car. There are some advantages and disadvantages to this approach. Firstly, it may be a challenge to find such a spark plug at this scale and compatible with the use of hydrogen peroxide. Additionally, it provides less control over the size of the spark gap itself. An advantage of this approach is that now only a single interface is required and an off the shelf system may be available. A difference compared to the first concept is the movement of the spark gap from the center of the decomposition chamber towards a position close to the chamber wall. The impact of this difference is unknown. A concept visualization is seen in Figure 5.4. For reference, the spark plug interface diameter in this visualization is 5 mm.

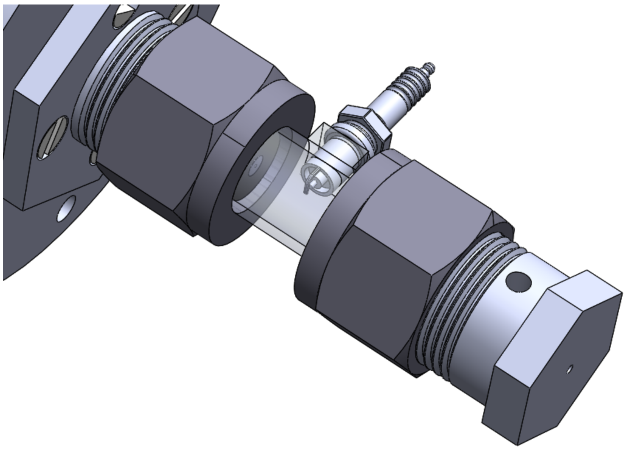

Figure 5.4: Spark initiated decomposition concept using a spark plug

5.3. Laser decomposition

The final alternative concept that is considered for the decomposition of hydrogen peroxide, is the use of a laser ignition system. The idea behind this, is to create a plasma arc somewhere in the flow path. This plasma arc heats the propellant to the point of thermal decomposition. This local decomposition will then trigger the thermal decomposition of the remaining flow. In [60] a pulsed ND:YAG laser was used to create plasma in the vicinity of a droplet of Ammonium Dinitramide, for ignition. A miniaturized laser ignition unit was used in [13], which was further developed in [42]. Though a laser system has been successfully used for the ignition of several propellant combinations, no proof was found that his method would work with hydrogen peroxide. Therefore, laboratory tests could be performed to investigate the feasibility of the method (5.3.1). Similar to what was done for the other alternative methods, a concept model was generated for the integration of a laser unit on the thruster (5.3.2).

5.3.1. Suggested test design

To test the concept of laser decomposition, a pulsed ND:YAG laser can be used to create the plasma arc. This could be done using the laser unit from [42]. The easiest approach for testing would be to attempt to initiate decomposition of liquid hydrogen peroxide in a small volume container. Alternatively, an acoustic levitator could be used to suspend a droplet in mid-air, as was done in [60]. With a larger volume, the decomposition reaction will be easy to see with the naked eye or a regular camera. For the decomposition of a single droplet it is advised to use a high speed camera, as it may be more difficult to observe. Though a simple laboratory test is advised before integration, another way of testing would be to simply integrate the technology onto the thruster, as it is easy to exchange the decomposition chamber and the existence of the thruster itself is not dependent on the success of the laser technology.

5.3.2. Integration of the laser ignition unit in the thruster

A miniaturized version of a laser ignition system for rocket engines has been produced in [42]. Though specific dimensions were unknown a simple approximate model of the laser device has been created in Solidworks to create a conceptual thruster design (Figure 5.5). Sizing of the model was done based on an image of the laser, accompanied by a ruler, as is seen in the reference.

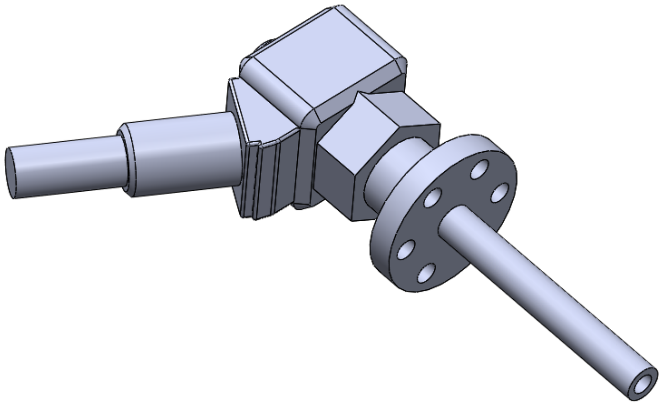

Figure 5.5: Simple approximate model of the laser ignition unit from [42]

The complete unit consists of two main parts; the laser head and a optical access tube with focusing window. Additionally, the laser head is mounted on a flange. Mounting on the thruster can be done by welding a fitting tube to house the optical access tube perpendicular to the decomposition chamber, positioned downstream of the injector Swagelok nut. On top of this tube a flange connection can be created to seal the tube and mount the laser head. A hole should be drilled into the decomposition chamber for the laser to enter. An graphic impression of the concept level interface is seen in Figure 5.6.

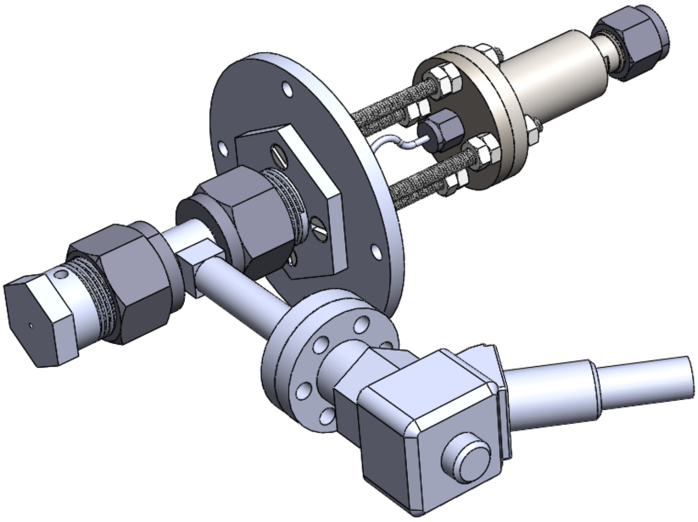

Figure 5.6: Laser decomposition integration concept using an approximated laser ignition unit from [42]

Though the laser unit is miniaturized, it seems relatively large compared to the thruster itself. For this project this is not considered a problem as it does not concern flight hardware. For potential future integration in reaction control systems that would use a 1N thruster however, the impact seems larger. A potential solution for this issue is found in using fiber optic cables and a laser distribution device [111] to transport the laser from a single laser head, placed at a different location in the spacecraft, to multiple thrusters. At this point only the laser focusing hardware is required to be integrated with the thruster. Though currently this technology is not ready, the potential has also been recognized by the authors of [42].

5.4. Conclusion

Three alternatives to the use of catalyst beds have been considered to initiate the decomposition of hydrogen peroxide in a monopropellant thruster. After full decomposition is achieved, the reaction is maintained due to thermal decomposition effects. Firstly, these thermal decomposition effects of hydrogen peroxide can be utilized by applying a heater to the decomposition chamber to initiate the process. A significant amount of research regarding this topic is already available and some success has already been achieved. Therefore, this concept has a very high chance of success. Though more detailed power requirement assessments could be performed through the means of extra laboratory testing, it is advised to directly integrate the technology on a decomposition chamber for use with the modular thruster, since such a variety of research is already available. A concept was generated for how this integration could be performed.

The second alternative considered uses a spark gap to initiate decomposition. Though research has been performed in the past on the ignition of hydrogen peroxide vapors using a spark gap, the required vapor composition seems not to be achievable in a monopropellant thruster. This is not a reason to disregard this technology however, as a generated spark could could still initiate decomposition due to significant local heating. As this concept is unproven, it is advised that some laboratory tests are performed prior to potential integration into the thruster.

The final concept describes the use of a high power laser to create a plasma arc within the propellant flow. This plasma arc should be able to start the decomposition process within the chamber. This concept is especially interesting due to the high frequency repeatability associated with pulsed lasers. Additionally, there is a future potential to use fiber optic cables to distribute the laser from a single laser head to several thrusters, minimizing the size of the system. Lasers have been used as an ignition source for other propellant combinations with success, however some laboratory experiments are advised, since it is not proven with hydrogen peroxide. Nevertheless, it seems likely that a hot plasma arc could initiate a thermal decomposition reaction. Therefore, direct integration could also be performed for testing of the technology on the thruster. Overall, the modular character of the thruster provides a unique opportunity to test these new technologies without the necessity of a dedicated thruster design.

6

Propellant feed system

The design of the propellant feed system was initiated by creating a design ideology (6.1). When the concept was clear, the system architecture was generated (6.2). Finally, the components of the propellant feed system were selected (6.3) and a final design was created (6.4). The findings of this chapter have been summarized in a concluding section (6.5).

6.1. Feed system concept

The design of the propellant feed system was started by listing the functions that the system should have. Firstly, the system is created to be easy to handle and transport (6.1.1). Several measurements are required from the system, but the measurement of the mass flow rate brings some complications to the design (6.1.2). Finally, the safety of the operator and the environment has to be taken into account during the design (6.1.3).

6.1.1. Transportation and deployment

Since the logic behind the design of the thruster itself is to maximize the flexibility in use, the same logic should be applied to the feed system. Because of the size of the thruster, the test setup is designed in a way that it is easily transportable to a test location, therefore the same ease in transportation will be expected of the propellant feed system. This is achieved by creating a frame of lightweight aluminium extrusions in which the propellant tanks and plumbing are mounted. Some aluminium panels are used to create a mounting structure and a place to house the components for manual operation of the propellant feed system. The execution of this concept is seen in Figure 6.1. A more detailed overview of the design is given in Section 6.4.

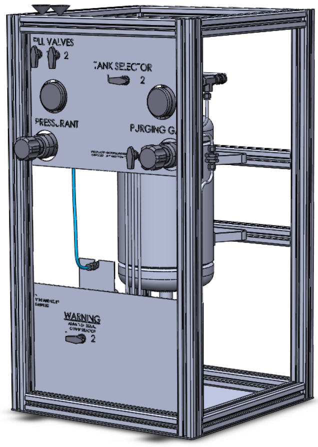

Figure 6.1: Concept propellant feed system in aluminium frame

6.1.2. Mass flow measurement

One of the measurements used for the thruster performance assessment is the mass flow rate. During steady-state operation, a stable flow is established, which can be measured using a mass flow meter with the correct measurement range. However, the propellant mass used is of interest for pulsed mode operation as well. The minimum on-time of the thruster is found to be equal to 50 ms, as per *MGT-096*. The lowest test on-time is found at 100 ms, as per *MGT-098*. For the mass flow meter selected in 7.2 the response time noted is 200 ms. Since the response time alone is already higher than the on-time, an alternative measurement method is employed. To determine the mass flow rate per thruster pulse, the propellant tank is weighed on a scale before and after each pulse train. The difference in mass is divided by the number of pulses to determine the propellant mass used per thruster pulse. To determine the required accuracy of the scale, a rough estimation of the propellant used per pulse train is made using the following equation:

$$m_{used} = T_{on} \cdot n \cdot \frac{F}{I_{sp}} \tag{6.1}$$

In which m is the propellant mass in kg, T_{on} is the pulse duration, n is the number of pulses in a pulse train, F is the thrust in N and I_{sp} is the specific impulse in s. The values for the thrust and specific impulse are taken from Section 3.1 and the values for T_{on} and n are taken from requirement *MGT-098*. This means the calculation was performed for the vacuum specific impulse of 98% hydrogen peroxide. During atmospheric firing and using a lower concentration of hydrogen peroxide the specific impulse will be lower, which increases the propellant mass used. This makes the calculation conservative. The calculation was performed for all specified pulse trains at each feed pressure. The pulse train with the lowest propellant consumption consists of 50 pulses with a T_{on} value of 100 ms. The propellant mass used was calculated at 0.924 g, which comes down to a value of 0.0185 g per pulse. An error of 0.1 g in the measurement would result in a 0.002 g error per pulse, which is approximately 11% This is considered rather large. A scale with a 0.01 g accuracy would lead to a maximum error in the pulse mass used of a little over 1%, which is considered acceptable. However, the maximum mass capability of scales with an accuracy of 0.01 g was usually found to be below 2 kg. This poses a rather strict mass limit on the propellant tank and its attachments, especially since a large propellant tank was already made available by ESA. Therefore, the choice was made to create a two-tank system, in which the large main tank is used for steady-state operation and a small secondary tank is used for pulsed mode operation. This small tank is mounted on top of a scale (Figure 6.2) and connected to the rest of the feed system using flexible tubing. Alternatively, a mass balance system could be used to compensate for some of the tank mass.

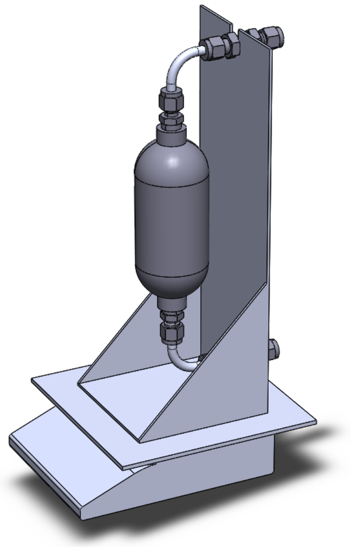

Figure 6.2: Impression of the small propellant tank on a scale

6.1.3. Safety considerations

Concerning operator safety, some considerations were made before designing the feed system architecture. In theory, a system could be designed using actuated options for each valve present. However, this would lead to a large, heavy and, most importantly, very expensive system. Therefore, several manual valves are used in the system. However, since the system will contain high-pressure corrosive propellant, it was decided that all valves required for pressurized operation should be actuated valves. In this manner, the operator can remain at a safe distance from the feed system at all times. Additionally, as the operator is not within the range of the propellant feed system, it can be moved closer to the test setup. Therefore, less tubing is required between the feed system and the thruster. In this way pressure losses are minimized.

It was considered that, should any component of the thruster, feed system or test setup fail, an emergency shutdown procedure should always be possible. This should be the case, even if control over the actuated valves is lost. Therefore the valve configuration (normally closed, normally open or dual-mode) is chosen such, that the system is returned to a safe state automatically when power is lost. This safe state includes the depressurization of the propellant tanks and purging of the propellant lines.

Finally, from discussion with the thesis supervisor in ESA, it was decided that the propellant temperature and pressure should be monitored in each tank to monitor propellant stability. Additionally, each tank should be accompanied by its own relief valve and backup relief valve.

6.2. Feed system architecture

The logic described in Section 6.1 was used as a guideline for the design of the final propellant feed system architecture (6.2.1). The design contains several actuated valves, which have been configured in a way that allows for an emergency shutdown procedure (6.2.2).

6.2.1. Architecture overview

The logic described in the previous section was used as a guideline for the design of the propellant feed system. This resulted in the generation of the architecture displayed in Figure 6.3. At the top of the figure, two separate nitrogen tanks are displayed. The nitrogen in the first tank serves as the pressurant gas for the system. A separate second nitrogen tank is used for the purging gas. The valves of the nitrogen gas tanks are indicated as GBV-1 & 2. Each of the tanks is outfitted with their own pressure reducing gas regulator (CGR-1 & 2). An analog pressure indicator is placed downstream of each of the regulators to assist in manually setting the correct system pressure. The purging gas pressure should always be higher than the pressurant gas pressure. Each of the lines is fitted with a filter (F-1 & 2) before the nitrogen enters the main system. The purging gas line is connected to the actuated purging valve (PV-1), whereas the pressurant gas flows through a check valve (CV-1) to prevent any flow back towards the nitrogen tank before it reaches the first actuated main tank valve (TMV-1). This is the point where the pressurant gas is connected to the propellant storage section of the feed system.

As was described in Section 6.1.2, the choice was made to measure the mass flow in pulsed mode operation by weighing the tank after a firing. A number of potential concepts were initially drafted to achieve this:

1. A single tank setup with a removable tank;
2. A dual tank setup with a removable tank;
3. A dual tank setup with a weight measuring system built into the feed system.

Initially, the concept of a removable tank using quick release fittings was created. After removal, the tank could be weighed separately from the system. This could be done for a single tank system while exchanging the large and smaller tanks. Alternatively, this could be done for a dual tank set up, with a more permanent setup for the large tank, as the size and weight of it would make it more difficult to handle. Especially since, after removal, the relief valves would have to remain on the tank and not in the rest of the feed system assembly. Several other disadvantages of this concept became clear. First of all, making a tank removable would mean that the system would have to be depressurized every time a mass measurement would take place. The act of removing the tank from the system, moving it towards the scale for weighing and reintegrating it into the feed system seems cumbersome. Therefore, the third alternative was chosen, which describes the permanent integration of both tanks and designing the weighing function into the feed system itself.

A disadvantage of the dual tank setup is the number of valves required within the feed system. First of all, each of the tanks has its own set of relief valves. Additionally, the initial design of the propellant feed system included actuated vent and main tank valves for each tank (in total six actuated valves). With the addition of the two actuated purging valves that are described further in this section, that brings

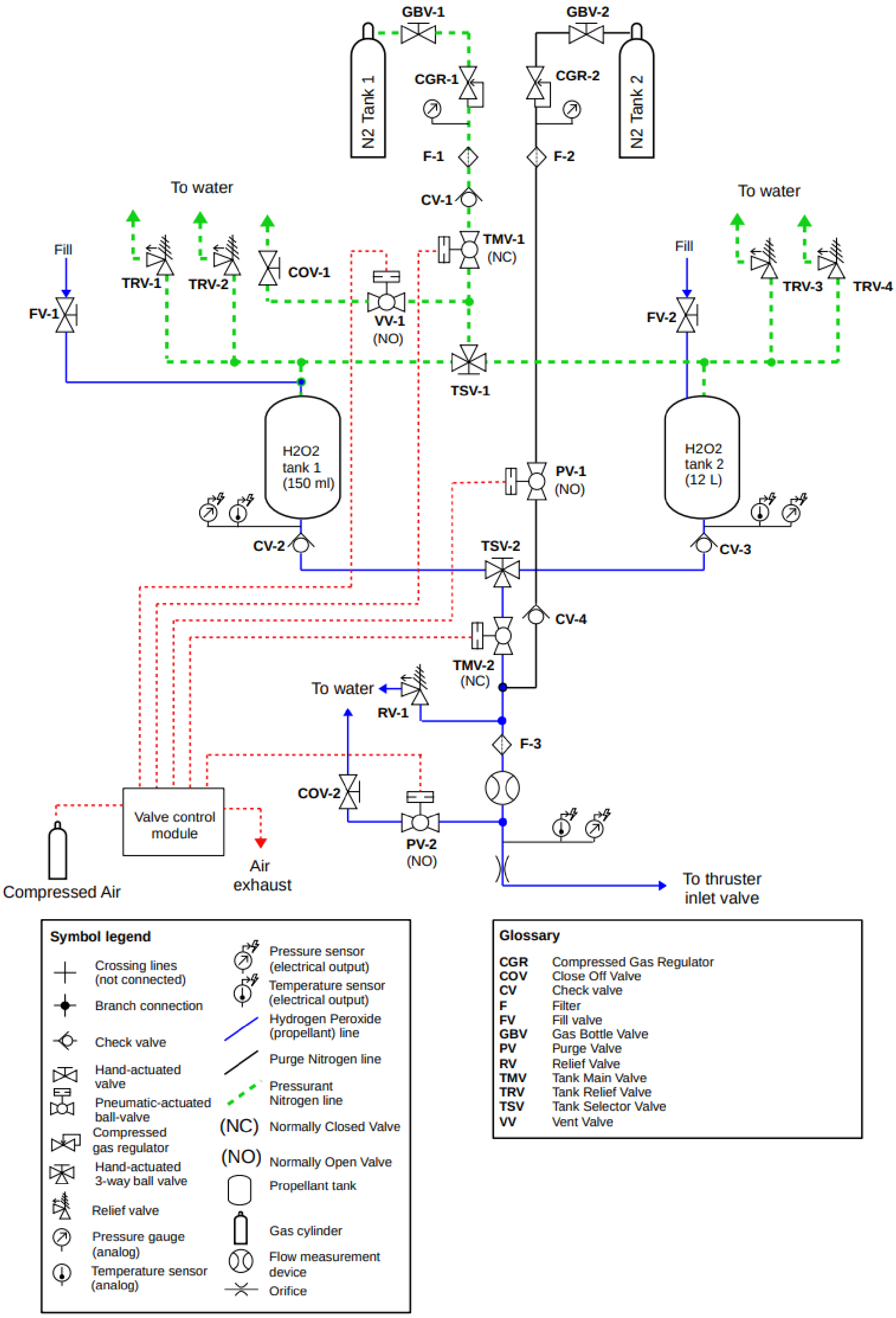

Glossary

CGR	Compressed Gas Regulator
COV	Close Off Valve
CV	Check valve
F	Filter
FV	Fill valve
GBV	Gas Bottle Valve
PV	Purge Valve
RV	Relief Valve
TMV	Tank Main Valve
TRV	Tank Relief Valve
TSV	Tank Selector Valve
VV	Vent Valve

Figure 6.3: Propellant feed system architecture

the total amount of actuated valves to eight. For these valves, pneumatic actuation was chosen, for which Swagelok has an off-the-shelf control module available. This control module can control up to six valves simultaneously, which would mean two modules are required for operation. Though a third party system could be used, it was considered beneficial to reduce the amount of actuated valves required. A solution was found by creating a tank selection system, which allowed the reduction in the number of actuated valves to five. Both propellant tanks are connected to a tank selector valve on the upstream (TSV-1) and downstream (TSV-2) side. Each tank has its own set of relief valves, but is connected to the same actuated vent valve (VV-1) and actuated main tank valves (TMV-1 & 2). Usage of this system implies that, at any given time, only one of the tanks should be pressurized, as no vent valve is available to the tank that is not in use. This means that the tank that is not in use can not be depressurized in case of an emergency shutdown. Though not pressurized, propellant can still be stored in the tank that is not in use. Therefore, each tank maintains its own set of relief valves (TRV-1, 2, 3 & 4). The main tank has a separate opening that is used for the filling line. The filling line of the smaller tank connects to the pressurant line, as no separate opening is available. The filling lines are outfitted with a manual valve (FV-1 & 2) to close the system. As described in Section 6.1.3 each of the thanks is outfitted with an electronic pressure and temperature sensor to monitor the propellant status. Flow of propellant back into the propellant tanks is prevented by placement of a check valve downstream, before reaching the second tank selector valve (TSV-2). At this point, the propellant reaches the second actuated main tank valve (TMV-2), which concludes the propellant storage section of the feed system. It is important to note that both tank selector valves should always be set in the same position before operation of the propellant feed system.

The propellant flow now reaches the main propellant line. Directly downstream of TMV-2, the purging line is connected to the main propellant line. A check valve (CV-4) is added, before the purging line connects, to prevent any flow of propellant into the purging line. As this line will contain pressurized propellant, a relief valve is added (RV-1). The propellant now flows through the mass flow sensor, followed by a last filter (F-3) to prevent upstream decontamination from entering the thruster. Here, the main fuel line connects to the outgoing purging line, which is outfitted with the second actuated purging valve (PV-2). Finally, a pressure and temperature sensor is connected to measure the final feed pressure and temperature, before the propellant flows through a calibrating orifice, into the inlet valve. The calibrating orifice is added to fine-tune the mass flow rate of the thruster. As valves VV-1 and PV-2 are open when not powered, manual valves (COV-1 & 2) are added to provide the capability of closing the feed system off entirely during storage. This prevents decontamination from entering the system.

6.2.2. Emergency shutdown

As a safety feature, the configuration of the actuated valves has been chosen such, that de-powering of the system brings it to a safe state. This means that even if a pneumatic line breaks, the system can still be brought to a safe state. As is seen in Figure 6.3, the propellant feed system contains five actuated valves. An overview of the valves and emergency function is shown in Table 6.1. The functionality of the emergency shutdown procedure becomes clear from the table above. As soon as the procedure is initiated, the main tank valves close to isolate the propellant tank, which is vented for depressurization. Subsequently, the purging lines open to remove the remaining propellant from the propellant line. Failure of one of these valves during the emergency procedure will always bring the system to a safe state. However, a valve could also fail during operation. The failure modes that occur are described in Table 6.2. Each of the failure modes can be detected, using the electronic pressure

Table 6.1: Configuration of actuated valves in the propellant feed system

Valve	Configuration	Unpowered function
TMV-1	Normally closed	Closes propellant tank from pressurant gas
TMV-2	Normally closed	Closes propellant tank from main propellant line
VV-1	Normally open	Opens to vent propellant tank and reduces pressure to ambient
PV-1	Normally open	Opens to start the flow of purging gas to the main propellant line
PV-2	Normally open	Opens to purge the propellant line

sensors in the feed system, by the behaviour described in the table.

Table 6.2: Feed system failure modes

Scenario	Failing valve	Failure behavior
1	TMV-1	Loss in tank pressure with each firing
2	TMV-2	Tank pressure maintained, loss in feed pressure with each firing
3	VV-1	Rapid loss in tank pressure, venting into water tank observed
4	PV-1	Feed pressure rapidly increases to purging gas pressure
5	PV-2	Rapid loss in feed pressure, purging into water tank observed

6.3. Components

The component selection for the propellant feed system was divided into several sections. First, the propellant tanks were selected (6.3.1). Secondly, a single tube diameter was chosen for the feed system and a selection was made of several types of connectors required for the design (6.3.2). A selection of valves was made (6.3.3), followed by the selection of other components, such as filters (6.3.4). The selection of feed system components has been mostly based on what is available at Swagelok, as many of the other components in this design are used from the same manufacturer. However, these components should be regarded as a guideline and could easily be replaced by suitable alternatives if so desired.

6.3.1. Propellant tanks

As was described before, the propellant feed system will contain two separate propellant tanks. The large propellant tank was assigned by ESA/ESTEC, as it is already available on site. It is a 12.6 L tank produced by Anton Christophers GmbH & Co KG, with a maximum allowable working pressure of 50 bar. For the smaller tank, a double-ended sample cylinder was chosen from Swagelok [89]. Options are available for several maximum working pressures, of which the lowest is 124 bar, which is sufficient for the feed system. Options with higher working pressure have an increase in weight. As was described in Section 6.1.2, a weight limitation exists for which a suitable scale can be found. Therefore, the heavier cylinders with higher working pressures are not considered. An overview of the potentially suitable options is given in Table 6.3. In [82] a typical tank ullage volume is in the range of 3 to 10%. For this calculation an ullage volume of 10% was chosen as a worst-case scenario for the propellant volume available in the tank. For the density of 87.5% hydrogen peroxide, a value of 1393 $kg\ m^{-3}$ was assumed.

Table 6.3: Overview of sample cylinder options from [89] for the small propellant tank

Material	Tank Volume [ml]	87.5% mass [g]	Empty mass [kg]	Wet mass [kg]
SS 304L	50	63.3	0.17	0.23
SS 304L	75	95.0	0.28	0.37
SS 304L	150	190.0	0.43	0.62
SS 304L	300	379.9	0.73	1.11
SS 316L	150	190.0	0.43	0.62
SS 316L	300	379.9	0.73	1.11

In Section 6.1.2 it was mentioned that the maximum mass that could be measured accurately enough with available scales is 2 kg. Taking into account an extra mass budget for a small tank frame, flexible hoses and connectors, it is expected that the 300 ml tanks may cause the mass budget to be exceeded. The largest expected propellant consumption during a single pulse train is expected to occur in a pulse train consisting of 20 pulses with T_{on} = 5 s or 10 pulses with T_{on} = 10 s at 22 bar feed pressure. Equation 6.1 was used, assuming 87.5% hydrogen peroxide and a specific impulse of 127 s, which was determined using RPA Lite [105] for 87.5% hydrogen peroxide with optimum expansion at atmospheric pressure. Using this method resulted in the highest expected propellant mass used by a single pulse train of approximately 81 g. This shows that the 75 ml tank is required as a minimum. To create an extra buffer and provide the opportunity to perform multiple pulse trains in a row, the 150 ml tank was finally chosen, which is available in both stainless steel 304L and 316L. The version chosen is the stainless steel 316L one (model number: 316L-HDF4-150), simply because this is the same material the Swagelok tubes fittings use [90]. The 75 ml tank can be used as a back-up solution in case the mass budget of the small tank assembly is exceeded.

6.3.2. Tubes and connectors

The selection of the propellant tube diameter was done mainly based on the interface diameter on the inlet valve selected in Section 3.4.3. The Parker Pulse Valve connects using a 1/4 inch tube fitting. Additionally, all other Swagelok components in the feed system were easily available with the same size of connectors [90]. Tubing with a 1/4 inch diameter is available in several wall thicknesses [91]. The smallest wall thickness is 0.035 inch, which has an allowable working pressure of 5100 PSI (351.6 bar), which is sufficient (part number: SS-T4-S-035-20). The feed system design uses several tee unions (part number: SS-400-3), as well as straight fittings (part number: SS-400-6). Space between two fittings is minimized by using port connectors (part number: SS-401-PC), rather than tubing when possible. For the connections to the main tank two G 1/2 connectors (part number: SS-400-1-8RS) and one 1/4 inch NPT connector (part number: SS-400-1-4) are required. For the connection to the small propellant tank, two of the same 1/4 inch NPT connectors are used. Additionally, two bulkhead connectors (part number: SS-400-61) are used to mount the tank in the small frame and connect to a suitable flexible tube, such as those described in [95].

6.3.3. Valves

Several types of valves have been used throughout the design of the propellant feed system. The complete architecture contains four hand-actuated valves. This function can be fulfilled by quarter turn plug valves available at Swagelok [88] (part number: SS-4P4T), made using stainless steel 316, PTFE, FKM and silicone-based lubricant for the wetted parts, which are all compatible with hydrogen peroxide [20, 22, 38, 80]. Additionally, two hand-actuated three-way valves were used. The wetted components of the 40G series by Swagelok valves are made using 300 series stainless steel and PTFE. Silicone-based lubricant is used. All of these are all compatible with hydrogen peroxide [20, 22, 38, 80]. A three-way version was available for the required tube diameter (part number: SS-43GXS4). In the feed system architecture, five relieve valves are present as well, for which the R3a series can be used (part number: SS-4R3A). The wetted components are made using a stainless steel 316, PTFE and FKM, all of which have been mentioned above as hydrogen peroxide compatible materials. One of the lubricants mentioned is based on Molybdenum disulfide, for which no compatibility data was found. Therefore, it is advised to contact the manufacturer to inform about the use of this lubricant. Finally, the five pneumatic valves were chosen. Two options were available at Swagelok. The first option is to apply a pneumatic actuator to a general-purpose ball valve [93]. Alternatively, pneumatically actuated bellows-sealed valves were found [85]. The latter was initially chosen for the propellant feed system due to the more attractive price point. However, it was later found that the stem tip in the most compatible models contained PCTFE, which is not compatible with high concentration hydrogen peroxide [80]. Therefore, the choice was made to use the stainless steel ball valve from the 40G series [93], with a pneumatic spring return actuator (part number: SS-43GS4-53-SR). Two are placed in Normally Closed configuration and three in Normally Open configuration.

6.3.4. Other components

Several filters have been placed in the architecture design of the propellant feed system. The main reason for the use of these filters is to prevent contamination from entering the propellant feed system, which could increase the decomposition rate. Additionally, *MGT-408* states particles with a diameter of more than 0.1 mm (100 μm) should be prevented from entering the fluid passage. These particles could block the injector, which was determined to have a diameter of 0.18 mm in Section 4.3.3. Additionally, during the search for mass flow rate sensors, often filter size requirements were found between 10 and 100 μm. A selection was made from the available filter options in [87]. They offer three different types of filters with tube fittings (F-, FW- and TF- series), all available in 1/4 inch sizes. Both the F- and TF-series filters use a gasket made out of either an aluminium alloy or silver-plated stainless steel 316. Since silver is a catalyst for hydrogen peroxide [3], and the exact aluminium alloy is unknown, these options were considered unsuitable. The FW-series filter is of all-welded stainless steel 316 construction. It uses a stainless steel 316 sintered element as a filter, with a pore size of either 0.5, 2, 7 or 15 μm. The catalog [87] provides flow rate - pressure drop relations, which show that the 0.5 μm has a higher pressure drop than the other options. For the others, the flow data in the catalog is the same. Therefore, the finest filter (2 μm pore size) is chosen out of the lower pressure drop options (part number: SS-4FW-2). This way, the pressure drop is minimized and the filter's capability is maximized.

For the check valves, a selection was made from [86] and [92]. Several valve types are fully compatible for use with hydrogen peroxide. The final selection was done based on the cracking and resealing pressures. The resealing pressure was chosen as low as possible, on the inlet side. This means no back-flow can exist. Of the options left, the option with the lowest cracking pressure was chosen. This resulted in the selection of the check valve with part number: SS-4CH-10). The cracking pressure of this check valve is between 0.46 and 1.1 bar. This means that the feed system pressures upstream may need to be increased to obtain a 22 bar feed pressure. Therefore, the feed pressure can be monitored using a pressure transducer.

Finally, a selection was made of the gas regulators for the pressurant and purging gas. A general-purpose pressure reducing valve is chosen from [94]. The model number (KPR-1JPA427H60020) was chosen based on the following characteristics:

- KPR: K-series pressure reducing regulator;
- 1: 316 Stainless steel body;
- J: Pressure controlling range 0-34.4 bar. The first option that includes MEOP (24 bar) and allows for a higher purging pressure;
- P: Maximum inlet pressure 206 bar. A common pressure for nitrogen bottles. This can be replaced by R, T or W to increase the pressure;
- A: Straight port configuration;
- 4: 1/4 female NPT, for use with Swagelok NPT - tube fitting connector from [90];
- 2: Seal material PEEK for compatibility with hydrogen peroxide [37, 72];
- 7: High flow coefficient for low pressure drop;
- H: Alloy C-276 diaphragm, no vent. For compatibility with hydrogen peroxide [24];
- 6: Knob with panel mount (use 2 for non panel mount version);
- 0: No isolation or relief valves;
- 0: No cylinder connections;
- 2: Inlet and outlet pressure indicator in bar (H for outlet only);
- 0: No other options.

6.4. Completed feed system design

A 3D model has been created of the feed system design and, though the architecture described in Section 6.2 should be considered an exact design, the 3D model describes a suggested layout. The design is not exact, as the hands-on nature of manufacturing provides an opportunity to find more convenient or effective placement of tubing and components. The design was started by creating an aluminium frame as was described in Section 6.1. This was followed by the placement of the main propellant tank. On the front side of the feed system assembly, two aluminium panels have been placed that both serve as a support structure for the tubing and a manual control panel. The upper control panel houses the compressed gas regulators (CGR-1 & 2), analog pressure indicators (Note: in the model a separate pressure indicator is used, rather than the dual pressure indicators chosen in Section 6.3.4), fill valves (FV-1 & 2), first tank selector valve (TSV-2) and the tank vent close-off valve (COV-1). An overview of the upper control panel is seen in Figure 6.4.

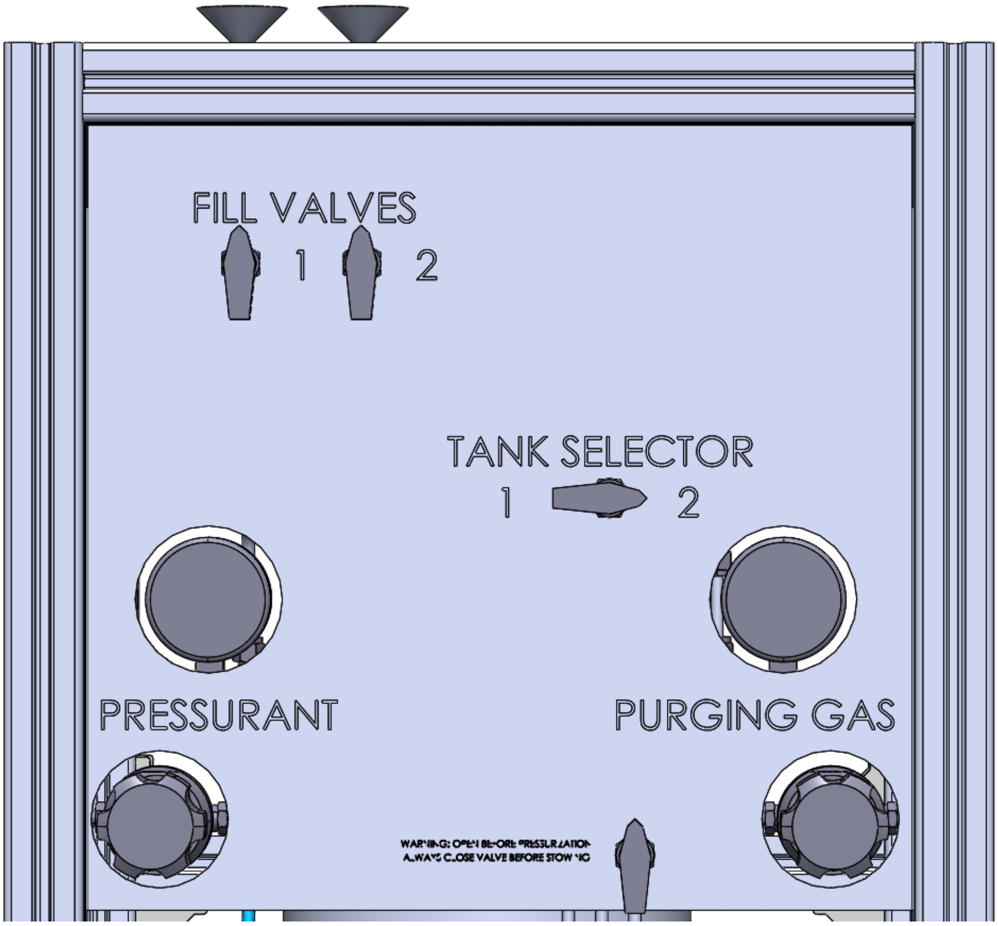

Figure 6.4: Feed system upper control panel (with a single pressure gauge per gas regulators)

A manifold like structure, composed of all valves upstream of the propellant tanks, is mounted on the backside of the control panel. All connections to the purging water tank are routed to the same area, mounted on the backside of the lower control panel. Each of the outflow tubes ends in a tube fitting. This way, tubes are connected that are suitable for the location of the water tank relative to the feed system and the whole feed system is retained within the frame. To reduce the number of connections, both relief valves for a single tank connect to the same outflow tube. The outflow tubes of both tanks remain separate. Additionally, the downstream tank selector valve (TSV-2) is found on the lower control panel. The small tank is placed on a scale as was shown in Figure 6.2 within the feed system frame. An overview of the complete feed system is seen in Figure 6.5. The (blue) colored tubes that run to and from the small propellant tank indicate flexible tubes. These are used to prevent interference with the propellant mass measurements. Finally, both nitrogen tanks can be connected directly to the compressed gas regulators on the backside of the upper control panel. The last components, downstream of the mass flow meter, are placed on the test setup frame, rather than on the feed system assembly. This is done to place the purging valve (PV-2) as close to the thruster inlet as possible to minimize the remaining propellant upon purging. When the test setup and feed system are disconnected, the broken connection should be plugged on both sides to prevent contamination from entering the system. This can be done by using an end cap [90], rather than a valve (as was used in the case of the purge and relief lines). Using a valve would allow contaminants in the system, as the small area downstream of the valve would be reintegrated into the system when both assemblies are reconnected. The frame of the propellant feed system was created using 40x40 mm aluminium extrusions. The complete assembly has a base dimension of 500x500 mm. This means the horizontal extrusions have a length of 420 mm. The length of the vertical extrusions is 900 mm, though they could be easily replaced by 1 m extrusions if these are obtained more easily.

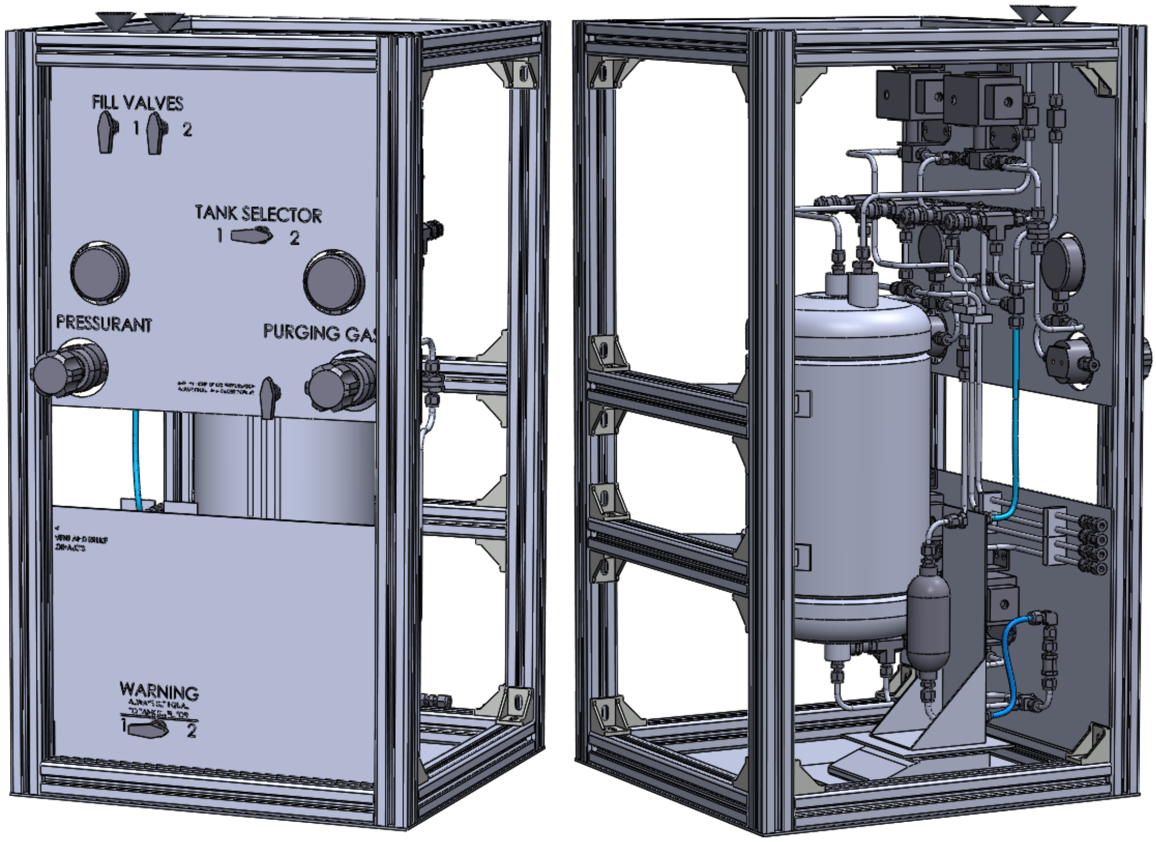

Figure 6.5: Overview of the complete feed system assembly

6.5. Conclusion

A single feed system assembly was designed using aluminium frame extrusions. The entire system is less than 1 m tall and has a base of 0.5 by 0.5 m. This allows for easy transportation between the test site and storage, as well as easy deployment of the system. The mass flow sensor used for the propellant feed system has a 200 ms response time. This means it is unable to detect the mass flow rate correctly for pulsed mode operation. Therefore, a dual tank setup is designed, in which the main tank is used for steady-state firings and a second, smaller tank (150 ml) is used for pulsed mode operation. The smaller tank is mounted onto a scale to measure the weight of the propellant used after every pulse train. It was determined a scale with an accuracy of 0.01 g was required. Taking into account commonly available scales, this puts the mass requirement of the small tank assembly at a maximum of 2 kg. Should this not be achievable, a mass balance system could be used to compensate for the mass of the tank. A system architecture was created using a combination of components available at Swagelok. Several actuated valves are used to allow the operator to be physically removed from the system during pressurized operation. The configuration of the actuated valves is chosen such that the feed system can always return to a safe state in case of failure. Control panels have been created on the final design, that simultaneously serve as mounting platforms for the components of the feed system. The components downstream of the mass flow sensors have been mounted on the test setup, to allow the purging line to be placed close to the thruster inlet valve. The components for the propellant feed system were selected for their compatibility with hydrogen peroxide. However, the compatibility of the lubricants in some components is not clear. Therefore, it is advised to contact the manufacturer to inquire about its properties and other potential possibilities.

7

Test setup and testing

The design process for the thruster test setup was started with the generation of a concept (7.1). Thereafter, an overview as created of the required sensors for testing and the interfaces with these sensors were designed (7.2). This was followed by the design of the complete test setup assembly. (7.3). Finally, a plan was created for the preparation of the test setup, as well as the test campaign (7.4). The main findings of this chapter have been summarized in a concluding section (7.5).

7.1. Test setup conceptual design

The conceptual design phase was started with an assessment of different methods that could be used for the measurement of thrust (7.1.1). Taking this information into consideration a conceptual design for the complete test setup was created (7.1.2).

7.1.1. Thruster orientation

To provide input for the conceptual design, several concepts were generated for the measurement of thrust. Three options were considered for the orientation of the thruster; a horizontal firing position, up-firing vertical position and a down-firing vertical position. For each orientation, a number of advantages and disadvantages were listed.

Horizontal thruster orientation The first option considered for the orientation of the thruster is a horizontal firing position. By using this concept the weight of the thruster is not carried by the load cell, but by a supporting structure. This means that a load cell can be used with a small range and thus a high measurement accuracy. Such a test setup was created for a small hydrogen peroxide monopropellant thruster in [65], where a structure carrying the thruster was connected to the main test setup structure by the means of so-called ”flexures”, allowing sideways motion. An alternative to these flexures could be a sliding rail. Both of these methods have the disadvantage that, especially at a low thrust level, friction could cause some dampening of the measurement or small errors. Another disadvantage is that, since the hot gas is ejected horizontally, a large testing area may be required.

Up-firing vertical thruster orientation The alternative to a horizontal firing orientation is a vertical one. This could be done by either firing the thruster upward or downward. The first option considered is the upward-firing of the thruster. An advantage of the vertical orientation is that the thruster can be directly attached to the load cell, thus removing the risk of any damping or errors potentially introduced by a guide rail or flexures. A downside of the direct attachment is that the weight of the entire thruster and the frame that holds it is carried by the load cell. This means that a load cell with a higher measurement range is required if no mass balance system is introduced, leading to lower measurement accuracy. It is expected that using a mass balance system could introduce extra vibration errors into the measurements. Firing in the upward direction means that the thruster will create a large fountain-like plume of hot steam and oxygen, which may lead to a larger space requirement. Additionally, since the plume is ejected in the upward direction, gravity can cause condensed water droplets to accumulate on the testing equipment.

Down-firing vertical thruster orientation The final considered orientation is the down-firing orientation. This orientation retains the advantage of being able to directly attach the thruster to the load cell. Additionally, since the plume is aimed downward, it can be fired directly into a water tank. This way, the amount of required space is reduced. The disadvantage of the reduced load cell accuracy mentioned in the up-firing case remains.

A summary of the advantages and disadvantages is found in Table 7.1.

Table 7.1: Overview of considered advantages and disadvantages of thruster orientation in the test setup

Orientation	**Advantages**	**Disadvantages**
Horizontal	- High accuracy load cell possible	- Friction of required guide rails or ”flexures” may influence test results - Large space requirement due to exhaust plume
Up-firing	- Direct attachment to load cell possible	- Lowered accuracy load cell when not using a mass balance system - Large space requirement due to ”fountain” of hot steam and oxygen - Gravity effects on exhaust plume may cause accumulation on hardware
Down-firing	- Easy direct attachment to load cell - Low space requirements	- Lowered accuracy load cell when not using a mass balance system

Taking all advantages and disadvantages into account, the choice was made to create a test setup using the down-firing vertical thruster orientation, as it seems like the safest, most compact solution. An assessment was done in Section 7.2.1 whether a direct measurement is achievable or a mass balance is required.

7.1.2. Chosen design concept

The final concept of the design uses the same logic as the design of the propellant feed system, described in Chapter 6. The system is created in such a way that it allows for easy deployment as well as transportation, which is possible because of the small scale of the thruster. The main structure of the test setup will consist of a frame created from aluminium extrusions. A small subframe is created that interfaces with the thruster, using smaller aluminium extrusions. At the top of the main frame a metal plate containing four holes is mounted. The vertical extrusions of the thruster subframe will pass through the holes, and are also topped with a small metal plate. This metal plate interfaces with a load cell that is mounted on the top plate of the main frame. This way, the thruster subframe is carried solely by the load cell. A water container is placed underneath the thruster to catch the exhaust plume. A quick overview of the concept is seen in Figure 7.1. A more detailed discussion of the design is found in Section 7.3.

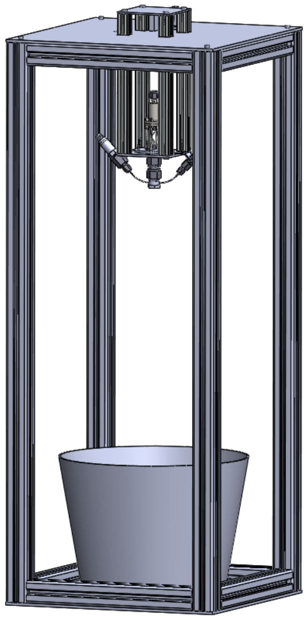

Figure 7.1: Test setup concept

7.2. Sensors and Measurements

The test setup is outfitted with several sensors, used for the characterization of the thruster. The measurement that influences the design of the test setup most significantly is the thrust measurement (7.2.1). Additionally, the chamber pressure and temperature are used in many performance calculations (7.2.2). Though the mass flow sensor is part of the propellant feed system, it has been described in this chapter, as the data it provides are also used for characterization of the catalyst bed or alternative technology (7.2.3).

7.2.1. Thrust measurement

As was seen in Figure 7.1, the thruster is mounted in a subframe that moves freely in the vertical direction. In theory, a load cell could be placed under the top plate of the subframe, the reduction in load on the load cell would lead to a direct measurement of the thrust. However, this means that the load cell would have to carry the entire weight of the subframe, thruster, pressure transducer, thermocouple and some of the tubing above the thruster. To determine whether some kind of mass balance system is required to reduce the direct force on the load cell a small assessment is performed. Though the exact weight is unknown, the resulting load is estimated at least an order of magnitude higher than the thrust to be measured. For example, if the total subframe assembly mass would be approximately 1.5 kg, a load cell might be chosen that can measure up to 3 kg, such as the one in [102]. This means that an error of 0.00067% over the total output as mentioned in the referenced document, would lead to an error of approximately 0.2 g, which is a load of approximately 0.002 N. For a minimum expected thrust of slightly over 0.2 N (Section 3.2). This leads to a thrust measurement error of slightly under 1% (under 0.2% for a 1 N measurement). To determine whether this is sufficient, some reference was sought in the requirements specification of the thruster. In *MGT-064* it is stated that the steady-state thrust at identical propellant supply conditions shall be predictable within +- 5% of nominal thrust (a 10% range). It was decided that the test setup should be able to measure the thrust with at least an order of magnitude lower than this 10%, thus 1%. This minimum accuracy is slightly less than the worst-case scenario for the referenced load cell above. Therefore, it was determined that a direct force measurement is accurate enough, provided that there is a mass limit on the thruster subframe below 3 kg. It is estimated that the subframe will not reach this mass limit. However, should the limit be breached, either a more accurate load cell is required, or a mass balance system should be created.

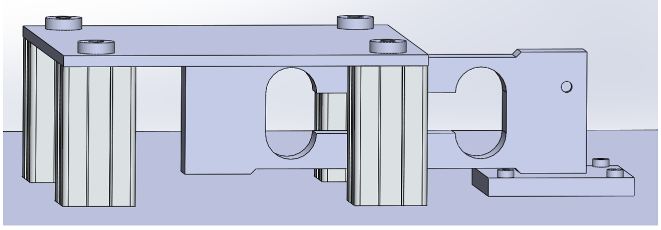

Figure 7.2: Mounted load cell for thrust measurement

7.2.2. Chamber temperature and pressure measurements

As was described in Section 4.6, the nozzle module contains two taps for measurements of the chamber pressure and temperature. Two 1/16 inch tubes are inserted into the holes drilled into the nozzle module and welded in place. The maximum wall thickness of the tube is chosen to minimize the added volume and thus, minimize the effect on the flow through the chamber. The thermocouple should be chosen compatible with a corrosive environment and a temperature range at least to the adiabatic decomposition temperature of 1218 $^{\circ}K$ plus an extra buffer. A common Type-K thermocouple meets these requirements. This type of thermocouple was also used with a 98% hydrogen peroxide monopropellant thruster in [67]. Using a 1/16 inch Swagelok tube with the maximum wall thickness available (0.020 inch) [91] leads to an internal tube diameter of 0.5715 mm. Therefore, a thermocouple with a 0.5 mm probe diameter can be used, using a thermocouple compression fitting. No compression fitting was found for a 1/16 inch tube, therefore an example was created in which the tube was welded to a reducing port connector from [90]. This is then connected to a Swagelok tube fitting with a compatible connection for a thermocouple compression fitting.

For the pressure transducer, a module was suggested that is already commonly used within the chemical propulsion section of ESA, namely the Keller PA-21 Y [26]. Since the maximum temperature at which the pressure transducer can operate is significantly below the adiabatic decomposition temperature, the connecting tube functions as a thermal standoff. The exact required length of this thermal stand-off should still be determined. For now, a value of approximately 50 mm is assumed, though this is easily adjusted in the manufacturing phase by adjusting the tube length. A short tube is desired, as the length will influence the accuracy of the measurements. Alternatively, the same manufacturer has a water- or air-cooled pressure transducer available, that can measure with a fluid temperature up to 1000 $^{\circ}C$ [27], which is above the adiabatic decomposition temperature. The models above serve as suggestions, as there may be a different suitable pressure transducer already available within ESA. Both the pressure transducer and the relatively heavy fittings for the thermocouple are attached to the thruster subframe using a mounting bracket as is seen in Figure 7.3. The design of these brackets may need to be adjusted, depending on the final required standoff tube length. Similar to the mounting of the thermocouple, the 1/16 inch tube is welded to a reducing port connector and a Swagelok fitting is used to create an interface with the pressure transducer.

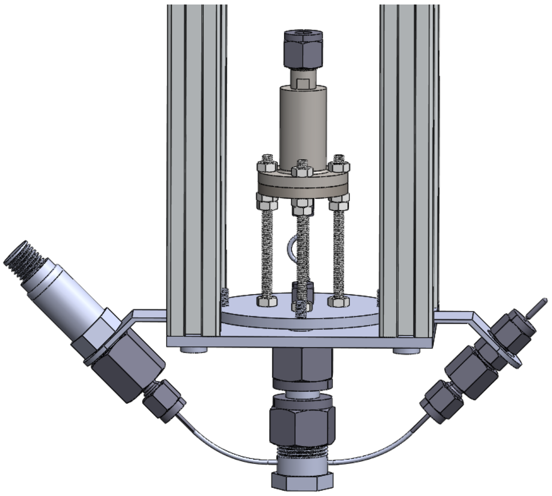

Figure 7.3: Pressure transducer and thermocouple mounted on the test setup

7.2.3. Mass flow measurement

Figure 7.4: Bronkhorst mini CORI-FLOW M14

The expected flow rates during operation of the thruster are between 0.17 g/s and 0.72 g/s, as was mentioned in Section 3.1.3. This translates to a range of 0.612 kg/h to 2.592 kg/h. For the mass flow measurement, several different types of flow meters exist. First of all, a volume flow measurement device could be used instead. Using the fluid density, the mass flow can then be calculated. This can be done using a turbine flow measurement device such as was done in [67]. However, no suitable option was found when taking into account the expected flow rates and material compatibility. Two other mass flow measurement concepts were considered. The first concept is a thermal mass flow meter [12]. This instrument uses two heater elements around a flow tube. The first functions as a temperature sensor, whereas the second is powered to create a small temperature difference between the two points. The mass flow is calculated using the varying power requirements to keep the temperature difference constant. A sensor of this type was not found for the mass flow ranges expected. The final considered concept is a Coriolis mass flow meter [10]. This instrument guides the flow through a vibrating tube. The flow affects the frequency of this vibration. The instrument measures the vibrations and is able to determine the mass flow rate from the data. A solution was found in the Bronkhorst mini CORI-FLOW mass flow meter [11]. The complete thruster mass flow range falls within the nominal range of the M14 model (0.1 kg/h - 10 kg/h). Additionally, all wetted materials are made using 316 stainless steel, which is compatible with hydrogen peroxide [20, 80]. The instrument can be used with pressures up to 200 bar. The typical response time mentioned is 200 ms. Therefore, a dual tank system is required, as described in Section 6.1.2.

7.3. Final test setup design

After further defining the design concept and integrating the designs of the sensor interfaces, a final design was created for the thruster test setup (7.3.1). Special attention has been given to the interface with the propellant feed system (7.3.2).

7.3.1. General description

The decision was made that the nozzle exit should be placed at least 0.5 m away from the water tank [108]. Assuming that the plume expands according to the nozzle divergence half-angle of 15 degrees, this means the minimum diameter of the water tank placed below is approximately 0.27 m. As a safety buffer, the diameter of the water tank was increased by approximately 20%, to 0.32 m. The frame base dimensions were chosen, taking into account the dimensions of the aluminium frame extrusions and the assumption that it should be possible to move the water tank freely through the frame. This leads to the rounded frame base dimensions of 400x400 mm. As 40x40 mm aluminium extrusions were chosen for the frame, this means the length of the horizontal extrusions is 320 mm. The length of the vertical aluminium extrusions is 1 m. For the thruster subframe, a base dimension of 100x100 mm was chosen. The vertical aluminium extrusions are created using a 20x20 mm profile and have a length of 250 mm.

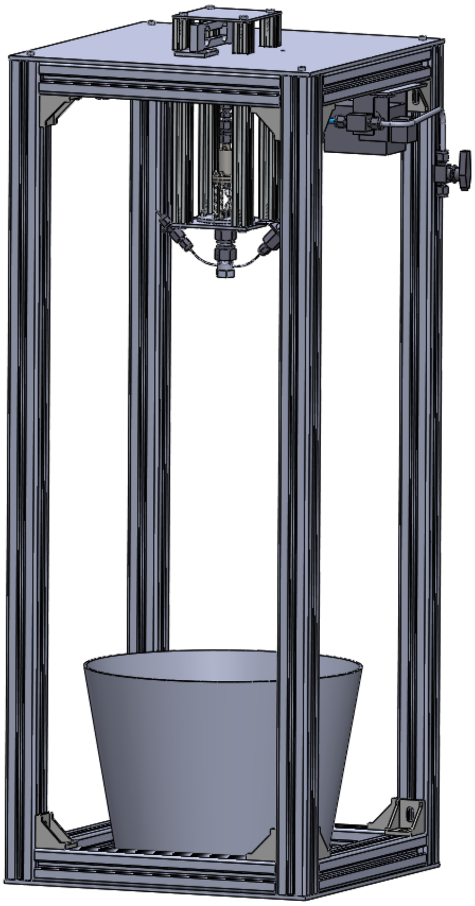

Figure 7.5: Overview of the completed test setup design

7.3.2. Interface with the propellant feed system

As was briefly mentioned in Section 6.4, the last part of the propellant feed system, downstream of the flow sensor, is placed on the test setup. This is done to place the purging line as close to the propellant inlet valve as possible. On top of the inlet valve a straight Swagelok fitting is connected, in which a disk with an orifice can be placed for flow trimming [90]. On top of that, a tee connector is placed. The tee connector connects to the upstream section of the propellant feed system on one side and with the pneumatic purging valve on the other. This is done using flexible tubes, to prevent interference with the thrust measurements. Downstream of the purging valve, a manual valve (COV-2 in Figure 6.3) is seen, to close the system off from contamination when stowed. A flexible tube can be connected to this valve, to guide the propellant to the purging water tank. On the upstream side of the tee connector, a pressure transducer and thermocouple are placed. A straight tube fitting is placed at the end, to connect to the propellant feed system assembly. This fitting should be plugged when the system is not in use. This can not be done using a valve as was done for the purge and relief lines, as contamination can build up in the disconnected side of the valve, which becomes part of the system when connected. In this design, some propellant will remain in the section upstream of the thruster inlet valve if the main propellant line is purged. This can therefore only be purged through the thruster. The vertical distance of this section is approximately 82 mm. The 1/4 inch tube selected for the feed system has a wall thickness of 0.065 inch. Taking this, and an assumed hydrogen peroxide density of 1430 $kg\,m^{-3}$ (Annex B) into account, the propellant mass in this section is calculated at 0.25 g. Before removing the thruster from the assembly, this should be purged through the thruster.

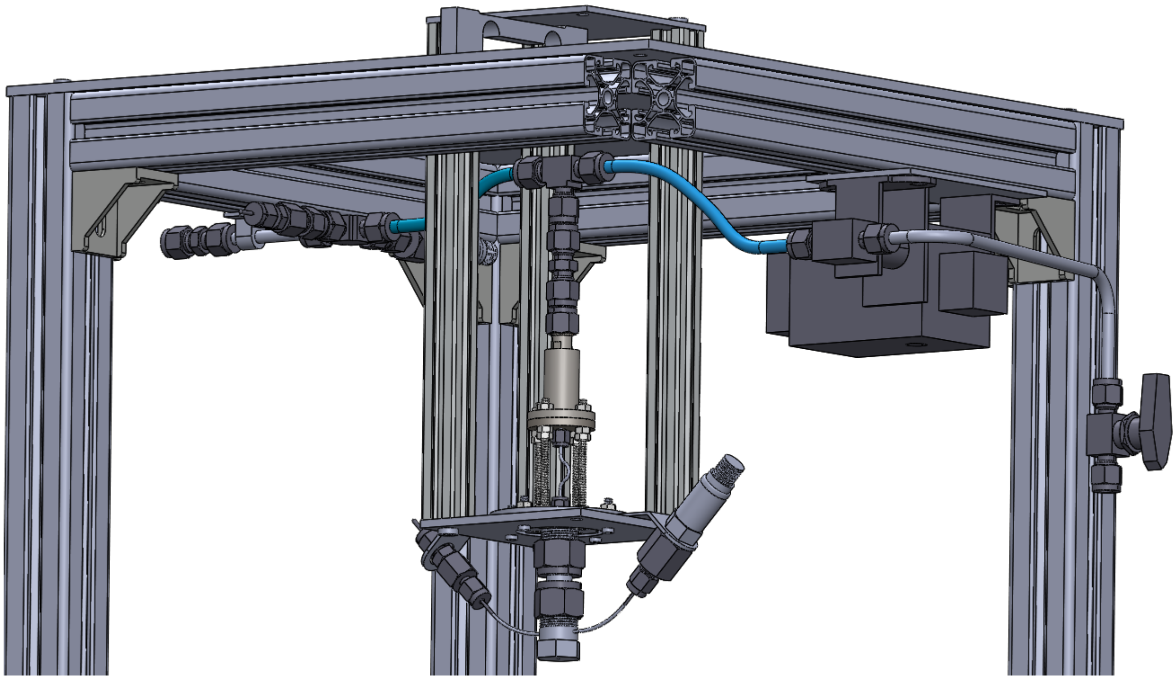

Figure 7.6: Interface of the test setup and thruster with the propellant feed system (structure section cut)

7.4. Testing

Before use of the thruster, propellant feed system and test setup, leak testing should be performed. This leak testing is performed on the entire feed system, as well as the thruster itself (7.4.1). Once all seals are confirmed to function properly, the thruster test campaign can be started (7.4.2).

7.4.1. Leak testing

Prior to first operation, the entire system should be leak tested. This applies mainly to the propellant feed system, though the thruster itself can also be leak tested. In order to perform a leak test, the propellant feed system is pressurized (low pressure) using the nitrogen pressurant, section by section. A spray bottle can be filled with a mixture of water and some kind of non-invasive soap. By spraying the soapy mixture onto the outside of connections in the propellant feed system, leaks will be visible in the form of bubbles. A basic workflow is found in Table 7.2. Names of components are referring back to Figure 6.3. Leak testing of the thruster can be performed by pressurizing the feed system (low pressure) and either plugging the nozzle, using a 1/2 inch Swagelok cap connection from [90] or creating a custom end cap connection. The thruster can be pressurized by opening the thruster inlet valve. If the nozzle is plugged or a custom end cap is used, the pressure is can be confirmed using the pressure transducer on the test setup. This can not be done if a standard Swagelok end cap is used. After pressurization, the leak test can be performed on the thruster using the soapy mixture. It should be kept in mind that the downstream Swagelok connection is only leak tested if the actual nozzle module is used. If a standard end cap is used, the connections to the pressure transducer and thermocouple can not be tested either. Therefore using the original nozzle module is advised.

Table 7.2: Leak testing procedure for the propellant feed system

Section number	**Actions**
1 (Upstream TMV-1)	From off-state. Initiate the valve control system. With TMV-1 unpowered (closed), open the pressurant gas valve (GBV-1) and set the desired pressure in the regulator (CGR-1). Confirm the correct pressure on the pressure gauge. Spray the soapy mixture on all connections upstream of TMV-1 and confirm leak tightness.
2 (Small tank side, upstream TMV-2)	From previous state. Turn TSV-1 and TSV-2 to Tank 1 (small tank), then open COV-1 and confirm FV-1 closed. Power (close) VV-1 and leave TMV-2 (normally closed) unpowered. Power (open) TMV-1. Confirm no out-gassing through the relieve valves and VV-1. Confirm Tank 1 pressurized using the pressure transducer. Perform leak test with the soapy mixture on all components between TMV-1 and TMV-2 on the small tank side.
3 (Large tank side, upstream TMV-2)	From previous state. Depower (close) TMV-1 and depressurize Tank 1 by depowering (opening) VV-1. Confirm ambient pressure in Tank 1 and power (close) VV-1. Switch TSV-1 and TSV-2 to Tank 2 (large tank). Confirm FV-2 closed and TMV-2 unpowered (closed). Power (open) TMV-1. Confirm no out-gassing through the relieve valves and VV-1 and Tank 2 pressurized using the pressure transducer. Due to the large volume of the tank, this requires a significant volume of nitrogen gas. Once pressure is stable, perform the leak test with the soapy mixture on all components between TMV-1 and TMV-2 on the large tank side.
4 (Purge line)	From previous state. Depower (close) TMV-1 and depressurize Tank 2 by depowering (opening) VV-1. Confirm ambient pressure in Tank 2 using the pressure transducer. Close GBV-1 and power (open) TMV-1 to vent the pressurant gas line. Depower (close) TMV-1 and close COV-1 to prevent foreign particles from entering the system while not in use. Power (close) PV-1 open GBV-2 and set purge line pressure (low) in CGR-2. Perform the leak test with the soapy mixture on all components upstream of PV-1.
5 (Main propellant line)	From previous state. Confirm thruster inlet valve or connection to thruster closed. Power (close) PV-2, confirm TMV-2 closed (unpowered) and open COV-2. Depower (open) PV-1 and confirm pressurization of the main propellant line using the pressure transducer. Confirm no out-gassing at RV-1 or COV-2. Perform the leak test with the soapy mixture on all components between PV-1 and the connection to the thruster.
Stowing	From previous state. Power (close) PV-1 and depower (open) PV-2 to purge the main propellant line. After purging, close COV-2 to prevent foreign particles from entering the system while not in use. Finally, close GBV-2 and depower the valve control module. Confirm all connections to the outside (COV-1, FV-1, FV-2, COV-2) closed. The system is now ready for stowing.

7.4.2. Thruster test campaign

Definition of the test campaign is based on the duty cycle requirements seen in *MGT-098*, coming from ESA. A workflow for the test campaign as been generated as follows:

1. Quality check
2. Duty cycle characterization
3. Quality check
4. Cold start testing
5. Quality check
6. Steady-state firing
7. Quality check

The above-mentioned order of activities applies to the testing of a catalyst bed. Initially, a quality check is performed to confirm the catalyst bed is functional. The end of this quality check also serves as the moment for the decision to move forward with testing of that particular catalyst bed. After each testing activity, an additional quality check is performed, before moving forward to the next testing phase. This quality check serves to confirm the catalyst bed still functions correctly. For the testing of an alternative technology, quality checks may not be required between the different test activities, as no catalyst bed degradation can occur. Descriptions of the testing activities are provided below.

Quality check A number of thruster firings were considered necessary for a quality confirmation in the full operating range. This list of firings is found in Table 7.3. It shows that for each feed pressure level, two steady-state firings are performed. This is followed by two series of long pulses and finally, two series of short pulses. Throughout the quality check, it was assumed that for pulses with T_{on} 1 s or below, a pulse train of 50 firings is used, whereas for longer pulses a pulse train of 10 firings is used.

Table 7.3: Test plan for the purpose of a quality check

Feed pressure [bar]	$\mathbf{T_{on}}[\mathbf{s}]$	$\mathbf{T_{off}}[\mathbf{s}]$	Duty Cycle [%]	Pulse train
22 / 15 / 5.5	10	0	100	1
22 / 15 / 5.5	30	0	100	1
22 / 15 / 5.5	10	1	90.9	10
22 / 15 / 5.5	5	1	83.3	10
22 / 15 / 5.5	0.5	1	33.3	50
22 / 15 / 5.5	0.1	1.9	5	50

Characterization For the characterization of the catalyst bed or alternative technology, the full list of defined duty cycles mentioned in requirement *MGT-098* has to be completed. The characterization tests are mentioned in Tables 7.4 and 7.5. The standard pulse train length for pulses under with T_{on} 1 s or below is 50. For T_{on} 5 s, the pulse train length is 20 pulses and for T_{on} 10 s, the pulse train length is 10 pulses. In cases were T_{off} is high (low duty cycle), the amount of pulses in a pulse train is reduced, as long pulse trains would dramatically increase testing duration. For all tests where T_{on} is equal to 0.1 s, the on-time is further reduced, if possible, to the minimum value of T_{on}.

Table 7.4: Characterization tests overview

Feed pressure [bar]	$\mathbf{T_{on}}$[s]	$\mathbf{T_{off}}$[s]	**Duty Cycle [%]**	**Pulse train**	**Comments**
22 / 15 / 5.5	1	1	50	50	
22 / 15 / 5.5	0.5	0.5	50	50	
22 / 15 / 5.5	0.2	0.2	50	50	
22 / 15 / 5.5	0.1	0.1	50	50	T_{on} = min T_{on} if < 0.1
22 / 15 / 5.5	1	9	10	50	
22 / 15 / 5.5	0.5	4.5	10	50	
22 / 15 / 5.5	0.2	1.8	10	50	
22 / 15 / 5.5	0.1	0.9	10	50	T_{on} = min T_{on} if < 0.1
22 / 15 / 5.5	10	1.11	90	10	
22 / 15 / 5.5	5	0.56	90	20	
22 / 15 / 5.5	1	0.11	90	50	T_{on} = min T_{on} if < 0.1
22 / 15 / 5.5	0.1	99.9	0.1	10	T_{on} = min T_{on} if < 0.1
22 / 15 / 5.5	0.1	19.9	0.5	20	T_{on} = min T_{on} if < 0.1
22 / 15 / 5.5	0.1	9.9	1	50	T_{on} = min T_{on} if < 0.1
22 / 15 / 5.5	0.1	0.4	20	50	T_{on} = min T_{on} if < 0.1
22 / 15 / 5.5	0.1	0.15	40	50	T_{on} = min T_{on} if < 0.1
22 / 15 / 5.5	0.1	0.067	60	50	T_{on} = min T_{on} if < 0.1
22 / 15 / 5.5	0.2	199.8	0.1	5	
22 / 15 / 5.5	0.2	39.8	0.5	20	
22 / 15 / 5.5	0.2	19.8	1	20	
22 / 15 / 5.5	0.2	3.8	5	50	
22 / 15 / 5.5	0.2	0.8	20	50	
22 / 15 / 5.5	0.2	0.3	40	50	
22 / 15 / 5.5	0.2	0.133	60	50	
22 / 15 / 5.5	0.2	0.05	80	50	
22 / 15 / 5.5	0.5	499.5	0.1	5	
22 / 15 / 5.5	0.5	99.5	0.5	10	
22 / 15 / 5.5	0.5	49.5	1	20	
22 / 15 / 5.5	0.5	9.5	5	50	
22 / 15 / 5.5	0.5	2	20	50	
22 / 15 / 5.5	0.5	0.75	40	50	
22 / 15 / 5.5	0.5	0.33	60	50	
22 / 15 / 5.5	0.5	0.125	80	50	
22 / 15 / 5.5	0.5	0.056	90	50	
22 / 5.5	1	999	0.1	5	
22 / 5.5	1	199	0.5	5	
22 / 5.5	1	99	1	10	
22 / 5.5	1	19	5	20	
22 / 5.5	1	4	20	50	
22 / 5.5	1	1.5	40	50	
22 / 5.5	1	0.67	60	50	
22 / 5.5	1	0.25	80	50	
22 / 5.5	1	0.053	95	50	

Table 7.5: Characterization tests overview (continued)

Feedpressure [bar]	$\mathbf{T_{on}[s]}$	$\mathbf{T_{off}[s]}$	Duty Cycle [%]	Pulse train	Comments
22 / 5.5	5	995	0.5	5	
22 / 5.5	5	495	1	5	
22 / 5.5	5	95	5	10	
22 / 5.5	5	20	20	20	
22 / 5.5	5	7.5	40	20	
22 / 5.5	5	3.33	60	20	
22 / 5.5	5	1.25	80	20	
22 / 5.5	5	0.263	95	20	
22 / 5.5	5	0.0505	99	20	
22 / 15 / 5.5	10	990	1	5	
22 / 15 / 5.5	10	190	5	5	
22 / 15 / 5.5	10	40	20	10	
22 / 15 / 5.5	10	15	40	10	
22 / 15 / 5.5	10	6.67	60	10	
22 / 15 / 5.5	10	2.5	80	10	
22 / 15 / 5.5	10	0.526	95	10	
22 / 15 / 5.5	10	0.101	99	10	

Cold starts To confirm requirement *MGT-112*, 30 cold start firings will be performed. These will be 5 s steady-state firings. The time between these firings is required to be sufficient for all thruster components to cool down to the ambient temperature.

Steady-state firing The final test, prior to the final quality check, is the steady-state test. As per requirement *MGT-086*, the single burn capability is required to be at least 30 minutes. Therefore a 30 minute steady-state firings is performed.

7.5. Conclusion

The first step in the design of the test setup was the determination of the thruster orientation. A list of advantages and disadvantages was created, which led to the selection of a vertical down-firing orientation. Similarly to the propellant feed system, the test setup was designed using aluminium frame extrusions. It is approximately 1m tall and has a base of 0.4 by 0.4 m. This means the complete setup is easily transported between storage and the testing location. An assessment was performed on the requirement of a mass balance system for the thruster measurement. However, it was determined that, by putting a maximum mass requirement of 3 kg on the thruster and thruster subframe, a direct measurement is possible with sufficient accuracy. A pressure transducer and thermocouple are placed on the subframe, connected to the taps on the thruster nozzle module using a 1/16 inch Swagelok tube. This tube doubles as a thermal standoff for the pressure transducer. The length of this tube is easily adjustable, but the minimum length required should still be determined. Alternatively, an actively cooled pressure transducer could be used. Some components of the feed system are mounted on the test setup, rather than on the feed system assembly, in order to move the purging line as close as possible to the thruster inlet valve. In the current configuration, approximately 0.25 g of propellant could remain in the propellant line, after purging. This should be purged through the thruster, prior to disconnecting it from the propellant feed system. Finally, a test procedure was created, for leak testing of the thruster and propellant feed system, and a plan was made for the thruster test campaign. The test campaign was designed based on the duty cycles listed in requirement MGT-098. It consists of three main phases: Duty cycle characterization, cold start testing and a long steady-state firing. Prior to and after every phase, a quality check is performed. After the complete test campaign, all thruster components should be inspected and replaced if necessary.

8

Manufacturing

As part of the design process, an assessment was done of the manufacturing process for the thruster custom components. The designs created utilize commercially available components as much as possible, to minimize manufacturing cost and effort. Though some brackets and panels need to be produced for the feed system and test setup, the manufacturing of these components is not further discussed, as this concerns simple components, which may require some altering during the construction of both systems. However, several custom components are used in the thruster that have been designed in detail. The method of manufacturing for custom components is dependent on the manufacturing tools available. Some components may be easy to manufacture using traditional production methods, such as milling and lathing, whereas others may benefit from additive manufacturing solutions. The selection of the manufacturing method should therefore be performed by ESA, depending on the most convenient solution at the time of making the decision. To support this process, an overview of potential manufacturing solutions was generated for each custom component. Since the components will interface with the Swagelok tube fitting system, information regarding the dimensions has been collected and measured when required (8.1). A description of potential manufacturing methods for the thermal standoff flange was created (8.2), followed by the manufacturing of the thermal standoff screws (8.3). Some advice is given on the manufacturing of the injector module (8.4) and nozzle module (8.5) as well, which are considered more complex to produce.

8.1. Swagelok Interfaces

As was described in Section 3.3, the concept for the thruster design was to use a combination of off-the shelf Swagelok tube fittings [90], with custom fittings bodies. The complete design was made in Chapter 4, in which three custom bodies were created:

1. Inlet valve flange
2. Injector module
3. Nozzle module

Both the inlet valve flange and nozzle module use a single Swagelok interface, whereas the injector module uses two. On the inlet valve flange, a fitting body is created for a 1/16 inch Swagelok tube fitting. The nozzle module is the fitting body for a 1/2 inch Swagelok tube fitting. The injector module functions as a fitting body for both the aforementioned tube fittings, one on each side of the module. Therefore the exact measurements of both the 1/16 inch and 1/2 inch Swagelok tube fittings were to be identified.

8.1.1. Dimensions

The determination of dimensions of the Swagelok interface was done based a straight union fitting (Figure 8.1). Reference was made to the available documentation [90]. An overview of the published data is seen in Table 8.1.

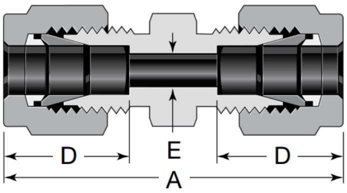

Figure 8.1: Swagelok straight union tube fitting [90]

Unfortunately, the documentation does not cover the complete descriptions of all dimensions. Since both 1/16 inch and 1/2 inch tube fittings were available at ESA/ESTEC, other dimensions were determined based on measurements using calipers.

Table 8.1: Published dimensions Swagelok interface (in inches) [90]

	Dimensions		
Tube OD	**A**	**D**	**E**
1/16	0.99	0.34	0.05
1/2	2.02	0.90	0.41

As is visible in Figure 8.1, an angled throat is used at the end of the fitting body. This angled section creates a compression fitting, by forcing the ferrule inward in the radial direction. Since the value of this angle was not found, a measurement was required. To determine the angle, custom angle gauges were created using a 3D printer 8.2. These were fitted into the fitting body until the correct angle was found. It is advised to check this angle with more accuracy, if possible, before manufacturing.

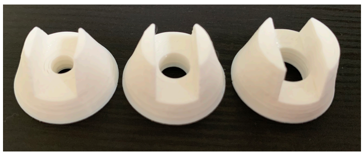

Figure 8.2: Custom 3D-printed angle gauges

8.1.2. Thread identification

For determination of thread dimensions, Swagelok has published a Thread Identification Guide [84]. This guide describes several steps for the identification of threads, though it uses a thread pitch gauge, which was not available. Therefore a different method was employed. From the specification [90] it is known that the Swagelok tube fittings use Unified Inch Screw Threads, which are specified in ASME B1.1 [5]. The thread outer diameter was measured for both tube fittings using calipers. With the data tables in ASME B1.1, now a limited number of threads is specified. To reduce the number of potential threads, the pitch was estimated using calipers. Using a 3D-printer, nuts and fitting bodies were created for the several potential thread options and interfaces with real Swagelok components (Figure 8.3), where only the correct thread was able to interface smoothly.

Figure 8.3: Confirming thread specifications with 3D printed interface (1/2 inch tube)

8.2. Thermal standoff flange

For the standoff flange, two main manufacturing methods are considered. The first method is using a lathe. The outer diameter of the standoff flange was determined by the outer diameter of the inlet valve at 33.8 mm. A conveniently available diameter for 316 stainless steel rods is 35 mm. An overview of the manufacturing steps is seen in Figure 8.4. After placing the rod into the lathe, the outer diameter of the flange is cut. The next step is to drill the center hole, which will hold the 1/16 inch capillary tube. Once this step is completed the smaller cylinder is cut to the outer diameter of the Swagelok interface thread. The diameter of the top millimeter of this smaller cylinder is reduced slightly further, according to the technical drawings. At this point, the angled inversion is cut into the end of the center hole. Alternatively, this step can be performed directly after the center hole is drilled. After these steps are completed, the material directly behind the flange is removed until the flange is cut off from the main rod. To finish the part, the four mounting holes are drilled and the Swagelok compatible thread is created using the correct threading die. If a multi-axis lathe is used it may be possible to create the mounting holes with the lathe. Additionally, when a Computer Numerical Controlled (CNC) lathe is used, it may be possible to create the thread using the lathe. The flat side of the flange may require some post-processing to create a smooth surface, to guarantee a proper seal with the inlet valve.

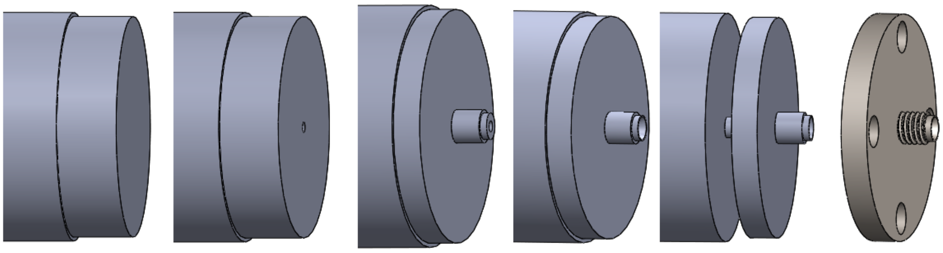

Figure 8.4: Progression of steps for manufacturing of the thermal standoff flange on a lathe

Alternatively, a 316 stainless steel block can be used for milling. Similar to the case using a lathe, the thread is created using a threading die. Due to the small dimensions of the components, a CNC mill is recommended. Additive manufacturing is another solution, though traditional machining of this component should not provide many difficulties. It is advised to make a decision based on the availability of tools and costs.

8.3. Standoff screws

Machining of the standoff screws is best done on a lathe (Figure 8.5). A MACOR rod with a diameter of 6 mm is conveniently found. The diameter at the end of the rod is reduced to the outer diameter of an M4 thread, over the length of the MACOR screw. While the rod is still mounted in the lathe, a regular die is used to create the M4 thread on the rod. At this point the screw is cut off in a similar way as was done for the standoff flange, leaving a portion of the full diameter rod. This last part functions as the screw head. Creating a slot in the head can be done in several ways. An example is by moving the cross slide of the lathe with a cutting tool across the head of the screw manually, while the lathe is not rotating.

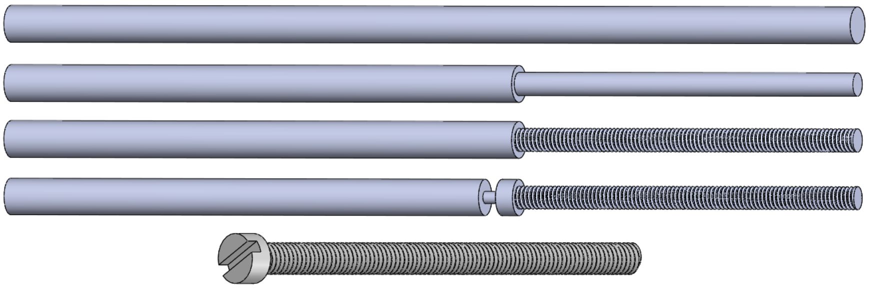

Figure 8.5: Manufacturing steps for the MACOR screws using a lathe

8.4. Injector module

Due to the relatively complex geometry of the injector module, additive manufacturing may provide a good solution for this component. Alternatively, a combination of milling and lathing may be required to produce the component with more traditional methods. A manufacturing concept is described following the steps displayed in Figure 8.6. The most convenient way to start the manufacturing process is by milling. The project can either be started with a 70 mm diameter, 316 stainless steel disk, with a thickness of at least 35 mm. Alternatively, a block with a minimum base of 70 by 70 mm and a thickness of 35 mm can be used. In this case, the circular shape can be created with the mill. The mill should be capable of drilling 35 mm down while remaining completely clear of the project (except for the drill bit). The first step in the manufacturing process is drilling a hole, all the way through, that fits the 1/16 inch capillary tube. Secondly, the material is removed on the outside of the Swagelok compatible fitting body. This is followed by the removal of material to create the hexagonal shape that will assist the Swagelok integration process. On top of the smaller cylinder, the material is removed to create the cylindrical body that holds the capillary tube, down to the end of the Swagelok compatible fitting body. The material within the fitting body is now removed to completely the capillary tube housing and create the 1/2 inch tube fitting body. Finally, the diagonal throat is created to finish the fitting body shape. At this point, the test setup mounting holes as well as the thermal standoff mounting holes are created. The injector module can now be removed from the mill and mounted in a lathe to manufacture the upstream side. In the lathe, the material is removed from the outside towards the center of the circular shape, to create the Swagelok compatible fitting body for the capillary tube. This is followed by the creation of the diagonal throat. To finish the injector module, the correct threads are created on both Swagelok compatible fitting bodies, using the appropriate thread die.

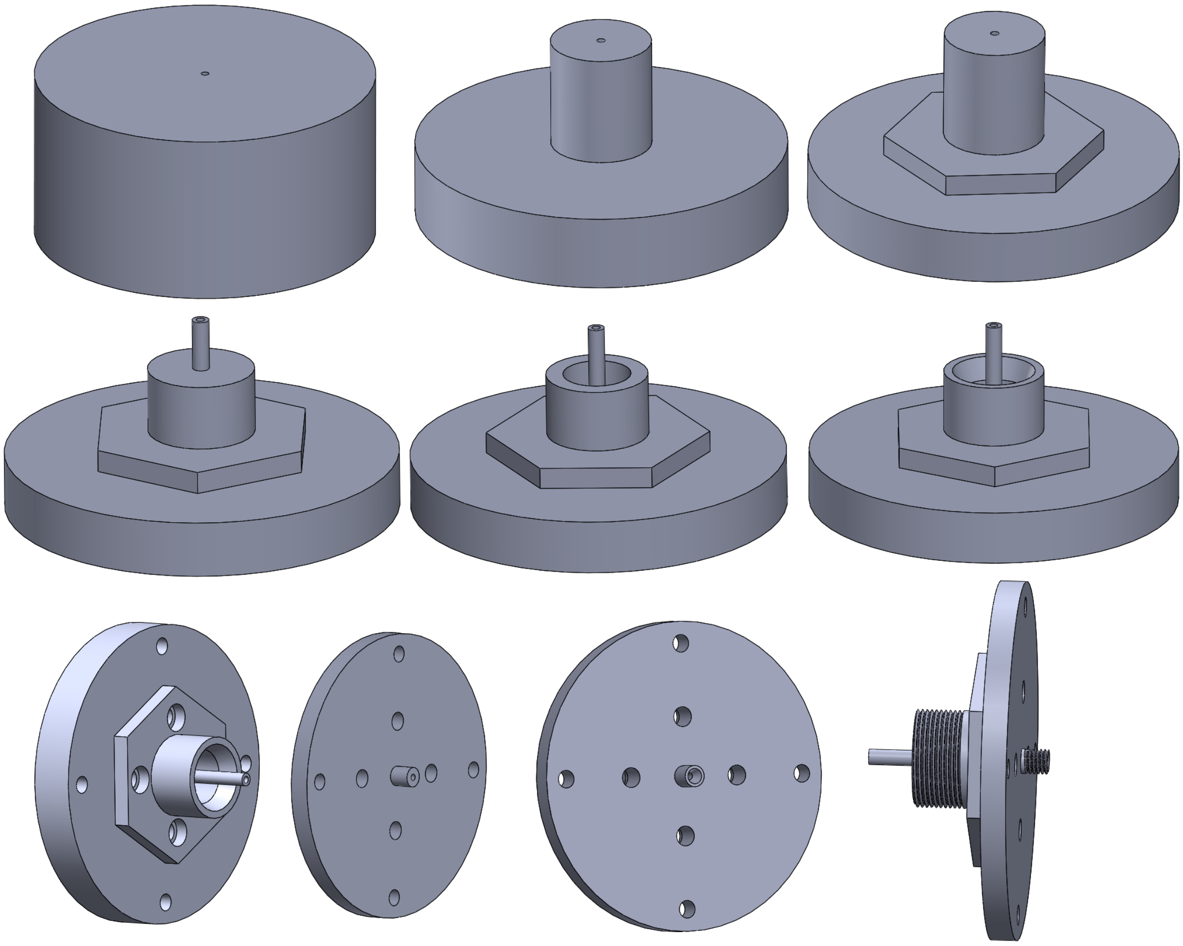

Figure 8.6: Manufacturing steps for the injector module

8.5. Nozzle module

Similarly to the manufacturing of the injector module, additive manufacturing solutions may prove useful for the production of the nozzle module. Though it can be done using a combination of lathing and milling, some difficulties may occur due to the small scale, especially in the converging area and nozzle throat. Nevertheless, because of the small dimensions, a CNC version of these tools is advised. An overview of the machining steps is seen in Figure 8.7. Should these methods be attempted, it is best done by choosing a hexagonal rod to start with and machining the upstream part down to a cylinder with the diameter equal to the outer diameter of the thread for the Swagelok interface. A suitable threading die is used to create the Swagelok interface thread on the outside of the cylinder. The next step is to remove the material in the cylinder. First, the main section that holds the tube is removed, then the angled inversion for the ferrules is created. This is followed by the removal of material at a diameter equal to the tube inner diameter, which creates the ledge that seats the tube. Another diameter reduction is used to create the ledge that seats the downstream catalyst bed retainer. This is followed by the removal of a section with a smaller diameter, which leaves some material in place that will later be turned into the contraction curve. After this section, the material is machined down at an angle, until a diameter slightly smaller than the final throat diameter is obtained. At this point, the holes for the temperature and pressure taps can be drilled in the sides and the recesses for the retainer tabs can be created. The latter can be done for example by using a mill or simply sliding the lathe cutting tool manually, while the lathe is not rotating. Alternatively, a drilling tool could be used on a lathe. The nozzle module can now be cut off of the hexagonal rod and mounted in reverse direction on the lathe. Now, the diverging section of the nozzle is created, including the nozzle throat. The curve of the nozzle throat can be created in post-processing of the component. Due to the small dimensions of the component, it is advised CNC versions of the lathe or mill are used or an additive manufacturing solution is used.

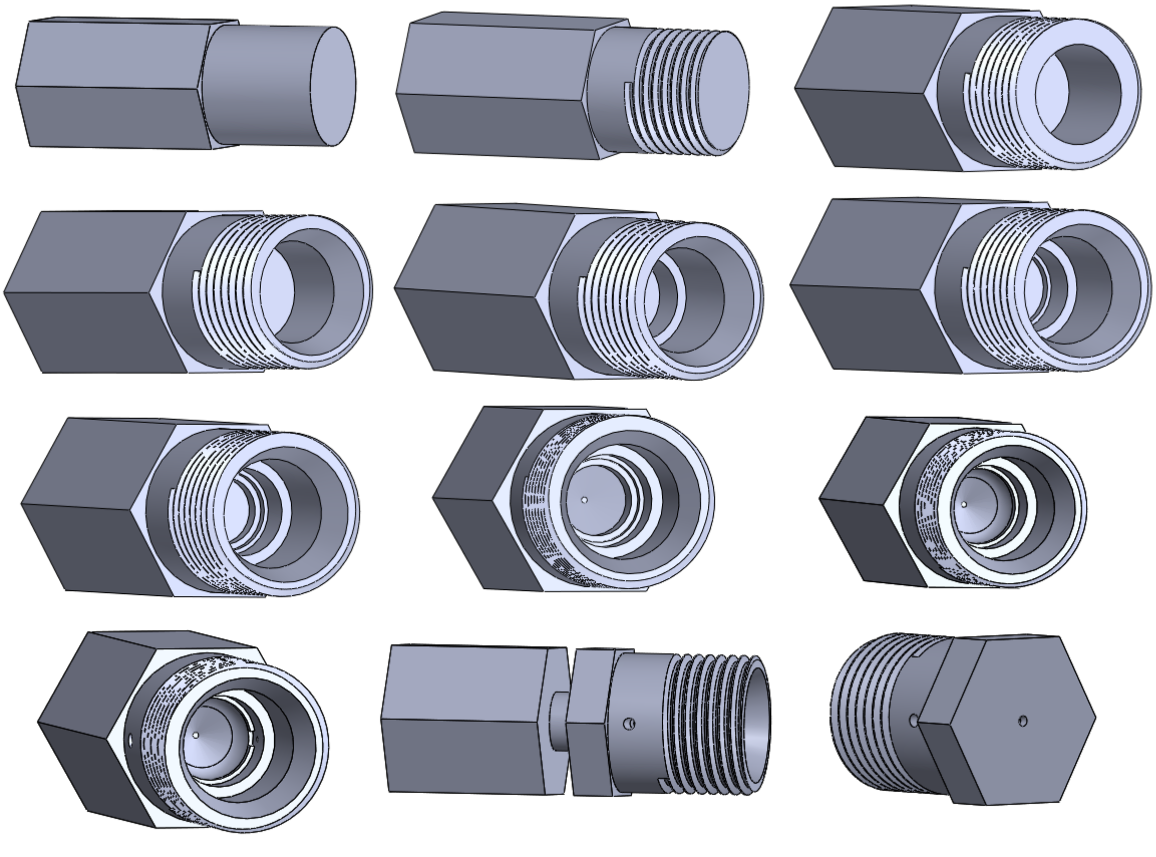

Figure 8.7: Manufacturing steps for lathing/milling of the nozzle module

8.6. Conclusion

Since the design is based on the use of commercially available Swagelok tube fittings, with custom fitting bodies, an overview was created of the dimensions of the available tube fittings. Unfortunately, not all dimensions have been published by Swagelok. The missing information was determined using tube fittings available at ESA utilizing caliper measurements, thread definitions from ASME B1.1 [5] and custom 3D-printed gauges. The missing dimensions have not been published in this report, as it is unknown whether this information is proprietary. It is advised that the throat angle in the tube fitting is confirmed using appropriate tools before manufacturing. Manufacturing guides using lathing and milling were created for the thermal standoff flange and threaded rods, as well as the injector and nozzle module. Due to the small dimensions, a CNC version of these machines is advised in the case of the injector and nozzle. Alternatively, additive manufacturing methods could be explored.

9

Conclusion

This work describes the design of a modular one Newton hydrogen peroxide thruster, including feed system and test setup. The design was motivated by increased interest in green propellants after the addition of hydrazine to the list of substances of very high concern in the REACH framework. The thruster is capable of testing different catalyst beds using different concentrations of hydrogen peroxide and a variety of initial conditions. Additionally, concepts have been generated for the testing of alternatives to catalyst beds. To support the design, the project goals were defined in the introduction of this thesis (9.1). Throughout the work, some issues were encountered that require attention before employing the designs. Therefore, some recommendations have been made for future activities (9.2).

9.1. Discussion

The discussion of the results of this work is performed by referring back to the goals set in the introduction of this thesis (Section 1). Each of the goals is listed below and followed by a description of the results.

1. **Create a mathematical model of the decomposition of hydrogen peroxide**
   Using Python programming, a mathematical code was developed to model the decomposition of hydrogen peroxide in catalyst beds. Initially, an attempt was made to base the model on existing models for hydrogen peroxide, but the complexity of these models proved to be out of the scope of this work. Therefore, a simplified model was created. Parts of the simplified model are based on the lessons learned from the previous attempts with the more complex models. The resulting model is successful in simulating the decomposition of hydrogen peroxide, though requires calibration with test results to provide absolute results. By varying several parameters, similar results were found to an existing model. The shape of the temperature profile from the model was used as input for the thermal assessment of the thruster.

2. **List the thruster requirements and generate a concept for the thruster**
   A requirement specification document was generated in cooperation with ESA. An overview was created of the key requirements, from which a performance assessment was performed. This resulted in an overview of the thrust, specific impulse and mass flow rate requirements over the complete operating range. A concept was created for the modular design of the thruster, after which a commercially available solution was found in Swagelok tube fittings, by creating custom fitting bodies capable of interfacing with the Swagelok components. Using a thermal assessment, the suitability of this solution was confirmed.

3. **Create the baseline design for use with catalyst beds, including thermal and structural analysis**
   The baseline design was created component by component. The inlet valve was already selected in the preparation phase of the design. The decomposition chamber diameter was chosen by combining catalyst bed loading data from literature with available tube diameters at Swagelok. This resulted in the selection of the 1/2 inch Swagelok tube fittings as the basis for the thruster

design. A thermal standoff was created to keep the maximum temperature in the inlet valve below 50 $°C$. This was done with the help of a thermal model in EcosimPro. An assessment was performed of the thermal stresses in the capillary tube, which resulted in the definition of a shape for the bending in the capillary tube. An injector module was created that attaches to the thermal standoff and interfaces with the test setup. The capillary tube and decomposition chamber are connected to this module using a Swagelok compatible interface. Similarly, a nozzle module was created that interfaces with the decomposition chamber using a Swagelok compatible interface. The design of catalyst bed retainers was included as well. An assessment of the pressure drop budget was completed for each thruster component.

4. **Generate a concept for the testing and integration of alternatives to catalyst beds**
   Three technologies were discussed that could provide an alternative to catalyst beds: thermal decomposition, spark initiated decomposition and laser initiated decomposition. For each of these technologies, a testing concept was created to assess the feasibility. Additionally, a concept level design was created for the integration of each technology on the thruster.

5. **Create the design of a propellant feed system**
   A design was created for a propellant feed system using two propellant tanks. The response time of the mass flow sensor is too high to be capable of measuring mass flow rates during pulsed mode operation. Therefore, one tank is used for steady-state operation and a second, smaller, tank for pulsed mode operation. The mass of the small tank will be weighed on an accurate scale before and after a pulse train, to determine the mass of the propellant used per pulse. The feed system is mounted in a frame made of aluminium extrusion allowing easy transport and deployment. The architecture of the feed system uses several actuated valves for safe pressurized operation. The configuration of these valves was chosen such, that the system can always be returned to a safe state.

6. **Create the design of a test setup and test plan**
   The test setup was designed in a similar way to the propellant feed system, utilizing a frame using aluminium extrusions. It was decided to place the thruster in a vertical, down-firing position, using a direct measurement of the thrust level. Additionally, a plan was created for leak testing of the propellant feed system and the thruster. Finally, a plan was made for the thruster test campaign, which is divided into three main parts: Duty cycle characterization, cold start testing and a long steady-state firing. Before and after each phase a quality check is performed through a number of test firings.

7. **Generate manufacturing guidelines**
   Since the thruster design uses custom fitting bodies, compatible with Swagelok tube fittings, an overview was made of the Swagelok tube fitting dimensions. Not all data was published by Swagelok. Therefore, some measurements were performed on tube fittings available at ESA. For each of the custom components in the thruster design, a manufacturing plan was using lathing, milling or a combination thereof.

9.2. Recommendations

Throughout the thesis, several topics have been highlighted that could be improved or require more work. Prior to employing the decomposition model for prediction of catalyst bed performance a number of improvements should be considered. First of all, it was found that the temperature model can cause errors in some cases, especially when the propellant inlet temperature is varied. Therefore, it is recommended that some attempts are made to either improve the temperature model or repair potential flaws. Additionally, at this stage, the model can only be used to compare the performance effects of varying conditions such as the feed pressure and mass flow rate on a single catalyst bed. Before using it for the prediction of more absolute values, the model should be calibrated using test data.

Because of the simple design of the decomposition chamber, the thruster provides the opportunity for convenient integration of alternative technologies for testing. For the testing of the thermal decomposition concept, a significant amount of research already exists. Due to the convenience, it is recommended that a thermal decomposition concept is integrated directly onto the thruster without doing more laboratory testing. Publicly available testing data should be used for the power requirement assessment. Since no proof currently exists that the decomposition of hydrogen peroxide in a thruster can be started using a spark, it is recommended that this technology concept is tested in a laboratory setting first. Finally, for the laser decomposition concept, the advice is given to test in a laboratory setting if practical. This concept is considered likely to work, which means alternatively it could be directly integrated onto the thruster. If this path is chosen, it is recommended to perform additional literature research to support the estimation of laser settings required.

In the case of the propellant feed system, a mass flow sensor was used with a response time of 200 ms. This was the cause for the design of a two-tank architecture to accurately weigh the propellant used in pulse mode. It is recommended to spend some extra time researching suitable mass flow sensors with better response times. The minimum ON-time of the thruster is set at 50 ms, if a mass flow sensor can be found with a significantly lower response time, a more simple, single-tank feed system could be employed.

The design of the test setup includes a pressure transducer and thermocouple, attached to the nozzle module of the thruster through a tube. In the case of the pressure transducer, the tube functions as a thermal standoff as the hot gas temperature is too high for the pressure transducer operating range. The minimum required length of this tube has not yet been determined. This should be done prior to operation. Alternatively, an actively cooled pressure transducer could be used.

Bibliography

[1] European Space Agency. Considering hydrazine-free satellite propulsion, . URL `https://www.esa.int/Our_Activities/Operations/Space_Safety_Security/Clean_Space/Considering_hydrazine-free_satellite_propulsion`. Last Accessed: 27-08-2019.

[2] European Space Agency. Green hydrogen peroxide (H2O2) monopropellant with advanced catalytics beds, . URL `http://www.esa.int/About_Us/Business_with_ESA/Small_and_Medium_Sized_Enterprises/SME_Achievements/Green_Hydrogen_Peroxide_H2O2_monopropellant_with_advanced_catalytic_beds`. Last Accessed: 27-08-2019.

[3] R. Amri, D. Gibbon, and T. Rezoug. The design, development and test of one newton hydrogen peroxide monopropellant thruster. *Aerospace Science and Technology*, 25(1):266–272, March 2013. doi: 10.1016/j.ast.2012.02.002.

[4] ASME. *Process Piping (ASME B31.3 - 2014)*. The American Society of Mechanical Engineers (ASME), 2015.

[5] ASME. *Unified Inch Screw Threads (UN, UNR, and UNJ Thread Forms)*. The American Society of Mechanical Engineers (ASME), 2020.

[6] British Stainless Steel Association. Elevated temperature physical properties of stainless steels. URL `https://www.bssa.org.uk/topics.php?article=139`. Last Accessed: 27-08-2019.

[7] S. U. Bhave and P. Sonawane. Analysis of Pump Piping Based on Piping Configurations. *International Journal for Innovative Research in Science & Technology*, 2(9), 2016.

[8] V. Bombelli, D. Simon, J. Moerel, and T. Marée. Economic Benefits of the Use of Non-Toxic Mono-Propellants for Spacecraft Applications. In *39th AIAA/ASME/SAE/ASEE Joint Propulsion Conference and Exhibit*, Joint Propulsion Conferences. American Institute of Aeronautics and Astronautics, July 2003. doi: 10.2514/6.2003-4783.

[9] G. Brenn, L. J. Deviprasath, F. Durst, and C. Fink. Evaporation of acoustically levitated multi-component liquid droplets. *International Journal of Heat and Mass Transfer*, 50(25):5073–5086, December 2007. doi: 10.1016/j.ijheatmasstransfer.2007.07.036.

[10] Bronkhorst. Coriolis mass flow measuring principle, . URL `https://www.bronkhorst.com/int/service-support/technologies/coriolis-mass-flow-measuring-principle/`. Last Accessed: 27-08-2019.

[11] Bronkhorst. MINI CORI-FLOW™ M14V14I, . URL `https://bronkhorst.com/en-us/products-en/liquid-flow/mini-cori-flow/m14v14i/`. Last Accessed: 27-08-2019.

[12] Bronkhorst. Thermal Mass flow sensor for liquids, . URL `https://bronkhorst.com/en-us/service-support/technologies/thermal-mass-flow-sensor-for-liquids/`. Last Accessed: 27-08-2019.

[13] M. Börner, C. Manfletti, G. Kroupa, and M. Oschwald. Laser ignition of an experimental combustion chamber with a multi-injector configuration at low pressure conditions. *CEAS Space Journal*, 9(3):299–311, September 2017. doi: 10.1007/s12567-017-0161-9.

[14] A. Cervone, L. Torre, L. d'Agostino, A. Musker, G. Roberts, C. Bramanti, and G. Saccoccia. Development of Hydrogen Peroxide Monopropellant Rockets. In *42nd AIAA/ASME/SAE/ASEE Joint Propulsion Conference & Exhibit*, Joint Propulsion Conferences. American Institute of Aeronautics and Astronautics, July 2006. doi: 10.2514/6.2006-5239.

[15] Rocketdyne Chemical and Material Sciences Department (Research Division). *Hydrogen Peroxide Handbook*. Air Force Rocket Propulsion Laboratory Research and Technology Division Edwards Air Force Base, California, Air Force Systems Command, United States Air Force, July 1967.

[16] MW Kellogg Company. *Design of Piping Systems*. Wiley-Interscience, revised second edition, 1976.

[17] J.W. Cornellise, H.F.R. Shoyer, and K.F. Wakker. *Rocket Propulsion and Spaceflight*. Pitman Publishing Ltd., London, 1979.

[18] S. Cortés Borgmeyer. 1N, 20N, 400N and heritage thruster - chemical monopropellant thruster family. URL `https://www.space-propulsion.com/brochures/hydrazine-thrusters/hydrazine-thrusters.pdf`. Last Accessed: 27-08-2019.

[19] Danfoss. Direct-operated 2/2-way solenoid valves Type EV210B and EV210BW. URL `https://assets.danfoss.com/documents/DOC308544329091/DOC308544329091.pdf`. Last Accessed: 27-08-2019.

[20] D. Davis, L. Dee, B. Greene, S. Hornung, M. McClure, and K. Rathgeber. Fire, Explosion, Compatibility and Safety Hazards of Hydrogen Peroxide. Technical report, January 2005. URL `https://ntrs.nasa.gov/search.jsp?R=20100040598`.

[21] S. Dolci, D. Belli Dell'Amico, A. Pasini, L. Torre, G. Pace, and D. Valentini. Platinum Catalysts Development for 98% Hydrogen Peroxide Decomposition in Pulsed Monopropellant Thrusters. *Journal of Propulsion and Power*, 31(4):1204–1216, 2015. doi: 10.2514/1.B35590.

[22] DuPont. DuPont Kalrez Chemical Resistance and Fluid Compatibility,Including All Chemicals Under the Clean Air Act, . URL `http://www.dymseal.com/pdf/General_Chemical_Resistance.pdf`. Last Accessed: 27-08-2019.

[23] DuPont. Teflon PTFE Properties Handbook, . URL `http://www.rjchase.com/ptfe_handbook.pdf`. Last Accessed: 27-08-2019.

[24] Emerson. Material Selection and Compatibility Considerations for Rosemount Pressure Transmitters, September 2018. URL `https://www.emerson.com/documents/automation/technical-note-material-selection-considerations-for-pressure-transmitters-rosemount-en-77770.pdf`. Last Accessed: 27-08-2019.

[25] H. S. Fogler. *Elements of chemical reaction engineering*. Upper Saddle River, N.J.: Prentice Hall PTR, third edition, 1999.

[26] Keller AG für Druckmesstechnik. Piezoresistive Pressure Transmitters For Industrial Applications - Series 21Y, . URL `https://keller-druck.com/en/products/pressure-transmitters/standard-pressure-transmitters/series-21y`. Last Accessed: 27-08-2019.

[27] Keller AG für Druckmesstechnik. Ultra-Fast and Precise Pressure Transmitters - Series M8coolHB, . URL `https://keller-druck.com/en/products/pressure-transmitters/high-temperature-pressure-transmitters/series-m8coolhb`. Last Accessed: 27-08-2019.

[28] R. Gentle, P. Edwards, and B. Bolton. *Mechanical Engineering Systems*. Butterworth-Heinemann, Oxford, United Kingdom, first edition, 2001.

[29] W.M. Haynes. *CRC handbook of chemistry and physics: A ready-reference book of chemical and physical data.* CRC Press, Boca Raton, 97 edition, 2016.

[30] Y. Ho, T. K. Chu, and American Iron and Steel Institute. Electrical Resistivity and Thermal Conductivity of Nine Selected AISI stainless Steels, September 1977.

[31] H.C. Hottel and R.B. Egbert. Radiant heat transmission from water vapor. *Transactions of the American Institute of Chemical Engineers*, 38(3):0531–0568, 1942.

[32] D. K. Huzel and D. H. Huang. *Design of Liquid Propellant Rocket Engines*. Scientific and Technical Information Office, National Aeronautics and Space Administration, 1967.

[33] M. Höpfner, M. Milz, S. Buehler, J. Orphal, and G. Stiller. The natural greenhouse effect of atmospheric oxygen (O2) and nitrogen (N2). *Geophysical Research Letters*, 39(10), 2012. doi: 10.1029/2012GL051409.

[34] Idelchik. *Handbook of Hydraulic Resistance (translated from Russian)*. Israel Program for Scientific Translations, 1966.

[35] F. P. Incropera. *Fundamentals of heat and mass transfer*. Wiley, Hoboken, N.J, 6th edition, 2007.

[36] American Iron and Steel Institute. High-temperature characteristics of stainless steels. URL `https://www.nickelinstitute.org/media/1699/high_temperaturecharacteristicsofstainlesssteel_9004_.pdf`. Last Accessed: 27-08-2019.

[37] VICI AG International. PEEK and Polymer Chemical Resistance. URL `https://sisw.cz/cz/downloads/polymer_resistance.pdf`.

[38] IPEX. EPDM & FKM Chemical Resistance Guide. 2009. URL `https://www.ipexna.com/media/1663/epdm-fkm-chemical-resistance-guide.pdf`. Last Accessed: 27-08-2019.

[39] GSR Ventiltechnik GmbH & Co. KG. RRV - Rapid Reaction Valve.

[40] GSR Ventiltechnik GmbH & Co. KG. RRV 95 - Rapid Reaction Valve, 2011.

[41] R. Koopmans, J. Shrimpton, G. Roberts, and A. Musker. A one-dimensional multicomponent two-fluid model of a reacting packed bed including mass, momentum and energy interphase transfer. *International Journal of Multiphase Flow*, 57:10–28, December 2013. doi: https://doi.org/10.1016/j.ijmultiphaseflow.2013.06.005.

[42] G. Kroupa and M. Börner. A miniaturized high energy laser for ignition of rocket engines. In *International Conference on Space Optics — ICSO 2018*. International Society for Optics and Photonics, July 2019. doi: 10.1117/12.2536117.

[43] K. Kuriki, H. Takegahara, J. Yokote, A. Kakamiand, and T. Tachibana. Feasibility Study of Plasma Chemical Thruster. In *Proceedings of the 30th International Electric Propulsion Conference*, Florence, Italy, September 2007.

[44] P.E. L.C. Peng. Quick Check on Piping Flexibility.

[45] B. Leckner. Spectral and total emissivity of water vapor and carbon dioxide. *Combustion and Flame*, 19(1):33–48, August 1972. doi: 10.1016/S0010-2180(72)80084-1.

[46] Calex Electronics Limited. Emissivity Table. URL `https://www.calex.co.uk/site/wp-content/uploads/2015/07/emissivity-tables.pdf`. Last Accessed: 27-08-2019.

[47] Solenoid Valves Ltd. 2/2 Stainless 1/8 – 1/4 Normally Closed 2 Way Direct Acting0 – 200 Bar Type WH, . URL `https://www.solenoid-valve.world/era-sib/18-14-stainless-solenoid-valve-0-200-bar-22-nclosed-wh`. Last Accessed: 17-08-2020.

[48] Solenoid Valves Ltd. 2/2 Stainless 1/8 – 1/4 Normally Closed 2 Way Direct Acting 0 – 200 Bar Type WPH, . URL `https://www.solenoid-valve.world/assets/generated/images/wph.pdf`. Last Accessed: 17-08-2020.

[49] Solenoid Valves Ltd. 2/2 Stainless 1/8 – 1/4 Normally Closed 2 Way Direct/Pilot Acting 500 Bar Type EN520, . URL `https://www.solenoid-valve.world/assets/generated/uploads/media_850.pdf`. Last Accessed: 17-08-2020.

[50] Solenoid Valves Ltd. 2/2 Stainless 1/8 – 1/4 Normally Closed 2 Way Direct Acting 0 – 150 Bar Type ADS8000, . URL `https://www.solenoid-valve.world/assets/generated/uploads/media_1862.pdf`. Last Accessed: 17-08-2020.

[51] A.S. Maas. *AE4S20 Sattelite Thermal Control - Lecture Notes*. Faculty of Aerospace Engineering at TU Delft. Issue 5.2.

[52] I. F. Macdonald, M. S. El-Sayed, K. Mow, and F. A. L. Dullien. Flow through Porous Media-the Ergun Equation Revisited. *Industrial & Engineering Chemistry Fundamentals*, 18(3):199–208, August 1979. doi: 10.1021/i160071a001.

[53] F. F. Maia, L.H. Gouvea, L.G.F Pereira, R. Vieira, and F. S. Costa. Development and Optimization of a Catalytic Thruster for Hydrogen Peroxide Decomposition. *Journal of Aerospace Technology and Management*, 6(1):61–67, February 2014.

[54] S. L. Manatt and M. R. R. Manatt. On the Analyses of Mixture Vapor Pressure Data: The Hydrogen Peroxide/Water System and Its Excess Thermodynamic Functions. *Chemistry - A European Journal*, 10(24):6540–6557, December 2004. doi: 10.1002/chem.200400104.

[55] Corning Incorporated Lighting & Materials. MACOR. URL `https://psec.uchicago.edu/ceramics/MACOR%20Data%20Sheet.pdf`. Last Accessed: 27-08-2019.

[56] B. J. McBride, S. Gordon, and M. A. Reno. Coefficients for Calculating Thermodynamic and Transport Properties of Individual Species, 1993.

[57] B. J. McBride, M. J. Zehe, and S. Gordon. NASA Glenn Coefficients for Calculating Thermodynamic Properties of Individual Species. page 297, 2002.

[58] L. Mezyk, Z. Gut, P. Paszkiewicz, P. Wolanski, and G. Rarata. Possibility of using thermal decomposition of hydrogen peroxide for low thrust propulsion system application. *Proceedings of the 7th European Conference for Aeronautics and Space Sciences. Milano, Italy, 3-6 july 2017*, 2017. doi: 10.13009/eucass2017-626.

[59] M. F. Modest. *Radiative Heat Transfer*. Elsevier, 2013. ISBN 978-0-12-386944-9. doi: 10.1016/C2010-0-65874-3.

[60] M. Negri, M. Wilhelm, C. Hendrich, N. Wingborg, L. Gediminas, L. Adelöw, C. Maleix, P. Chabernaud, R. Brahmi, R. Beauchet, Y. Batonneau, C. Kappenstein, R. Koopmans, S. Schuh, T. Bartok, C. Scharlemann, U. Gotzig, and M. Schwentenwein. New technologies for ammonium dinitramide based monopropellant thrusters – The project RHEFORM. *Acta Astronautica*, 143: 105–117, February 2018. doi: https://doi.org/10.1016/j.actaastro.2017.11.016.

[61] National Institute of Standards and Technology. NIST Chemistry Webbook. URL `https://webbook.nist.gov/chemistry/`. Last Accessed: 27-08-2019.

[62] M. Palmer, G. Roberts, and A. Musker. Design, Build and Test of a 20 N Hydrogen Peroxide Monopropellant Thruster. In *47th AIAA/ASME/SAE/ASEE Joint Propulsion Conference & Exhibit*. American Institute of Aeronautics and Astronautics. doi: 10.2514/6.2011-5697.

[63] Parker. Fast Switching Valve, . URL `https://www.parker.com/parkerimages/English%20Catalogues/8674UK.pdf`. Last Accessed: 27-08-2019.

[64] Parker. Pulse Valves, . URL `https://ph.parker.com/us/12051/en/pulse-valves-miniature-high-speed-high-vacuum-dispense-valve`. Last Accessed: 27-08-2019.

[65] A. Pasini, L. Torre, L. Romeo, A. Cervone, L. d'Agostino, A. Musker, and G. Saccoccia. Experimental Characterization of a 5 N Hydrogen Peroxide Monopropellant Thruster Prototype. In *43rd AIAA/ASME/SAE/ASEE Joint Propulsion Conference & Exhibit*. American Institute of Aeronautics and Astronautics. doi: 10.2514/6.2007-5465.

[66] A. Pasini, L. Torre, L. Romeo, A. Cervone, and L. D'Agostino. Testing and Characterization of a Hydrogen Peroxide Monopropellant Thruster. *Journal of Propulsion and Power*, 24(3):507–515, May 2008. doi: 10.2514/1.33121.

[67] A. Pasini, G. Pace, and D. Valentini. Design and Testing of a 98% H2O2 Pulsed Thruster. 2016.

[68] John H. Perry. Chemical engineers' handbook. *Journal of Chemical Education*, 27(9):533, September 1950. ISSN 0021-9584. doi: 10.1021/ed027p533.1. URL `https://doi.org/10.1021/ed027p533.1`. Publisher: American Chemical Society.

[69] Victrex plc. Chemical Resistance VICTREX PEEK Polymers. URL `https://www.victrex.com/~/media/literature/ko/chemical-resistance-brochure----4_4.pdf`.

[70] B. E. Poling, J. M. Prausnitz, and J. P. O'Connell. *The properties of gases and liquids*. McGraw-Hill, New York, 5th ed edition, 2001. ISBN 978-0-07-011682-5.

[71] J. Quesada Mañas, P. Gurumallappa, and B.V.S. Jyoti. Hypergolicity and Ignition Delay Study of Green Bipropellant System without Catalyst. In *Proceedings of the 1st Aerospace Europe Conference (AEC2020)*, Bordeaux, France, February 2020.

[72] VICI Jour Research. PEEK and Polymer Chemical Resistance. page 2. URL `https://www.vici-jour.com/support/resistance.php`. Last Accessed: 27-08-2019.

[73] C. N. Satterfield, G. M. Kavanagh, and H. Resnick. Explosive Characteristics of Hydrogen Peroxide Vapor. *Industrial & Engineering Chemistry*, 43(11):2507–2514, November 1951. doi: 10.1021/ie50503a034.

[74] C. N. Satterfield, P. J. Ceccotti, and A. H. R. Feldbrugge. Ignition Limits of Hydrogen Peroxide Vapor. *Industrial & Engineering Chemistry*, 47(5):1040–1043, May 1955. doi: 10.1021/ie50545a046.

[75] C. N. Satterfield, F. Feakes, and N. Sekler. Ignition Limits of Hydrogen Peroxide Vapor at Pressures above Atmospheric. *Journal of Chemical & Engineering Data*, 4(2):131–133, April 1959. doi: 10.1021/je60002a007.

[76] E.W. Schmidt. *Hydrazine and Its Derivatives: Preparation, Properties, Applications*. Hydrazine and Its Derivatives: Preparation, Properties, Applications. Wiley-Interscience, 2001. ISBN 978-0-471-41553-4. Issue: v. 2.

[77] W. C. Schumb, C. N. Satterfield, and R. L. Wentworth. *Hydrogen Peroxide*. New York, Reinhold Pub. Corp., 1955.

[78] M. J. Sidi. *Spacecraft Dynamics and Control: A Practical Engineering Approach*. Cambridge Aerospace Series. Cambridge University Press, Cambridge, 1997. doi: 10.1017/CBO9780511815652.

[79] V. V. Sorokin. Calculation of two-phase adiabatic flow in a pebble bed. *High Temperature*, 46(3): 432–434, June 2008. doi: 10.1134/S0018151X08030231.

[80] IS MED Specialties. Hydrogen Peroxide Material Compatibility Chart. URL `https://www.industrialspec.com/images/files/hydrogen-peroxide-material-compatibility-chart-from-ism.pdf`. Last Accessed: 27-08-2019.

[81] R. A. Spores. GPIM AF-M315E Propulsion System. In *51st AIAA/SAE/ASEE Joint Propulsion Conference*, Orlando, FL, July 2015. American Institute of Aeronautics and Astronautics. doi: 10.2514/6.2015-3753.

[82] G.P. Sutton and O. Biblarz. *Rocket Propulsion Elements, Ninth Edition*. Wiley, 2017.

[83] Swagelok. Product Catalog. URL `https://www.swagelok.com/en/toolbox/product-catalog`. Last Accessed: 27-08-2019.

[84] Swagelok. Thread and End Connection Identification Guide, May 2012. URL `https://www.swagelok.com/downloads/webcatalogs/en/MS-13-77.pdf`. Last Accessed: 27-08-2019.

[85] Swagelok. High-Pressure, Pneumatically Actuated Bellows-Sealed Valves, 2014. URL `https://www.swagelok.com/downloads/webcatalogs/en/MS-01-76.pdf`. Last Accessed: 27-08-2019.

[86] Swagelok. Check Valves: C, CA, CH, CP, and CPA Series, 2017. URL `https://www.swagelok.com/downloads/webcatalogs/en/MS-01-176.pdf`. Last Accessed: 27-08-2019.

[87] Swagelok. Filters, 2017. URL `https://www.swagelok.com/downloads/webcatalogs/EN/MS-01-92.PDF`. Last Accessed: 27-08-2019.

[88] Swagelok. Plug Valves, 2017. URL `https://www.swagelok.com/downloads/webcatalogs/en/MS-01-59.pdf`. Last Accessed: 27-08-2019.

[89] Swagelok. Sample Cylinders, Accessories, and Outage Tubes, 2017. Last Accessed: 27-08-2019.

[90] Swagelok. Gaugeable Tube Fittings and Adapter Fittings, 2018. URL `https://www.swagelok.com/downloads/webcatalogs/EN/MS-01-140.PDF`. Last Accessed: 27-08-2019.

[91] Swagelok. Stainless Steel Seamless Tubing and Tube Support Systems, 2018. URL `https://www.swagelok.com/downloads/webcatalogs/EN/MS-01-181.PDF`. Last Accessed: 27-08-2019.

[92] Swagelok. All-Welded Check Valves: CW Series, 2019. URL `https://www.swagelok.com/downloads/webcatalogs/en/MS-02-89.PDF`. Last Accessed: 27-08-2019.

[93] Swagelok. One-Piece Instrumentation Ball Valves, 2019. URL `https://www.swagelok.com/downloads/webcatalogs/en/MS-02-331.pdf`. Last Accessed: 27-08-2019.

[94] Swagelok. Pressure Regulators: K Series, 2019. URL `https://www.swagelok.com/downloads/webcatalogs/EN/ms-02-230.pdf`. Last Accessed: 27-08-2019.

[95] Swagelok. Hose and Flexible Tubing, 2020. URL `https://www.swagelok.com/downloads/webcatalogs/en/MS-01-180.pdf`. Last Accessed: 27-08-2019.

[96] J. A. Tallmadge. Packed bed pressure drop—an extension to higher Reynolds numbers. *AIChE Journal*, 16(6):1092–1093, November 1970. doi: 10.1002/aic.690160639.

[97] N. C Tang. Plastic-deformation analysis in tube bending. *International Journal of Pressure Vessels and Piping*, 77(12):751–759, October 2000. doi: 10.1016/S0308-0161(00)00061-2.

[98] Engineering Toolbox. Air - Density, Specific Weight and Thermal Expansion Coefficient at Varying Temperature and Constant Pressures, 2003. URL `https://www.engineeringtoolbox.com/air-density-specific-weight-d_600.html`. Last Accessed: 27-08-2019.

[99] Engineering Toolbox. Air - Specific Heat at Constant Pressure and Varying Temperature, 2004. URL `https://www.engineeringtoolbox.com/air-specific-heat-capacity-d_705.html`. Last Accessed: 27-08-2019.

[100] Engineering Toolbox. Air - Thermal Conductivity, 2009. URL `https://www.engineeringtoolbox.com/air-properties-viscosity-conductivity-heat-capacity-d_1509.html`. Last Accessed: 27-08-2019.

[101] Engineering Toolbox. Air - Prandtl Number, 2018. URL `https://www.engineeringtoolbox.com/air-prandtl-number-viscosity-heat-capacity-thermal-conductivity-d_2009.html`. Last Accessed: 27-08-2019.

[102] VPG Transducers. Tedea-Huntleigh model 1004, 2015. URL `http://www.vishaypg.com/docs/12002/1004.pdf`. Last Accessed: 27-08-2019.

[103] A. L. Tsykalo and A. G. Tabachnikov. Density, viscosity, and bond energy of molecules in aqueous hydrogen peroxide solutions. *Theoretical and Experimental Chemistry*, 2(6):604–605, November 1966. doi: 10.1007/BF01000968.

[104] S. Tuttle, S. Morgan, A. Quinn, and G. Johnson. Reaction Control Thruster Thermal Design for a Mission to Mercury. *Journal of Spacecraft and Rockets*, 54(5):1134–1141, September 2017. doi: 10.2514/1.A33795.

[105] RP Software+Engineering UG. RP Software+Engineering UG. URL `http://propulsion-analysis.com/`. Last Accessed: 27-08-2019.

[106] N. Ul Haq, R. Aziz Khan, and R. Mehmood. *Design, development and testing of 1N Hydrogen Peroxide thruster*. January 2017. doi: 10.1109/IBCAST.2017.7868112.

[107] RSG Regel und Steuergeräte GmbH. 2/2-Wege Coaxialventil - Baureihe 267.

[108] F. Valencia Bel. Personal correspondence, 2019.

[109] M. Ventura and P. Mullens. The use of hydrogen peroxide for propulsion and power. In *35th Joint Propulsion Conference and Exhibit*, Joint Propulsion Conferences. American Institute of Aeronautics and Astronautics, June 1999. doi: 10.2514/6.1999-2880.

[110] M. Ventura, E. Wernimont, S. Heister, and S. Yuan. Rocket Grade Hydrogen Peroxide (RGHP) for use in Propulsion and Power Devices - Historical Discussion of Hazards. In *43rd AIAA/ASME/SAE/ASEE Joint Propulsion Conference & Exhibit*, Joint Propulsion Conferences. American Institute of Aeronautics and Astronautics, July 2007. doi: 10.2514/6.2007-5468.

[111] A. P. Yalin. High power fiber delivery for laser ignition applications. *Optics Express*, 21(S6): A1102, November 2013. doi: 10.1364/OE.21.0A1102.

[112] B. Yavuz. *Implementation of Expansion Loops*. October 2015. doi: 10.13140/RG.2.1.4645.0648.

[113] B. T. C. Zandbergen and Delft University of Technology. Faculty of Aerospace Engineering. *Thermal rocket propulsion (version 2.01): Ae4-S01*. Delft University of Technology. Faculty of Aerospace Engineering, 2004.

[114] H. Ziebland, R.C. Parkinson, and North Atlantic Treaty Organization. Advisory Group for Aerospace Research and Development. Propulsion and Energetics Panel. *Heat Transfer in Rocket Engines*. AGARDograph. North Atlantic Treaty Organization, Advisory Group for Aerospace Research and Development, 1971.

A

List of physical constants and conversion factors

A list of physical constants used throughout the work is provided in Table A.1.

Symbol	Definition	Value	Unit
g	Standard gravity	9.806	m/s^2
σ	Stefan Boltzmann constant	$5.67 \cdot 10^{-8}$	$W/m^2/K^4$
R_c	Universal gas constant	8.3145	$J/K/mol$

Table A.1: List of used physical constants [113]

Additionally, a number of conversion factors has been identified in Table A.2.

Conversion	Factor
$inch$ to mm	25.4
psi to Pa	6894.75729
$mmHg$ to Pa	133.322368

Table A.2: List of used conversion factors

B

Material Properties

Throughout the thesis, a large amount of material properties have been used. Especially in the decomposition model from Chapter 2, a significant amount of calculations has been performed for several properties of hydrogen peroxide, water and oxygen (B.1). Additionally, air properties, as well as mechanical properties of 316 stainless steel and MACOR, have been used for the thermal and structural analysis of components (B.2).

B.1. Fluid properties for the decomposition model

B.1.1. Molecular weights

The molecular weights of hydrogen peroxide, water and oxygen have been used in the decomposition model and are listed in Table B.1.

Component	Molecular weight
H_2O_2	34.0147
H_2O	18.0153
O_2	31.9988

Table B.1: Molecular weights of species used in the decomposition model [61]

B.1.2. Density

During the initial phase of the decomposition process, both hydrogen peroxide and water are in the liquid phase. Therefore, the liquid density of each of these components is calculated. For the liquid density of both hydrogen peroxide and water, relations were found in [41]. The authors calculated the density of pure liquid hydrogen peroxide using the following equation from [103]:

$$\rho_{l,H_2O_2} = 1597 + 0.0784T_l - 0.00197T_l^2 \tag{B.1}$$

In which T_l is the temperature in K and ρ_l is the density in $kg\ m^{-3}$ For the liquid density of water, they used the calculation from [68]:

$$\rho_{l,H_2O} = (A + B \cdot T_{l,C} + C \cdot T_{l,C}^2 + D \cdot T_{l,C}^3 + E \cdot T_{l,C}^4/(1 + G \cdot T_{l,C}) \cdot 1000 \tag{B.2}$$

In which $T_{l,C}$ is the temperature of the liquid in $^{\circ}C$. The variables A to G are defined in Table B.2. The density in the gas phase is calculated for the entire gas mixture, by use of the ideal gas law [113]:

$$\rho_g = \frac{P}{RT} \tag{B.3}$$

In which P is the pressure in Pa, R is the specific gas constant in $J\ kg^{-1}\ K^{-1}$ and T is the temperature in K.

Constant	Value
A	0.9998396
B	18.224944×10^{-3}
C	-7.92221×10^{-6}
D	-55.44846×10^{-9}
E	149.7562×10^{-12}
F	$-393.2952 \times 10^{-15}$
G	18.159725×10^{-3}

Table B.2: Water liquid density constants as quoted in [41] from [68]

B.1.3. Vapour pressure

For the calculation of the vapour pressures of a pure component, the following relation was found in [41], which has been taken from [54]:

$$\log_{10} p_{vap} = A + \frac{B}{T_l} + C \cdot \log_{10} T_l + D \cdot T_l + E \cdot T_l^2 + F \cdot T_l^3 + G \cdot T_l^4 \tag{B.4}$$

In which p_{vap} is the vapour pressure in $mmHg$ and T_l is the temperature in K. The values for the parameters A to G are found in Table B.3.

Constant	$H_2O_2(T < 363.15K)$	$H_2O_2(\geq 363.15K)$	H_2O
A	24.8436	38.8572	19.389127
B	-3511.54	-3627.72	-2861.9133
C	-4.61453	-11.2133	-3.2418662
D	-3.60245×10^{-3}	-4.74132×10^{-3}	$-1.0799994 \times 10^{-4}$
E	-7.73423×10^{-6}	0	$-7.9189289 \times 10^{-6}$
F	1.78355×10^{-8}	0	1.5411774×10^{-8}
G	-2.27008×10^{-13}	0	$-8.1926991 \times 10^{-12}$

Table B.3: Constants for the pure component vapour pressure calculation [41, 54]

B.1.4. Enthalpy and specific heat

The enthalpy and specific heats have been calculated for gaseous hydrogen peroxide, liquid water and gaseous oxygen using the following equation specified in [41], as was taken from [61]:

$$H^\circ = A \cdot t + \frac{B}{2} \cdot t^2 + \frac{C}{3} \cdot t^3 + \frac{D}{4} \cdot t^4 - \frac{E}{t} + F \tag{B.5}$$

$$C_p = A + B \cdot t + C \cdot t^2 + D \cdot t^3 + \frac{E}{t^2} \tag{B.6}$$

Where H is the enthalpy in $J\ mol^{-1}$, C_p is the specific heat in $J\ mol^{-1}\ K^{-1}$ and t is calculated as $t = T/1000$, where T is the temperature in K. The values for the parameters A to G are found in Table B.4.

Constant	$H_2O_{2(g)}$	$H_2O_{(l)}$	$O_2\ (T \leq 700)$	$O_2\ (T > 700)$
A	34.25667	-203.6060	31.32234	30.03235
B	55.14445	1523.29	-20.23531	8.772972
C	-35.15443	-3196.413	57.86644	-3.988133
D	9.08744	2474.455	-36.50624	0.788313
E	-0.422157	3.855326	-0.007374	-0.741599
F	-13.8034	-256.5478	-8.903471	-11.32468

Table B.4: Enthalpy constants of oxygen and liquid water [41, 61]

For the Enthalpy of steam (gaseous water) the following calculations were used from [57]:

$$H^\circ = \left(\frac{A}{T^2} + \frac{B}{T} \cdot \ln T + C + D \cdot \frac{T}{2} + E \cdot \frac{T^2}{3} + F \cdot \frac{T^3}{4} + G \cdot \frac{T^4}{5} + \frac{H}{T}\right) * R_c * \frac{T}{1000} \tag{B.7}$$

$$C_p = (\frac{A}{T^2} + \frac{B}{T} + C + D \cdot T + E \cdot T^2 + F \cdot T^3 + G \cdot T^4) \cdot R_c \tag{B.8}$$

In which R_c is the universal gas constant in $J K^{-1} mol^{-1}$. The values of the parameters A to G are found in Table B.5.

Constant	$H_2O_{(g)}\ (T \leq 1000\ K)$	$H_2O_{(g)}\ (T > 1000\ K)$
A	$3.947960830E + 04$	$1.034972096E + 06$
B	$5.755731020E + 02$	$-2.412698562E + 03$
C	$9.317826530E - 01$	4.646110780
D	$7.222712860E - 03$	$2.291998307E - 03$
E	$-7.342557370E - 06$	$-6.836830480E - 07$
F	$4.955043490E - 09$	$9.426468930E - 11$
G	$-1.336933246E - 12$	$-4.822380530E - 15$
H	$-3.303974310E + 04$	$-1.384286509E + 04$

Table B.5: Enthalpy constants of steam (gasous water) [57]

B.1.5. Viscosity

For the calculation of the dynamic viscosity of hydrogen peroxide solutions, an equation was used that has been fitted to experimental data at ESA [108]. It is given as the following:

$$\eta_L = EXP\left[\frac{1}{A/T + B/T^2 + C\ln T + D \cdot x_{H_2O_2} + E \cdot x_{H_2O_2} + F \cdot x_{H_2O_2}/T + G \cdot}\right] \tag{B.9}$$

In which η_L is the dynamic viscosity in Pas, T is the temperature in K and $x_{H_2O_2}$ is the hydrogen peroxide mass fraction (0.98 for 98%). The values for the constants A to G are given in Table B.6.

Constant	**Value**
A	263.6414493
B	-27367.27532
C	0.414061249
D	-0.054949
E	0.004703055
F	13.41977711
G	-3.078536604

Table B.6: Constants for the calculation of the viscosity of aqueous hydrogen peroxide solutions [108]

For the calculation of the viscosity of the pure gas components, the following relation was used [56]:

$$\ln \eta = A \ln T + \frac{B}{T} + \frac{C}{T^2} + D \tag{B.10}$$

The parameters A to D for this equation are dependent on the temperature and are found in Tables B.7 and B.8.

Constant	$H_2O_{2(g)}$	$H_2O_{(g)}$	$O_{2(g)}$
A	0.99686871×10^0	0.78387780×10^0	0.61936357×10^0
B	-0.41461068×10^2	-0.38260408×10^3	-0.44608607×10^2
C	0.871729×10^4	0.49040158×10^5	-0.13460714×10^4
D	-0.15770256×10^1	0.85222785×10^0	0.19597562×10^1

Table B.7: Gas viscosity constants T < 1000 K [56]

For the determination of the viscosity of a gas mixture a special calculation is required. This was done using the method of Reichenberg, which is described in [70]. All equations below have been taken

Constant	$H_2O_{2(g)}$	$H_2O_{(g)}$	$O_{2(g)}$
A	0.57419481×10^0	0.50714993×10^0	0.63839563×10^0
B	-0.50408983×10^3	-0.68966913×10^3	-0.12344438×10^1
C	0.48898234×10^5	0.87454750×10^5	-0.22885810×10^5
D	0.17621537×10^1	0.30285155×10^1	0.18056937×10^1

Table B.8: Gas viscosity constants T ≥ 1000 K [56]

from this reference. The gas mixture viscosity is calculated using:

$$\eta_m = \sum_{i=1}^{n} K_i \left(1 + 2\sum_{j=1}^{i-1} H_{ij}K_j + \sum_{j=1 \neq i}^{n} \sum_{k=1 \neq i}^{n} H_{ij}H_{ik}K_jK_k \right) \tag{B.11}$$

In which η_m is the mixture viscosity in $Pa\ s$ and n is the number of pure components in the mixture. K_i is calculated using:

$$K_i = \frac{y_i\eta_i}{y_i + \eta_i \sum_{k=1\neq i}^{n} y_k H_{ik}[3 + (2M_k/M_i)]} \tag{B.12}$$

In which M_i is the molar mass of the component i, y_k is the mole fraction of the component k, η_i is the viscosity of the pure component i in $Pa\ s$ and H_{ik} is calculated using:

$$H_{ij} = \left[\frac{M_iM_j}{32(M_i + M_j)^3}\right]^{(1/2)} (C_i + C_j)^2 \frac{[1 + 0.36T_{rij}(T_{rij} - 1)]^{(1/6)}F_{Rij}}{(T_{rij})^{(1/2)}} \tag{B.13}$$

In which T_{rij} is calculated using:

$$T_{rij} = \frac{T}{(T_{ci}T_{cj})^{(1/2)}} \tag{B.14}$$

In which T is the temperature in K and T_{ci} is the critical temperature of component i in K. An overview of the critical temperatures is found in Table B.9. The variables C_i are calculated using:

$$C_i = \frac{M_i^{1/4}}{(\eta_iU_i)^{1/2}} \tag{B.15}$$

In which U_i is calculated using:

$$U_i = \frac{[1 + 0.36T_{ri}(T_{ri} - 1)]^{(1/6)}F_{ri}}{(T_{ri})^{(1/2)}} \tag{B.16}$$

Where T_{ri} is calculated as:

$$T_{ri} = \frac{T}{T_{ci}} \tag{B.17}$$

And F_{ri} is determined using the following equation:

$$F_{ri} = \frac{T_{ri}^{3.5} + (10\mu_{ri})^7}{T_{ri}^{3.5}[1 + (10\mu_{ri})^7]} \tag{B.18}$$

In which μ_{ri} is the reduced dipole moment. It is calculated using:

$$\mu_{ri} = 52.46\frac{\mu_i^2P_c}{T_c^2} \tag{B.19}$$

In which μ_i is the dipole moment (found in Table B.11) in Debye (D) , and P_c is the critical pressure (found in Table B.10) in bar. Finally, F_{rij} is calculated (for use in Equation B.13) as:

$$F_{rij} = \frac{T_{rij}^{3.5} + (10\mu_{rij})^7}{T_{rij}^{3.5}[1 + (10\mu_{rij})^7]} \tag{B.20}$$

In which μ_{rij} is calculated as:

$$\mu_{rij} = (\mu_{ri}\mu_{rj})^{(1/2)} \tag{B.21}$$

Component	Critical temperature [K]
H_2O_2	728
H_2O	647
O_2	154.58

Table B.9: Critical temperatures of gas components [61]

Component	Critical pressure [bar]
H_2O_2	220
H_2O	220.64
O_2	50.43

Table B.10: Critical pressures of gas components [61]

Component	Dipole moment [D]
H_2O_2	2.26
H_2O	1.8546
O_2	0

Table B.11: Used dipole moments for gas components from [77] and [29]

B.2. Properties for thermal and structural analysis

B.2.1. Air properties

For the calculation of the convective resistance for the free convection from the chamber wall to the environment, several properties of air have been used. An overview of the thermal conductivity (k), dynamic viscosity (μ), kinematic viscosity (ν), thermal expansion coefficient (β) and density (ρ) is found in Table B.12. The values used in the calculations have been determined through interpolation.

T [°C]	k [$mW/m/K$]	μ ($\cdot 10^{-6}$) [$Pa\ s$]	ν ($\cdot 10^{-6}$) [m^s/s]	β [$1000/K$]	ρ [kg/m^3]
-10	23.59	16.65	12.43	3.84	1.341
-5	23.97	16.90	12.85	3.76	1.316
0	24.36	17.15	13.28	3.69	1.292
5	24.74	17.40	13.72	3.62	1.268
10	25.12	17.64	14.16	3.56	1.246
15	25.50	17.89	14.61	3.50	1.225
20	25.87	18.13	15.06	3.43	1.204
25	26.24	18.37	15.52	3.38	1.184
30	26.62	18.60	15.98	3.32	1.164
40	27.35	19.07	16.92	3.21	1.127
50	28.08	19.53	17.88	3.12	1.093
60	28.80	19.99	18.86	3.02	1.060
80	30.23	20.88	20.88	2.85	1.000
100	31.62	21.74	22.97	2.70	0.9467
125	33.33	22.79	25.69	2.51	0.8868
150	35.00	23.80	28.51	2.33	0.8338
175	36.64	24.78	31.44	2.22	0.7868
200	38.25	25.73	34.47	2.10	0.7451
225	39.83	26.66	37.60	2.01	0.7078
300	44.41	29.28	47.54	1.76	0.6168
412	50.92	32.87	63.82	1.52	0.5238
500	55.79	35.47	77.72	1.32	0.4567

Table B.12: Overview of thermal conductivity, viscosity, thermal expansion coefficient and density of air [98, 100]

Additionally, an overview of the Prandtl numbers and specific heats at constant pressure is found in Table B.13.

$T\ [K]$	$T\ [C]$	$Pr\ [-]$	$C_p\ [kJ/kg/K]$
260	-13.2	0.713	1.006
273	0	0.711	1.006
280	6.9	0.710	1.006
289	15.6	0.709	1.006
300	26.9	0.707	1.006
320	46.9	0.705	1.007
340	66.9	0.703	1.009
360	86.9	0.701	1.010
380	106.9	0.700	1.012
400	126.9	0.699	1.014
500	226.9	0.698	1.030
600	326.9	0.703	1.051
700	426.9	0.710	1.075
800	526.9	0.717	1.099

Table B.13: Overview of the Prandtl numbers and specific heats at constant pressure in air [99, 101]

B.2.2. Stainless Steel 316 properties

An overview of the 0.2% yield strength, ultimate tensile strength and elastic modulus at a range of temperatures is provided in Table B.14.

T [C]	**0.2% Yield [MPa]**	**UTS [MPa]**	**Elastic modulus [GPa]**	
			Tension	**Shear**
27	290	579	193	
149	201	517	190	73
260	172	503	181	69
371	159	500	172	65
482	148	484	162	61
593	140	452	153	57
704	131	345	143	54
816	110	186	132	52

Table B.14: Structural data for 316 stainless steel [36]

The thermal conductivity of 316 stainless steel is used extensively in the thermal models. Therefore, an overview of the used data is found in Table B.15. For the determination of the radiative heat transfer from the hot gas to the inner chamber wall, as well as the radiative heat transfer from the outer chamber wall to the environment, the emissivity of 316 stainless steel is calculated. An overview of data used is given in Table B.16.

T [K]	300	350	400	500	600	700	800	900	1000
k [W/m/K]	13.44	14.32	15.16	16.8	18.36	19.87	21.39	22.79	24.16

Table B.15: Values for the thermal conductivity of 316 stainless steel [30]

T [C]	24	232	949
Emissivity [-]	0.28	0.57	0.66

Table B.16: Values for the emissivity of polished 316 stainless steel [46]

B.2.3. MACOR properties

Finally, the stainless steel in the thermal standoff threaded rods was replaced by the ceramic material MACOR. For the thermal model, the conductivity values for this material are required. These values were determined from a figure from the manufacturer, which is found in Figure B.1.

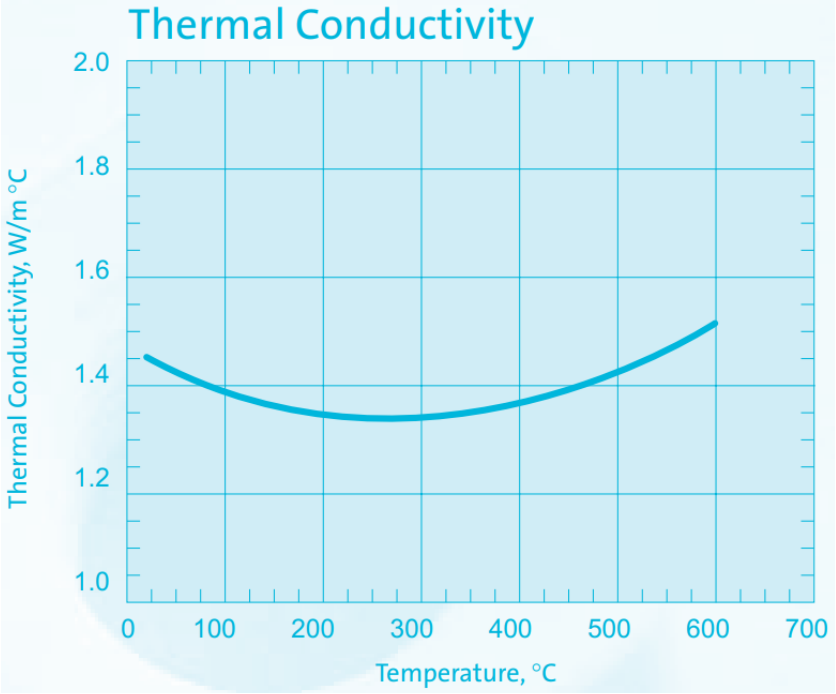

Figure B.1: Thermal conductivity graph for MACOR [55]

C

Requirement Specification Documentation

Contents

1 DOCUMENTATION

The following documents form a part of this specification to the extent specified herein. In the event of conflict between this specification and any of the applicable documents referenced below, this conflict shall be notified to ESA via the technical officer of the activity.

1.1 Applicable Documents

AD/2.1(a)	%%	H2O2 EVONIK Fluid Procurement Spec
AD/2.1(b)	%%	Jet A-1 Fluid Procurement Spec
AD/2.1(c)	ISO 14951-4-1999	Space systems – Fluid Characteristics – Part 4: Helium
AD/2.1(d)	ISO 14951-3-1999	Space systems – Fluid Characteristics – Part 3: Nitrogen
AD/2.1(e)	A-A-59150A	Cleaning Compound, Solvent HFE
AD/2.1(f)	ISO 14951-9-1999	Space systems – Fluid Characteristics – Part 9: Argon
AD/2.1(g)	ASTM D770-05	Isopropyl Alcohol
AD/2.1(h)	ISO 14951-10-1999	Space systems – Fluid Characteristics – Part 10: Water

1.2 Reference Documents

Throughout this specification Applicable Documents are referred to in the text as RD(x)

RD/2.2(a)	Q-ST-70-01C	Product assurance - Cleanliness and contamination control
RD/2.2(b)	E-ST-35-06C	Cleanliness requirements for spacecraft propulsion components, subsystems and systems
RD/2.2(c)	E-10-03A	Testing
RD/2.2(d)	ASTM-E-1742	Standard Practice for Radiographic Examination
RD/2.2(e)	E-ST-20C	Engineering Electrical and electronic
RD/2.2(f)	E-ST-32C Rev 1	Engineering Structural general requirements
RD/2.2(g)	E-ST-32-01C Rev 1	Engineering Fracture control
RD/2.2(h)	E-ST-32-02C Rev 1	Engineering Structural design and verification of pressurised hardware
RD/2.2(i)	E-ST-32-08C	Engineering Materials
RD/2.2(j)	E-ST-32-10C Rev 1	Engineering Structural factors of safety for spaceflight hardware
RD/2.2(k)	E-ST-33-01C	Engineering Mechanisms
RD/2.2(l)	E-ST-35C Rev 1	Engineering Propulsion general requirements
RD/2.2(m)	E-ST-35-01C	Engineering Liquid and electric propulsion for spacecraft
RD/2.2(n)	E-ST-35-10C	Engineering Compatibility testing for liquid propulsion systems

RD/2.2(o)	Q-ST-70C	Product assurance - Material, mechanical parts and processes
RD/2.2(p)	Q-ST-70-22C	Product assurance - Control of limited shelf-life materials
RD/2.2(q)	Q-ST-70-36C	Product assurance - Material selection for controlling stress-corrosion cracking
RD/2.2(r)	Q-ST-70-37C	Product assurance - Determination of the susceptibility of metals to stress corrosion cracking
RD/2.2(s)	Q-ST-70-45C	Product assurance - Mechanical testing of metallic materials
RD/2.2(t)	Q-ST-70-02C	Product assurance - Thermal Vacuum outgassing test for the screening of space materials
RD/2.2(u)	E-ST-20-07C	Engineering Electromagnetic compatibility
RD/2.2(v)	Q-ST-40C	Product assurance - Safety
RD/2.2(w)	E-ST-31C	Thermal Control

1.3 Acronyms

AD	Applicable Documents
AWG	American Wire Gauge
CI	Configuration Item
COTS	Commercial Off-the-Shelf
ECSS	European Cooperation for Space Standardisation
EM	Engineering Model
EMC	Electro-magnetic compatibility
ESA	European Space Agency
FCV	Flow Control Valve
FM	Flight Model
HFE	Hydro Fluoro Ether
i.a.w.	In accordance with
ICD	Interface Control Document
ISO	International Organisation for Standardisation
MDP	Maximum Design Pressure
NDT	Non-Destructive Testing
PFM	Proto-Flight Model
ppm	parts per million
QM	Qualification Model
RAMS	Reliability, Availability, Maintainability & Safety
RCT	Reaction Control Thruster
RD	Reference Document
SoW	Statement of Work
STM	Structural-Thermal Model
Tbc	To be confirmed
Tbd	To be defined
TCA	Thruster Chamber Assembly
TLV	Thruster Latch Valve

2 REQUIREMENTS

2.1 Performance

2.1.1 Functional Performance

2.1.1.1 Operating pressures

Nominal Operating Pressures

MGT-002
The pressure operation shall take into account the propellant ignition pressure conditions and the state-of-the-art for COTS. The nominal supply pressure (measured at FCV inlet) is 22 bar.

MGT-004
The Maximum Expected Operating Pressure that the TCA shall withstand shall be 24 bar.

Proof Pressure

MGT-010
The TCA shall meet the requirements of this specification after being subjected to a proof pressure of 1.5x MEOP.

Burst Pressure

MGT-016
The thrust chamber shall withstand a pressure of 2.5 times the maximum expected combustion chamber operating pressure without rupture. The definition of the chamber MEOP has to take transient effects into account i.a.w. RD/2.2(h).

Roughness

MGT-020
Steady state chamber pressure oscillations shall not exceed more than 10% (1σ) of the local average chamber pressure for the whole pressure range.

2.1.1.2 Leakage Rates

External Leakage

MGT-030
The maximum permissible external propellant leakage through the thruster mechanical joints shall be 10E-06 scc/s GHe with valve opened and pressurised at least to MEOP and the thruster nozzle plugged.

2.1.1.3 Overpressure

MGT-042
The equipment shall operate within specification after having been subjected to the poof pressure specified in paragraph 3.2.1.1.

2.1.1.4 Step Start Pressure Surge

MGT-050
The unit performance shall not be degraded when being subjected to a pressure spike with a value of 0 bar to 3 x MEOP within a duration of 20 ms (liquid at FCV inlet). No permanent damage shall result from this pressure spike.

2.1.1.5 Thruster Firing Performance Requirements

MGT-054
There shall be no thermal restrictions on the number of pulses in any pulse train and on the length of any continuous burn. Thruster restart shall not be constrained by environmental conditions or firing history. The thruster assembly shall be capable of successful pulsed or continued operation within specification requirements at all valve and thrust chamber temperatures, which might result from thermal soak-back after any firing. It shall be possible to restart and operate the thruster within appropriate specifications regardless of when or for how long the thruster was last fired.

2.1.1.5.1 Standard Conditions

MGT-056
Nominal performance data shall be based upon the standard temperature and pressures specified herein and exclude measurement errors unless otherwise noted or specified. The standard conditions shall be:

Ambient pressure:	1013 mbar (Absolute)
Feed Pressure	5.5 to 24 bar
Ambient temperature	+20 C
Propellant inlet temperature:	+7 /+60 °C

All performance requirements shall be met regardless of the gas saturation state of the propellants.

2.1.1.5.2 Steady State Performance

These requirements apply for the operating pressure and temperature ranges in 3.2.1.6.1, unless otherwise stated.

MGT-060
The time required to reach Steady-state conditions shall be i.a.w. what the state-of-art can achieve. Typically, steady-state specific impulse performance (no thermal equilibrium) is required when the ON-times exceed 5 seconds.

Thrust

MGT-062
The nominal thrust shall be 1 N at a propellant feed pressure of 22 bar at ambient feed temperature. The following thrust ranges shall be achieved:

Feed pressure [bar]	Thrust [N]
24	0.99 – 1.2
15	0.65 – 0.72
5.5	0.26 – 0.32

All values refer to vacuum thrust. They shall be adapted for sea-level testing.

MGT-063
The thruster shall not evolve by more than 2% at identical supply conditions once steady-state conditions have been reached.

MGT-064
The BOL steady state thrust at identical propellant supply conditions shall be predictable within ± 5% of nominal thrust.

MGT-066
The BOL steady state thrust shall be repeatable within ± 5% with the same equipment and propellant supply conditions in the whole supply window.

MGT-068
The thrust rise time shall be lower than 200 ms. This is described as the required time to achieve 90% of the nominal thrust from the electrical command sent to open the valve.

MGT-070
The thrust decay time shall be less than 300 ms. This is described as the required time to achieve 10% of the nominal thrust from the electrical command sent to close the valve.

MGT-072
The thrust overshoot at the start-up of a steady-state firing or at the first pulse in the worst-case condition shall be less than 100%.

Specific Impulse

MGT-074
At BOL, the minimum delivered vacuum specific impulse shall not be less than:
- 173 s at 24 bar feed pressure
- 169 s at 15 bar feed pressure
- 160 s at 5.5 bar feed pressure

This requirement refers to 98% H_2O_2. Should a different concentration be used the values shall be adapted accordingly.

Roughness

MGT-078
Steady state thrust oscillations shall not exceed more than 10%(1σ) of the local average thrust for the whole pressure range.

Longest Single Burn

MGT-086
The thruster shall be capable of achieving a longest continuous steady state firing of at least 30 minutes (goal is more than 60 minutes).

2.1.1.5.3 Pulse Mode Performance Requirements

These requirements apply for the standard conditions from para. 3.2.1.6.1. and for the nominal operating voltage of the valve unless otherwise stated.

Impulse Bit

MGT-088
The thruster shall be capable of producing an impulse bit within the following range. The impulse bits shall be characterized during the testing defined in MGT-098.

Feed Pressure [bar]	MIB Requirement [Ns]	MIB Goal [Ns]
22	< 0.07	< 0.035
5.5	< 0.023	< 0.012

MGT-090
The impulse bit shall be repeatable pulse-to-pulse within the following ranges for pulse trains with a minimum length of 50 pulses:

Feed Pressure [bar]	Repeatability [%]
22	< 5 (2σ)
15	< 10 (2σ)
5.5	< 15 (2σ)

Centroid Delay

MGT-092
The pulse centroid delay is defined as the delay between the centre of the "valve open" signal and the centre of the area under the thrust v time curve. The centroid delay time shall be less than 150 ms.

Minimum On Time

Typically, the minimum On-time is defined as the time from the command is sent to the valve until 90% of the thrust is measured. This includes:

- Time to open the valve completely
- Time to fill the dribble volume
- Decomposition of the propellant in contact with the catalyst
- Generation of 90% of the nominal thrust at a given inlet pressure

MGT-096
The thruster shall be capable of producing a repeatable pulse with a minimum ON-time sufficient to fulfil requirement MGT-088. The minimum ON-time shall be less than 50 ms within the full operating pressure and temperature range.

Pulse Mode Duty Cycles

The duty cycle is defined as the ratio of the ON-time and the total time between the starts of two pulses: Duty Cycle [%] = T-on / (T-on + T-off) * 100%. A duty cycle of 100% describes a continuous firing.

MGT-098
The thruster shall be capable of pulse mode duty cycles for pulse trains up to 50 firings, including single pulses. The following duty cycle testing shall be performed:

T_on [s]	**0.1**	**0.2**	**0.5**	**1**	**5**	**10**	**30**
Duty Cycles [%]	0.1	0.1	0.1	0.1	0.5	1.0	100.0
	0.5	0.5	0.5	0.5	1.0	5.0	
	1.0	1.0	1.0	1.0	5.0	20.0	
	5.0	5.0	5.0	5.0	20.0	40.0	
	10.0	10.0	10.0	10.0	40.0	60.0	
	20.0	20.0	20.0	20.0	60.0	80.0	
	40.0	40.0	33.3	40.0	80.0	90.0	
	50.0	50.0	40.0	50.0	83.3	90.9	
	60.0	60.0	50.0	60.0	90.0	95.0	
		80.0	60.0	80.0	95.0	99.0	
			80.0	90.0	99.0	100.0	
			90.0	95.0	100.0		

A graphic representation of the duty cycles is found in the figure below:

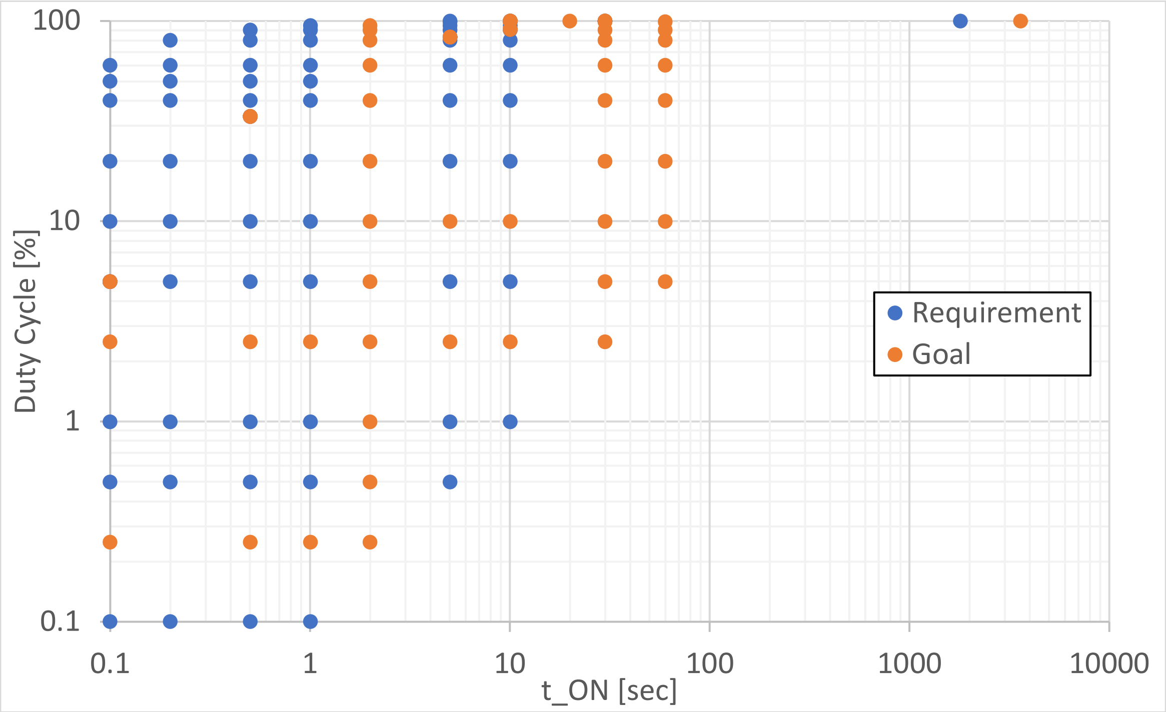

MGT-100
The thruster shall be capable to operate in "Off Modulation" mode.
Note: “Off-modulation” mode is defined as pulses mode duty cycles above 90%.

MGT-102
The thruster shall not have any degradation to any pulse mode duty cycle, pulse train in the whole qualification pressure range.

2.1.1.5.4 Cycle Requirements

MGT-110
The maximum number of hot firings distributed over the different duty cycles (See Table 1) required from the thruster shall be 8000 (goal is 13000).

MGT-112
The thruster shall withstand 30 cold starts at ambient temperature conditions and with a feed pressure of 22 bar.

MGT-116
The thruster shall be capable of completing at least 200 full thermal cycles (goal is more than 900). These start from 50C or pre-heating temperature (whichever is higher) up to steady-state temperature.

MGT-118
The thruster shall be capable of achieving a total propellant throughput of more than 5 kg (goal is more than 20 kg).

MGT-120
The thruster shall be capable of delivering a total impulse of more than 6 kNs (goal is 23 kNs).

MGT-122
The total cumulative on-time that can be achieved shall be at least 3.0 hours (goal is more than 12 hours).

2.1.2 Electrical Characteristics

2.1.2.1 Flow Control Valve/Thruster Latch Valve

MGT-170
The valve opening response time shall be less than 15 ms in the whole pressure and temperature range.

MGT-172
The valve closing response time shall be less than 10 ms in the whole pressure and temperature range.

2.1.2.2 Temperature Sensors

RCT-180
Temperature sensors shall have an operating range that cover the operational pressure range at the position it is installed.

2.1.2.3 Pressure Sensors

RCT-190
Pressure sensors shall have an operating range that cover the operational pressure range at the position it is installed.

2.1.2.4 Grounding

RCT-198
All wired interfaces shall use wired returns and not structure, and shall be electrically isolated from the thruster casing.

2.1.3 Operating Requirements

2.1.3.1 Operating Media

MGT-250
The equipment shall be designed to operate with the following media:
a. Working Media
The equipment shall meet the requirements of this specification when used in conjunction with the following mediums:

- Relevant Operating Propellants to AD/2.1(a) and AD/2.1(b)
- Gaseous Helium to AD/2.1(c)

b. Test Media

- Gaseous Nitrogen to AD/2.1(d)
- HFE-7100 to AD/2.1(e)
- Argon Gas to AD/2.1(f)
- Isopropyl Alcohol (IPA) to AD/2.1(g)
- Deionised/Demineralised Water to AD/2.1(h)

2.1.3.2 Fluid/Equipment Temperature

MGT-254
The equipment shall meet the requirements of this specification when operating within the following ranges of fluid and equipment temperatures:
a. Normal Operating 278 K to 323 K
b. Acceptance 273 K to 328 K (Equipment only)
c. Qualification 268 K to 333 K (Equipment only)
d. Non-operating Temperature 283 K to 323 K
e. Storage Temperature 253K to 333K (Equipment only)

MGT-278
The temperature in the inlet valve body shall not exceed 323 K to prevent unwanted decomposition effects in the inlet valve or propellant feed system.

2.2 Design Criteria

2.2.1 General Design Criteria

The equipment shall be designed with positive margins of safety to meet the requirements of the specification prior to exposure, during exposure and after exposure to the environments specified in RD/2.2(h).

Environments experiences during fabrication (see note), transportation and storage shall be controlled so as to be significantly less severe than environments specified herein.

Components using sliding surfaces for their actuation and operation as well as components with bellows inside the fluid containing part shall not be allowed without the consent of ESA.

Note: Exceptions where the process is an integral part of fabrication are to be approved by ESA.

2.3 Physical Characteristics

2.3.1 Configuration and Dimensions

MGT-300
The equipment shall comply with the dimensions, plus their tolerances, and the configuration as defined in Section 3.4.2 and the Equipment ICD. The equipment shall be designed to minimise particle generation caused by abrasion or impact between moving parts.

2.3.2 Interfaces

2.3.2.1 Interface with the Propulsion Thruster valve

MGT-310
The TCA shall be designed to be compatible for the assembly to the proposed test valve.

MGT-312
The interface with the thruster valve shall fulfil the following conditions:

- It shall minimise the dribble volume
- External leak tightness shall be guaranteed under critical environmental conditions (including dry/wet cycles, heat soak back and cold starts). This shall include redundant seals.

2.3.2.2 Interface with the Support Structure

RCT-314
The interface to the support structure, external configuration, centre of gravity, and all critical dimensions shall be designed and controlled according to Equipment ICD.

2.3.2.3 Interface with Thermal Control Subsystem (TCS)

MGT-316
The equipment design shall permit the attachment of the following TCS hardware:

- Heaters
- Temperature Sensors

MGT-317
A temperature sensor shall be attached to the combustion chamber of the thruster. The exact location of this hardware shall be defined in the Equipment ICD and agreed with ESA.

MGT-318
The TCA shall be able to evacuate the heat generated during and after the firing. This shall be modelled by means of a Thermo-Mechanical Model and verified by test i.a.w. RD/2.2(w).

2.3.2.4 Interface with Ground Support Equipment (GSE)

MGT-320
The equipment design shall allow for internal leak testing at the nozzle. In the case of special handling or operating precautions being necessary these shall be included in the suppliers Handling and Transportation Procedures. It is acknowledged that only those leak check adaptors and alignment measuring devices delivered by the supplier shall be used.

2.3.3 Cleanliness

MGT-328
Particle & Non-Volatile Residue shall be established i.a.w. RD/2.2(b).

2.3.4 Flow trimming

MGT-332
The thruster shall be capable of being trimmed to a mass flow rate i.a.w. the thrust (see MGT-062) needs. It shall allow trimming with a tolerance of +/-10% of the required value.

2.4 Design and Construction

2.4.1 Selection of Specification and Standards

MGT-384
All specifications and standards intended for use in the design and construction of the equipment shall be in accordance with the requirements defined in Sections 2.1 & 2.2.

2.4.2 Materials, Parts and Processing

MGT-388
Each material, part and process shall be controlled by a detailed specification and shall satisfy the applicable requirements of RD/2.2(o).

2.4.2.1 Dissimilar Metals

MGT-390
Contact of dissimilar metals with each other, as defined in RD/2.2(o) shall be avoided wherever possible. Protection against electrolytic corrosion that can result from such contact shall be provided by surface treatment of the metals.

2.4.2.2 Corrosion of Materials

MGT-394

a. Stress Corrosion Sensitivity
Metals and alloys that are susceptible to stress corrosion cracking shall not be used. Heat treating of alloys to obtain non-stress-corrosion sensitive conditions is allowed.

b. Corrosion Resistance
Materials shall be corrosion resistant type or suitably treated to resist corrosive effects likely to result from exposure to the environmental conditions specified herein.
Protective coating shall not crack, chip, peel or scale with age when subjected to the environmental extremes specified.

2.4.2.3 Ceramic Materials [if applicable]

RCT-398
Ceramic materials or coatings that may crack or break under any combination of operating conditions or environments specified herein shall not be used.

2.4.2.4 Seals

RCT-400
Any seals used shall comply with all the applicable requirements of this specification.

2.4.2.5 Lubricants and Sealants

RCT-402
Lubricants and sealants shall be used only if essential for equipment assembly. Their use shall be minimised and subject to ESA.

2.4.2.6 Surface Finish

MGT-406
The surface of the equipment shall be adequately finished to prevent deterioration from exposure to the specified environments that might jeopardise fulfilment of the specified performance. No cadmium of zinc plating shall be used on any components.

2.4.2.7 Contamination and Cleanliness

MGT-408
Contamination
Operation of the thruster shall not result in the release or generation of particles entering the fluid passage bigger than 0.1 mm. Being exhausted externally to the equipment. The interior of the equipment shall be designed and fabricated to prevent cleaning and prevent the entrapment of contaminants. Equipment shall contain no chips, slag, particulate matter, oil, grease, liquid or other foreign material.

2.4.2.8 Fluid Compatibility

MGT-412
All equipment shall be compatible with the working media of Section 3.2.3.1a. for the lifetimes quoted in this specification without performance degradation or increase in external leakage. The equipment shall also be compatible with the test media of Section 3.2.3.1b. and any fluids used by the equipment suppliers and subcontractors to test, clean or dry the equipment for periods of exposure of at least 2 months. The use of halogenated solvents in contact with titanium alloys shall be agreed with ESA.

2.5 Safety

2.5.1 General

MGT-432
All equipment shall be designed and fabricated i.a.w. RD/2.2(v).

2.5.2 Toxic or Hazardous Materials.

MGT-436
Where toxic or hazardous materials are used in equipment, that equipment shall bear a label that identifies the hazardous source, e.g. "Warning - this unit contains ...". In addition, the following hazard reduction criteria shall be implemented.

- The provision of warning notes in manufacturing documents.
- Special handling constraints and procedures.
- Scrap disposal controls.

Warning labels shall not degrade the ability of the equipment to fulfil the requirements of this document or degrade its function.

The supplier/subcontractor shall identify to ESA any potential hazards that have not been eliminated by design.

2.5.3 Explosive Atmospheres

MGT-444
The electrically operated valve assemblies shall be non-hazardous when operating in an explosive atmosphere.

D

Decomposition model python code

```python
# Simplified hydrogen peroxide decomposition model
# Authors: Thim Franken; Ferran Valencia Bel
# Master thesis: Design of a 1N hydrogen peroxide monopropellant thruster,
# including feed system and test setup
#
# Delft University of Technology


''' Import modules '''
import numpy as np
import matplotlib.pyplot as plt

''' Define custom functions '''

def H(Species, Phase, T): # Calculate Enthalpies
    Tl = T/1000.

    if Species == 'H2O2' and Phase == 'G':
        a1 = 4.27611269E00
        a2 = -5.42822417E-04
        a3 = 1.67335701E-05
        a4 = -2.15770813E-08
        a5 = 8.62454363E-12
        b1 = -1.77542989E04

        H = (a1 + a2*T/2. + a3*T**2/3. + a4 * T**3/4. + a5*T**4//5. + b1/T)\
        * Rc * T/1000

    elif Species == 'H2O2' and Phase == 'L':

        H = (193.158-187.341)*(T-298.15)-187.341

    elif Species == 'H2O' and Phase == 'G':
        if T <= 1000:
            A = 3.947960830E+04; B = 5.755731020E+02; C = 9.317826530E-01;
            D = 7.222712860E-03; E = -7.342557370E-06; F = 4.955043490E-09;
            G = -1.336933246E-12; Hc = -3.303974310E+04

        else:
            A = -1.034972096E+06; B = -2.412698562E+03; C = 4.646110780;
            D = 2.291998307E-03; E = -6.836830480E-07; F = 9.426468930E-11;
            G = -4.822380530E-15; Hc = - 1.384286509E+04

        H = (A / T**2 + B / T * np.log(T) + C + D * T / 2. + E * T**2 / 3. \
            + F * T**3 / 4. + G * T**4 / 5. + Hc / T)* Rc * T / 1000

    else:
        if Species == 'H2O' and Phase == 'L':
            A = -203.6060; B = 1523.29; C = -3196.413; D = 2474.455; \
            E = 3.855326; F = -256.5478

        elif Species == 'O2' and T <= 700:
            A = 31.32234; B = -20.23531; C = 57.86644; D = -36.50624;
            E = -0.007374; F = -8.903471;

        elif Species == 'O2' and T > 700:
            A = 30.03235; B = 8.772972; C = -3.988133; D = 0.788313;
            E = -0.741599; F = -11.32468

        H = A * Tl + B * Tl**2/2. + C * Tl**3/3. + D * Tl**4/4 - E / Tl + F

    return H

def Cp(Species, Phase, T): # Calculate Cps
    Tl = T/1000.
```

```
    if Species == 'H2O2' and Phase == 'L':
        Cp = 0.626 * 4.18 * MW_H2O2

    elif Species == 'H2O2' and Phase == 'G':
        A = 34.25667; B = 55.14445; C = -35.15443; D = 9.08744;
        E = -0.422157

        Cp = A + B * Tl + C * Tl**2 + D * Tl**3 + E / Tl**2

    elif Species == 'H2O' and Phase == 'L':
        A = -203.6060; B = 1523.29; C = -3196.413; D = 2474.455; E = 3.855326
        Cp = A + B * Tl + C * Tl**2 + D * Tl**3 + E / Tl**2

    elif Species == 'H2O' and Phase == 'G' and T <= 1000:
        A = -3.947960830E+04; B = 5.755731020E+02; C = 9.317826530E-01;
        D = 7.222712860E-03; E = -7.342557370E-06; F = 4.955043490E-09;
        G = -1.336933246E-12
        Cp = (A/T**2 +B/T + C + D*T + E*T**2 + F*T**3 + G*T**4)*Rc

    elif Species == 'H2O' and Phase == 'G' and T > 1000:
        A = 1.034972096E+06; B = -2.412698562E+03; C = 4.646110780;
        D = 2.291998307E-03; E = -6.836830480E-07; F = 9.426468930E-11;
        G = -4.822380530E-15
        Cp = (A/T**2 +B/T + C + D*T + E*T**2 + F*T**3 + G*T**4)*Rc

    elif Species == 'O2' and T <= 700:
        A = 31.32234; B = -20.23531; C = 57.86644; D = -36.50624;
        E = -0.007374
        Cp = A + B * Tl + C * Tl**2 + D * Tl**3 + E / Tl**2

    elif Species == 'O2' and T > 700:
        A = 30.03235; B = 8.772972; C = -3.988133; D = 0.788313;
        E = -0.741599;
        Cp = A + B * Tl + C * Tl**2 + D * Tl**3 + E / Tl**2

    return Cp

def viscliq(Conc, T): #Calculate aqueous H2O2 solution viscosity

    F = 13.41977711
    E = 0.004703055
    D = -0.054949
    C = 0.414061249
    B = -27367.27532
    A = 263.6414493
    G = -3.078536604

    mu_l = np.exp(1/(A/T + B/T**2 +C * np.log(T)\
                     + D * Conc + E * Conc**2 + F*Conc/T + G))

    return mu_l

def viscgas(Species, T): # Calculate gas phase pure component viscosities

    if Species == 'H2O2':
        if T < 1000:
            A = 0.99686871e0
            B = -0.41461068e2
            C = 0.871729e4
            D = -0.15770256e1
        else:
            A = 0.57419481e0
            B = -0.50408983e3
            C = 0.48898234e5
```

```
            D = 0.17621537e1

    elif Species == 'H2O':
        if T < 1000:
            A = 0.78387780E0
            B = -0.38260408E3
            C = 0.49040158E5
            D = 0.85222785E0
        else:
            A = 0.50714993E0
            B = -0.68966913E3
            C = 0.87454750E5
            D = 0.30285155E1

    elif Species == 'O2':
        if T < 1000:
            A = 0.61936357E0
            B = -0.44608607E2
            C = -0.13460714E4
            D = 0.19597562E1
        else:
            A = 0.63839563E0
            B = -0.12344438E1
            C = 0.22885810E5
            D = 0.18056937E1


    exponent = A * np.log(T) + B/T + C/T**2 + D
    mu = np.exp(exponent) * 1e-7 #convert to Pa s

    return mu

def ViscG_Mix(T, yis): # Calculate gas mixture viscosity

    Species = ['H2O2', 'H2O', 'O2']
    Tcs = [728., 647., 154.58] # Critical temperatures
    Pcs = [220., 220.64, 50.43] # Critical ressures
    Dipoles = [2.26, 1.8546, 0.] # Dipole moments
    Molars = [34.0147, 18.01528, 2*15.999] # Molar masses

    RedDips = []
    for i in range(len(Species)):
        RedDip = 52.46 * Dipoles[i]**2*Pcs[i]/Tcs[i]**2
        RedDips.append(RedDip)

    DipIJ = np.zeros((len(Species),len(Species)))
    for i in range(len(Species)):
        for j in range(len(Species)):
            DipIJ[i][j] = (RedDips[i]*RedDips[j])**.5

    Viscs = np.zeros(len(Species))
    Tris = np.zeros(len(Species))
    Fris = np.zeros(len(Species))
    Uis = np.zeros(len(Species))
    Cis = np.zeros(len(Species))
    Kis = np.zeros(len(Species))

    Trijs = np.zeros((len(Species), len(Species)))
    Frijs = np.zeros((len(Species), len(Species)))
    Hijs = np.zeros((len(Species), len(Species)))

    for i in range(len(Species)):
        Viscs[i] = viscgas(Species[i],T)
        Tris[i] = T/Tcs[i]
        Fris[i] = (Tris[i]**3.5 + (10. * RedDips[i])**7.)\
```

```
        /(Tris[i]**3.5*(1.+(10.*RedDips[i])**7.))
        Uis[i] = (1.+0.36*Tris[i]*(Tris[i]-1.))**(1./6.)*Fris[i]/(Tris[i]**.5)
        Cis[i] = Molars[i]**.25 /((Viscs[i]*Uis[i])**.5)

    for i in range(len(Species)):
        for j in range(len(Species)):
            Trijs[i][j] = T/((Tcs[i]*Tcs[j])**.5)

            Frijs[i][j] = (Trijs[i][j]**3.5 + (10. * DipIJ[i][j])**7)\
            /(Trijs[i][j]**3.5*(1.+(10*DipIJ[i][j])**7))

            Hijs[i][j] = ((Molars[i]*Molars[j])/(32.*(Molars[i]+Molars[j])\
                **3))**.5* (Cis[i]+Cis[j])**2* (1. + 0.36 * Trijs[i][j] *\
                (Trijs[i][j]-1.))**(1./6.)* Frijs[i][j]/(Trijs[i][j]**.5)

    for i in range(len(Species)):
        Part = 0
        for k in range(len(Species)):
            if k != i:
                Part += yis[k]*Hijs[i][k]*(3.+(2.*Molars[k]/Molars[i]))
        Kis[i] = yis[i]*Viscs[i]/(yis[i]+Viscs[i]*Part)

    ViscMix = 0
    for i in range(len(Species)):
        Sum1 = 0
        for j in range(i):
            Sum1 += Hijs[i][j]*Kis[j]

        Sum2 = 0
        for j in range(len(Species)):
            for k in range(len(Species)):
                if j != i and k != i:
                    Sum2 += Hijs[i][j] * Hijs[i][k] * Kis[j] * Kis[k]

        ViscMix += Kis[i] * (1. + 2 * Sum1 + Sum2)

    return ViscMix


def rhoH2O2_l(Tl): #Liquid density hydrogen peroxide
    rho_H2O2_l = 1597 + 0.0784*Tl-0.00197*Tl**2

    return rho_H2O2_l

def rhoH2O_l(Tl): #Liquid density water
    r = [0.9998396, 0.018224944, -7.92221e-06, -5.544846e-08, 1.497562e-10,\
         -3.932952e-13, 0.018159725] # Density constants

    Tlc = Tl - 273.15

    rhoH2O_l = (r[0] + r[1] * Tlc + r[2] * Tlc ** 2 + r[3] * Tlc ** 3\
                + r[4] * Tlc ** 4 +  r[5] * Tlc ** 5)/(1. + r[6] * Tlc) * 1000

    return rhoH2O_l

def VapPressCalc(Species, Tl): #Calculate vapor pressures

    if Species == 'H2O2':
        if Tl < 363.15:
            Vars = [24.8436, -3511.54, -4.61453, -3.60245E-3, -7.73423E-6, \
                    1.78355E-8, -2.27008E-13]
        else:
            Vars = [38.8572, -3627.72, -11.2133, -4.74132E-3, 0, 0, 0]
    else:
        Vars = [19.389127, -2861.9133, -3.2418662, -1.0799994E-4, \
```

```
                -7.9189289E-6, 1.5411774E-8, -8.1926991E-12]

    log10pvap = Vars[0] + Vars[1]/Tl + Vars[2]* np.log10(Tl) + Vars[3] * Tl\
    + Vars[4] * Tl**2 + Vars[5] * Tl ** 3 + Vars[6] * Tl ** 4

    pvap = 10 ** log10pvap

    return pvap*133.322368

''' End of function definition '''

''' Initialization '''
# Gas constant
global Rc
Rc = 8.314

# Molecular weights
MW_H2O2 = 34.0147 #g/mol
MW_H2O = 18.01528 #g/mol
MW_O2 = 2 * 15.999 #g.mol

# Starting variables
T0 = 298.15; T = T0 # Starting temperature [K]
P = 17.87e5 # Upstream pressure [Pa]
Lbed = 0.03 # Catalyst bed lenght simulated [m]
FA0 = 0.0006 # 0.00085 # Mass flow rate [kg/s]
DEG = 0 # Catalyst bed degradation [%]
CONC_0 = 0.98 # Hydrogen peroxide mass%

# Thruster specificc
Dia = 10.218e-3 # Chamber diameter
A_surf = .25*np.pi*Dia**2 # Cat. Bed. Frontal surface area
dp = 3.22e-3 # Pellet diameter
eps_f = 0.36 + dp/Dia+0.7*(dp/Dia)**2 #Void fraction
eps_s = 1. - eps_f

# Catalyst bed interface area constant
AS = 4*eps_s/dp

# Tallmadge equation constants (Pressure drop)
K = 150./dp**2 * eps_s**2/(1.-eps_s)**3
eta = 4.2/dp**(7./6.)*eps_s**(7./6.)/(1-eps_s)**3

# Propellant initial conditions
CONC_H2O2_0G = CONC_0 * P/ (Rc*T0)
CONC_H2O2_0L = (1.0479 + 2.455e-3 * CONC_0 * 100 + 1.781e-5 * \
                (CONC_0 * 100)**2 - 6.76e-4 *(T0 - 273.15) - 2.4e-7 * \
                (T0 - 273.15)**2 - 3.98e-6 * CONC_0 * 100 * \
                (T0 - 273.15)) * 1.0e6 / MW_H2O2
DENS0 = CONC_H2O2_0L
CONC_H2O2_G = CONC_H2O2_0G
CONC_H2O2_L = CONC_H2O2_0L

# Total molecular weight initial condition
MW_TOTAL = 1. / (CONC_0 / MW_H2O2 + (1-CONC_0) / MW_H2O)

# Vapour pressure & fractions initial conditions
xh2o_0 = (1. - CONC_0) / MW_H2O * MW_TOTAL
xh2o2_0 = CONC_0 / MW_H2O2 * MW_TOTAL
VAP_H2O2_0 = VapPressCalc('H2O2', T0)
VAP_H2O_0 = VapPressCalc('H2O', T0)
VAP_FRACTION_H2O2_0 = VAP_H2O2_0 / P
VAP_FRACTION_H2O_0 = VAP_H2O_0 / P
VAP_FRACTION_H2O2 = VAP_FRACTION_H2O2_0
VAP_FRACTION_H2O = VAP_FRACTION_H2O_0
```

```
# Enthalpies initial conditions
H_H2O2_0 = CONC_0 / MW_H2O2 * MW_TOTAL * (VAP_FRACTION_H2O2_0 * \
        (34.25667*(T0/1000.)+55.18445*(T0/1000.)**2/2-35.15443*(T0/1000.)**3\
         /3+9.08744*(T0/1000.)**4/4+0.422157/(T0/1000.)-13.8034) + \
         (1-VAP_FRACTION_H2O2_0) * (-187.86))

H_H2O_0_L = H('H2O', 'L', T0)
H_H2O_0_G = H('H2O', 'G', T0)
H_H2O_0 = (VAP_FRACTION_H2O_0 * H_H2O_0_G\
         + (1.-VAP_FRACTION_H2O_0) * H_H2O_0_L) * (1. - CONC_0) / MW_H2O * \
           MW_TOTAL

# Simulation parameters
dL = 0.00001 # Step size [m]
L = 0.; Ls = [0.] # Starting point
XG = 0. # Initial gas conversion factor
XL = 0. # Initial liquid conversion factor
X = 0. # Initial total conversion factor

''' Table generation for data logging '''
# Conversions
XsG = [XG]; XsL = [XL]; Xs = [X];

# Temperatures
Ts = [T]

# Reaction Rates
rasg = []; rasl = [];
Kcgs = []; Kcls = []; Ktgs = []; Ktls = []
CONC_H2O2_Gs = []

# Fluid parameters
muls = []; mugs = []; rhols = []; rhogs = []; vs = []; Ps = [P]
rhotots = []

# Enthalpies
HsH2OG = []; HsH2OL = []; HsH2O = []; HsO2 = []; HsDelta = []

# Flow rates
FGs = []; F_TOTs = []; F_H2O2_Ls = []; F_H2O2_Gs = []
F_H2Os = []; F_H2O2s = []; F_H2OsG =[]; F_O2s = []

# Liquid/gas fractions
epss_l = []; epss_g = []

''' Flow initial conditions '''
# Flow rates
F_H2O2_L = CONC_0 * FA0 * ( 1. - VAP_FRACTION_H2O2_0 ) * 1000 / MW_H2O2
F_H2O2_Ls.append(F_H2O2_L)

F_H2O2_G = CONC_0 * FA0 * VAP_FRACTION_H2O2_0 * 1000 / MW_H2O2
F_H2O2_Gs.append(F_H2O2_G)

F_H2O2 = F_H2O2_L + F_H2O2_G; F_H2O2s.append(F_H2O2)
F_H2O = (1-CONC_0) * FA0 * 1000. / MW_H2O; F_H2Os.append(F_H2O)
F_H2O_L = F_H2O * (1. - VAP_FRACTION_H2O_0)
F_H2O_G = F_H2O * VAP_FRACTION_H2O_0; F_H2OsG.append(F_H2O_G)
F_O2 =  0; F_O2s.append(F_O2)
F_G = F_H2O2_G + F_H2O_G + F_O2; FGs.append(F_G)
F_L = F_H2O2_L + F_H2O_L; F_TOT = F_G + F_L; F_TOTs.append(F_TOT)

# Mole fractions
FrH2OL = F_H2O_L / F_L; FrH2O2L = F_H2O2_L / F_L; FrL = F_L/F_TOT;
FrH2O2G = F_H2O2_G / F_G; FrH2OG = F_H2O_G / F_G; FrO2G = F_O2 / F_G;
```

```
FrG = F_G/F_TOT;

# Molar weights
MW_L = FrH2O2L * MW_H2O2 + FrH2OL * MW_H2O
MW_G = FrH2O2G * MW_H2O2 + FrH2OG * MW_H2O + FrO2G * MW_O2

# Liquid/gas fraction
Eps_l = FrL*MW_L/(FrL*MW_L+FrG*MW_G)
Eps_g = FrG*MW_G/(FrL*MW_L+FrG*MW_G)
epss_l.append(Eps_l)
epss_g.append(Eps_g)

# Mass fractions
mFrH2OL = FrH2OL * MW_H2O / (FrH2OL * MW_H2O + FrH2O2L * MW_H2O2)
mFrH2O2L = FrH2O2L * MW_H2O2 / (FrH2OL * MW_H2O + FrH2O2L * MW_H2O2)

# Densities
rho_H2O_l = rhoH2O_l(T)
rho_H2O2_l = rhoH2O2_l(T)
rho_g = P/((Rc*1000/MW_G)*T)
rho_l = 1./ (mFrH2OL/rho_H2O_l + mFrH2O2L/rho_H2O2_l)
rhotot = 1./(Eps_l/rho_l + Eps_g/rho_g)

# Velocities
v = FA0/(rhotot*A_surf*eps_f)
vg = [v]
vs = [v]
evaporated1 = 0

''' MAIN LOOP '''
started = False
while L < Lbed: # Simulate over the full catalyst bed length

    if T > 550: # Increase resolution at high temperatures (high reaction rate)
        dL = 0.000001

    if started == True:
        if T == Ts[-2]:
            dL = 0.01
    started = True

    L += dL; Ls.append(L) # Make step (first order forward)

    ''' DECOMPOSITION REACTION CALCULATIONS '''

    # Calculate catalyst reaction surface
    AS_L = AS * Eps_l
    AS_G = AS * Eps_g

    # Reaction rate constants
    Kc_g = 10.*np.exp(-4.18E3/Rc/T) * AS_G * (1. - DEG)
    Kt_g = 1.0E15*np.exp(-2E5/Rc/T)
    Kc_l = 2.6E4*np.exp(-52.5E3/Rc/T) * AS_L * (1. - DEG)
    Kt_l = 6.3E5*np.exp(-71E3/Rc/T)

    Kcgs.append(Kc_g); Kcls.append(Kc_l)
    Ktgs.append(Kt_g); Ktls.append(Kt_l)

    # Reaction rates
    ra_g = -(Kc_g + Kt_g)*CONC_H2O2_G; ra_l = -(Kc_l + Kt_l)*CONC_H2O2_L
    rasg.append(ra_g); rasl.append(ra_l)

    if X == 1:
        ra_g = 0
        ra_l = 0
```

```
# Conversion per phase
dXg_dL = -ra_g / ( CONC_0 * FA0 * VAP_FRACTION_H2O2 * 1000. / MW_H2O2 )\
                * A_surf
dXl_dL = -ra_l / ( 1e-7 + CONC_0 * FA0 * (1. - VAP_FRACTION_H2O2) * 1000.\
                  / MW_H2O2 ) * A_surf

# Change to overall conversion rate
DFH2O2G = dXg_dL * dL * F_H2O2_G
DFH2O2L = dXl_dL * dL * F_H2O2_L
DFH2O2 = DFH2O2L + DFH2O2G
dX = DFH2O2/F_H2O2s[0]
X += dX; X = min(X,1); Xs.append(X)

# Updated vapour pressure (part of non physical evaporation calculation)
VAP_H2O2 = VapPressCalc('H2O2', T)
VAP_H2O = VapPressCalc('H2O', T)

if (VAP_H2O2/P) < 1:
    VAP_FRACTION_H2O2 = VAP_H2O2 / P
else:
    VAP_FRACTION_H2O2 = 1.

if (VAP_H2O/P) < 1:
    VAP_FRACTION_H2O = VAP_H2O / P
else:
    VAP_FRACTION_H2O = 1.

''' FLOW RATE AND FRACTION CALCULATIONS '''
# Updated flow rates (mol/s)
## Total flow rates (using conversion X)
F_H2O2 = CONC_0 * FA0 * 1000 / MW_H2O2 * (1. - X)
F_H2O = F_H2Os[0] + CONC_0 * FA0 * 1000. / MW_H2O2 * X
F_O2 = CONC_0 * FA0 * 1000. / MW_H2O2 * 0.5 * X

## Liquid/Gas updates using vapour fraction assumption (mol/s)
F_H2O2_L = F_H2O2 * (1. - VAP_FRACTION_H2O2);
F_H2O2_G = F_H2O2 * VAP_FRACTION_H2O2;
F_H2O_L = F_H2O * (1. - VAP_FRACTION_H2O)
F_H2O_G = F_H2O * VAP_FRACTION_H2O;

## Gas, Liquid and Total flow rate (mol/s)
F_G = F_H2O2_G + F_H2O_G + F_O2
F_L = F_H2O2_L + F_H2O_L
F_TOT = F_G + F_L;

if F_L == 0 and evaporated1 == 0:
    print T
    evaporated1 = 1

## Storing data
F_H2O2s.append(F_H2O2); F_H2Os.append(F_H2O); F_O2s.append(F_O2)
F_H2O2_Ls.append(F_H2O2_L); F_H2O2_Gs.append(F_H2O2_G)
F_H2OsG.append(F_H2O_G)
FGs.append(F_G); F_TOTs.append(F_TOT)

## Gas molar fractions and molar weight
FrH2O2G = F_H2O2_G / F_G;
FrH2OG = F_H2O_G / F_G;
FrO2G = F_O2 / F_G;
ygis = [FrH2O2G, FrH2OG, FrO2G]
MW_G = FrH2O2G * MW_H2O2 + FrH2OG * MW_H2O + FrO2G * MW_O2

## Liquid molar fractions, mass fractions and molar weight
if F_L > 0:
```

```
    FrH2OL = F_H2O_L / F_L
    FrH2O2L = F_H2O2_L / F_L
    mFrH2OL = FrH2OL ∗ MW_H2O / (FrH2OL ∗ MW_H2O + FrH2O2L ∗ MW_H2O2)
    mFrH2O2L = FrH2O2L ∗ MW_H2O2 / (FrH2OL ∗ MW_H2O + FrH2O2L ∗ MW_H2O2)
    MW_L = FrH2O2L ∗ MW_H2O2 + FrH2OL ∗ MW_H2O

else:
    FrH2OL = 0
    FrH2O2 = 0
    mFrH2OL = 0
    mFrH2O2L = 0
    MW_L = 0

## Molar Fraction liquid/gas flow
FrL = F_L/F_TOT;
FrG = F_G/F_TOT;

## Mass fractions liquid/gas flow
Eps_l = FrL∗MW_L/(FrL∗MW_L+FrG∗MW_G)
Eps_g = FrG∗MW_G/(FrL∗MW_L+FrG∗MW_G)
epss_l.append(Eps_l)
epss_g.append(Eps_g)

''' HEAT CALCULATIONS '''
# Updated Cps
Cp_H2O2_L = Cp('H2O2', 'L', T); Cp_H2O2_G = Cp('H2O2', 'G', T)
Cp_H2O_L = Cp('H2O', 'L', T); Cp_H2O_G = Cp('H2O', 'G', T)
Cp_O2 = Cp('O2', 'G', T)

# Updated Enthalpies
H_H2O_G = H('H2O', 'G', T)
H_H2O_L = H('H2O', 'L', T)
H_O2 = H('O2', 'L', T)
H_H2O2_G = H('H2O2', 'G', T)
H_H2O2_L = H('H2O2', 'L', T)

H_H2O = VAP_FRACTION_H2O ∗ H_H2O_G + (1. − VAP_FRACTION_H2O) ∗ H_H2O_L
H_H2O2 = VAP_FRACTION_H2O2 ∗ H_H2O2_G + (1. − VAP_FRACTION_H2O2) ∗ H_H2O2_L

# Enthalpy change
delta_H = (H_H2O + 0.5 ∗ H_O2 − H_H2O2_0 − H_H2O_0) ∗ 1000

# Storing tables
HsH2OG.append(H_H2O_G)
HsH2OL.append(H_H2O_L)
HsH2O.append(H_H2O)
HsO2.append(H_O2)
HsDelta.append(delta_H)

# Updated Temperature
dT_dL = (ra_g + ra_l) ∗ A_surf ∗ eps_f ∗ (delta_H)/(F_H2O2_G ∗\
        Cp_H2O2_G + F_H2O2_L ∗ Cp_H2O2_L + F_H2O_L ∗ Cp_H2O_L +\
        F_H2O_G ∗ Cp_H2O_G + F_O2 ∗ Cp_O2)
T += dT_dL ∗ dL; Ts.append(T)

''' UPDATED FLUID PROPERTIES '''
#Densities, fractions
rho_H2O_l = rhoH2O_l(T); rho_H2O2_l = rhoH2O2_l(T)
rho_g = P/((Rc∗1000/MW_G)∗T)

CONC_H2O2_G = F_H2O2_G/(Eps_g∗FA0/rho_g); CONC_H2O2_Gs.append(CONC_H2O2_G)

if F_L > 0:
    rho_l = 1./ (mFrH2OL/rho_H2O_l + mFrH2O2L/rho_H2O2_l)
    rhotot = 1./(Eps_l/rho_l + Eps_g/rho_g)
```

```
        CONC_H2O2_L = F_H2O2_L/(F_L*MW_L/1000./rho_l)

    else:
        rho_l = 0
        rhotot = rho_g
        CONC_H2O2_L = 0

    rhotots.append(rhotot); rhols.append(rho_l); rhogs.append(rho_g)

    #Velocities
    v = FA0/(rhotot*A_surf*eps_f); vs.append(v)

    #Viscosities
    if F_L > 0:
        mu_L = viscliq(FrH2O2L, T)
    else:
        mu_L = 0

    if F_G > 0:
        mu_G = ViscG_Mix(T, ygis)
    else:
        mu_G = 0

    muls.append(mu_L); mugs.append(mu_G)

    ''' Pressure Drop Tallmadge (from Koopmans) '''
    v0l = v * eps_f # Superficial velocity
    DPoverL = K * mu_L * v0l + eta * rho_l**(5./6.) * v0l**(11./6.)\
                * mu_L**(1./6.)
    DPoverLg = K * mu_G * v0l + eta * rho_g**(5./6.) * v0l**(11./6.)\
                * mu_G**(1./6.)

    if P > 1e5: # Stop when pressure reached 1 bar (model will break at low P)
        P -= (DPoverL + DPoverLg) * dL  *1000
    Ps.append(P)

''' PLOTTING FIGURES '''
plt.figure()

# Length vs. Conversion
plt.subplot(421)
plt.title('Length vs. Conversion (X)')
plt.grid()
plt.plot(Ls, Xs)
plt.xlabel('Length [m]')
plt.ylabel('Conversion [-]')

# Length vs. Temperature
plt.subplot(422)
plt.title('Length vs Temperature')
plt.grid()
plt.plot(Ls, Ts)
plt.xlabel('Length [m]')
plt.ylabel('Temperature [K]')

#Length vs. Fluid density
plt.subplot(423)
plt.title('Length vs. Fluid density')
plt.plot(Ls[0:-1], rhols)
plt.plot(Ls[0:-1], rhogs)
plt.plot(Ls[0:-1], rhotots)
plt.xlabel('Length [m]')
plt.ylabel('Density [kg/m^3]')
plt.legend()
```

```
# Viscosities vs. Temperature
plt.subplot(424)
plt.title('Viscosity vs. Temp')
plt.plot(Ts[0:-1], muls, label = 'l')
plt.plot(Ts[0:-1], mugs, label = 'g')
plt.xlabel('T [K]')
plt.ylabel('Viscosity [Pa s]')
plt.legend()

#Length vs. Velocity
plt.subplot(425)
plt.title('Length vs. Velocity')
plt.plot(Ls, vs)
plt.xlabel('Length [m]')
plt.ylabel('Velocity [m/s]')

#Length vs. Pressure
plt.subplot(426)
plt.title('Length vs. Pressure')
plt.plot(Ls, np.array(Ps)/1e5) #display in bar
plt.xlabel('Length [m]')
plt.ylabel('Pressure [Bar]')

# Calculatie species mole fractions
FractionsH2O2 = (np.array(F_H2O2_Ls) + np.array(F_H2O2_Gs))/np.array(F_TOTs)
FractionsH2O = np.array(F_H2Os)/np.array(F_TOTs)
FractionsO2 = np.array(F_O2s)/np.array(F_TOTs)

# Length vs. Species mole fractions
plt.subplot(427)
plt.title('Length vs. Mole fractions')
plt.plot(Ls, FractionsH2O2, label = 'H2O2')
plt.plot(Ls, FractionsH2O, label = 'H2O')
plt.plot(Ls, FractionsO2, label = 'O2')
plt.xlabel('Length [m]')
plt.ylabel('Mole Fraction [-]')
plt.legend()

# Enthalpies
plt.subplot(428)
plt.plot(Ls[0:-1], HsH2OL, label = 'H2O L')
plt.plot(Ls[0:-1], HsH2OG, label = 'H2O G')
plt.plot(Ls[0:-1], HsH2O, label = 'H2O Tot')
plt.plot(Ls[0:-1], HsO2, label = 'O2')
plt.xlabel('Length [m]')
plt.ylabel('Enthalpy [kJ/mol]')

plt.show()
```